NASA Contractor Report 3186

Effects of Precursor Heating on Radiative and Chemically Reacting Viscous Flow Around a Jovian Entry Body

S. N. Tiwari and K. Y. Szema

GRANT NSG-1492
OCTOBER 1979

NASA

NASA Contractor Report 3186

Effects of Precursor Heating on Radiative and Chemically Reacting Viscous Flow Around a Jovian Entry Body

S. N. Tiwari and K. Y. Szema
Old Dominion University Research Foundation
Norfolk, Virginia

Prepared for
Langley Research Center
under Grant NSG-1492

National Aeronautics
and Space Administration

Scientific and Technical
Information Branch

1979

TABLE OF CONTENTS

(continued)

TABLE OF CONTENTS - CONCLUDED

LIST OF TABLES

LIST OF FIGURES

(continued)

LIST OF FIGURES - CONTINUED

(continued)

LIST OF FIGURES - CONTINUED

(continued)

LIST OF FIGURES - CONTINUED

(continued)

LIST OF FIGURES - CONCLUDED

SUMMARY

The influence of changes in the precursor region flow properties (resulting from absorption of the radiation from the shock layer) on the entire shock-layer flow phenomena around a Jovian entry body is investigated under physically realistic conditions. In the precursor region, the flow is considered to be inviscid and the variations in flow properties are determined by employing the small perturbation technique as well as the thin-layer approximation. The flow in the shock layer is assumed to be steady, axisymmetric, and viscous. The analysis is carried out by considering both the chemical equilibrium and nonequilibrium composition of the shock-layer gas. The effects of transitional range behavior (slip boundary conditions on the body surface and at the shock wave) are included in the analysis of high altitude entry conditions.

Realistic thermo-physical and radiation models are used, and results are obtained by employing the implicit finite difference technique in the shock layer and an iterative procedure for the entire shock layer-precursor zone. Results obtained for a 45° hyperboloid blunt body entering Jupiter's atmosphere at zero angle of attack indicate that preheating of the gas significantly increases the static pressure and temperature ahead of the shock for entry velocities exceeding 36 km/sec. The nonequilibrium radiative heating rate to the body is found to be significantly higher than the corresponding equilibrium heating. The precursor heating, in general, increases the radiative and convective heating to the body, and this increase is slightly higher for the nonequilibrium conditions.

LIST OF SYMBOLS

A_ν radiative strength of source, ergs (Eq. 7.22)

a_ν quantity defined in (Eq. 7.8a), in cm-sec/erg

b_ν quantity defined in (Eq. 7.8b)

C_i mass fraction of species i in the shock layer, ρ_i/ρ

C_α mass fraction of species in the precursor zone

C_P equilibrium specific heat of mixture, $\Sigma C_i\ C_{P,i}$

$C_{P,i}$ specific heat of species i, $C^*_{P,i}/C^*_P$

D dissociation energy, erg/mole

D_{ij} binary diffusion coefficient

F_j perturbation potential function (Eq. 7.27)

G_j quantity defined in (Eq. 7.28a)

H_j quantity defined in (Eq. 7.28b)

H_T total enthalpy, $h = (u^2 + v^2)/2$

H_ν specific irradiance of frequency ν, erg/cm^2

$H_{o\alpha}$ enthalpy of species α, cal/mole

h specific enthalpy, h^*/V^{*2}, (also Planck constant)

h" specific enthalpy, erg/gm

I ionization energy, erg/mole

J_i mass diffusion flux of species i, $J^*_i\ R^*_N/\mu^*_{ref}$

K_H net rate of production of species H, gm/cm^3-sec

$H_{H_{2+}}$ net rate of production of species H_{2+}, gm/cm^3-sec

K_α net rate of production of species α, gm/cm^3-sec

k thermal conductivity of mixture, $k^*/\ ^*_{ref}\ C^*_P$, ' (also Boltzmann constant)

Le Lewis number, $\rho^*\ D^*_{ij}\ C^*_P/k^*$

M^*	molecular weight of mixture
M	free stream Mach number
m_1	net weight of a H_2 molecule, gm/molecule
N_{H_2}	number density of H_2
n	coordinate normal to the bow shock, n^*/R_N^*
P	pressure, $P^*/(\rho_\infty^* V_\infty^{*2})$
Pr	Prandtl number, $\mu^* C_p^*/k^*$
P	quantity defined in (Eq. 7.7b)
Q_R	divergence of net radiant heat flux, erg/cm^3-sec
q_R	net radiant heat flux, $q_R^*/(\rho_\infty^* V_\infty^{*3})$
q (0)	specific radiative flux density at shock wave, erg/cm^2
R	universal gas constant = 8.3143E7 erg/mole-K
R_c	radius of the radiating gas cap, cm
R_s	radius of the bow shock wave, cm
R^*	universal gas constant
R_b^*	radius of the body
R_N^*	body nose radius (same as R_n^*)
R_s^*	radius of the bow shock
r	radius measured from axis of symmetry to a point on the body surface, r^*/R_N^*
r_s	radius measured from axis of symmetry to a point on the bow shock, r_s^*/R_N^*
s	coordinate along the bow shock, s^*/R_N^*
T	temperature, T^*/T_{ref}^*
T^*	dimensional temperature
R_{ref}^*	reference temperature, $V^*/C_{p\infty}^*$
u	velocity tangent to body surface, u^*/V_∞^*

u'	velocity tangent to bow shock, cm/sec
v	velocity normal to doby surface, u^*/V_∞^*
v'	velocity normal to bow shock, cm/sec
x	coordinate along the body surface, x^*/R_N^*
Y_D	photodissociation yield
Y_I	photoionization yield
y	coordinate normal to the body surface, y^*/R_N^*
Z	altitude of entry, km (Table 1)
α	shock angle defined in Fig. 1
ε	Reynolds number parameter or surface emittance
θ	body angle defined in Fig. 1
η	transformed y coordinate, y/y_s
κ	body curvature, κ^*/R_N^*
κ_ν	spectral absorption coefficient
μ	viscosity of mixture, $\mu^*/{}^*_{ref}$
μ_{ref}	reference viscosity, $\mu^*(T^*_{ref})$
ξ	coordinate along the body surface, $\xi = x$
ρ	density of mixture, ρ^*/ρ_∞^*
σ	Stefan Boltzmann constant
τ	optical coordinate
τ_o	optical thickness
ϕ	potential function defined in (Eq. 7.11)
Φ	potential function defined in (Eq. 7.3)

Subscripts

i	ith species
s	shock value
w	wall value
∞	free-stream condition
ν	radiation frequency
1	first order perturbation quantities

1. INTRODUCTION

A space vehicle entering a planetary atmosphere encounters a wide range of flow conditions ranging from free molecular flow at high altitudes to continuum flow at low altitudes. Since experimental facilities cannot adequately simulate conditions expected during entry into the outer planetary atmospheres, most of the required information must be obtained from theoretical studies.

During the high speed entry, the atmospheric friction works as a brake to slow the spacecraft and the gas around the body in the formed shock layer is heated by the dissipated kinetic energy. Radiation plays a very important role in the analysis of flow phenomena around an entry body at high speeds. In many instances, the radiative energy transferred to the body from the high temperature shock layer gas exceeds the convective and aerodynamic heat transfer. Radiative energy transfer from the shock layer of a blunt body into the free stream reduces the total enthalpy of the shock layer while increasing the enthalpy of the free stream gases. Because of this increase in enthalpy, the entire flow field ahead of the shock layer and around the body is influenced significantly. The phenomena of change in flow properties ahead of the shock wave due to the energy interaction from the shock layer is called the "praecursor" or "praecurrere" (prae = before + currere = run) which means "forerunner." In the present context, therefore, the precursor flow region is considered to be the region ahead of a shock wave in which the flow field parameters have been changed from free stream conditions due to absorption of radiation from the incandescent shock layer. Most of the radiative energy transferred from the shock layer into the

cold region ahead of the shock is lost to infinity unless it is equal to or greater than the energy required for dissociation of the cold gas. When the photon energy is greater than the dissociation energy, it is strongly absorbed by the cold gas in the ultraviolet continuum range. The absorbed energy dissociates and ionizes the gas and this results in a change of flow properties in the precursor region. In particular, the temperature and pressure of the gas is increased while velocity is decreased. The change in flow properties of the precursor region, in turn, influences the flow characteristics within the shock layer itself. The problem, therefore, becomes a coupled one and iterative methods are required for its solution.

Only a limited number of analyses on radiation induced precursor flow is available in the literature. Works available until 1968 are discussed, in detail, by Smith [1,2]*. By employing the linearized theory of aerodynamics, Smith investigated the flow in the precursor region of a reentry body in the earth's atmosphere. The cases of plane, spherical, and cylindrical point sources were considered and solutions were obtained for a range of altitudes and free stream conditions. It was found that for velocities exceeding 18 km/sec, precursor flow effects are greatest at altitudes between 30 and 46 km. It was further concluded that preheating of air may cause an order of magnitude increase in the static pressure and temperature ahead of the shock wave for velocities exceeding 15 km/sec. A few other works, related to the effects of upstream absorption by air on the shock layer radiation, are discussed by Liu [3,4]. Some works on precursor ionization for air as well as hydrogen-helium atmosphere are presented in [5-9].

---

* The numbers in brackets indicate references.

In the analysis of most shock-layer flow phenomena, the contribution of radiation-induced precursor effects usually is neglected. Garrett [10] presented a detailed review of the various methods used for solving the radiating flow field at the stagnation region. Also, various methods of solution of radiating shock layer are discussed by Anderson [11]. Sutton [12] separated the radiating flow field into an outer inviscid layer and an inner boundary layer; the two solutions are coupled by radiative transport through both layers and by the boundary displacement thickness. Kumar, Tiwari, and Graves [13] considered the entire shock layer as viscous flow region and used a time-dependent method to obtain the solutions for small angle of attack. Davis [14] presented a method for solving the viscous shock-layer equations for stagnation and down stream flow. Moss [15-17] applied this method of solution to reacting multicomponent mixtures. The precursor effects were neglected in all the above studies. However, a limited number of studies which include this effect are available in the literature. Lasher and Wilson [18,19] investigated the level of precursor absorption and its resultant effect on surface radiation heating for earth's entry conditions. They concluded that, for velocities less than 18 km/sec, precursor heating effects are relatively unimportant in determining the radiative flux reaching the surface. At velocities greater than 18 km/sec, the amount of energy loss from the shock layer and resultant precursor heating correction was found to be significantly large. Liu [3,4] also investigated the influence of upstream absorption by cold air on the stagnation region shock layer radiation. The thin layer approximation was applied to both the shock layer and the preheating zone (the precursor region). The problem was formulated for inviscid

flow over smooth blunt bodies but the detailed calculations were carried out only for the stagnation region. The general results were compared with results of two approximate formulations. The first approximate formulation neglects the upstream influence and the second one essentially uses the iterative procedure described by Lasher and Wilson [18,19]. The results are compared for different values of a radiation/convection parameter.

As mentioned earlier, the cold gas absorbs energy only by photodissociation and photoionization in the precursor region. The absorption coefficients are a continuous nonzero function of photon energy (because of bound-free transition) for all values of photon energy exceeding the dissociation potential of the molecule. A critical review of ultraviolet photoabsorption cross sections for molecules of astrophysical and aeronomical interest, available in the literature up to 1971, are given by Hudson [20]. Specific information on photoionization and absorption coefficients of molecular hydrogen is available in [20,21].

In the shock layer region, the gas may be treated as gray or nongray. Anderson [11] concluded that a gray gas analysis is not sufficiently accurate for entry applications and suggested use of nongray models. The frequency dependence of the absorption of coefficient for a nongray gas may be treated either in detail or by a "step model." There exists several computer programs for the detailed frequency dependence of the absorption coefficient which are developed by Nicolet [22], Wilson [23], and Thomas [24]. In a step model, the frequency dependence is broken into a number of discrete steps. Falanga and Olstad [25] presented a 38-step model for 90% CO_2 and 10% N_2 (by

volume) mixture which included 15 steps to model the continuum and 23 steps to model the line contribution to the radiation transport. Zoby, Sutton, and Moss [26] developed a 58-step model for hydrogen and helium mixture. The transitions considered in this model are: the bound-bound, bound-free and free-free transitions for atomic hydrogen, the bound-free and free-free transitions for the negative hydrogen ion, and the Lyman and Werner band systems for molecular hydrogen. This 58-step model is fairly accurate and compares very well with the results of Nicolet's detailed model for hydrogen/helium species [27].

The total radiative transport is an integral over both the frequency spectrum and the physical space. The methods for calculating the divergence of the radiative flux and other conservation equations are available in [28-30].

It is very well documented in the literature that the degree of rarefraction of a flow is measured by the Reynolds number. Therefore, for a fixed blunt body at low altitudes where the Reynolds number is high, the flow will behave like an ordinary viscous flow which lies within the scope of the Navier-Stokes equations. At higher altitudes, where the Reynolds number is low, the theory of free molecular flow can be used. The transition zone between these two regions has been divided into several subregions which are discussed in greater detail by Hayes and Probstein [31], and Cheng [32] has provided the different methods of solution valid within each region. In the continuum range, the flow phenomena is investigated through use of the Navier-Stokes equations. In the transition range (from the continuum end), however, use of the Navier-Stokes equations is still justified for the main flow field but the boundary conditions cannot be satisfied in the usual manner. Thus,

the characteristic feature of flow of a slightly rarefied gas, which sharply distinguishes it from the continuum flow, is the change in the boundary conditions at the body surface [33] and shock wave [34-35]. Instead of using the Rankine-Hugoniot conditions as boundary conditions at the shock wave, Probstein and Pan [34,35] introduced the concept of "shock wave slip" as interpretation of the transported effects behind the shock. Rott and Lenard [36] have shown that the effects of velocity slip and temperature jump on the body surface cannot be neglected in comparison with other low Reynolds number corrections. A semi-macroscopic argument which leads to the simple expression for velocity slip and temperature jump is given in [33,36].

From the literature survey, it is quite clear that no work is available which considers the influence of precursor heating on the shock layer flow phenomena around a Jovian entry body. A few studies that are available deal only with the case of chemical equilibrium in the shock layer; the case of shock layer chemical nonequilibrium flow has not been considered. Also, no consideration has been given to investigate the transitional range shock layer flow phenomena encountered at high Jovian entry altitudes. In an actual entry situation, the influence of precursor heating, nonequilibrium chemistry in the shock layer, and transitional range flow phenomena may be strongly coupled. Thus, it is essential to investigate the extent of influence of each phenomena separately and jointly in order to assess the true behavior of flow around the entry body. This information is of vital importance in determining the convective and radiative heating of the entry body.

The main purpose of this study, therefore, is to investigate the influence of changes in the precursor region flow properties on the

entire shock layer flow phenomena around a Jovian entry body. The cases of shock layer chemical equilibrium as well as chemical nonequilibrium are considered, and the effects of transitional range behavior are included in the analyses of high altitude entry conditions. In order to accomplish these objectives in a systematic manner, the entire problem has been divided into four subproblems as:

1. Investigation of the radiation induced precursor region flow phenomena.
2. Effects of shock and body slip conditions on viscous equilibrium flow.
3. Influence of precursor heating on viscous equilibrium flow.
4. Influence of precursor heating on viscous nonequilibrium flow.

Basic formulation of the entire problem is presented in Chap. 2. The boundary conditions for different flow regimes are given in Chap. 3. Information on thermodynamic and transport properties for each species considered in different flow regimes are given in Chap. 4. Information on chemical reactions and reaction rates for both equilibrium and non-equilibrium conditions are given in Chap. 5. Discussions on radiation models and radiative flux equations are presented in Chap. 6. Solution procedures for the precursor and shock layer regions are discussed, in some detail, in Chap. 7. Discussions of all results are presented in Chap. 8.

2. BASIC FORMULATION

The physical model and coordinate system for a Jovian entry body is shown in Fig. 1. The entire flow field ahead of the body can be divided essentially into three regions: the free stream, the precursor region, and the shock layer. The flow properties are considered to be uniform at large distances from the body. In this section, governing equations are presented for the precursor as well as shock layer region. However, it would be appropriate here to discuss first the Jovian atmospheric and entry conditions.

2.1 Free-Stream Region

Information on Jupiter's atmospheric conditions are available in [37-39]. In the past, the nominal composition of the atmosphere was assumed to be 85 percent hydrogen and 15 percent helium by mole fraction. Recently, this has been changed to 89 percent hydrogen and 11 percent helium [39]. For different altitudes of entry, the free-stream conditions used in this study are given in Tables 1 and 2. The temperature of the atmosphere (i.e., T_∞) is taken to be constant at 145 K and the free-stream enthalpy can be calculated by following the procedure given in [1,2] as

$$H_\infty = 1.527\ R\ T_\infty \tag{2.1}$$

where R = 8.315 Joules/K-mole is the universal gas constant. The number density of hydrogen can be calculated by the ideal gas law and the relation can be expressed as

$$N_{H_2} = (7.2431172 \times 10^{22})\ (P_\infty/T_\infty) X_{H_2} \tag{2.2}$$

where X_{H_2} is the mole fraction of H_2 and P_∞ has the units of N/m^2.

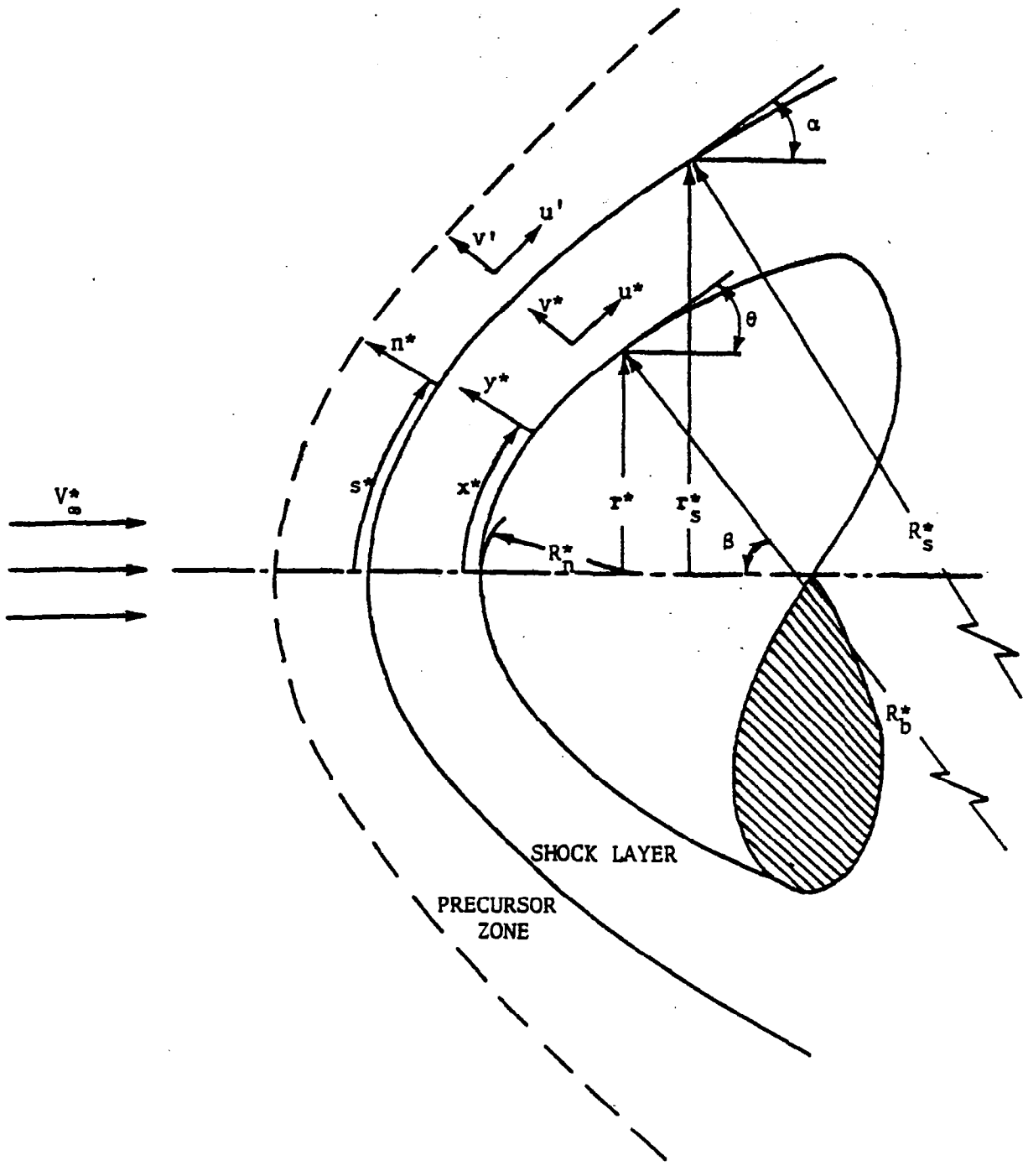

Fig. 1 Curvilinear orthogonal coordinate systems for thin-layer approximation.

Table 1 Altitude and free-stream Jupiter entry conditions.

Z km	$\bar{V}_\infty$ cm/sec	ρ_∞ g/cm^3	T_∞ K	p_∞ dyne/cm^2	$\rho_\infty \bar{V}^3_\infty$	ε
116	3.909E6	4.65E-7	145	2.44E3	2.777E13	0.006645
143	4.517E6	1.27E-7	145	6.66E2	1.17E13	0.01272
190	4.736E6	1.33E-8	145	69	1.412E12	0.03930
225	4.756E6	2.50E-9	145	13	2.69E11	0.09064
261	4.758E6	4.53E-10	145	2.38	4.879E10	0.2129

Table 2 Free-stream and shock conditions for Jovian entry.

Free stream	V_∞, km/sec	T_s, K	q(0), erg/cm^2
Z = 95, km	38	16,610	1.35 E12
ρ_∞ = 1.29 E-3, kg/m^3	35	15,400	7.75 E11
P = 673, N/m	32	14,080	3.52 E11
	30	13,550	2.01 E11
Z = 103	40	16,890	1.16 E11
ρ_∞ = 8.56 E-4	35	15,040	4.70 E11
P_∞ = 448	33	14,250	3.28 E11
	30	12,810	1.142 E11
Z = 116	45	18,227	1.09 E12
ρ_∞ = 4.65 E-4	39.09	15,886	4.76 E11
P_∞ = 244	35	14,480	2.18 E11
	30	12,480	4.87 E10
Z = 131	43.21	16,390	3.86 E11
ρ_∞ = 2.32 E-4	38	15,210	1.61 E11
P_∞ = 122	35	13,880	8.72 E10
	30	12,030	1.90 E10
Z = 150	42	15,050	9.60 E10
ρ_∞ = 9.29 E-5	40	14,520	6.96 E10
P_∞ = 49	35	13,140	2.57 E10
	30	11,600	6.20 E9

2.2 Precursor Region

In this region, the flow is considered to be steady and inviscid. To investigate the changes in flow properties in this region, both the small perturbation theory of classical aerodynamics and the thin-layer approximation of hypersonic flow have been used in this study. Fundamental principles of these approximations are briefly discussed in the following subsections.

2.2.1 Small Perturbation Theory

For application of the small perturbation theory, basic conservation equations for the precursor region can be written as [40,41]

Mass Continuity:

$$\nabla \cdot (\rho \bar{V}) = 0 \tag{2.3}$$

Momentum:

$$\rho (\bar{V} \cdot \nabla \bar{V}) = -\nabla p \tag{2.4}$$

Energy:

$$\rho (\bar{V} \cdot \nabla H_T) = Q_R \tag{2.5}$$

Species Continuity:

$$\rho (\bar{V} \cdot \nabla C_\alpha) = K_\alpha \tag{2.6}$$

State:

$$p = \rho R T \sum_\alpha (C_\alpha / W_\alpha) \tag{2.7}$$

where the total enthalpy per unit mass is given by

$$H_T = H + V^2/2$$

In the above equations, $Q_R = \nabla \cdot q_R$ is the net rate of radiant energy absorbed per unit volume per unit time, K_α represents the net rate of production of species α per unit volume per unit time, and w_α is the molecular weight of species α.

As a result of increased fluid enthalpy, the entire flow field in the precursor region is perturbed. By following the small perturbation technique of classical aerodynamics, the flow properties can be expressed in perturbation series as [1,2, 40-43]

$$\rho = \rho_\infty (1 + \quad_1 + \quad_2 + \ldots) \tag{2.8a}$$

$$P = P_\infty (1 + P_1 + P_2 + \ldots) \tag{2.8b}$$

$$V = V_\infty (k + V_1 + V_2 + \ldots) \tag{2.8c}$$

$$H = H_\infty + V_\infty^2 (H_1 + H_2 + \ldots) \tag{2.8d}$$

$$T = T_\infty + T_1 + T_2 + \ldots \tag{2.8e}$$

$$C_\alpha = C_{\alpha\infty} + C_{\alpha 1} + C_{\alpha 2} + \ldots \tag{2.8f}$$

In these equations, all the perturbation variables (except temperature) are expressed in nondimensional form. The unit vector k represents the direction of unperturbed free-stream velocity.

If Q_R and K_α can be considered as first-order perturbation terms, then substitution of Eqs. (2.8) into Eqs. (2.3)-(2.7) results in the first-order perturbation equations as

Continuity:

$$\nabla \cdot \bar{V}_1 + \partial \rho_1 / \partial z = 0 \tag{2.9}$$

Momentum:

$$\partial \bar{V}_1 / \partial z = -(1/\gamma M_\infty^2) \nabla p \tag{2.10}$$

Energy:

$$\partial H_{T_1} / \partial z = Q_R / (\rho_\infty V_\infty^3) \tag{2.11}$$

Species:

$$\partial C_{\alpha_1} / \partial z = K_\alpha / (\rho_\infty V_\infty) \tag{2.12}$$

where

$$H_{T_1} = H_1 + V_{1z} \tag{2.13}$$

and γ represents the ratio of specific heats.

The boundary conditions are that perturbation quantities vanish at $z \to \infty$ and that no singularities exist except at the origin.

The radiation effect on the gas ahead of the shock produces H_2^+, H, and electrons e by photodissociation and photoionization, and also increases the enthalpy. Any other species which may be produced are neglected. The contribution of radiation to the gas pressure is neglected. It is further assumed that the internal degrees of freedom of various species (i.e., vibrational and electronic modes) are not exited. For this gas model, the equation of state (for the first order perturbation) can be expressed as [1,2]

$$P_1 = (400/180.17)\ [(C_H + C_{H_2^+})/2] + (T_1/T) + \rho_1 \tag{2.14}$$

By following the procedure described by Smith [1,2], the first-order perturbation relation for enthalpy is found to be

$$H_1 = (1/V_\infty^2)\ \{1.527\ RT_1 + [(5/4)RT_\infty + I/2]C_{H_2^+} + [(3/4)RT_\infty + D]C_H\} \tag{2.15}$$

where I and D represent the ionization and dissociation energy respectively. It should be pointed out here that D in the above equation actually represents half the energy required for dissociation.

As pointed out earlier, the upstream gas absorbs the energy radiated from the shock layer in the ultraviolet continuum range. The radiation from the perturbed gas due to recombination (i.e., emission) is neglected. The amount of radiative energy absorbed by the perturbed gas per unit volume and time, Q_R, is given by

$$Q_R = N_{H_2} \int_0^\infty H_\nu\ \sigma(\nu)d\nu \tag{2.16}$$

where N_{H_2} is the number density of H_2, H_ν is specific irradiance and $\sigma(\nu)$ is the photon absorption cross section of H_2 at frequency ν.

In determining the rate of production of species in the precursor region, only photodissociation and photoionization are considered. Recombination is assumed to be a second order effect and, therefore, is neglected in the present linearized treatment. The net rate of production of species, therefore, is given by [1, 28]

$$K_H = m_1 N_{H_2} \int_0^\infty (H_\nu/h\nu)\, \sigma_D(\nu) d\nu \tag{2.17a}$$

$$K_{H_2^+} = m_1 N_{H_2} \int_0^\infty (H_\nu/h\nu)\, \sigma_I(\nu) d\nu \tag{2.17b}$$

where m_1 represents the weight of an H_2 molecule (in grams per molecule), and $\sigma_D(\nu)$ and $\sigma_I(\nu)$ are the absorption cross section for photodissociation and photoionization, respectively.

2.2.2 Thin Layer Approximation

The concept of thin shock layer theory (usually applied to hypersonic shock layer flows [31]) is also applied to investigate the precursor effects. The curvilinear orthogonal coordinate system, shown in Fig. 1 is selected and the differential equations for a hypersonic plane or axisymmetric flow can be written in the present coordinate system as [42]

$$(\partial/\partial s)(\rho u r^j) + (\partial/\partial n)(\rho v X r^j) = 0 \tag{2.18}$$

$$\rho[u(\partial u/\partial s) + (Xv(\partial u/\partial n) - Kuv] + (\partial p/\partial s) = 0 \tag{2.19}$$

$$\rho[u(\partial v/\partial s) + Xv(\partial v/\partial n) + Ku^2] + X(\partial p/\partial n) = 0 \tag{2.20}$$

$$\rho[(u/X)(\partial H/\partial s) + v(\partial H/\partial n)] + (Xr^j)^{-1}[(\partial/\partial n)(Xr^j q_R)] = 0 \tag{2.21}$$

$$\rho[(u/X)(\partial C_\alpha/\partial s) + v(\partial C_\alpha/\partial n) - K_\alpha = 0 \tag{2.22}$$

where $K = K(s) = 1/R_s$, $X = 1 + Kn$, and $j = 0$, for plane flows and 1 for axisymmetric flows. It should be noted that, according to the notations

used in Fig. 1, all quantities appearing in the above equations should have a prime superscript (i.e., u', v', ρ', H', etc.), and all physical coordinates should have a superscript * (i.e., s*, n*, r*, etc.). However, for the sake of clarity, these notations have been omitted from the equations.

If the precursor region is assumed thin, then one can make the approximations that $(n/R_s)<<1$, $\partial/\partial s << \partial/\partial n$, and r^j is not a function of n. In this case X = 1, and Eqs. (2.18)-(2.22) reduce to simpler forms as [42]

$$(\partial/\partial n)\ (\rho v) = 0 \tag{2.23}$$

$$\rho v(\partial u/\partial n) = 0 \tag{2.24}$$

$$\rho v(\partial v/\partial n) + (\partial p/\partial n) = 0 \tag{2.25}$$

$$\rho v(\partial H/\partial n) + (\partial q_R/\partial n) = 0 \tag{2.26}$$

$$\rho v(\partial C_\alpha/\partial n) - K_\alpha = 0 \tag{2.27}$$

The similarity between these equations and the small perturbation Eqs. (2.9)-(2.12) should be noted.

In present application to the hydrogen-helium atmosphere, Eq. (2.27) will be written for atomic hydrogen and hydrogen ions. In Eq. (2.26), H represents the total enthalpy and is given by the relation

$$H = H_T = h + (u^2 + v^2)/2 \tag{2.28}$$

where

$$h" = 1.527\ RT + [(5/4)\ RT + I/2]C_{H_2^+} + [(3/4)RT + D]C_H \tag{2.29}$$

Note that Eq. (2.29) is slightly different than the relation for perturbation enthalpy given by Eq. (2.15).

2.3 Shock-Layer Region

In this region, the flow conditions for which the present analysis is carried out are axisymmetric, steady, laminar, viscous, and compressible. It is further assumed that the gas is in local thermodynamic equilibrium and the tangent slab approximation is valid for radiative transport. The reacting multicomponent gas mixture is treated in both chemical equilibrium and nonequilibrium conditions.

2.3.1 Chemical Equilibrium

The viscous shock layer conservation equations presented in [14-17] are a set of equations that are valid uniformly throughout the shock-layer region. The methods of obtaining these equations are discussed in detail in those references. First the conservation equations are written for both the inviscid and the boundary-layer regions in the body-oriented coordinate system. Then these equations are nondimensionalized in each of the two flow regions with variables which are of order one. Terms in the resulting sets of equations are retained up to second order in the inverse square root of Reynolds number. Upon combining these two sets of equations, so that terms up to second order in both regions are retained, a set of equations uniformly valid to second order in the entire shock layer is obtained. The nondimensional form of the viscous shock-layer equations that are applicable in the present case can be written as

Continuity:

$$(\partial/\partial x)\ [(r+y\cos\theta)\rho u] + (\partial/\partial y)\ [(1+y\kappa)(r+y\ x\cos\theta)\rho v]=0 \quad (2.30)$$

X-momentum:

$$\rho\left(\frac{u}{1+y\kappa}\frac{\partial u}{\partial x} + v\frac{\partial u}{\partial y} + \frac{uv\kappa}{1+y\kappa}\right) + \frac{1}{1+y\kappa}\frac{\partial p}{\partial x}$$
$$= \varepsilon^2\left\{\frac{\partial}{\partial y}\left[\mu\left(\frac{\partial u}{\partial y} - \frac{u\kappa}{1+y\kappa}\right)\right] + \mu\left(\frac{2\kappa}{1+y\kappa} + \frac{\cos\theta}{r+y\cos\theta}\right)\cdot\left(\frac{\partial u}{\partial y} - \frac{u\kappa}{1+y\kappa}\right)\right\} \quad (2.31)$$

Y-momentum:

$$\rho\left(\frac{u}{1+y\kappa}\frac{\partial v}{\partial x}+v\frac{\partial v}{\partial y}-\frac{u^2\kappa}{1+y}\right)+\frac{\partial p}{\partial y}=0 \tag{2.32}$$

Energy:

$$\begin{aligned}&\rho\left(\frac{u}{1+y\kappa}\frac{\partial H}{\partial x}+v\frac{\partial H}{\partial y}\right)-v\frac{\partial p}{\partial y}+\frac{p\kappa u^2 v}{1+y\kappa}\\&=\varepsilon^2\left\{\frac{\partial}{\partial y}\left[\frac{\mu}{Pr}\frac{\partial H}{\partial y}-\frac{\mu}{Pr}\sum_{i=1}^{N_s}h_i\frac{\partial C_i}{\partial y}-\sum_{i=1}^{N_s}h_i J_i+\frac{\mu}{Pr}(Pr-1)u\frac{\partial u}{\partial y}\right.\right.\\&\left.-\frac{\mu\kappa u^2}{1+y\kappa}\right]+\left(\frac{\kappa}{1+y\kappa}+\frac{\cos\theta}{r+y\cos\theta}\right)\left[\frac{u}{Pr}\frac{\partial H}{\partial y}-\frac{\mu}{Pr}\sum_{i=1}^{N_s}h_i\frac{\partial C_i}{\partial y}\right.\\&\left.\left.-\sum_{i=1}^{N_s}h_i J_i+\frac{\mu}{Pr}(Pr-1)u\frac{\partial u}{\partial y}-\frac{\mu\kappa u^2}{1+y\kappa}\right]\right\}-\left[\frac{\partial q_R}{\partial y}\right.\\&\left.+q_R\left(\frac{\kappa}{1+y\kappa}+\frac{\cos\theta}{r}\right)\right]\end{aligned} \tag{2.33}$$

where

$$H = h + u^2/2.$$

The terms used to nondimensionalize the above equations are defined as

$$\begin{aligned}
&x = x^*/R_n^* && v = v^*/V_\infty^* && Pr = C_p^*\mu^*/K^*\\
&y = y^*/R_n^* && \rho = \rho^*/\rho_\infty^* && Le_{ij} = \rho^* C_p^* D_{ij}^*/K^*\\
&r = r^*/R_n^* && \mu = \mu^*/\mu_{ref}^* && L_{ij} = \rho^* C_p^* D_{ij}^*/K^*\\
&K = K^*/(\mu_{ref} C_{p\infty}^*) && C_p = C_p^*/C_{p\infty}^* && p = p^*/(\rho_\infty^* V_\infty^{*2})\\
&q_R = q_R^*/(\rho_\infty^* V_\infty^{*3}) && \mu_{ref} = \bar{\mu}^*(V_\infty^{*2}/C_{p\infty}^*) && T = T^* C_{p\infty}^*/V_\infty^{*2}\\
&h = h^*/V_\infty^{*2} && \kappa = \kappa^*/R_n^* && u = u^*/V_\infty^*\\
&J_i = J_i^* R_n^*/\mu_{ref}^* && \varepsilon = \left[\mu_{ref}^*/(\rho_\infty^* V_\infty^* R_n^*)\right]^{1/2}
\end{aligned} \tag{2.34}$$

In Eq. (2.33), J_i represents the mass flux relative to the mass average velocity and is given by the expression [14,44]

$$J_i = -(\mu/Pr)\left[\sum_{K=1}^{NI} \bar{b}_{ik}\,(\partial C_K/\partial Y) + (L_i^T/T)\,(\partial T/\partial Y)\right] \qquad (2.35a)$$

where

$$\bar{b}_{iK} = \begin{cases} Le_i, & i = K \\ \Delta\bar{b}_{iK}, & i \neq K \end{cases}$$

$$Le_i = \sum_{\substack{j=1 \\ j\neq 1}}^{NI} \left(\frac{C_j}{M_j}\right) \sum_{\substack{j=1 \\ j\neq 1}}^{NI} (C_j/M_j L_{ij})$$

$$\Delta\bar{b}_{iK} = Le_i - \left\{ (M_i/M)Le_{iK} + [1-(M_i/M_K)] \sum_{j=1}^{NI} Le_{ij} C_j \right\}$$

The last term in Eq. (2.35a) represents the contribution of thermal diffusion. The quantity Le_{ij} represents the multi-component Lewis number, and L_{ij} represents the binary Lewis Semenov numbers; both are defined in Eq. (2.34). If thermal diffision can be neglected and L_{ij} can be taken as constant for all species, then Eq. (2.35a) reduces to

$$J_i = -(\mu/Pr)L_{ij}(\partial C_i/\partial y) \qquad (2.35b)$$

In the present study, use is made of Eq. (2.35b), and the value for L_{ij} is taken to be 1.1 [45,46].

The expression for the equation of state for a hydrogen/helium mixture is given by Zoby et al [47] as

$$T^* = C_T[(p^*/1013250)^{\ell}/(\rho^*/0.001292)^{K}] \qquad (2.36a)$$

$$H^* = C_H[(p^*/1013250)^{m}/(\rho/0.001292)^{n}](RT_o/M) \qquad (2.36b)$$

where

$$K = 0.65206 = 0.04407\ \ell n(X_{H2})$$

$$\ell = 0.67389 - 0.04637\ \ell n(X_{H_2})$$

$$m = 0.95252 - 0.1447\ \ell n(X_{H_2})$$

$$n = 0.97556 - 0.16149\ \ell n(X_{H_2})$$

$$U_t = V_\infty \sin\theta\ [1 + 0.7476(1-X_{H_2})]$$

$$CTU = -545.37 + 61.608\ U_t - 22459\ U_t^2 + 0.039922\ U_t^3 - 0.00035148\ U_t^4 + 0.0000012361\ U_t^5$$

$$CHU = 5.6611 - 0.52661\ U_t^2 + 0.020376\ U_t - 0.00037861\ U_t^3 + 0.0000034265\ U_t^4 - 0.000000012206\ U_t^5$$

$$C_T = CTU + 61.2\ (1-X_{H_2})$$

$$C_H = CHU - 0.3167(1-X_{H_2})$$

and H_{X_2} represents the mole fraction of H_2.

The set of governing equations presented above has a hyperbolic/parabolic nature. The hyperbolic nature enters through the normal momentum equation. If the shock layer is assumed to be thin, then the normal momentum equation can be expressed as

$$\rho u^2 \kappa/(1 + y\kappa) = (\partial p/\partial y) \qquad (2.37)$$

If Eq. (2.32) is replaced with Eq. (2.37), then the resulting set of equations is parabolic. These equations can, therefore, be solved by using numerical procedures similar to those used in solving boundary-layer problems [14,15].

2.3.2 Chemical Nonequilibrium

For the condition of chemical nonequilibrium, the basic governing equations (continuity, X-momentum, Y-momentum, and energy) are essentially the same as given for the chemical equilibrium condition. The

species continuity equation, however, is needed and this is given by the relation

$$\rho\left(\frac{u}{1+n\kappa}\frac{\partial c_i}{\partial s}+v\frac{\partial c_i}{\partial n}\right)=\dot{w}_i-\frac{\varepsilon^2}{(1+n\kappa)(r+n\cos\theta)^j}\left\{\frac{\partial}{\partial n}\left[(1+n\kappa)(r+n\cos\theta)^j J_i\right]\right\} \quad (2.38)$$

where $\dot{w}_i$ represents the rate of production of chemical species in the shock layer. The equation of state given by Eq. (2.36) is valid only for the chemical equilibrium case. For the case of chemical nonequilibrium, the equation of state is given by the relation [28]

$$p^*v^* = \sum_i (N_i)\, R^*T^* \quad (2.39)$$

where N_i is the number of moles for the i-th species. This result is reminiscent of the thermal equation of state for a perfect gas. The sum in parentheses, however, is not a constant since the total number of moles change as the chemical balance changes.

3. BOUNDARY CONDITIONS

As pointed out earlier, the slip boundary conditions are not important at low altitudes but they cannot be neglected at higher altitudes. Since both the slip and no-slip conditions have been used in this study, they will be discussed separately in this chapter.

3.1 No-Slip Boundary Conditions

At the body surface (wall), no velocity slip and no temperature jump are assumed. Consequently, the velocities at the surface are

$$v = 0 \tag{3.1}$$

$$u = 0 \tag{3.2}$$

The wall temperature for this study is specified as

$$T_w = \text{constant} \tag{3.3}$$

The Rankine-Hugoniot relations are used to determine the flow properties immediately behind the shock. The nondimensional form of the shock relations can be written as [45]

Continuity:

$$\rho_{s-} v_{s-} = -\sin\alpha \tag{3.4}$$

Momentum:

$$u'_{s-} = \sin\alpha \tag{3.5}$$

$$p_{s-} = p_{s+} + \sin^2\alpha(1-1/\rho_{s-}) \tag{3.6}$$

Energy:

$$h_{s-} = h_{s+} + (\sin^2\alpha/2)(1-1/\rho^2_{s-}) \tag{3.7}$$

where α is shown in Fig. 1, and u'_s and v'_s are velocity components expressed in a shock-oriented coordinate system. The relations for u_s and v_s in the body-oriented coordinate system can be written as

$$u_s = u'_s \sin(\alpha + \beta) + v'_s \cos(\alpha + \beta) \tag{3.8}$$

$$v_s = - u'_s \cos(\alpha + \beta) + v'_s \sin(\alpha + \beta) \qquad (3.9)$$

where angle β is indicated in Fig. 1.

3.2 Slip Boundary Conditions

Shidlovsky [33] has shown that at the body surface the velocity slip and temperature jump conditions are of the same order as the Knudsen number. The Knudsen number, K_n, is defined as the ratio of the particle's mean free path ℓ and the characteristic dimension L of the body (i.e., $K_n = \ell/L$). The ordinary boundary conditions (which correspond to continuum conditions) are obtained when $K_n \to 0$. However, for the transitional range (i.e., for $K_n \to 0(1)$), in order to be consistent with the Navier-Stokes equations of motion, a linear relation between the conditions at the wall and the flow should be assumed. This can be done by a semi-macroscopic argument which leads to the simple expression for velocity slip and temperature jump as [48-51]

$$U = \varepsilon^2 A_1 (\mu/P)(P/\rho)^{1/2} (\partial u/\partial y) \qquad (3.10)$$

$$T = T_w + \varepsilon^2 A_2 (K/P (P/\rho)^{1/2} (\partial T/\partial y) \qquad (3.11)$$

$$V = 0 \qquad (3.12)$$

where A_1 and A_2 are constants and are given by

$$A_1 = [(2-\sigma_1)/\sigma_1] (\pi/2)^{1/2}, \quad A_2 = (15/8)[(2-\sigma_2)/\sigma_2] (\pi/2)^{1/2}$$

The terms σ_1 and σ_2 are slip and thermal accommodation coefficients respectively and are dependent on the nature of the surface and fluid. However, in actual flight conditions both σ_1 and σ_2 are expected to be 1.

Since the transport and thickness effects are important at higher altitudes, the conditions imposed at the shock cannot be calculated by using the classical Rankine-Hugoniot relations. Probstein and Pan [34] have shown that the thickness effect is of a higher order in σ and,

therefore, it is neglected in the present study. The information on thickness effect can be found in [52,53]. In the present case, the shock may still be considered "thin" when compared to the thickness of the viscous shock layer. As such, the thin-layer approximation $(\partial/\partial X')<<(\partial/\partial y')$ and $y'/R_s<<1$ can be used in the shock transition zone. The notations x' and y' are used for the shock surface curvilinear orthogonal coordinates in Fig. 1. By using Stokes assumption and applying the hypersonic thin layer approximation, the governing equations for the shock transition zone can be expressed as [54]

Continuity:

$$\rho_\infty^* V_\infty^* = \rho_s^* v_s^* \tag{3.13}$$

x'-momentum:

$$p^* + \rho_\infty^* V_\infty^* v_s^* - (4/3)\mu^* \ \partial v_s^*/\partial y^* = \rho_\infty^* V_\infty^{*2} + p_\infty^* \tag{3.14}$$

y'-momentum:

$$\rho_\infty^* V_\infty^* u - \mu^* \ \partial u^*/\partial y^* = \rho_\infty^* V_\infty^* U_\infty^* \tag{3.15}$$

Energy:

$$\rho_\infty^* V_\infty^* H^* - (\mu^*/Pr)\ \partial/\partial y\{H-(1-Pr)u^{*2}/2 - [1-(4/3)Pr]v^{*2}/2\} = \rho_\infty^* V_\infty^* H_\infty^* \tag{3.16}$$

where $H^* = h^* + (u^{*2} + v^{*2})/2$.

At the down stream edge of the transition zone both v and $(4/3)[\mu(\partial v/\partial y)]$ are reduced to high-order quantities under a high shock compression ration. Therefore, a set of modified transport boundary conditions immediately behind the shock can be written as

$$\rho_\infty^* V_\infty^* = \rho^* v^* \tag{3.17}$$

$$\rho_\infty^* V_\infty^* u_s^* - \mu_s^* (\partial u^*/\partial y)_s = \rho_\infty^* V_\infty^* U_\infty^* \tag{3.18}$$

$$p_s^* + \rho_\infty^* V_\infty^* v_s^* = p_\infty^* + \rho_\infty^* V_\infty^{*2} \tag{3.19}$$

$$\rho_\infty^* V_\infty^* (H_s^* - H_\infty^*) = \{ (\mu_s/Pr) \partial/\partial y^* [H^* - (1-Pr) u_s^{*2}/2] \} \tag{3.20}$$

By introducing $v = \bar{v} \sin \alpha$, $u = \bar{v} \cos \alpha$ and nondimensionalizing all the quantities, the final modified Rankine-Hugoniot conditions are obtained as

$$\rho_s v_s' = \sin \alpha \tag{3.21}$$

$$u_s' = \cos \alpha - (\varepsilon^2 \mu_s / \sin \alpha)(\partial u_s'/\partial y') \tag{3.22}$$

$$p_s = p_\infty + \sin^2 \alpha \, (1 - 1/\rho_s) \tag{3.23}$$

$$h_s = h_\infty - (\varepsilon^2 \mu_s \, Pr \sin \alpha)(\partial h/\partial y') + (1/2)[u_s' - \cos \alpha)^2 + \sin^2 \alpha - v_s'^2 \tag{3.24}$$

$$u_s = u_s' \sin(\alpha + \beta) + v_s' \cos (\alpha + \beta) \tag{3.25}$$

$$v_s = v_s' \sin(\alpha + \beta) - v_s' \cos (\alpha + \beta) \tag{3.26}$$

As mentioned before, use of slip boundary conditions are made in investigating the shock layer flow phenomena at relatively high entry altitudes.

4. THERMODYNAMIC AND TRANSPORT PROPERTIES

Thermodynamic properties for specific heat, enthalpy, and free energy, and transport properties for viscosity and thermal conductivity are required for each species considered in different flow regimes. For the precursor zone as well as shock layer, the general expression for total enthalpy, specific enthalpy, and specific heat at constant pressure are given respectively by

$$H_T = h + (u^2 + v^2)/2 \tag{4.1}$$

$$h = \Sigma C_i h_i \tag{4.2}$$

$$C_p = \Sigma C_i C_{Pi} \tag{4.3}$$

However, specific relations for H and C_p for the two regions are quite different.

For the precursor region, the relation for the specific enthalpy is obtained by following the procedure described by Smith [1] as

$$h'' = 1.4575RT + (0.75RT + D)C_H + (1.25RT + I/2)C_{H_2^+} \tag{4.4}$$

where D and I represent the dissociation and ionization energy respectively, and their values are available in [55]. The derivation of Eq. (4.4) essentially follows from the consideration of Eq. (4.2). If it is assumed that the internal energy of each particle can be described only by translational and rotational modes, then the relation for specific enthalpy of each species can be expressed as

$$h_{He} = \frac{3}{2} RT + p/\rho = \frac{5}{2} RT \tag{4.5}$$

$$h_{H_2} = \frac{3}{2} RT + \frac{2}{2} RT + p/\rho = \frac{7}{2} RT \tag{4.6}$$

$$h_{H_2^+} = \frac{3}{2} RT + \frac{2}{2} RT + p/\rho + I = \frac{7}{2} RT + I \tag{4.7}$$

$$h_H = \frac{3}{2} RT + p/ + D = \frac{5}{2} RT + D \tag{4.8}$$

$$h_e = \frac{5}{2} RT \tag{4.9}$$

Also, from the conservation of charged particles one can write

$$C_e/M_e = C_{H_2^+}/M_{H_2^+} \tag{4.10}$$

Now, for 85 percent H_2 and 15 percent He on volume basis (or 76 percent H_2 and 24 percent He on mass basis), Eq. (4.2) is written as

$$(C_\alpha/M_\alpha)h_\alpha = (0.26/4)(5RT/2) + [(0.74 - C_{H_2^+} - C_H)/2](7RT/2) + [(5RT/2 + D)]C_H + (7RT/2 + I)(C_{H_2^+}/2) + (5RT/2)(C_{H_2^+}/2) \tag{4.11}$$

A simplification of the above equation results in Eq. (4.4).

In the shock layer region, Eqs. (4.2) and (4.3) are used to calculate H and C_p. With x_i representing the mole fraction of the ith species, the expressions for h_i and C_{pi} are found from Refs. 56 and 57 as

$$H_i = RT[a_1 + (a_2/2)T + (a_3/3)T^2 + (a_4/4)T^3 + (a_5/5)T^4 - a_6/T] \tag{4.12}$$

$$C_{Pi} = R(a_1 + a_2T + a_3T^2 + a_4T^3 + a_5T^4) \tag{4.13}$$

where R is the universal gas constant (=1.98726 cal/mole - K) and T is the local fluid temperature in K. For different species, values of the constants a_1, a_2, . . . a_6 are given in [57], and for species under present investigation they are listed in Table 3. It should be pointed out here that in this study, instead of employing Eq. (2.36b), Eqs. (4.1), (4.2), and (4.12) are used to calculate the enthalpy variation in the shock layer. This is because slightly better results are obtained by using the above set of equations.

Table 3 Coefficient for evaluation of the specific heat at constant pressure and enthalpy for various hydrogen/helium species.

Species	Coefficients						Temp. Range K
	a_1	a_2	a_3	a_4	a_5	a_6	
	2.5	0	0	0	0	2.547162E+4	≥ 300
H	2.5	0	0	0	0	2.547162E+4	> 1,000
	2.475164	7.366387E-5	-2.537593E-8	2.386674E-12	4.551431E-17	2.523626E+4	> 6,000
	3.057445	2.676520E-3	-5.809916E-6	5.521039E-6	-1.812273E-12	-9.889047E+2	≥ 300
H_2	3.10019	5.111946E-4	5.264421E-8	-3.490997E-11	3.694534E-15	-8.773804E+2	> 1,000
	3.363	4.656000E-4	-5127000E-8	2.802000E-12	4.905000E-17	-1.018000E+3	> 6,000
	2.5	0	0	0	0	1.840334E+5	> 300
H^+	2.5	0	0	0	0	1.840334E+5	> 1,000
	2.5	0	0	0	0	1.840334E+5	> 6,000
	2.5	0	0	0	0	-7.453749E+2	> 300
He	2.5	0	0	0	0	-7.453749E+2	> 1,000
	2.5	0	0	0	0	-7.453749E+2	> 6,000
	2.5	0	0	0	0	2.853426E+5	> 300
He^+	2.5	0	0	0	0	2.853426E+5	> 1,000
	2.5	0	0	0	0	2.853426E+5	> 6,000
	2.5	0	0	0	0	-7.453749E+2	> 300
e^-	2.5	0	0	0	0	-7.453749E+2	> 1,000
	2.508	-6.332000E-6	1.364000E-9	-1.094000E-13	2.934000E-18	-7.45000E+2	> 6,000

For the shock-layer gas, the mixture viscosity and thermal conductivity are obtained by using the semi-empirical formulas of Wilke [58] as

$$\mu = \sum_{i=1}^{N} [x_i \mu_i / (\sum_{j=1}^{N} x_j \phi_{ij})] \tag{4.14}$$

$$K = \sum_{i=1}^{N} [x_i K_i / (\sum_{j=1}^{N} x_j \phi_{ij})] \tag{4.15}$$

where

$$\phi_{ij} = [1 + (\mu_i/\mu_j)^{1/2} (M_j/M_i)^{1/4}]^2 / \{\sqrt{8}[1 + (M_i/M_j)]\}^{1/2}$$

and M_i is the molecular weight of species i. For hydrogen/helium species, specific relations for viscosity and thermal conductivity are given in [59,60]. The viscosity of H_2 and He, as a function of temperature, can be obtained from reference [59] as

$$\mu_{H_2} = (0.66 \times 10^{-6})(T)^{3/2}/(T + 70.5), \text{ N sec/m}^2 \tag{4.16}$$

$$\mu_{He} = (1.55 \times 10^{-6})\ (T)^{3/2}/\ (T + 97.8), \text{ N sec/m}^2 \tag{4.17}$$

The thermal conductivity of H_2 and H are obtained from Ref. 60 as

$$K_{H_2} = 3.212 \times 10^{-5} + (5.344 \times 10^{-3})T \tag{4.18}$$

$$K_H = 2.496 \times 10^{-5} + (5.129 \times 10^{-8})T \tag{4.19}$$

The viscosity of H and thermal conductivity of He are obtained from the relation between viscosity and thermal conductivity of monatomic gases as given in Ref. 58 by

$$K = (15/4)(R/M)\mu \tag{4.20}$$

Very little information is available on transport properties of other species such as H_2^+, H^+, e^-, etc. Fortunately, transport properties are

important only in the boundary-layer region where the temperature is not high enough to produce these species.

It should be noted that all relations presented in this section are expressed in dimensional form.

The heat transfer to the wall due to conduction and diffusion is referred here as the convective heat flux and is given by the relation [15,46] as

$$q_c = -\varepsilon^2[K(\partial T/\partial y) + (\mu\, Le/Pr) \sum_{i=1}^{N} (\partial C_i/\partial y)h_i] \qquad (4.21)$$

where Pr is the Prandtl number, Le is Lewis number and the value for Le is taken to be 1.1 [45,46] in the present study.

5. CHEMICAL REACTIONS

Analyses of chemically reacting flows are usually simplified by assuming the chemical equilibrium behavior of the gas mixture. While this assumption may be justified in some cases, in many realistic problems this may lead to serious errors. Thus, in order to understand the degree of physical reality, it becomes essential to analyze the complex gas mixture under the conditions of chemical nonequilibrium. In this chapter, information on chemical equilibrium and nonequilibrium reactions and reaction rates are provided for the shock layer gas mixture of a Jovian entry body.

5.1 Chemical Equilibrium

In the chemical equilibrium case, a computer code developed by Sutton [26] is used in this study. The number density of eight chemical species, H_2, H, H^+, H^-, e^-, He^+, He^+ and He^{++} are calculated by the chemical reactions and rate constants given in Table 4. In general, the reactions can be expressed by

$$\Sigma\, a_i A_i \rightleftarrows \Sigma\, b_i B_i \tag{5.1}$$

The number density of particles (particle/m^3) is related to the equilibrium rate constant and can be expressed as [28]

$$K_j = [\Pi N^{b_i}(B_i)]/[\Pi N^{a_i}(A_i)] \tag{5.2}$$

The conversion equations for hydrogen and helium nuclei and charge are

$$N_H + 2N_{H2} + N_{H^+} + N_{H^-} = N_H^o \tag{5.3}$$

$$N_{He} + N_{He^+} + N_{He^{++}} + N_{He}^o \tag{5.4}$$

$$N_{H^+} + N_{He^+} + 2N_{He^{++}} - N_{H^-} = N_{e^-} \tag{5.5}$$

Table 4 Reaction scheme and rate constants for chemical equilibrium conditions.

REACTIONS	RATE CONSTANTS	PARTICLES/M^3
1. $H_2 \rightleftarrows 2H$	$k_1 = 4.699E22\ T^{1/2}$	$(1-\exp(-6331/T))\ \exp(-51964/T)$
2. $H \rightleftarrows H^+ + e^-$	$k_2 = 2.411E15\ T^{1.5}$	$\exp(-157810/T)$
3. $He \rightleftarrows He^+ + e^-$	$k_3 = 9.645E15\ T^{1.5}$	$\exp(-285287/T)$
4. $He^+ \rightleftarrows He^{++} + e^-$	$k_4 = 2.411E15\ T^{1.5}$	$\exp(-631310/T)$
5. $H^- \rightleftarrows H + e^-$	$k_5 = 9.643E15\ T^{1.5}$	$\exp(-8750/T)$

Table 5 Reaction scheme and rate constants for chemical nonequilibrium conditions.

Reactions	Rate constants in cm^3 sec^{-1} mole^{-1}
1. $H + e \rightleftarrows H^+ 2e$	$k_1=2.27E13\ T_e^{1/2}\ \exp(-1578E5/T_e)$
2. $He + e \rightleftarrows He^+ + 2e$	$k_2=1.33E13\ T_e^{1/2}\ \exp(-2.852E5/T_e)$
3. $H + e \rightleftarrows H^* + e$, $H^* + e \rightleftarrows H^+ + 2e$	$k_3= 4.11E13\ T_e^{1/2}\ \exp(-1.160E5/T_e)$
4. $He + e \rightleftarrows He^* + e$, $He^* + e \rightleftarrows He^+ = 2e$	$k_4= 2.24E13\ T_e^{1/2}\ \exp(-2.320E5/T_e)$
5. $H + H \rightleftarrows H^* + H$, $H^* + H \rightleftarrows H^+ + e + H$	$k_5=6.20E10\ T^{1/2}\ \exp(-1.160E5/T)$
6. $H + He \rightleftarrows H^* + He$, $H^* + He \rightleftarrows H^+ + e + He$	$k_6=4.89E10\ T^{1/2}\ \exp(-1.160E5/T)$
7. $H_2 + He \rightleftarrows H + H + He$	$k_7=4.33E18\ T^{-1}\ [1-\exp(-15E8/T^2)]\ \exp(-52340/T)$
8. $H_2 + H_2 \rightleftarrows H + H + H_2$	$k_8=2.5\ k_7$
9. $H_2 + H \rightleftarrows H + H + H$	$k_9=14.0\ k_7$
10. $H_2 + H^+ \rightleftarrows H + H + H^+$	$k_{10}=k_9$
11. $H_2 + e \rightleftarrows H + H + e$	$k_{11}=k_9$

The number densities of the hydrogen and helium nuclei are calculated by

$$N_H^o = 2x_{H_2}(A_o\rho/M_o) \tag{5.6}$$

$$N_{He}^o = x_{He}(A_o\rho/M_o) \tag{5.7}$$

where

$$M_o = 2.016x_{H_2} + 4.003x_{He}$$

In the above equations, A_0 represents Avogadro's constant, ρ is the mixture density in g/cm^3, x_{H_2} is the mole fraction of molecular hydrogen, and x_{He} is the mole fraction of helium.

The solution procedure for obtaining the eight unknown number densities is discussed in [26]. The closed-form solutions are obtained by solving Eq. (5.2) for each reaction independently. This is accomplished by setting the appropriate values in Eqs. (5.3)-(5.5) equal to zero if the species are not present in the reaction. The closed-form solutions for the number densities (in particles/cm^3) of each species are given by

$$H_2: \quad N_{H_2} = (N_H^o/2) + (K_1/8)[1 + 8N_H^o/K_1)^{1/2} - 1]$$

$$H^+: \quad N_{H^+} = (K_2/2)[(1 + 4N_H^o/K_2)^{1/2} - 1]$$

$$H: \quad N_H = N_H^o - 2N_{H_2} - N_{H^+}$$

$$H_e^+: \quad N_{He}^+ = (D_1/2)[(1 + 4K_3N_{He}^o/D_1^2)^{1/2} - 1], \quad D_1 = K_3 + N_{H^+}$$

$$He^{++}: \quad N_{He}^{++} = (D_2/2)[(1 + 4K_4N_{He}^o/D_2^2)^{1/2} - 1], \quad D_2 = K_4 + N_H + N_{He}^o$$

$$He: \quad N_{He} = N_{He}^o - N_{He} + N_{He}^{++}$$

$$e^-: \quad N_{e^-} = N_{H^+} + N_{He}^+ + 2N_{He}^{++}$$

$$H^-: \quad N_{H^-} = N_H N_{e^-}/K_5 \tag{5.8}$$

5.2 Chemical Nonequilibrium

When chemical reactions proceed at a finite rate, knowledge of the rate of production terms, $\hat{W}_i$, which appear in the species continuity equations, are required. The reaction scheme describing important collisional processes in hydrogen-helium ionizing shock waves has been modeled by Leibowitz [8] after the results of argon ionization studies. Eleven separate reaction steps describe the dissociation of molecular hydrogen, excitation of electronic states of hydrogen and helium, and ionization of the atomic hydrogen and helium by collisions with atoms and electrons. A complete discussion on these reaction schemes is available in [61] and [62]. The eleven reactions and corresponding rate constants are given in Table 5.

In a complex gas mixture containing a total of ℓ species, of which X_i are capable of undergoing m elementary chemical reactions, the chemical equation for the general elementary reaction r can be written as [28]

$$\sum_{i=1}^{\ell} a_{i,r} X_i \rightleftarrows \sum_{i=1}^{\ell} b_{i,r} X_i \tag{5.9}$$

where $a_{i,r}$ and $b_{i,r}$ are the stochiometric coefficients appearing on the left and right in the reaction r. By applying the principle of detailed balancing, the backward rate constant, $K_{b,r}$, is obtained by dividing the forward rate constant, $K_{f,r}$, by the equilibrium constant $K_{c,r}$ which is given in Table 1.

The total rate of change in X_i is given by the relation [28]

$$\frac{dX_i}{dt} = \sum_{i=1}^{m} (b_{i,r}-a_{i,r})K_{f,r}\left[\prod_{i=1}^{\ell} (X_i)^{a_{i,r}} - \frac{1}{K_{c,r}} \prod_{i=1}^{\ell} (X_i)^{b_{i,r}}\right] \tag{5.10}$$

This is the general rate equation for a complex gas mixture. The rate of production of chemical species, $\hat{W}_i$, now can be expressed by

$$\hat{W}_i = M_i^*(dx_i^*/dt)(R_n^*/\rho_\infty^* V_\infty^*) \tag{5.11}$$

Equations (5.9)-(5.11), along with other fluid mechanical equations, equation of state, and the electron energy equation, are solved numerically to obtain the concentration of all species. In order to have a reasonable rate of convergence in the numerical scheme, however, it is important to express the rate of production term in a proper form. This is accomplished by splitting $\hat{W}_i$ into two separate contributions as [15,63,64]

$$\hat{W}_i/\rho = (\hat{W}_i)^\circ - (\hat{W}_i)^1 c_i \tag{5.12}$$

The reasons for doing this are explained in the cited references.

5.2.1 Electron Temperature

Because of a large ratio of atom (or ion) mass to electron mass, electrons transfer energy rapidly by collisions with other electrons but only slowly by elastic collisions with atoms or ions. Consequently, a different temperature is given to atoms (heavy particles) and electrons in the same gas. The electron temperature is obtained from the solution of the electron energy equation. A detailed discussion of the electron energy equation is given by Appleton and Bray [65]. For a one-dimensional steady shock wave in a H_2-He mixture, the resulting equation can be expressed as [61]

$$3[e]m_e\bar{\nu}R(T-T_e)-\Theta_H(R_1-R_{1r}+R_3-R_{3r})-\Theta_{He}(R_2-R_{2r}+R_4-R_{4r})=0 \tag{5.13}$$

where

$$\nu_{ek} = N_k V_e Q_{ek} \tag{5.14a}$$

$$V_e = (8\ k\ T_e/\pi m_e)^{1/2} \tag{5.14b}$$

$$Q_{ek} = A_k[\exp(-a_k E)-\exp(-b_k E)] \tag{5.14c}$$

$$E = (1/2)\ V^2 \tag{5.14d}$$

$$V = 4(kT_e/2\pi\mu)^{1/2} \tag{5.14e}$$

$$\mu = MaMb/(Ma+Mb) \tag{5.14f}$$

$$\bar{\nu} = \sum_k \nu_{ek}/m_k \tag{5.14g}$$

In Eq. (5.13), [e] represents the concentration of electrons, θ_k is the ionization energy per mole of species k, and R_i and R_{ir} are the forward and backward production rates for electrons respectively. In Eq. (5.14b), ν_{ek} represents the collisional frequency, n_k is the number density of species K, V_e is the average electron velocity, and Q_{ek} represents the elastic collision cross section for species k. In Eq. (5.14e), E represents the relative kinetic energy, V is the relative speed, and μ is the reduced mass. The values of coefficients A_k, a_k, and b_k appearing in Eq. (5.14d) are available in Ref. 59. By substituting Eqs. (5.10) and (5.14) into Eq. (5.13), an explicity expression for the electron temperature, in terms of the species concentration and heavy particle temperature, can be obtained as

$$T_e=T - [(k_1+k_3)(X_2-X_4/K_{c,H})+(k_2+k_4)(X_3-X_5/K_{c,He})]/X_1 \tag{5.15}$$

where k_1, k_2, k_3, k_4 are rate constants in Table 5 and

$$X_1 = 1/(3[e]m_e\bar{\nu}R) \tag{5.16a}$$

$$X_2 = \Theta_H[H][e] \tag{5.16b}$$

$$X_3 = \Theta_{He}[He][e] \tag{5.16c}$$

$$X_4 = \Theta_H[H^+][e] \tag{5.16d}$$

$$X_5 \quad \Theta_{He}[H_e^+][e] \tag{5.16e}$$

Use of the electron temperature is made in evaluating the radiative flux in the shock layer.

6. RADIATION MODEL

An appropriate expression for the radiative flux, q_R, is needed for the solution of the energy equation presented in the second chapter. This requires a suitable transport model and a meaningful spectral model for variation of the absorption coefficient of the gas. In this chapter, appropriate expressions for the spectral and total radiative flux are given and information on the spectral absorption by the hydrogen/helium gas is presented.

6.1 Radiative Flux Equation

The equations for radiative transport, in general, are integral equations which involve integration over both frequency spectrum and physical coordinates. In many physically realistic problems, the complexity of the three-dimensional radiative transfer can be reduced by introduction of the "tangent slab approximation." This approximation treats the gas layer as a one-dimensional slab in calculation of the radiative transport. Radiation in directions other than normal to either the body or shock is neglected. Discussions on the validity of this approximation for planetary entry conditions are given in [66-70].

As mentioned earlier, the tangent slab approximation for radiative transfer is used in this study. It should be pointed out here that the tangent slab approximation is used only for the radiative transport and not for other flow variables. For a nonscattering medium and diffuse nonreflecting bounding surfaces, a one-dimensional expression for the spectral radiative flux is given by [27-29]

$$q_{R\nu}(\tau_\nu) = 2\pi \{\varepsilon_\nu [B_\nu(0)E_3(\tau_\nu) - B_\nu(\tau_{o\nu})E_3(\tau_{o\nu} - \tau_\nu)] + \int_0^{\tau_\nu} B_\nu(t)E_2(\tau_\nu - t)dt - \int_{\tau_\nu}^{\tau_{o\nu}} B_\nu(t)E_2(t - \tau_\nu)dt\} \qquad (6.1)$$

where

$$\tau_\nu = \int_0^y \alpha_\nu(y')dy'$$

$$E_n(t) = \int_0^1 \exp(-t/\mu)\mu^{n-2}d\mu$$

$$B_\nu = (h\nu^3/c^2)[\exp(h\nu/KT) - 1]$$

The quantities $B_\nu(0)$ and $B_\nu(\tau_{o\nu})$ represent the radiosities of the body surface and shock respectively.

The expression of total radiative flux is given by

$$q_R = \int_0^\infty q_{R\nu}(\tau_\nu)d\nu \qquad (6.2)$$

To obtain specific relations for the total radiative flux for the precursor and shock-layer regions, it is essential to know the spectral absorption characteristics of the absorbing-emitting species in these regions.

In the precursor region, the radiative contribution from the free stream usually is neglected. For a diffuse, nonreflecting shock front, the expression for one-dimensional radiative flux for this region is obtained from Eqs. (6.1) and (6.2) as

$$q_R(n) = 2\int_0^\infty \{q_\nu(0)E_3(\kappa_\nu n) + \pi\kappa_\nu \int_0^\infty B_\nu(T)E_2[\kappa_\nu(n-n')]dn'\}d\nu \qquad (6.3)$$

where $q_\nu(0) = \varepsilon_\nu \pi B_\nu(T_s)$. In obtaining the above equation, it was assumed that the absorption coefficient κ_ν is independent of position.

The information on the spectral absorption model for hydrogen/helium species in the precursor region is given in [42] and is briefly discussed in subsection 6.2. The model essentially consists of

approximating the actual absorption of active species by three different step models. For this model, Eq. (6.3) can be expressed as [43]

$$q_R(n) = 2\pi \sum_{i=1}^{N} \{(15/\pi^5) q(0) E_3(\kappa_i n) \int_{v_{1i}}^{v_{2i}} [v^3/(e^v - 1)]dv + \kappa_i \int_0^n E_2[\kappa_i(n - n')] \int_{\nu_{1i}}^{\nu_{2i}} B_\nu(T) d_\nu dn'\} \quad (6.4)$$

where $V = h\nu/kT_s$ and $q(0) = \varepsilon\sigma T_s^4$. In writing the above equation, it has been assumed that the shock front radiates in the precursor zone as a gray body.

In the shock layer, the radiative energy from the bow shock usually is neglected in comparison to the energy absorbed and emitted by the gas layer. This implies that the transparent shock front does not absorb but emits radiation. The expression for the net radiative flux in the shock layer, therefore, is given by

$$q_R = 2 \int_0^\infty [q_\nu(0) E_3(\tau_\nu) + \int_0^{\tau_\nu} B_\nu(t) E_2(\tau_\nu - t)dt - \int_{\tau_\nu}^{\tau_{o\nu}} B_\nu(t) E_2(t - \tau_\nu)dt]d\nu \quad (6.5a)$$

In this equation, the first two terms on the right represent the radiative energy transfer towards the bow shock while the third term represents the energy transfer towards the body. Upon denoting these contributions by q_R^+ and q_R^-, Eq. (6.5a) can be written as

$$q_R = q_R^+ - q_R^- \quad (6.5b)$$

A few spectral models for absorption by the hydrogen/helium species in the shock layer have been proposed in the literature [22-26]. For Jovian entry conditions, the absorption by helium is usually neglected.

The spectral absorption of hydrogen species was represented by a 58-step model by Sutton [26] and was approximated by a 30-step model by Tiwari and Subramanian [27]. The results of these step models are compared with the detailed model of Nicolet [22] in [27]. The 58-step model proposed by Sutton is employed in this study. The details of radiative absorption and computational procedure are given in [26]. The information on spectral absorption by this model is summarized in subsection 6.2. In essence, the step model replaces the frequency integration in Eq. (6.5) by a summation over 58 different frequency intervals. In each interval, the absorption coefficient is taken to be independent of frequency. For this model, Eq. (6.5) can be expressed as

$$q_R = 2\pi \sum_{j=1}^{N} \{\varepsilon_\nu B_\nu(T_w) E_3[\int_o^y \alpha_\nu(y')dy'] + \int_o^y \alpha_\nu(\xi) B_\nu(\xi) E_2[\int_\xi^y \alpha_\nu(y')dy']d\xi - \int_y^{y_s} \alpha_\nu(\xi) B_\nu(\xi) E_2[\int_y^\xi \alpha_\nu(y')dy']d\xi\} \tag{6.6}$$

where y_s denotes the shock location and N represents the number of spectral intervals. In each of the jth intervals, the absorption coefficient is assumed constant while the Planck function is not. In accordance with Eq. (6.5b), Eq. (6.6) can be expressed in terms of q_R^+ and q_R^- and for a gray body one finds

$$q_R^+(y) = (4\pi h/c^2) \sum_{j=1}^{N} \{\varepsilon F(\nu_j, T_w) E_3[\int_o^y \alpha_{\nu j}(y')dy'] + \int_o^y (KT/h)^4 F(\nu_j, T) \alpha_{\nu j}(\xi) E_2[\int_\xi^y \alpha_{\nu j}(y')dy']d\xi\} \tag{6.7a}$$

$$\bar{q}_R(y) = -(4\pi h/c^2)\sum_{j=1}^{N}\{\int_{y}^{y_s}(KT/h)^4 F(\nu_j,T)\alpha_{\nu j}E_2[\int_{y}^{\xi}\alpha_{\nu j}(y')$$

$$x\ dy']d\xi\} \qquad (6.7b)$$

where

$$F(\nu_j,T_w) = \int_{\nu_{j1}}^{\nu_{j2}}\{\nu^3/[\exp(h\nu/KT_w) - 1]\}d\nu$$

$$F(\nu_j,T) = \int_{\nu_{j1}}^{\nu_{j2}}\{\nu^3/[\exp(v) - 1]\}dv,\ v = h\nu/KT$$

From the knowledge of the temperature distribution normal to the body, Eqs. (6.7) can be solved by numerical integration over frequency and space. The final temperature profile is obtained through an iterative procedure. Use of Eqs. (6.7) is made in obtaining the radiative flux towards the body and shock as well as the net radiative flux.

For evaluation of the radiative flux, usually it is essential to express the exponential integrals $E_n(t)$ in simpler approximate forms. Quite often, these integrals are approximated by appropriate exponential functions [28,29]. In this study, it was established that better results are obtained if the exponential integrals are expressed in series form for small and large arguments. The series expansion of the exponential integral of first order is given as

For $t < 1$:

$$E_1(t) = -0.5772 - \ln t + t - \frac{t^2}{2(2)!} + \frac{t^3}{3(3)!} + \ldots \qquad (6.8a)$$

For $t \geq 1$:

$$E_1(t) = \exp(-t)\,\frac{a_0 + a_{1t} + a_{2t}{}^2 + a_{3t}{}^3 + t^4}{t(b_0 + b_{1t} + b_{2t}{}^2 + b_{3t}{}^3 + t^4)} \qquad (6.8b)$$

where

$a_0 = 0.26777343$ $\quad b_0 = 3.958469228$

$a_1 = 8.63476089$ $\quad b_1 = 21.09965309$

$a_2 = 18.059016973$ $\quad b_2 = 25.63295614$

$a_3 = 8.57322874$ $\quad b_3 = 9.5733223454$

Relations for exponential integrals of higher order are obtained by employing the recursion relations given in [29].

6.2 Radiation Absorption Model

Appropriate spectral models for gaseous absorption are needed for solutions of the radiative flux equations. Information on spectral absorption by the precursor and shock-layer species is presented in this section.

6.2.1 Spectral Absorption Model for Precursor Region

In the precursor region, the photoionization absorption coefficient is a continuous nonzero function of photon energy (because of bound-free transition) for all values of photon energy that exceed the ionization potential of the atom. Similar remarks apply to the photodissociation and radiative recombination. A critical review of ultraviolet photo-absorption cross sections for molecules of astrophysical and aeronomic interest, available in the literature up to 1971, is given by Hudson [20]. Specific information on photoionization and absorption coefficient of molecular hydrogen is available in [20,21, 71-74].

Photoionization and absorption cross sections of H_2, as obtained from Refs. 20, 21, and 71-74, are plotted in Fig. 2. From this figure, it is evident that the ionization continuum starts at about 804 Å and continues towards lower wavelengths. Between the wavelengths of 600 Å

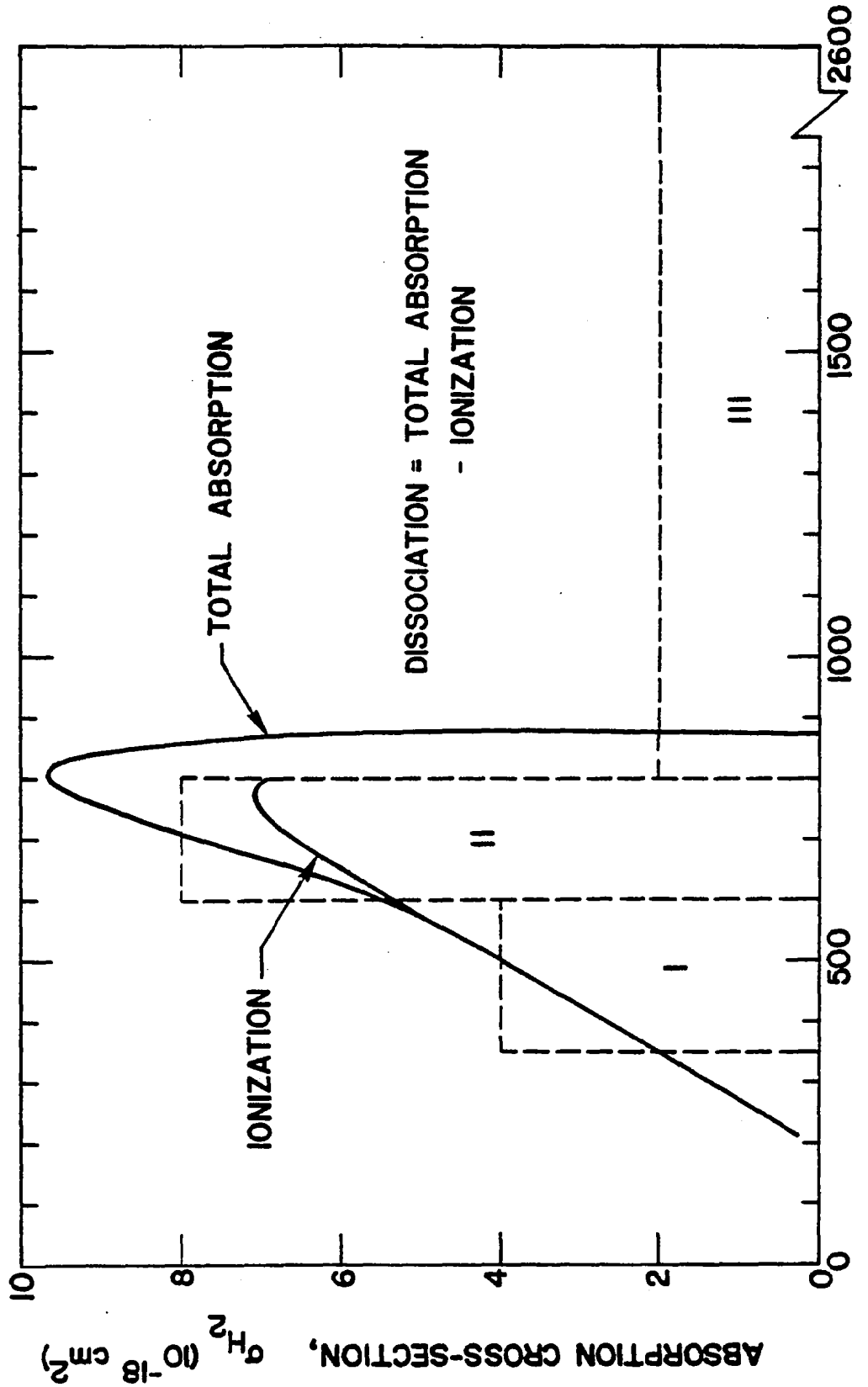

Fig. 2 Absorption cross section of H_2 in ultraviolet region.

and 804 Å, the absorption cross section for the ionization continuum is included in the total absorption (i.e., absorption due to ionization as well as dissociation). For wavelengths below 600 Å, however, the ionization continuum absorption is equal to the total absorption. The total absorption cross section for the continuum range below 804 Å can be closely approximated by the two rectangles (I and II) shown in the figure with broken lines. The ratio of the ionization cross section to the total absorption cross section (i.e., the value of Y_I) is taken to be unity for rectangle I and 0.875 for rectangle II. For wavelengths greater than 804 Å (where h is below ionization energy), the value of Y_I is taken to be zero. Little information is available in the literature on the absorption cross section for dissociation of H_2 molecules. There is strong evidence, however, that photodissociation starts at about 2600 Å and continues towards lower wavelengths to about 750 Å [69,71]. There are also a few diffuse bands in this spectral range [71,73]. Thus, it becomes difficult to evaluate the absorption cross section in this spectral range. For this study, the absorption cross section in the spectral range between 804 Å and 2600 Å was approximated by rectangle III. The specific values of $\sigma(\nu)$ for the three rectangles are found to be $\sigma_I(\nu)$ = 4.1 E-18, $\sigma_{II}(\nu)$ = 8.2 E-18, and $\sigma_{III}(\nu)$ = 2.1 E-18. The value of Y_D is taken to be zero for rectangle I and 0.125 for rectangle II. The numerical procedure for employing this model in the radiative flux equations is discussed in detail in Ref. 42 and is summarized in Chap. 7.

6.2.2 Spectral Absorption Model for Shock-Layer Region

As mentioned earlier, the 58-step model proposed by Sutton [26] for spectral absorption by the hydrogen species in the shock layer is employed

in this study. For atomic hydrogen, all three transitions (bound-bound, bound-free, and free-free) are considered. The total absorption of the jth step is a summation of the average absorption for the ith transitions in the jth step, i.e.,

$$\bar{\kappa}_j = \sum_i \kappa_{ij} \tag{6.9a}$$

$$\kappa_{ij} = (1/\Delta\nu_j) \int_{\nu_j}^{\nu_j+\Delta\nu_j} \kappa_i d\nu \tag{6.9b}$$

$$\kappa_i = f(T, N_i, \nu) \tag{6.9c}$$

where N_i represents the number density in cm^{-3}.

For the free-free transition, the absorption coefficient is calculated by

$$\kappa_{ff}^H = (2.61E - 35) N_e N_{H^+} / (\nu^3 T^{1/2}) \tag{6.10}$$

The absorption coefficient for bound-free transitions is calculated by employing two separate relations as

$$\kappa_{bf}^H = (1.99E - 14)(N_H/\nu^3) \sum_{n_\ell=1}^{4} (1/n_\ell^3)\exp(C_1), \quad 1 \leq n_\ell \leq 4 \tag{6.11a}$$

$$\kappa_{bf}^H = (6.31E - 20)(TN_H/\nu^3)\exp(C_2)\exp(C_3), \quad 5 \leq n_\ell \leq n_{\ell,\,max} \tag{6.11b}$$

where

$$C_1 = (-157780/T)[1 - (1/n_\ell^2)]$$

$$C_2 = (-157780/T)(1 - \delta/13/6)$$

$$C_3 = [(157780/T)(1/25 - \delta/13/6)] - 1$$

$$\delta = (1.79E - 5)(N_e^{2/7})/(T^{1/7})$$

In the above equations, n_ℓ represents the principal quantum numbers, δ is the reduction in ionization potential in eV, and the values 157780 and 13.6 are the ionization potential in K and eV respectively.

The bound-bound transitions are included for principal quantum numbers up to five. The absorption coefficient is calculated by using the relation

$$\kappa_{bb}^{H} = SL(\nu) \tag{6.12}$$

where S is the line strength and L(ν) is the line shape factor. The line strength is given by the relation

$$S = (1.10E - 16) f n_{\ell}^2 N_H \exp[(-157780/T)(1 - 1/n_{\ell}^2)] \tag{6.13}$$

The line shape factor is given by the relation

$$L(\nu) = \gamma/\{\pi[\gamma^2 + (\nu - \nu_o)^2]\} \tag{6.14}$$

where ν_o is the frequency at the line center and γ is the line half-width, and these are given by

$$\nu_o = 13.6[(1/n_{\ell}^2) - (1/n_u^2)] \tag{6.15}$$

$$\gamma = a[1.05E\ 15(n_u^2 - n_{\ell}^2)N_e^{2/3}] \tag{6.16}$$

The constant a in the above equation is taken to be 0.642 for the first line and unity for the remaining lines.

The absorption coefficients for the free-free and bound-free transitions of the negative hydrogen are

$$\kappa_{ff}^{H^-} = (6.02E - 39) N_H N_e / \nu^3 \tag{6.17}$$

$$\kappa_{bf}^{H^-} = (2.89E - 17)(\beta^4 - 4\beta^3 + 3.64\beta^2 + 0.73\beta) N_{H^-} \tag{6.18}$$

where $\beta = 1.502/\nu$. The threshold for the bound-free transition of H^- is 0.757 eV.

The absorption coefficient for molecular hydrogen in the jth step is obtained in accordance with Eq. (6.9) and is expressed as

$$\kappa_j^{H_2} = f_j(T) N_{H2} \tag{6.19}$$

where $f_j(T)$ is dependent on the particular step. The molecular bands cover the steps from 7 to 17 eV.

Further details on constructing the step-function model and utilizing it in the radiative flux equations are given in Refs. 25-27.

7. SOLUTION PROCEDURE

An iterative procedure has been used to couple the precursor and shock-layer solutions. In this method, the shock-layer solutions are obtained first with no consideration of precursor effect. From this solution, the radiative flux at the shock front (which influences the precursor region flow) is determined. By employing this value of the radiative flux, different precursor region variables are calculated through use of Eqs. (2.18) through (2.25). Values of these flow variables are obtained just ahead of the bow shock, and then the Rankine-Hugoniot relations are used to determine the conditions behind the shock. These conditions are used to obtain new shock-layer solutions from which a new value of the radiative flux at the shock is calculated. The procedure is continued until the radiative flux at the shock becomes invariant.

The solution procedures for the precursor and shock-layer regions are described in some detail in following subsections.

7.1 Precursor Region Solution

As pointed out earlier, two methods (the small perturbation theory and the thin-layer approximation) are employed in this study to investigate the precursor region flow phenomena. The solution procedure for these methods is discussed separately in this section.

7.1.1 Small Perturbation Theory

Since the problem treated by thin layer method is linear, it is permissible to obtain a solution for arbitrary frequency, and then integrate this solution over the spectrum to obtain the general solution. Thus, in the development that follows, flow-field perturbations will be considered for a unit frequency interval. Consequently, Eqs. (2.11) and (2.12) now can be written as

$$\partial H_{T_1}/\partial z = N_{H_2}\,\sigma(\nu)/(\rho_\infty V_\infty^3)\; H_\nu \tag{7.1}$$

$$\partial C_{H_2^+}/\partial z = [m_1\, N_{H_2}\, Y_I\, \sigma(\nu)/(\rho_\infty\, V_\infty\, h\nu)]H_\nu \tag{7.2a}$$

$$\partial C_H/\partial z = [m_1\, N_{H_2}\, Y_D\, \sigma(\nu)/(\rho_\infty\, V_\infty\, h\nu)]H_\nu \tag{7.2b}$$

where Y_D and Y_I represent photodissociation and photoionization yields respectively.

It can be shown that the flow under consideration is irrotational [1,2]. Thus, there exists a potential ϕ such that

$$\overline{V}_1 = \nabla\phi \tag{7.3}$$

For z-direction, integration of Eq. (2.8) results in

$$p_1 = -(\gamma M_\infty^2)\; \partial\phi/\partial z = -(\gamma M_\infty^2)V_{1z} \tag{7.4}$$

Eq. (2.9) can now be expressed as

$$\nabla^2\phi + \partial\rho_1/\partial z = 0 \tag{7.5}$$

In order to evaluate $\partial\rho_1/\partial z$ and to relate H_1 to other variables, it is necessary to consider the gas model and radiation. For the precursor region gas model, the expressions for pressure and enthalpy variations are given by Eqs. (2.14) and (2.15) respectively. Now, in order to express the governing equations in terms of perturbation potential, first p_1 is eliminated by combining Eqs. (2.14) and (7.4). The resulting equation is then differentiated with respect to z and use is made of Eq. (7.2). Next, Eqs. (2.15), (2.16), (7.1), and (7.3) are combined to give

$$\partial\rho_1/\partial z = -\Gamma\; \partial^2\phi/\partial z^2 - P_\nu\, H_\nu \tag{7.6}$$

where

$$\Gamma = 0.727\; \gamma\; M_\infty^2 \tag{7.7a}$$

$$P_\nu = a_\nu + b_\nu/h\nu \tag{7.7b}$$

$$a_\nu = N_{H_2}\, \sigma(\nu)/(\rho_\infty V_\infty H_\infty) \tag{7.8a}$$

$$b_\nu = -(a_\nu m_1/2)[(I - 0.89\, RT_\infty)Y_I + (2D - 1.89\, RT_\infty)\, Y_D] \tag{7.8b}$$

Upon combining Eqs. (7.5) and (7.6), the governing equation for the flow is obtained as

$$\nabla^2_{x,y}\phi - \Gamma\, \partial^2\phi/\partial z^2 = P_\nu\, H_\nu \tag{7.9}$$

For the axisymmetric case, this is expressed as

$$r^{-1}\, \partial/\partial r\, (r\partial\phi/\partial r) - \Gamma\, \partial^2\phi/\partial z^2 = P_\nu\, H_\nu \tag{7.10}$$

Eqs. (7.9) and (7.10) are seen to be the classical potential equations for compressible flow with a forcing term proportional to radiation added. The potential for the flow induced by a radiant source with a spectral distribution is obtained by integrating the contributions of each frequency as

$$\Phi = \int_0^\infty \phi\, d\nu \tag{7.11}$$

As discussed by Smith [1,2], solutions of the governing equations, presented in the previous section, can be obtained in special cases depending on the model used for the distribution of spatial radiation. If the radius of the radiating gas cap, R_c, is large compared to the photon mean free path, then the problem can be treated like radiation from a plane source. On the other hand, when the radius of the radiating gas cap is small, then the problem can be treated like a spherical point source for radiation from the gas cap and a cylindrical point source for radiation from the wake. Note that, in general, R_c may not be the same as the radius of the bow shock, R_s.

7.1.1.1 Radiation From a Plane Source. For radiation from a plane source, it is essential to integrate the H_ν contribution over the plane,

as attenuated by passage through the absorbing medium. The relation for H_ν, in this case, is given by [28]

$$H_\nu = 2q_\nu(0)\ E_2(-\kappa_\nu z) \tag{7.12}$$

where $q_\nu(0)$ is the spectral radiative flux density at the shock wave, κ_ν is the spectral absorption coefficient, and $E_n(t)$ is the exponential integral of order n. The expression for κ_ν (which may also be interpreted as inverse of the photon mean free path) is given by

$$\kappa_\nu = N_{H_2}\ \sigma(\nu) \tag{7.13}$$

In this form κ_ν represents the absorption coefficient of H_2 molecules. If the number density N_{H_2} (and hence, κ_ν) can be taken to be independent of z (which is a good approximation for small ionization and dissociation), then the optical depth is defined by

$$\zeta = \kappa_\nu z \tag{7.14}$$

For the plane radiating source (where $\nabla^2_{x,y}\phi = 0$), therefore, a combination of Eqs. (7.9), (7.12), and (7.14) results in a simpler expression, the integration of which results in [42]

$$\phi = -[2\ P_\nu\ q_\nu(0)/(\Gamma\kappa_\nu^2)]E_4(-\zeta) \tag{7.15}$$

where the boundary condition of $(\partial\phi/\partial\zeta)\to 0$ as $\zeta\to\infty$ has been used.

From Eq. (7.3), the velocity perturbations, ahead of the shock front, can now be written as $V_{1x} = V_{1y} = 0$, and

$$v_{1z} = -[2\ P_\nu\ q_\nu(0)/(\Gamma\kappa_\nu)]E_3(-\zeta) \tag{7.16}$$

From Eq. (7.4), the expression for pressure perturbation is found to be

$$p_1 = [2\ \gamma\ P_\nu\ q_\nu(0)/\kappa_\nu]E_3(-\zeta) \tag{7.17}$$

where it was assumed that $(M^2/T)\simeq 1$. Similarly, the expressions for density perturbation, total enthalpy, static enthalpy, and species concentration are found to be [2,42]

$$\rho_1 = [2\ P_\nu\ q_\nu(0)/(\Gamma\kappa_\nu)]E_3(-\zeta) \tag{7.18}$$

$$H_{T_1} = [2\ q_\nu(0)/(\rho_\infty\ V_\infty^3)]E_3(-\zeta) \tag{7.19}$$

$$H_1 = 2q_\nu(0)\{[1/(\rho_\infty\ V_\infty^3)] + P_\nu/(\Gamma\kappa_\nu)\ E_3(-\zeta) \tag{7.20}$$

$$C_H = [2\ W_{H_2}\ m_1/(\rho_\infty\ V_\infty\ h\nu)]Y_D(\nu)\ q_\nu(0)E_3(-\zeta) \tag{7.21a}$$

$$C_{H_2^+} = [2\ W_{H_2}\ m_1/(\rho_\infty\ V_\infty\ h\nu)]Y_I(\nu)\ q_\nu(0)E_3(-\zeta) \tag{7.21b}$$

By employing Eqs. (7.17), (7.18), and (7.21), Eq. (2.5) is solved for the temperature variation. For this case now, all flow properties at any point upstream of the shock can be determined.

7.1.1.2 Radiation From Spherical and Cylindrical Point Sources. The physical model for radiation from spherical and cylindrical point sources is shown in Fig. 3. A spherical point source is a source which radiates equally in all directions. A cylindrical point source is a source which radiates as a cylinder of infinitesimal radius and length. For both cases, the incident radiation at any field point s is given by [1,2]

$$H_\nu = (A_\nu/s^2)\ \exp(-\kappa_\nu s)(\sin\theta)^j \tag{7.22}$$

In this equation, A_ν represents the radiative strength of the source, s is the distance from the source and θ is the angle between the free stream velocity vector and a line from the field point to the center of the source. The superscript j is equal to zero for a spherical point source and one for a cylindrical point source.

Eq. (7.22) can be substituted in Eqs. (7.9)-(7.10) to obtain the corresponding equations for the perturbation potential. Within the confines of the assumptions made in obtaining Eq. (7.22), however, both problems (spherical as well as cylindrical point source) can be considered to be axisymmetric. The governing equation for the perturbation potential, therefore, can be written as

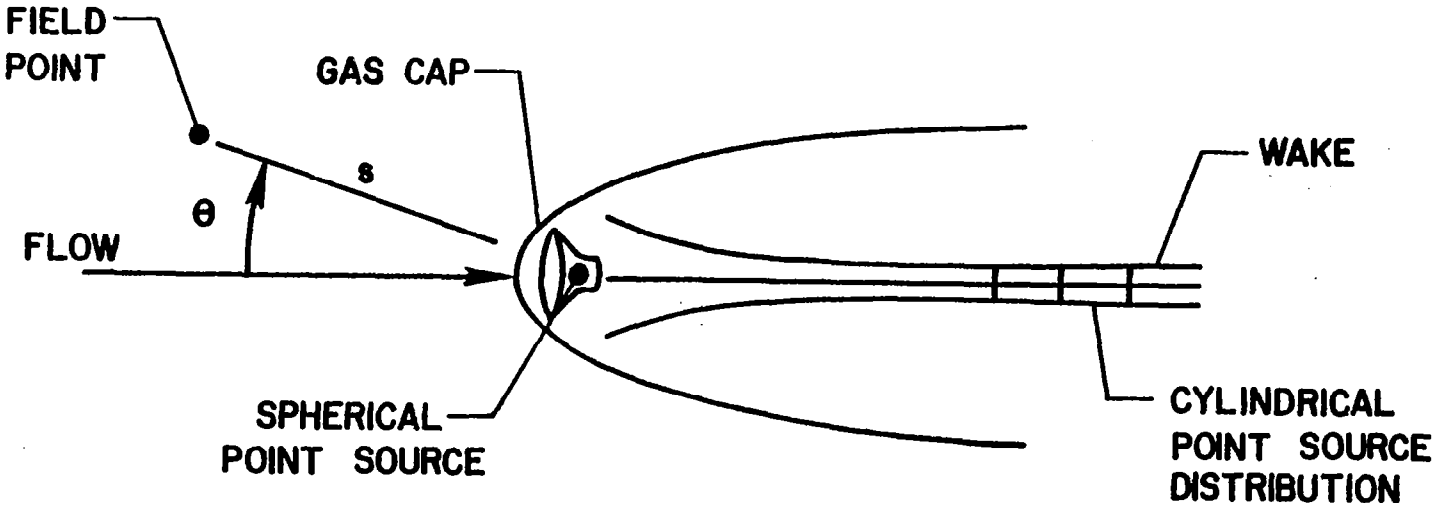

Fig. 3 Approximation of radiating flow by point sources.

$$\eta^{-1}\,\partial/\partial\eta(\eta\partial\phi'/\partial\eta) - \Gamma\,\partial^2\phi'/\partial\zeta^2 = \Lambda\,\mu^{-2}\,e^{-\mu}\,(\sin\theta)^j \qquad (7.23)$$

where

$$\mu = \kappa_\nu s, \quad \eta = \kappa_\nu r, \quad \phi' = \kappa_\nu \phi, \quad \Lambda = \Lambda(\nu) = \kappa_\nu\, P_\nu\, A_\nu$$

A procedure for general solution of this equation is suggested by Smith [1]. For entry flow, however, $M_\infty^2 >> 1$ and Eq. (7.23) can be solved by expanding ϕ in a series in $(1/\Gamma)$ in the vicinity of the body. Thus, one can express as

$$\phi' = -(\kappa_\nu/\Gamma)[F_j(\zeta,\eta) + (1/\Gamma)F_j^{(1)}(\zeta,\eta) + (1/\Gamma)\,F_j^{(2)}(\zeta,\eta) + \ldots] \qquad (7.24)$$

where F_j's are function for perturbation potential. Substitution of this relation into Eq. (7.23) gives

$$\partial^2 F_j/\partial\zeta^2 = \mu^{-2}\exp(-\mu)(\sin\theta)^j \qquad (7.25)$$

and

$$\partial^2 F_J^{(n)}/\partial\zeta^2 = -\eta^{-1}\,\partial/\partial\eta(\eta\,\partial F_j^{(n-1)}/\partial\eta) \qquad (7.26)$$

The problem, therefore, is reduced to quadratures in the vicinity of the body. In the present analysis, only the terms in $(1/\Gamma)$ will be retained. By integrating Eq. (7.25) twice, the expression for F_j is obtained as

$$F_j(\zeta,\eta) = \int_{-\infty}^{\infty} \mu_o^{-2}\exp(-\mu_o)(\eta/\mu_o)^j\,(\zeta - \zeta_o)d\zeta_o \qquad (7.27)$$

where $\mu_o^2 = \eta^2 + \zeta^2$. For convenience, let us denote

$$G_j(\zeta,\eta) = \partial F_j/\partial\zeta = \int_{-\infty}^{\zeta} \mu^{-2}\exp(-\mu_o)(\eta/\mu_o)^j\,d\zeta_o \qquad (7.28a)$$

$$H_j(\zeta,\eta) = \partial F_j/\partial\eta = \int_{-\infty}^{\zeta} \mu^{-3}\exp(-\mu_o)\{(\eta/\mu)^j\,[\eta + (\eta/\mu_o)(2+j)] - j\}(\zeta - \zeta_o)d\zeta_o \qquad (7.28b)$$

With these definitions of F_j, G_j, and H_j, the perturbation quantities can be expressed as [2,42]

$$\phi' = -(\Lambda/\Gamma)F_j(\zeta,\eta) \tag{7.29}$$

$$v_{1r} = (\Lambda/\Gamma)H_j(\zeta,\eta) \tag{7.30}$$

$$v_{1z} = -(\Lambda/\Gamma)G_j(\zeta,\eta) \tag{7.31}$$

$$p_1 = \gamma\Lambda G_j(\zeta,\eta) \tag{7.32}$$

$$\rho_1 = (\Lambda/\Gamma)G_j(\zeta,\eta) \tag{7.33}$$

$$H_{T_1} = (\kappa_\nu A_\nu/\rho_\infty V_\infty^3)G_j(\zeta,\eta) \tag{7.34}$$

$$C_H = (m_1 A_\nu \kappa_\nu^2/\rho_\infty V_\infty h\nu)Y_D(\nu)\ G_j(\zeta,\eta) \tag{7.35a}$$

$$C_{H_2^+} = (m_1 A_\nu \kappa_\nu^2/\rho_\infty V_\infty h\nu)Y_i(\nu)\ G_j(\zeta,\eta) \tag{7.35b}$$

Note that for the case of spherically radiating point source j = 1 in the above equations. Also, these equations are obtained for arbitrary frequency. The expression for total potential, for this case, can be obtained by combining Eqs. (7.11) and (7.24) as

$$\Phi = -(1/\Gamma) \int_0^\infty [\Lambda(\nu)/\kappa\nu]F_j(\zeta,\eta)d\nu \tag{7.36}$$

Furthermore, it should be noted that the above solutions are valid in the region where $[\mu^{-2} \exp(-\mu)\ (\sin\theta)^j]$ does not vanish. This is the case of spherically symmetric flow ahead of the entry body and is of primary concern in the present study. Other cases involving cylindrical point source are discussed in [1,2].

The procedure for expressing the perturbation equations in terms of the photoabsorption model employed in the precursor region is given, in detail, in [42].

7.1.2 Thin Layer Approximation

A direct integration of Eqs. (2.23) through (2.27) results in the following governing equations for the precursor region

$$\rho v = \rho_\infty v_\infty \tag{7.37}$$

$$\rho_\infty v_\infty (u - u_\infty) = 0 \tag{7.38}$$

$$\rho_\infty v_\infty (v - v_\infty) + (p - p_\infty) = 0 \tag{7.39}$$

$$\rho_\infty v_\infty (H - H_\infty) + q_R = 0 \tag{7.40}$$

$$\rho_\infty v_\infty (\partial C_\alpha / \partial n) - K_\alpha = 0 \tag{7.41}$$

where it has been assumed that $q_{R\infty} = 0$.

In Eq. (7.40), H represents the total enthalpy and is given by a combination of Eqs. (4.1) and (4.4). The expression for the radiative flux, q_R, is given by Eq. (6.4). For the present application, Eq. (7.41) will be written for atomic hydrogen and hydrogen ions. By following the procedure outlined in [1,42] the expressions for species concentration are found to be

$$C_H = 2\beta_4 \sum_{i=1}^{N} Y_{D_i} E_3(\tau_i)(kT_s)^{-1} I(v_i) \tag{7.42}$$

$$C_{H_2^+} = + - 2\beta_4 \sum_{i=1}^{N} Y_{I_i} E_3(\tau_i)(kT_s)^{-1} I(v_i^2) \tag{7.43}$$

where

$$\beta_4 = (15/\pi^4)[q(0)m_1/(\rho_\infty V_\infty)]$$

$$I(v_i^2) = \int_{v_{1i}}^{v_{2i}} \{v^2/[\exp(v) - 1]\}dv$$

and m_1 represents the weight of the H_2 molecule in grams per molecule.

Note that there are nine algebraic equations to evaluate the nine unknowns ρ, v, u, p, h, H, C_H, $C_{H_2^+}$. The solutions of this set of algebraic equations are obtained by using the Gauss-Seidel method [74]. The properties at the infinity are used as the first initial guess in the Gauss-Seidel method. The iteration is continued until all the quantities in this region become invariant. The flow chart of the computational procedure is illustrated in Figs. 4 and 5.

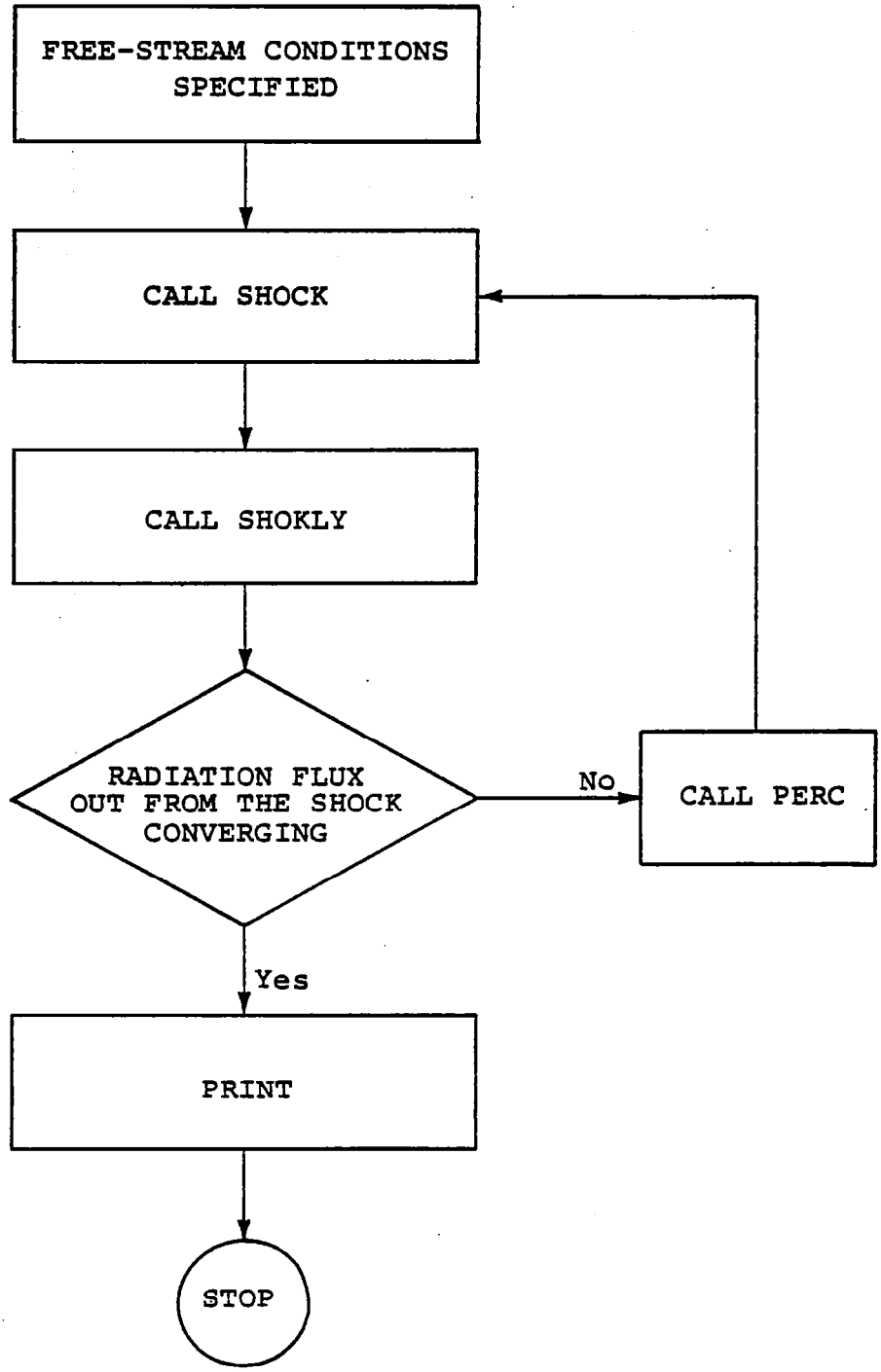

Fig. 4 Flow chart for combined precursor/shock-layer solution procedure.

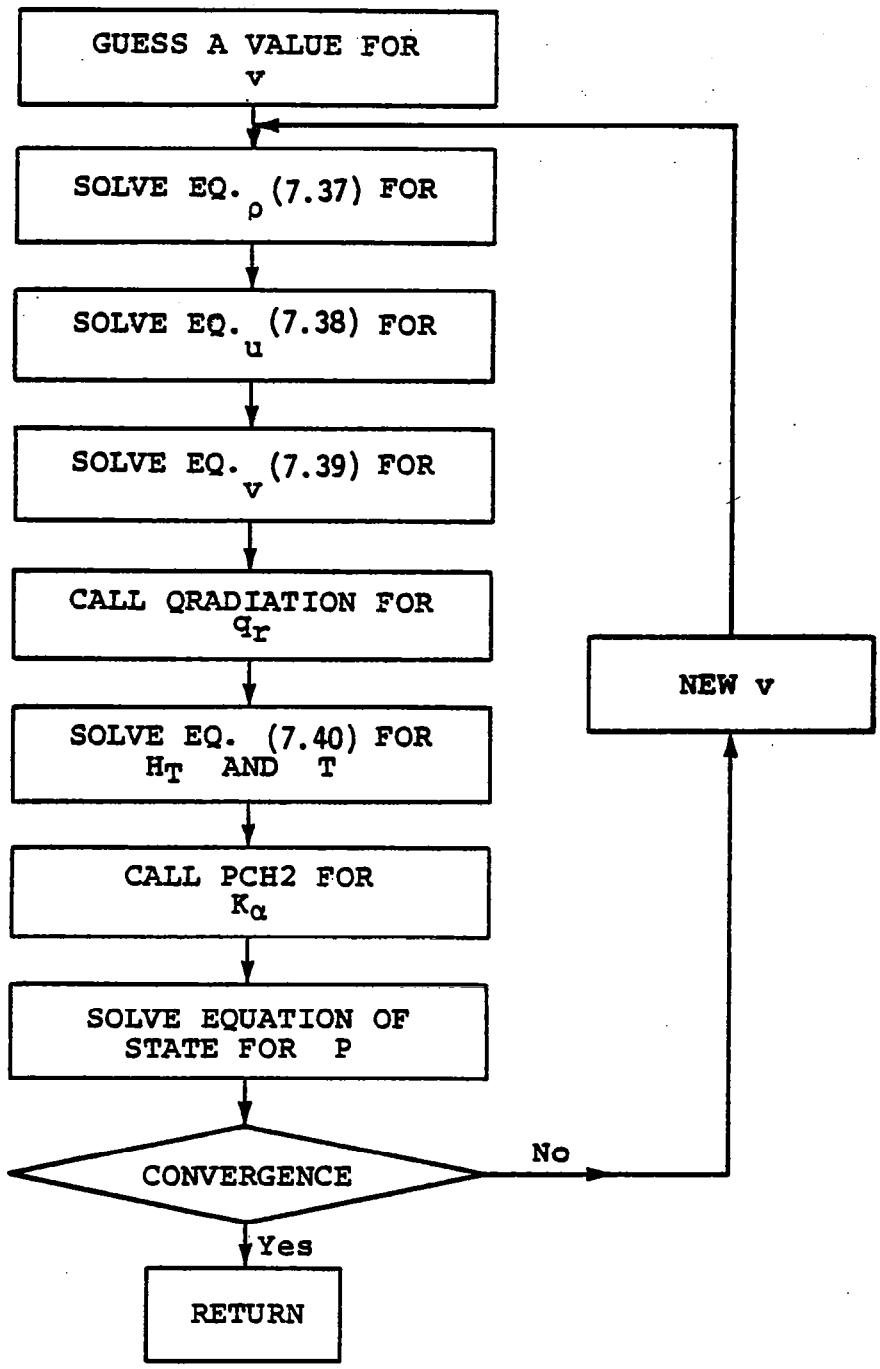

Fig. 5 Flow chart for subroutine PERC used in the precursor region solution procedure.

7.2 Shock-Layer Region

A numerical procedure for solving the viscous shock-layer equations for stagnation and downstream regions is given by Davis [14]. Moss applied this method of solution to reacting multicomponent mixtures in [15,17]. A modified form of this procedure is used in this study to obtain solutions of the viscous shock-layer equations. In this method, a transformation is applied to the viscous shock-layer equations in order to simplify the numerical computations. In this transformation most of the variables are normalized with their local shock values. The transformed variables are [15]

$$\eta = y/y_s \qquad \bar{p} = p/p_s \qquad \bar{\mu} = \mu/\mu_s$$

$$\xi = x \qquad \bar{\rho} = \rho/\rho_s \qquad \bar{K} = K/K_s$$

$$\bar{u} = u/u_s \qquad \bar{T} = T/T_s \qquad \bar{C}_p = C_p/C_{ps}$$

$$\bar{v} = v/v_s \qquad \bar{H} = H/H_s \qquad (7.44)$$

The transformations relating the differential quantities are

$$\frac{\partial}{\partial x}( ) = \frac{\partial}{\partial \xi}\frac{1}{y_s}(dy_s/d\xi)\eta\frac{\partial}{\partial \eta}( ) \qquad (7.45)$$

and

$$\frac{\partial}{\partial y}( ) = \frac{1}{y_s}\frac{\partial}{\partial \eta}( ), \quad \frac{\partial^2}{\partial y^2}( ) = \frac{1}{y_s^2}\frac{\partial^2}{\partial \eta^2}( ) \qquad (7.46)$$

The transformed equations can be expressed in a general form as

$$\partial^2 W/\partial\eta^2 + a_1 \partial W/\partial\eta + a_2 W + a_3 + a_4 \partial W/\partial\xi = 0 \qquad (7.47)$$

The quantity W represents $\bar{u}$ in the X-momentum equation, $\bar{T}$ in the temperature energy equation, $\bar{H}$ in the enthalpy energy equation, and C_i in the species continuity equations. In most cases, the coefficients a_1 to a_4 to be used in this study are exactly the same as given in [15]. However,

there is one exception. Since radiation is included in the present study, the coefficients of the energy equation are different from those used in [15]. For example, in the enthalpy energy equation, coefficients a_1, a_2, and a_4 are the same as given in [15], but a_3 is different, and this is given by

$$a_3 = \frac{P_{r,s}\bar{P}_r y_s^2}{\mu_s \bar{\mu} H_s}\left[\frac{1}{y_s}\frac{\partial \Psi}{\partial \eta} + \left(\frac{\kappa}{1 + y_s \eta \kappa} + \frac{\cos\theta}{r + y_s \eta \cos\theta}\right)\Psi\right]$$

$$+ \frac{y_s P_r \rho_s v_s \bar{v}}{\varepsilon^2 \mu_s \bar{\mu} H_s}\frac{\partial p}{\partial \eta} - \frac{y_s \bar{P}_r P_{r,s}}{\varepsilon^2 \mu_s H_s \bar{\mu}}\left[\frac{1}{y_s}\frac{\partial q_R}{\partial \eta}\right.$$

$$\left. + q_R\left(\frac{\kappa}{1 + y_s \eta \kappa} + \frac{\cos\theta}{r + y_s \cos\theta}\right)\right] \qquad (7.48)$$

where

$$\dot{\psi} = \frac{\mu_s}{y_s Pr,_s}\left[\frac{0.1\bar{\mu}}{Pr}\sum_{i=1}^{N} h_i \frac{\partial C_i}{\partial \eta} + \frac{u_s^2 \bar{\mu}\bar{u}}{\bar{Pr}}(Pr,_s \bar{P}_r - 1)\frac{\partial \bar{\mu}}{\partial \eta}\right]$$

$$- \frac{\mu_s \mu_s^2 \kappa \bar{\mu} u^2}{1 + y_s \eta \kappa}$$

Other transformed equations are the same as given in [15].

The surface boundary conditions in terms of transformed variables are

$$\bar{\mu} = 0, \quad \bar{v} = 0, \quad \bar{T} = \bar{T}_w \qquad (7.49)$$

The transformed shock conditions are found to be

$$\bar{u} = \bar{v} = \bar{T} = \bar{H} = \bar{\rho} = \bar{p} = 1 \qquad (7.50)$$

at $n = 1$.

The second order partial differential equations as expressed by Eq. (7.47), along with the surface boundary and shock conditions, are

solved by employing an implicit finite-difference method. In order to obtain numerical solutions for the downstream region, it is necessary to have an accurate stagnation streamline solution. Since the shock shape is affected by the downstream flow, a truncated series of shock standoff distance is used to develop the stagnation streamline equations. As such, the shock standoff distance is expressed by

$$y_s = y_{1s} + y_{2s}\,\xi^2 + \cdots \tag{7.51}$$

Since ξ is small and the curvature κ is approximately one in the stagnation region, it is logical to say that (see Fig. 1)

$$\beta \simeq \xi \tag{7.52}$$

Since $\theta = (\pi/2) - \beta$, there is obtained

$$\begin{aligned}\alpha &= \theta + \tan^{-1}[(\partial n_s/\partial\xi)/(1 + \kappa y_s)] \\ &= (\pi/2) + \xi\{[2y_{2s}/(1 + y_{1s})] - 1\}\end{aligned} \tag{7.53}$$

By using Eqs. (7.51) to (7.53), the shock relations [Eqs. (3.4)-(3.9)] can be expressed in terms of expanded variables as

$$v^*_{s-} = 1/\rho_{s-},\quad v_{s-} = 1/\rho_{s-} \tag{7.54}$$

$$u^*_{s-} = -\xi[2y_{2s}/(1 + y_{1s}) - 1] \tag{7.55}$$

$$u_{s-} = \xi\{1 - [2y_{2s}/(1 - y_{1s})](1 + 1/\rho_{s-})\} \tag{7.56}$$

$$\begin{aligned}p_{s-} = p_{s+} &+ (1 - 1/\rho_{s-}) + \xi^2\{(1 - 1/\rho_{s-}) \\ &\cdot [1 - 2y_{2s}/(1 + y_{1s})]^2\}\end{aligned} \tag{7.57}$$

$$h_{s-} = h_{s+} + (1 - 1/\rho_{s-})/2 \tag{7.58}$$

In Eqs. (7.54) through (7.58), only p_s and u_s involve y_{2_s} in the first terms of their expansion. Thus, a series expansion for the flow

variables is assumed about the axis of symmetry with respect to non-dimensional distance ξ near the stagnation streamline as

$$p(\xi,\eta) = p_1(\eta) + p_2(\eta)\xi^2 + \text{---} \tag{7.59a}$$

$$u(\xi,\eta) = u_1(\eta)\xi + \text{---} \tag{7.59b}$$

$$v(\xi,\eta) = v(\eta) + \text{---} \tag{7.59c}$$

$$\rho(\xi,\eta) = \rho_1(\eta) + \text{---} \tag{7.59d}$$

$$T(\xi,\eta) = T_1(\eta) + \text{---} \tag{7.59e}$$

$$\mu(\xi,\eta) = \mu_1(\eta) + \text{---} \tag{7.59f}$$

$$K(\xi,\eta) = K_1(\eta) + \text{---} \tag{7.59g}$$

$$C_p(\xi,\eta) = C_{p1}(\eta) + \text{---} \tag{7.59h}$$

$$C_i(\xi,\eta) = C_{i1}(\eta) + \text{---} \tag{7.59i}$$

Since y_{2s} is a function of downstream flow, it cannot be determined by the stagnation solutions. Thus, a value of $y_{2s} = 0$ is assumed initially. This assumption is removed by iterating on the solution by using the previous shock standoff distances to define y_{2s}.

The new form of x-momentum and energy equations in the ξ,η can be written as

$$\frac{\partial^2 W}{\partial \eta^2} + a_1 \frac{\partial W}{\partial \eta} + a_2 W + a_3 = 0 \tag{7.60}$$

For x-momentum, $W = \bar{u}$ and coefficients a_1, a_2, and a_3 are exactly the same as given in [15]. For the enthalpy equation, $W = \bar{H}$ and again a_1 and a_2 are the same as defined in [15] but a_3 is given by

$$a_3 = (Pr_{,1s} y_{1s}^2/\mu_{1s} H_{1s})(Pr_{,1}/\bar{\mu}_1)[(1/y_{1s})(\partial\Psi/\partial\eta) + 2\Psi/(1 + \eta y_{1s})] + (y_{1s}\bar{P}_r p_s v_s \bar{v}_1/\epsilon^2 \mu_s \tilde{\mu} H_s)(\partial \bar{p}_1/\partial\eta) \tag{7.61}$$

Other stagnation streamline equations are the same as given in [15]. It should be noted that at the body surface $\bar{p}_1 = 1$ and $\bar{p}_2 = 0$.

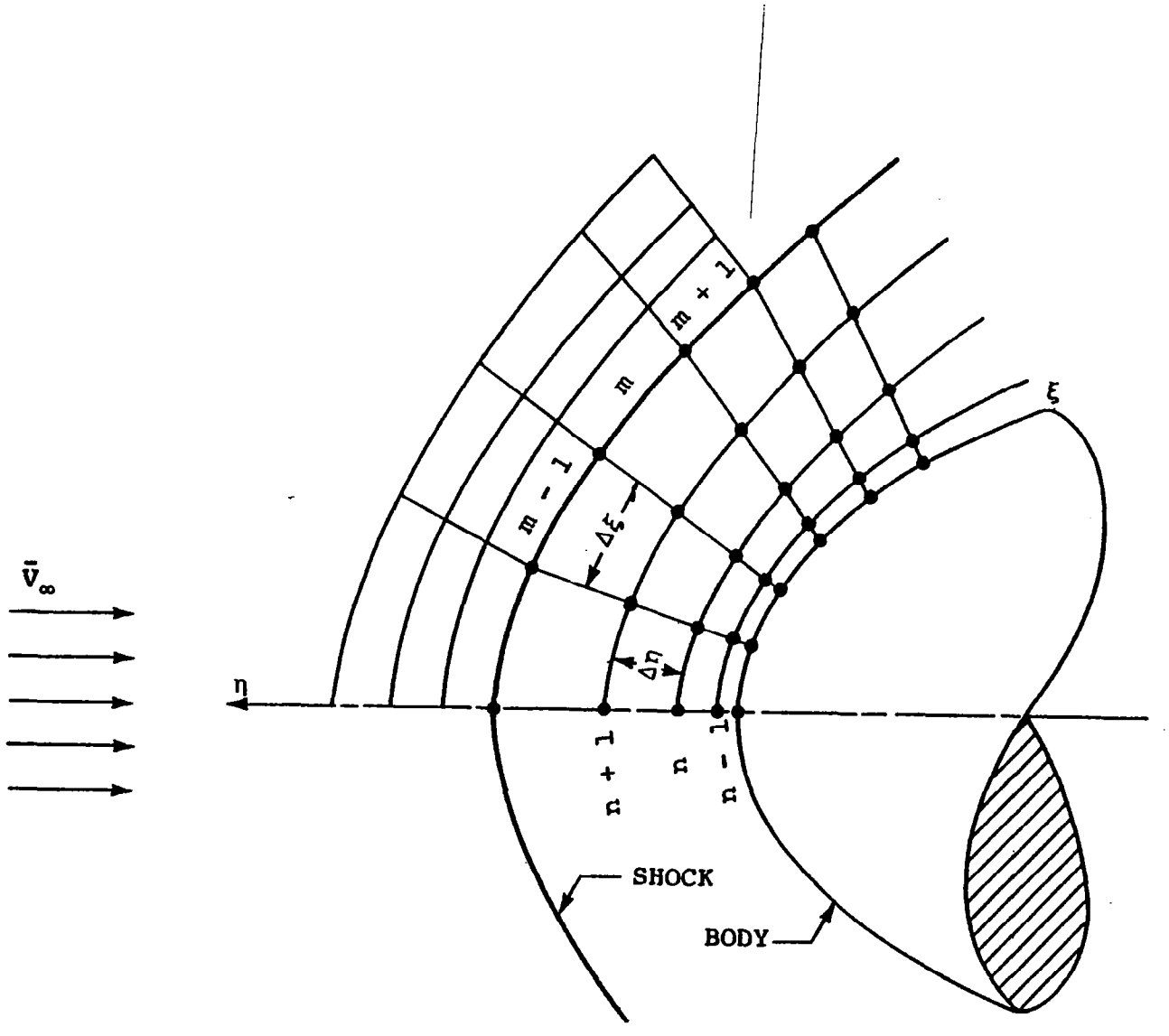

Fig. 6 Finite difference representation of flow field.

As mentioned earlier, the governing second-order partial differential equations are solved by employing an implicit finite-difference method. For this purpose, the shock layer is considered as a network of nodal points with a variable grid space in the η-direction. The scheme is shown in Fig. 6 where m is a station measured along the body surface and n denotes the station normal to the body surface. The derivatives are converted to finite-difference form by using Taylor's series expansions. Thus, unequal space central difference equations in the η-direction at point m, n can be written as

$$\left(\frac{\partial W}{\partial \eta}\right)_n = \frac{\Delta\eta_{n-1}}{\Delta\eta_n(\Delta\eta_{n-1} + \Delta\eta_n)} W_{m,n+1} - \frac{\Delta\eta_n}{\Delta\eta_{n-1}(\Delta\eta_{n-1} + \Delta\eta_n)} W_{m,n-1}$$

$$+ \frac{\Delta\eta_n - \Delta\eta_{n-1}}{\Delta\eta_n \Delta\eta_{n-1}} W_{m,n} \qquad (7.62a)$$

$$\left(\frac{\partial^2 W}{\partial \eta^2}\right)_n = \frac{2}{\Delta\eta_n(\Delta\eta_n + \Delta\eta_{n-1})} W_{m,n+1} - \frac{2}{\Delta\eta_n \Delta\eta_{n-1}} W_{m,n}$$

$$+ \frac{2}{\Delta\eta_{n-1}(\Delta\eta_n + \Delta\eta_{n-1})} W_{m,n-1} \qquad (7.62b)$$

$$\left(\frac{\partial W}{\partial \xi}\right)_m = \frac{W_{m,n} - W_{m-1,n}}{\Delta\xi} \qquad (7.62c)$$

A typical difference equation is obtained by substituting the above equations in Eqs. (7.47) or (7.60) as

$$W_{m,n} = -(D_n/B_n) - (A_n/B_n)W_{m,n+1} - (C_n/B_n)W_{m,n-1} \qquad (7.63)$$

where

$$A_n = (2 + a_1\Delta\eta_{n-1})/[\Delta\eta_n(\Delta\eta_n + \Delta\eta_{n-1})]$$

$$B_n = -[2 - a_1(\Delta\eta_n - \Delta\eta_{n-1})]/(\Delta\eta_n \Delta\eta_{n-1}) - a_2 - a_4/\Delta\xi_{m-1}$$

$$C_n = (2 - a_1\Delta\eta_n)/[\Delta\eta_{n-1}(\Delta\eta_n + \Delta\eta_{n-1})]$$

$$D_n = a_3 - a_4 W_{m-1,n}/\Delta\xi_{m-1}$$

Now, if it is assumed that

$$W_{m,n} = E_n W_{m,n+1} + F_n \tag{7.64}$$

or

$$W_{m,n-1} = E_{n-1} W_{m,n} + F_{n-1} \tag{7.65}$$

then by substituting Eq. (7.65) into Eq. (7.63), there is obtained

$$W_{m,n} = [-A_n/(B_n + C_n E_{n-1})]W_{m,n+1} + (-D_n - C_n F_{n-1})/(B_n + C_n E_{n-1}) \tag{7.66}$$

By comparing Eqs. (7.64) and (7.66), one finds

$$E_n = -A_n/(B_n - C_n E_{n-1}) \tag{7.67}$$

$$F_n = (-D_n - C_n F_{n-1})/(B_n + C_n E_{n-1}) \tag{7.68}$$

Now, since E_1 and F_1 are known from the boundary conditions, E_n and F_n can be calculated from Eqs. (7.67) and (7.68). The quantities $W_{m,n}$ at point m, n can now be calculated from Eq. (7.64).

The overall solution procedure starts with evaluation of the flow properties immediately behind the shock by using the Rankine-Hogoniot relations. With known shock and body surface conditions, each of the second-order partial differential equations are integrated numerically by using the tridiagonal formalism of Eq. (7.47) and following the procedure described by Eqs. (7.63) to (7.68). As mentioned before, the solutions are obtained first for the stagnation streamline. With this solution providing the initial conditions, the solution is marched downstream to the desired body location. The first solution pass provides

only an approximate flow-field solution. This is because in the first solution pass the thin shock-layer form of the normal momentum equation is used, the stagnation streamline solution is assumed to be independent of downstream influence, the term $dy_s/d\xi$ is equated to zero at each body station, and the shock angle α is assumed to be the same as the body angle θ. All these assumptions are removed by making additional solution passes.

In the first solution pass, the viscous shock-layer equations are solved at any location m after obtaining the shock conditions (to establish the outer boundary conditions) from the precursor region solutions. The converged solutions at station m-1 are used as the initial guess for the solutions at station m. The solution is then iterated locally until convergence is achieved.

For the stagnation streamline, guess values for dependent variables are used to start the solution. In the first local iteration, both $(\partial y_s/\partial \xi)$ and $(\partial W/\partial \xi)$ are assumed to be zero. The energy equation then is integrated numerically to obtain a new temperature. By using this temperature, new values of thermodynamic and transport properties are calculated. Next, the x-momentum equation is integrated to find the $\bar{u}$ component of velocity. The continuity equation is used to obtain both the shock standoff distance and the $\bar{v}$ component of velocity. The pressure $\bar{P}$ is determined by integrating the normal momentum equation. The equation of state is used to determine the density. For example, the integration of the stagnation streamline continuity equation from 0 to η results in

$$[(1 + y_{1s}\eta)^2 \rho_{1s} v_{1s} \rho_1] v_1 = (-2 y_{1s} \rho_{1s} u_{1s}) A \qquad (7.69)$$

where

$$A = \int_0^{\eta} (1 + y_{1s}\eta)\bar{\rho}_1\bar{u}_1 d\eta \tag{7.70}$$

This equation gives the v-velocity component along the stagnation streamline. However, integration of the continuity equation from $\eta = 0$ to $\eta = 1$ results in

$$(1 + y_{1s})^2\rho_{1s}v_{1s} = -2\rho_{1s}u_{1s}y_{1s}(B + C) \tag{7.71}$$

where

$$B = \int_0^I \bar{\rho}_1\bar{u}d\eta, \quad C = y_{1s} \int_0^1 \bar{\rho}_1\bar{u}_1\eta d\eta$$

The shock standoff distance can be obtained from the solution of Eq. (7.71) as

$$y_{1s} = \frac{-(2v_{1s}+2Bu_{1s})+[(2v_{1s}+2Bu_{1s})^2-4(v_{1s}+2Cu_{1s})v_{1s}]^{1/2}}{2(v_{1s}+2Cu_{1s})} \tag{7.72}$$

Similarly, other quantities at the stagnation streamline are obtained.

With known stagnation streamline solution and body surface and shock conditions, the above procedure is used to find solutions for any body location m. The downstream shock standoff distance and the v-velocity component are obtained by integrating the continuity equation in the η-direction from 0 to 1, and o to η respectively. Integration of the continuity equation from $\eta = 0$ to $\eta = 1$ results in

$$\frac{\partial}{\partial\xi}[y_s^2 \cos\theta\ \rho_s u_s \int_o^1 \bar{\rho}\bar{u}\eta d\eta + y_s r\rho_s u_s \int_o^1 \bar{\rho}\bar{u}d\eta$$

$$= (r + y_s \cos\theta)[y_s^1\rho_s u_s - (1 + y_s\kappa)\rho_s v_s] \tag{7.73}$$

By defining, for station m

$$C_1 = \cos\theta\ \rho_s u_s \int_0^1 \bar{\rho}\bar{u}\eta d\eta, \quad C_2 = r\rho_s u_s \int_0^1 \bar{\rho}\bar{u}d\eta$$

and denoting the same relations by C_3 and C_4 for station m-1, Eq. (7.73) can be expressed in terms of a difference equation as

$$[(C_1 y_s^2 + C_2 y_s)_m - (C_3 y_s^2 + C_4 y_s)_{m-1}]/\Delta\xi$$

$$= r\rho_s u_s y'_{sm} + \cos\theta\ \rho_s u_s y'_{sm} y_{sm} - r\rho_s v_s$$

$$- r\rho_s v_s \kappa y_{sm} - \cos\theta\ \rho_s v_s y_{sm} - \cos\theta\ \rho_s v_s \kappa y_{sm}^2 \qquad (7.74)$$

This can be expressed in a quadratic form as

$$(AA) y_{sm}^2 + (BB) y_{sm} + (CC) = 0 \qquad (7.75)$$

where

$$AA = C_1 + \cos\theta \kappa \rho_s v_s \Delta\xi$$

$$BB = C_2 + r\rho_s v_s \kappa \Delta\xi - \cos\theta\ \rho_s u_s y'_s \Delta\xi + \cos\theta\ \rho_s v_s \Delta\xi$$

$$CC = -[C_3 (y_s)_{m-1}^2 + C_4 (y_s)_{m-1} + r\rho_s u_s y'_s \Delta\xi - r\rho_s v_s \Delta\xi]$$

The shock standoff distance at station m is obtained from Eq. (7.75) as

$$y_{sm} = \{ - (BB) + [(BB)^2 - 4(AA)(CC)]^{1/2} \}/2(AA) \qquad (7.76)$$

The v-velocity component can be obtained in a similar manner. Integration of the continuity equation from 0 to y gives

$$\frac{\partial}{\partial\xi} [{}_0\int^{\eta} y_{sm}(r + y_{sm}\eta \cos\theta)\rho_s u_s \bar{\rho}\bar{u} d\eta]$$

$$+ (r + y_{sm}\eta \cos\theta)[(1 + \eta y_{sm}\kappa)(\rho_s v_s \bar{\rho}\bar{v})$$

$$- y'_{sm}\eta\rho_s u_s \bar{\rho}\bar{u}] = 0 \qquad (7.77)$$

As before, this can be expressed in terms of a difference equation as

$$\{[(KK)_m - (KK)_{m-1}]/\Delta\xi\} + (II)_m \bar{v} + (JJ)_m = 0 \qquad (7.78)$$

where

$$(II)_m = (r + y_{sm}\eta \cos\theta)(1 + y_{sm}\eta\kappa)\rho_s v_s \bar{\rho}$$

$$(JJ)_m = -(r + y_{sm}\eta \cos\theta) y'_{sm}\eta\rho_s u_s \bar{\rho}\bar{u}$$

$$(KK)_m = {}_0\int^{\eta} y_{sm}(r + y_{sm}\eta \cos\theta)\rho_s u_s \bar{\rho}\bar{u} d\eta$$

Thus, the v-velocity component at each point on the station m can be obtained from Eq. (7.78). Other quantities at station m are obtained

by a similar manner. As mentioned before, the first pass is only an approximate solution because of several inherent assumptions. These assumptions are removed by iteration in the next pass. For the subsequent solution passes, the shock angle and y_{2s} are given by

$$\alpha = \theta + \tan^{-1}[y'_{sm}/(1 + \kappa y_{sm})] \tag{7.79}$$

$$y_{s2} = (y_{s3} - y_{s1})/4(\Delta\xi)^2 \tag{7.80}$$

The flow diagrams for computation procedure are shown in Fig. 4 and Figs. 7 to 13.

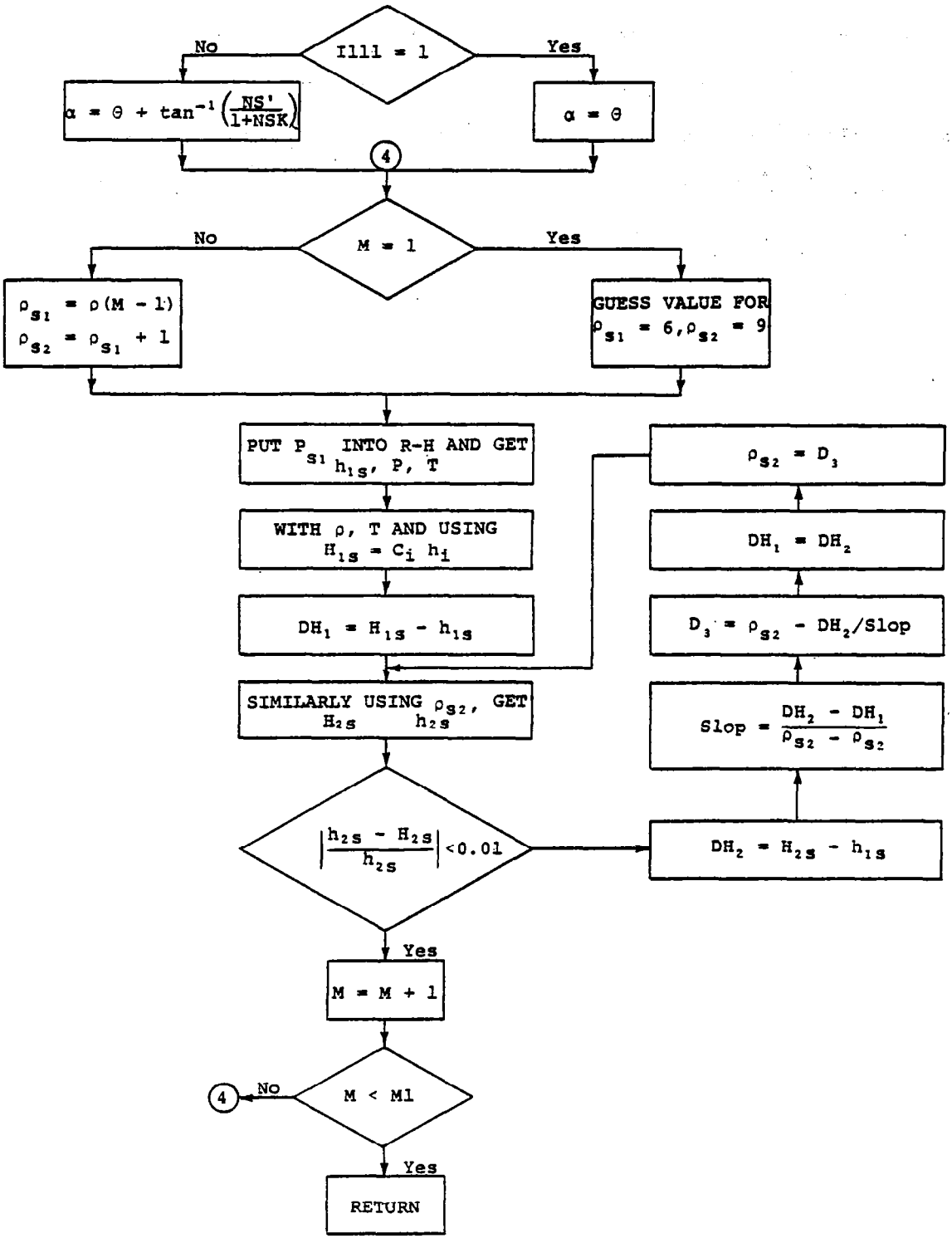

Fig. 7 Flow chart for subroutine SHOCK for shock-layer solution.

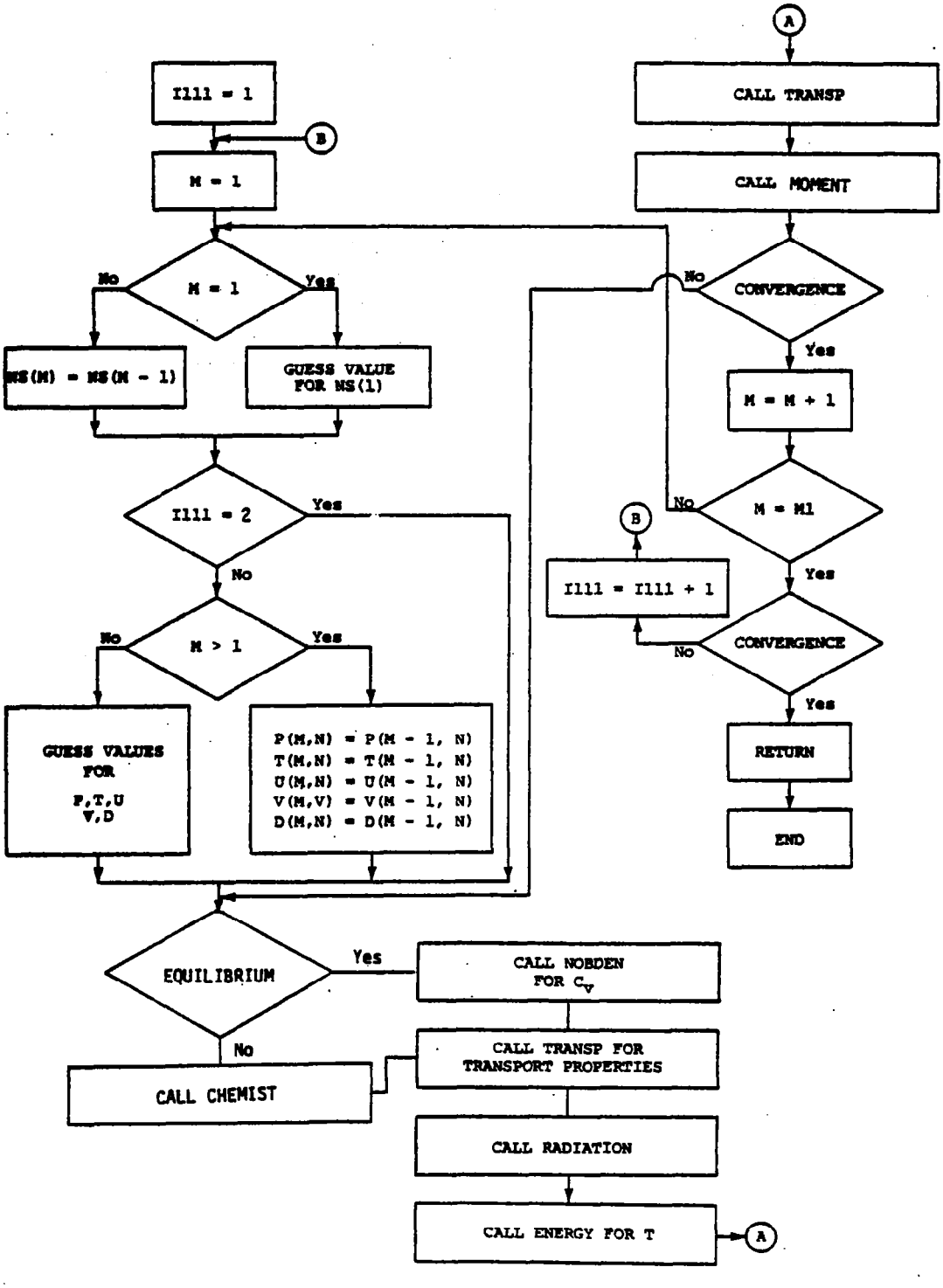

Fig. 8 Flow chart for subroutine SHOKLY for shock-layer solution.

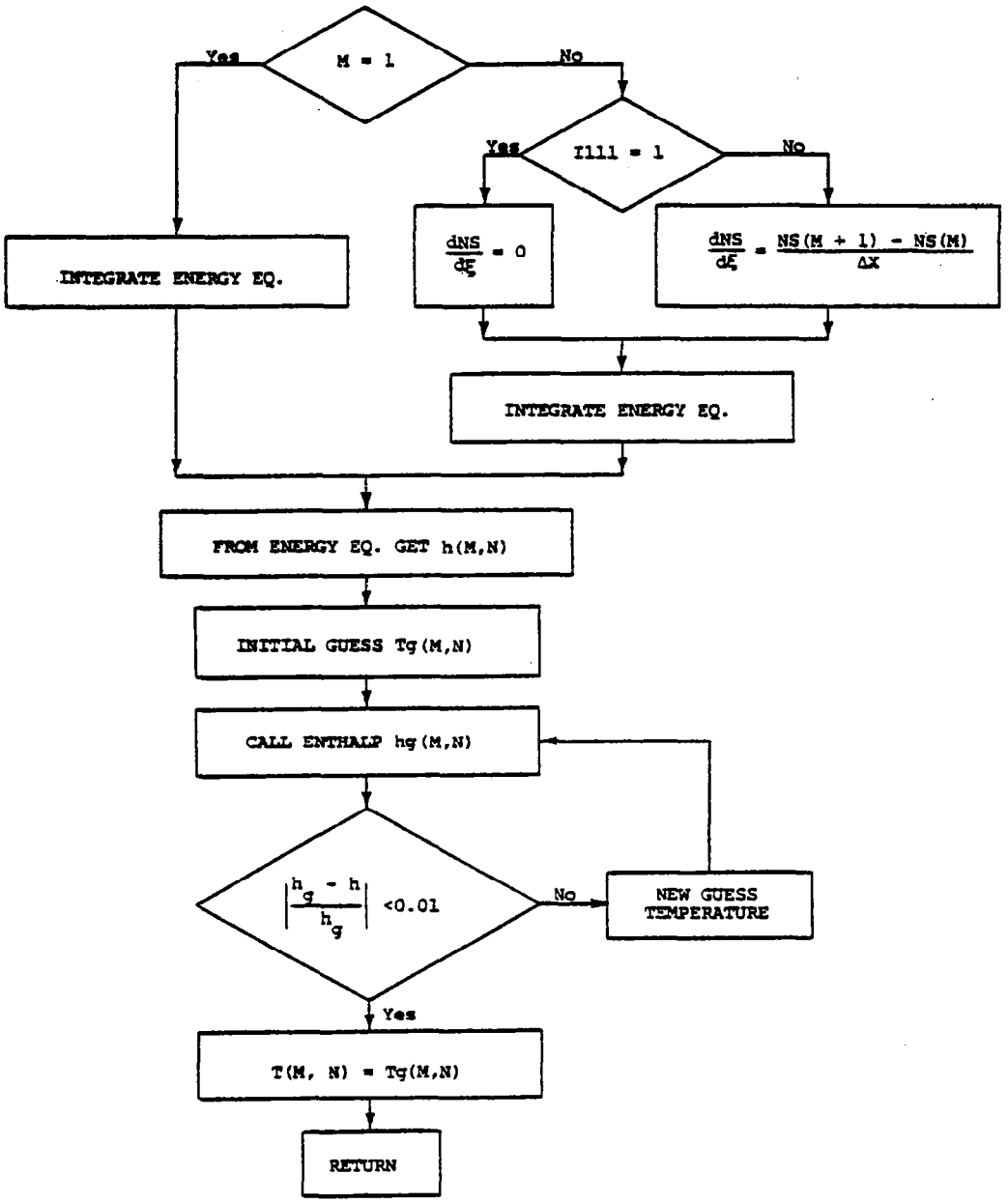

Fig. 9 Flow chart for subroutine ENERGY for shock-layer solution.

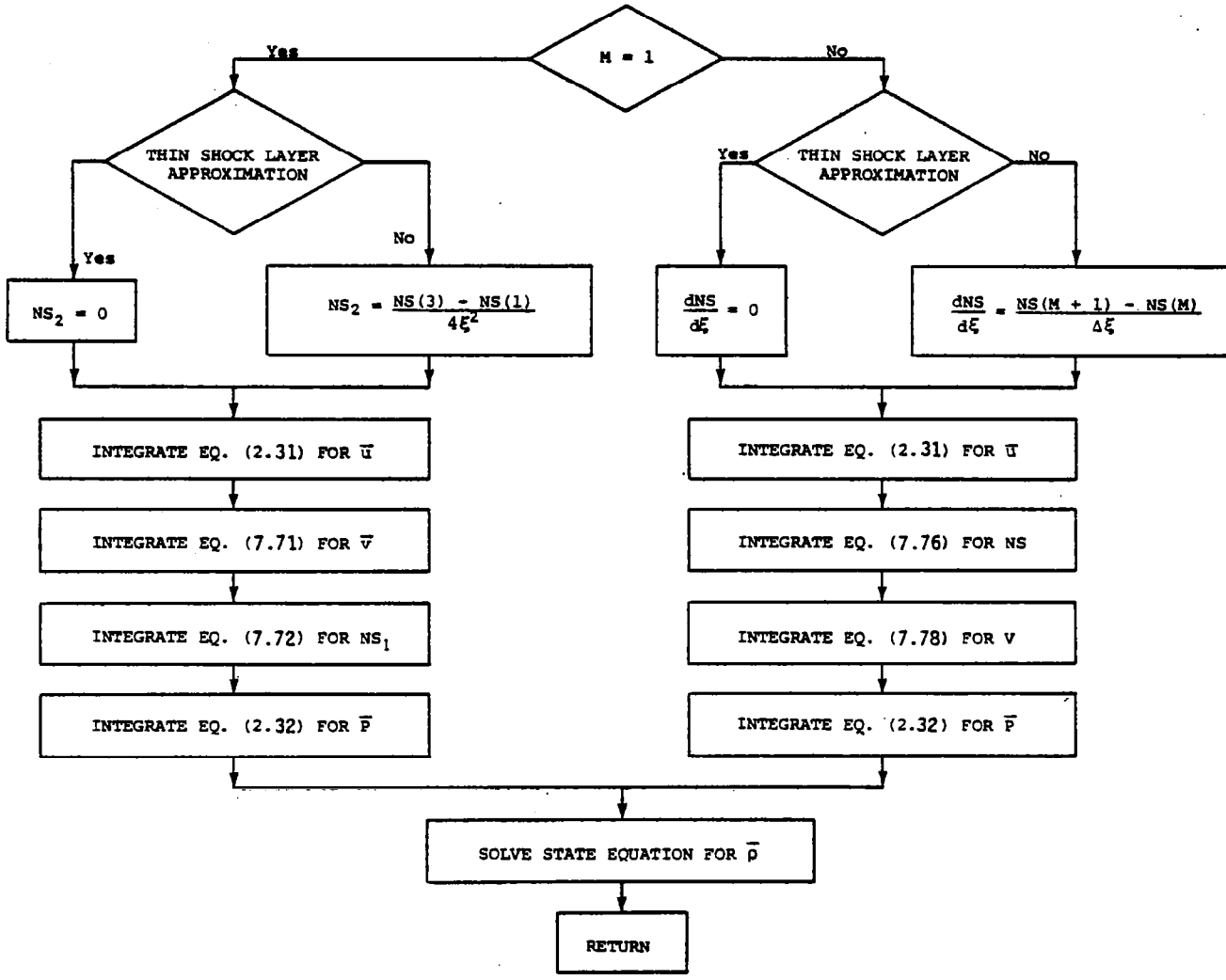

Fig. 10 Flow chart for subroutine MOMENTM for shock-layer solution.

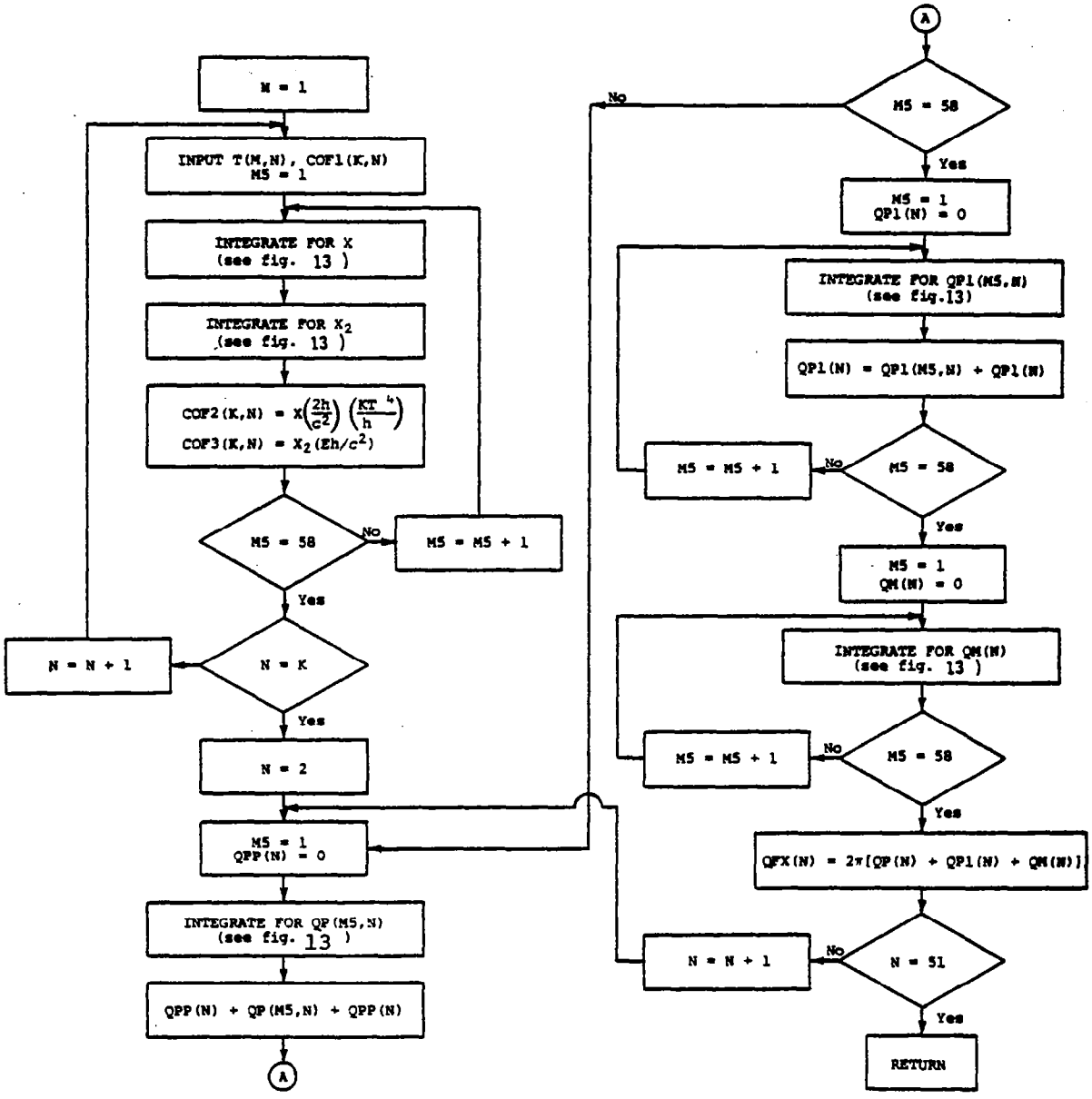

Fig. 11 Flow chart for subroutine RADIATION for shock-layer solution.

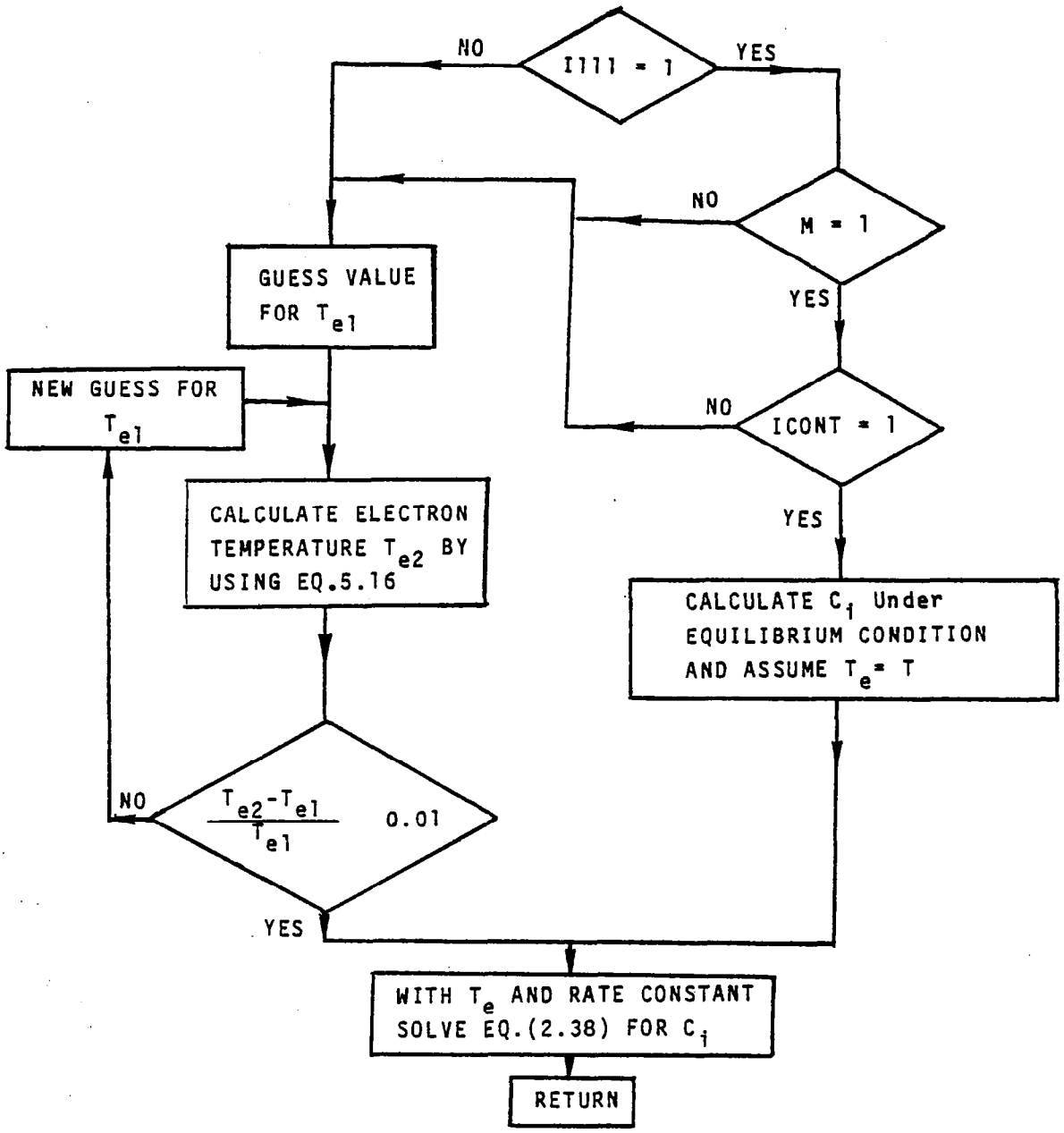

Fig. 12 Flow chart for subroutine CHEMIST for shock-layer solution.

$$X = \int_{\nu_{K1}}^{\nu_{K2}} \left\{ \nu^3 / \left[\exp(\nu) - 1 \right] \right\} d\nu$$

$$X_2 = \int_{\nu_{K2}}^{\nu_{K1}} \left\{ \nu^3 / \left[\exp(\kappa\nu) - 1 \right] \right\} d\nu$$

$$QP(M5,N) = \int_0^N COF2(M5,N)\ COF1(M5,N)\ E_2\left[\int_0^N \alpha_j(N')dN' \right] d\xi$$

$$QP1(M5,N) = \int_0^N COF3(M5,N)\ E_3\left[\int_0^N \alpha_j(N')dN' \right] d\xi$$

$$QM(N) = \int_0^N COF2(K,N)\ COF3(K,N)\ E_2\left[\int_N^{\xi} \alpha_j(N')dN' \right] d\xi$$

Fig. 13 Definition of integrals used in subroutine RADIATION.

8. RESULTS AND DISCUSSION

For this study, the entry body considered is a 45° hyperboloid blunt body which enters the Jovian atmosphere at a zero degree angle of attack. The body surface is assumed to be gray having a surface emittance of 0.8. Unless specified otherwise, the surface temperature is taken to be uniform at 4,564K. For the case of chemical equilibrium in the shock layer, all results were obtained by considering a body nose radius of $R_N^* = 23$ cm. For chemical nonequilibrium conditions, however, three different nose radii (12, 23, and 45 cm) were considered. The nominal composition of the free stream atmosphere was considered to be 85 percent hydrogen and 15 percent helium for most calculations. However, comparative results were also obtained for the 89 percent hydrogen and 11 percent helium nominal atmosphere.

First, results are presented for variation in flow properties only in the precursor region. These results were obtained with known values of radiative heat flux at the shock front. Next, chemical equilibrium shock layer results, obtained by considering slip conditions, are presented. With these results providing the basis for further investigation, complete precursor region-shock layer coupled solutions were obtained for both chemical equilibrium and chemical nonequilibrium in the shock layer. These results are presented in the last two sections of this chapter.

8.1 Precursor Region

In the precursor region, the results were obtained only for the range of entry velocities for which free-stream and shock conditions were available (see Table 1). As mentioned before, precursor-region results were obtained by employing both the small perturbation method and the thin

layer approximation. First small perturbation results are presented, and then some key results of this method are compared with the results of the thin layer approximation.

By employing the small perturbation method, the perturbation quantities V_{1z}, P_1, C_H, C_{H_2}, and T_1 were calculated numerically and the results are illustrated in Figs. 14-22. In Figs. 14-18, perturbation quantities are shown as a function of distance from the shock for different altitudes and a constant entry velocity of 35 km/sec. In Figs. 19-23, the perturbation quantities (just ahead of the bow shock) are illustrated as a function of the free-stream velocities. Since $\rho_1 = -V_{1z}$, separate results were not illustrated for the density perturbation. From these figures it is evident that the magnitude of perturbation quantities, in general, depend on the distance from the shock, altitude of entry, and entry speeds.

Figures 14-18 show that at a fixed entry velocity, the perturbation effects are greater for lower altitudes and at locations just ahead of the shock. This, however, would be expected because the number densities of participating species are greater at lower altitudes and at these altitudes most radiative energy from the shock gets absorbed in the immediate vicinity of the shock front. At higher altitudes, perturbation effects are significant to a larger distance from the shock front. This is because, at these altitudes, the number densities of participating species are small and radiation effects are felt farther into the free-stream. Specific results presented in Figs. 14-18 indicate that the use of the small perturbation theory is justified in determining the velocity, density, mass fraction and total enthalpy variations. For example, just

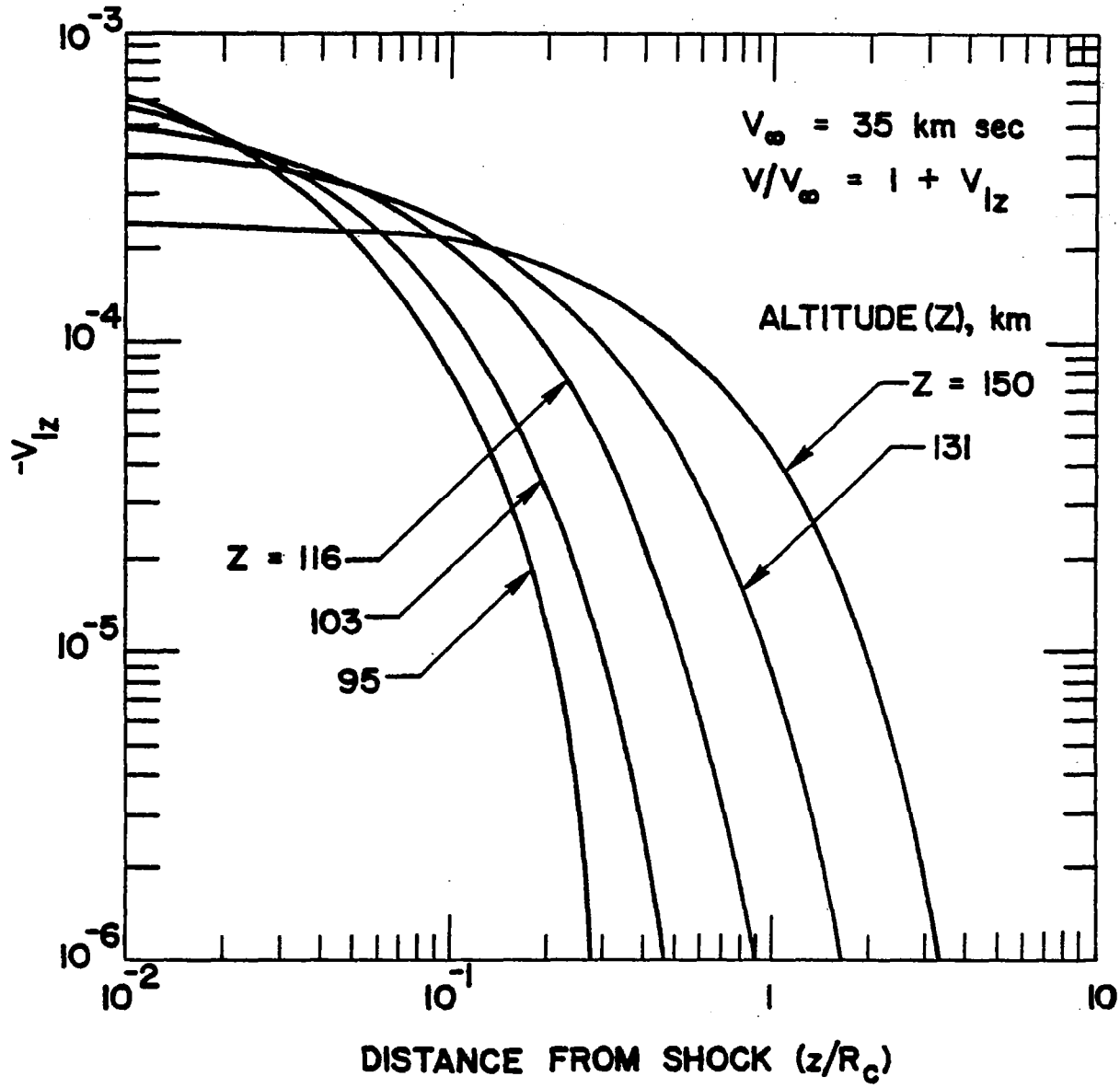

Fig. 14 Velocity perturbation as a function of distance from the shock at different altitudes and a constant free-stream velocity.

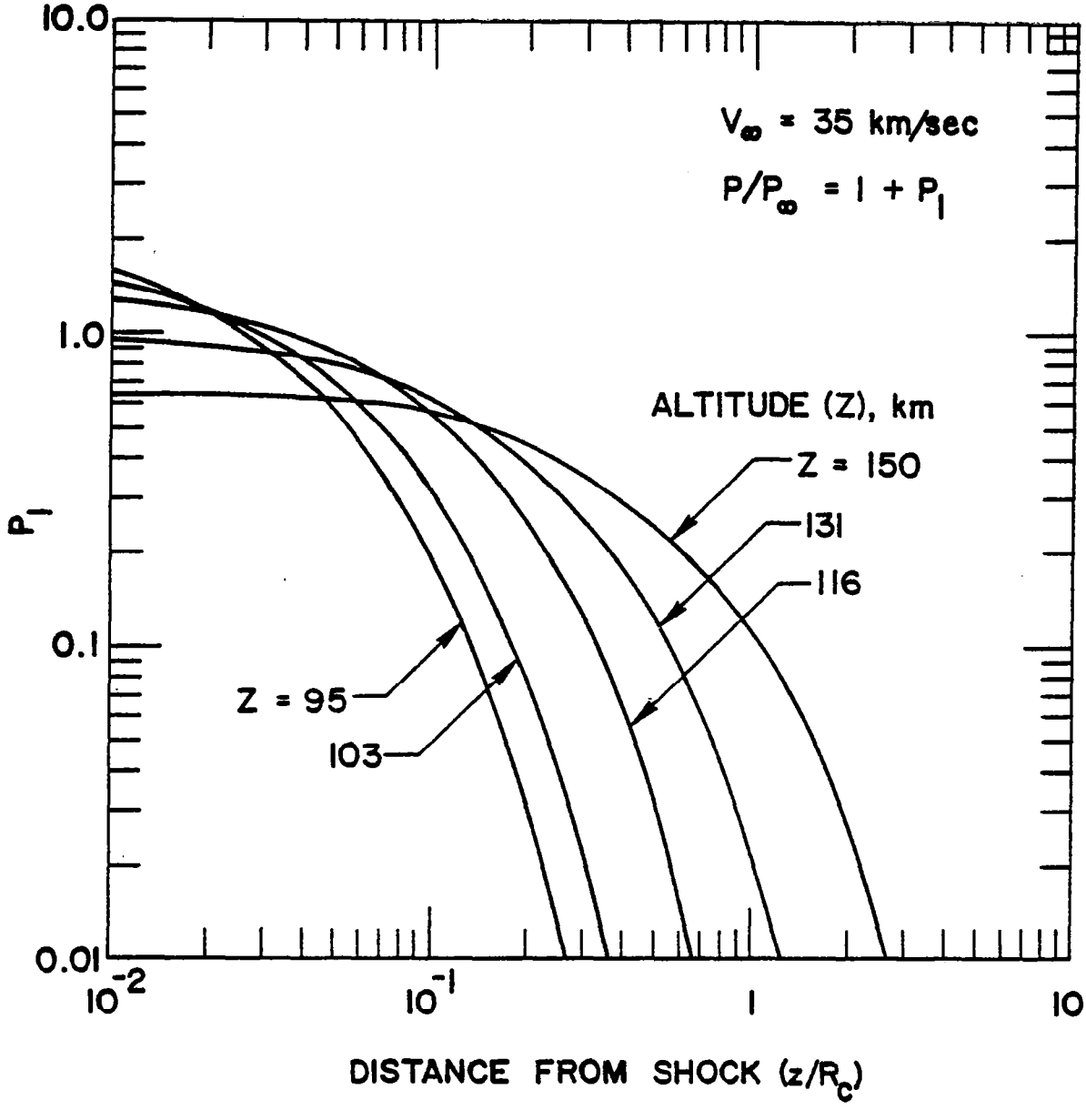

Fig. 15 Pressure perturbation as a function of distance from the shock at different altitudes and a constant free-stream velocity.

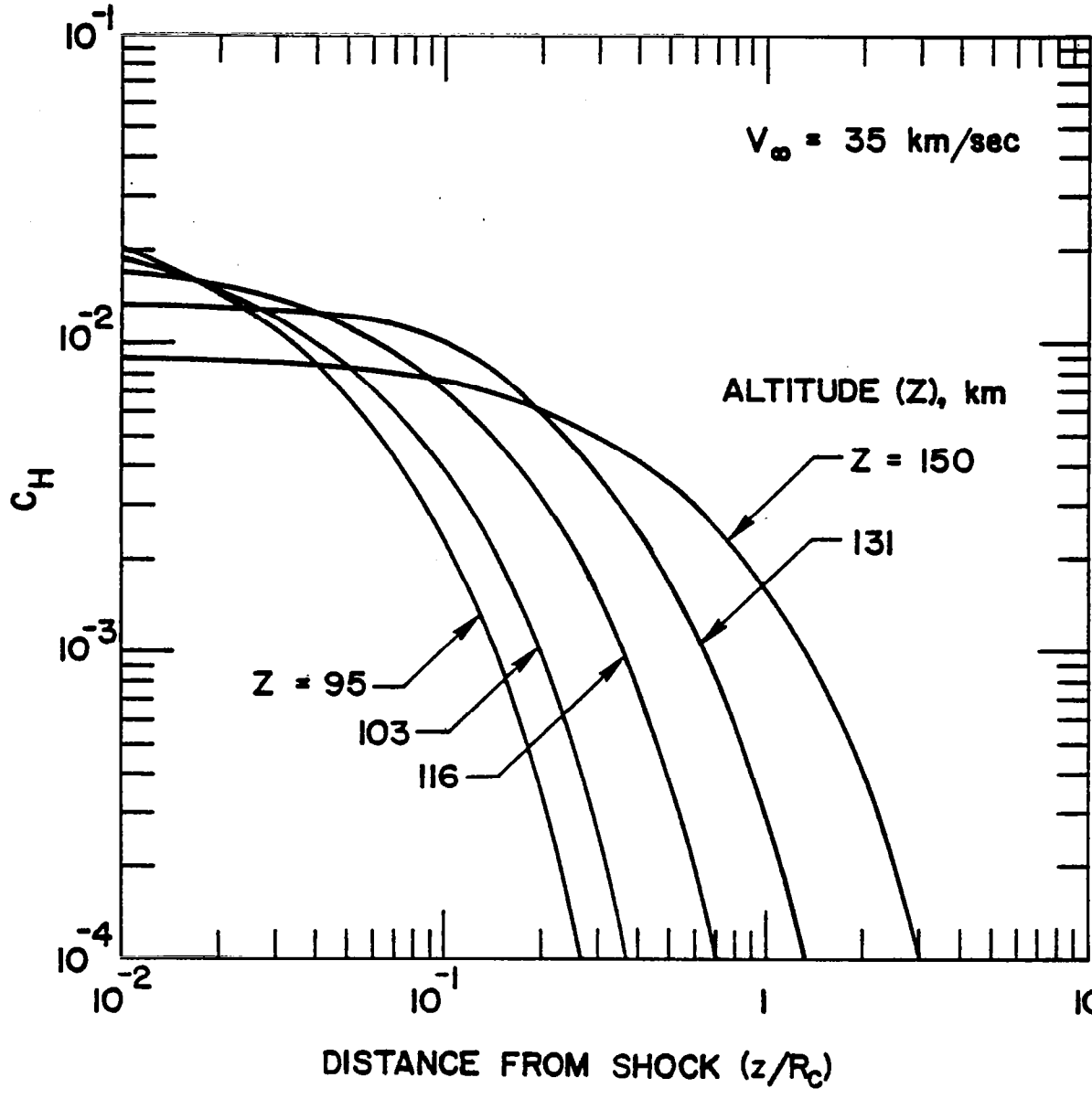

Fig. 16 Mass fraction of H as a function of distance from the shock at different altitudes and a constant free-stream velocity.

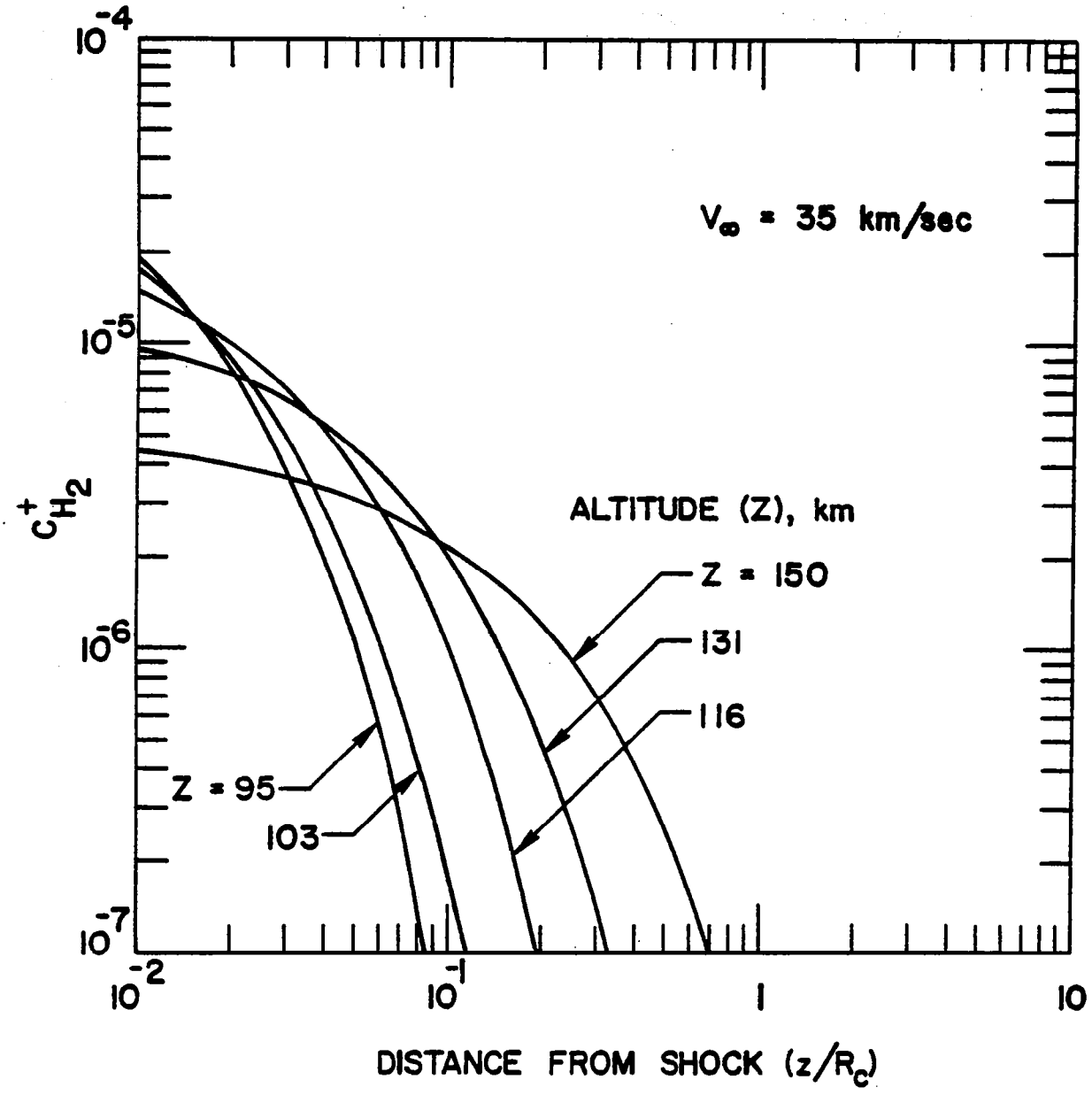

Fig. 17 Mass fraction of H_2^+ as a function of distance from the shock at different altitudes and a constant free-stream velocity.

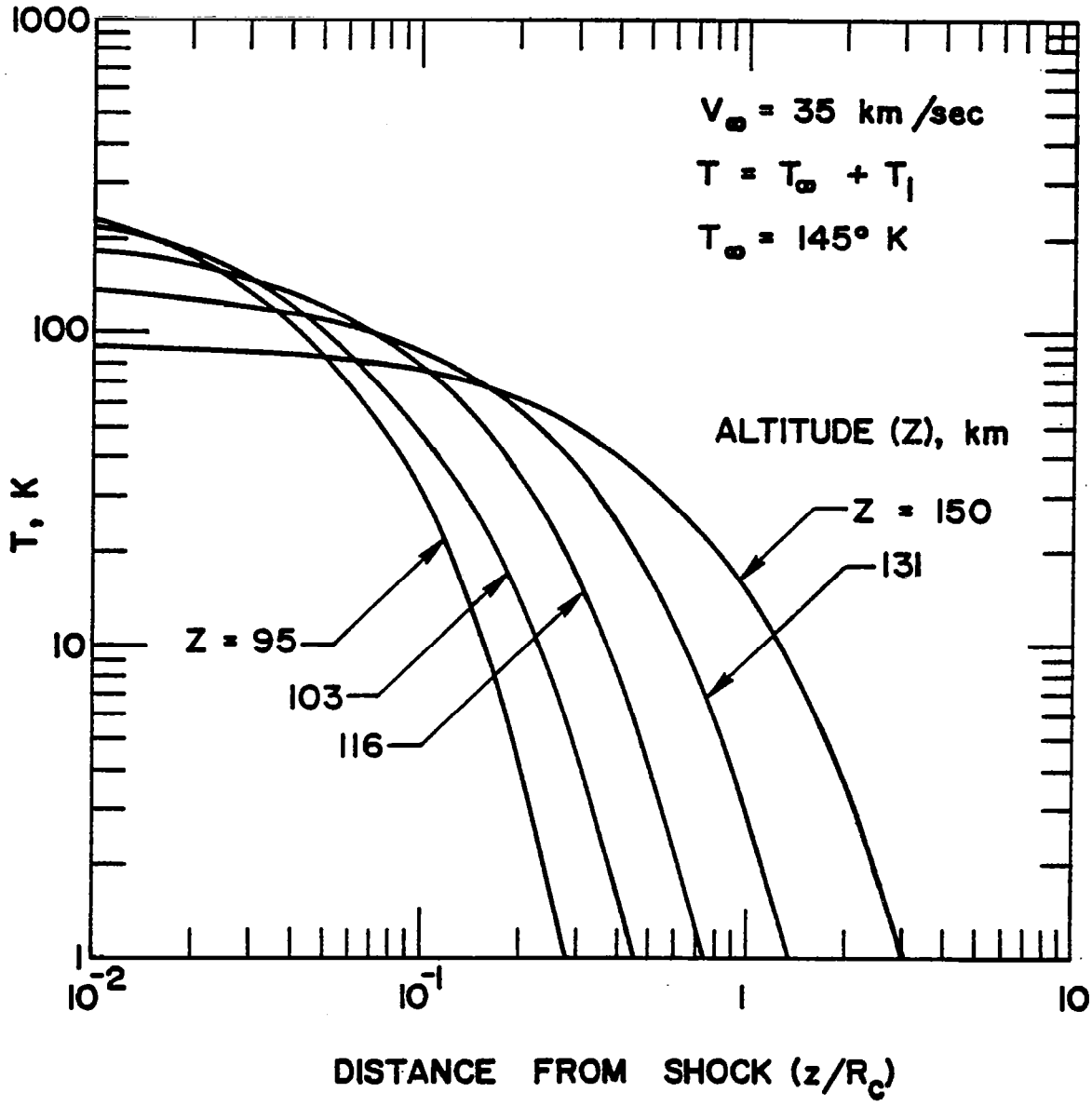

Fig. 18 Temperature perturbation as a function of distance from the shock at different altitudes and a constant free-stream velocity.

ahead of the shock, the value of (V/V_∞) is 0.9992 for Z = 95 km and is equal to 0.99975 for Z = 150 km. Similarly, $H_{T_1} = 6.8 \times 10^{-3}$ for Z = 95 km and $H_{T_1} = 2.4 \times 10^{-3}$ for Z = 150 km (i.e., 0.68% increase in total enthalpy at 95 km and 0.24% increase at 150 km). The static pressure and temperature variations, however, cannot be considered small, This is because for Z = 95 km, $P_1 = 2$ and $T_1 = 300$ K, and for Z = 150 km, $P_1 = 0.64$ and $T_1 = 94$ K. For these variations, therefore, one could question the validity of the small perturbation theory.

For different altitudes of entry, perturbation results (just ahead of the shock) are illustrated in Figs. 19-23 as a function of entry velocities. These results again indicate that the perturbation effects are greater for lower altitudes. As would be expected, for any specific altitude, the effects are larger for higher entry velocities. This is a direct consequence of greater radiative energy transfer from the shock to the free-stream at high entry speeds. For the most part, variations in the velocity, mass fractions, and total enthalpy again are seen to be small. For example, for an entry body at an altitude of 95 km, the total enthalpy of the gas (H_{T_1}) entering the shock wave is increased from about 0.68 percent at V = 36 km/sec to 1 percent at V = 38 km/sec. For Z = 150 km, however, H_{T_1} increases from 0.24 percent at 35 km/sec to 0.66 percent at 42 km/sec. The variations in the static pressure and temperature, in some cases, are seen to be several times greater than the ambient values. These large variations, however, occur for conditions where dissociation is high and the validity of the entire theory is questionable [1,2].

By employing the governing equations (Eqs. 2.9-2.13) and the spectral information of Sec. 6.2.1, numerical results were obtained for

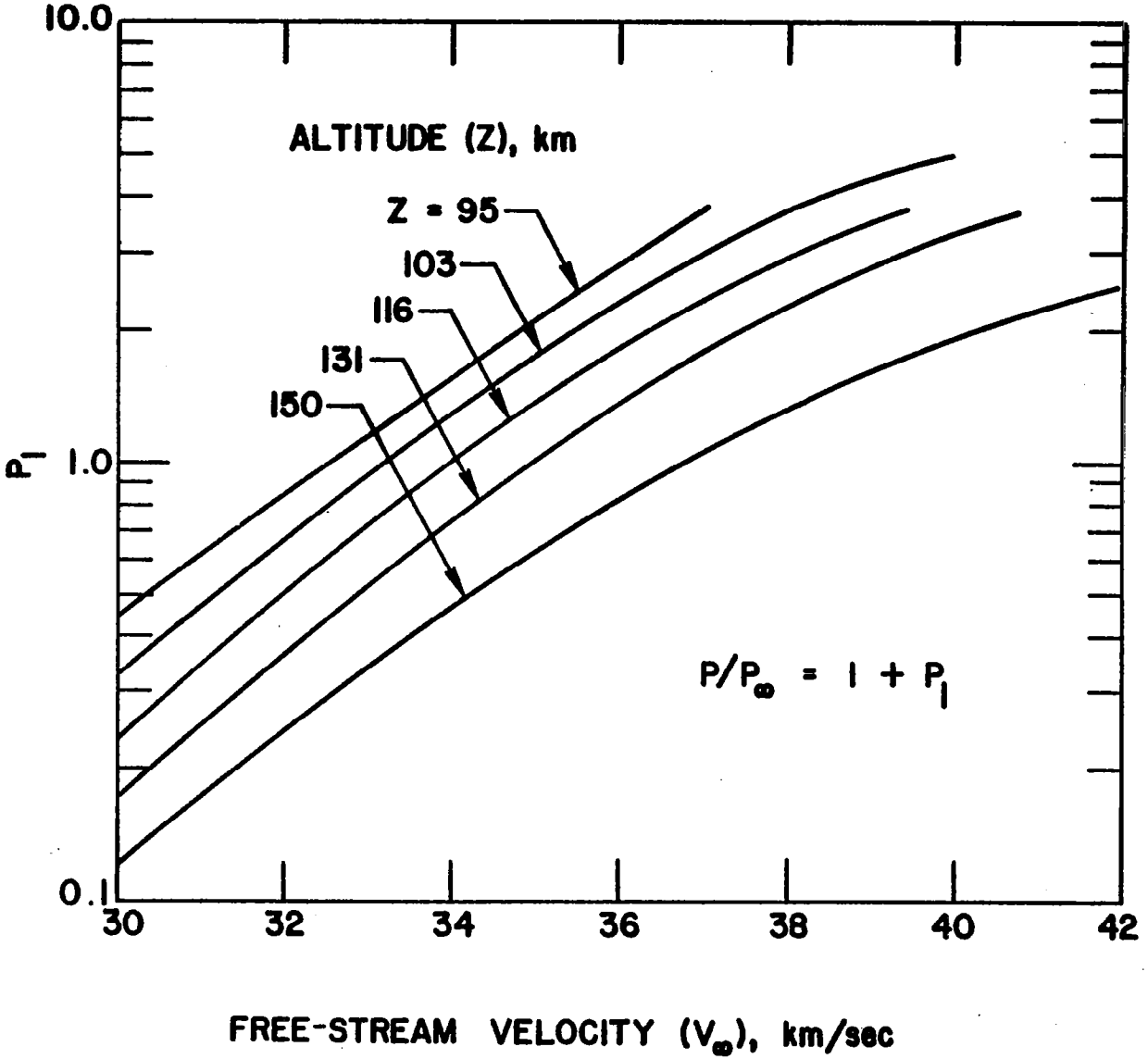

Fig. 19 Pressure perturbation (just ahead of the shock) as a function of free-stream velocity for constant altitudes.

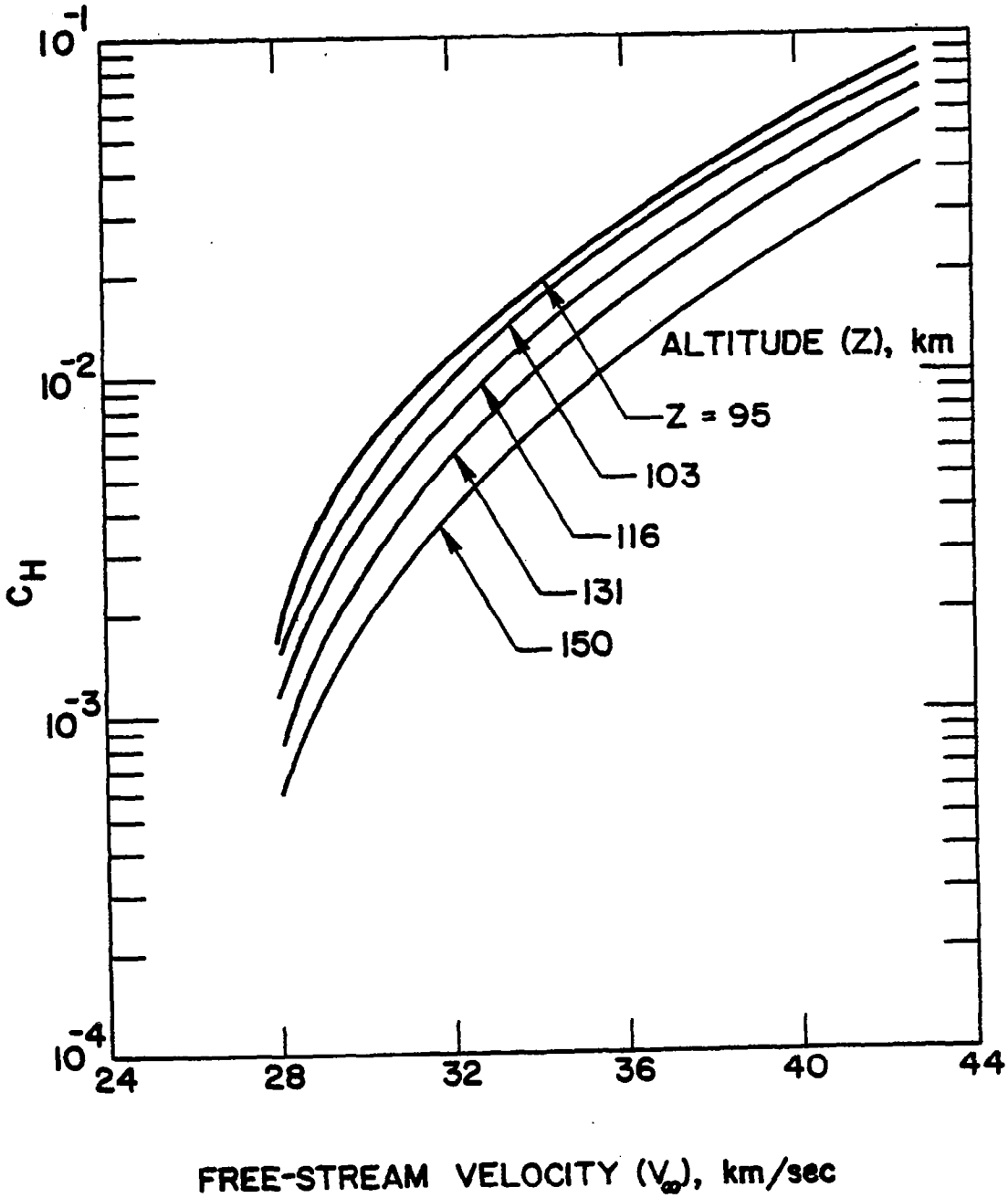

Fig. 20 Mass fraction of H (just ahead of the shock) as a function of free-stream velocity for constant altitudes.

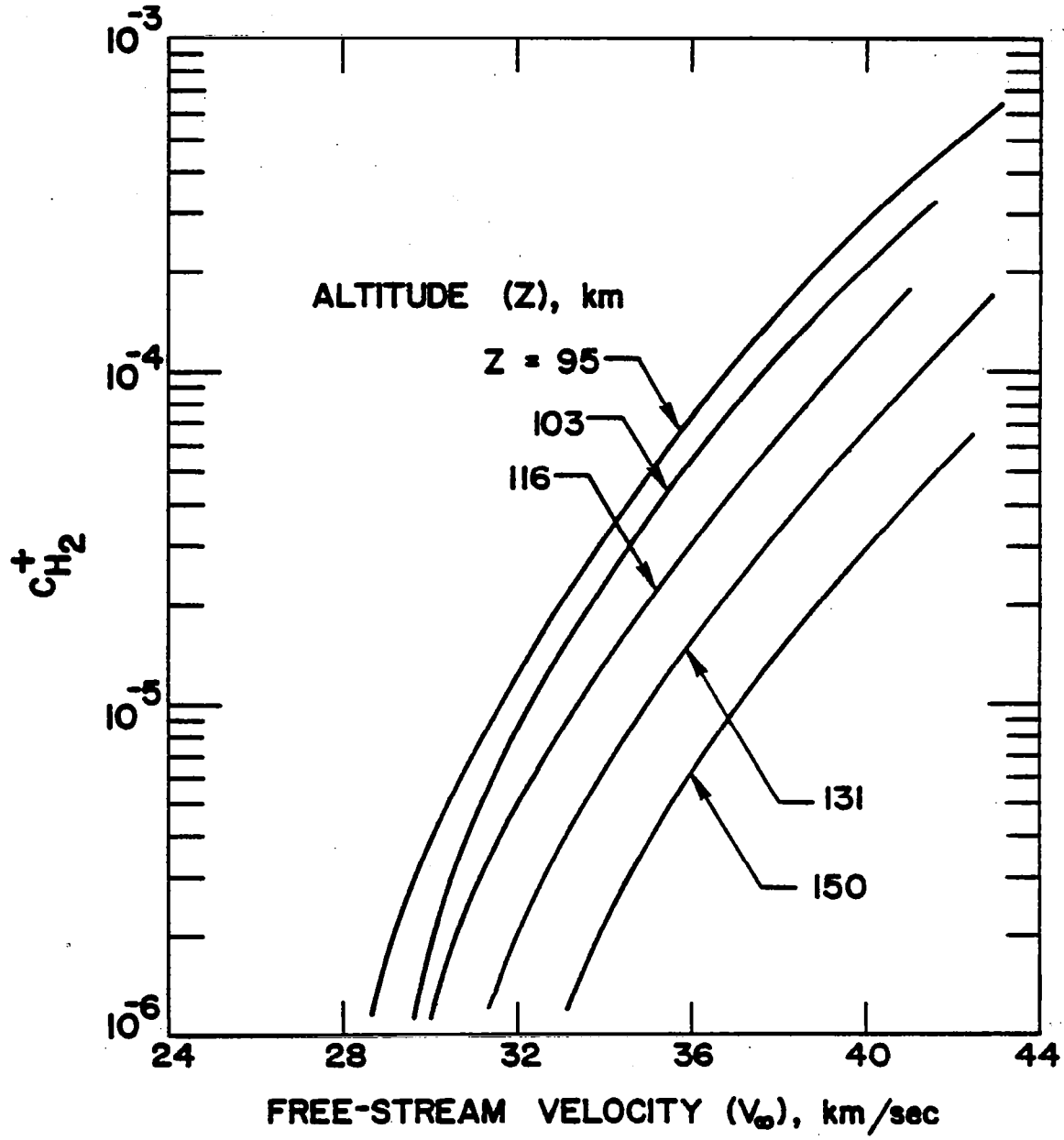

Fig. 21 Mass fraction of H_2^+ (just ahead of the shock) as a function of free-stream velocity for constant altitudes.

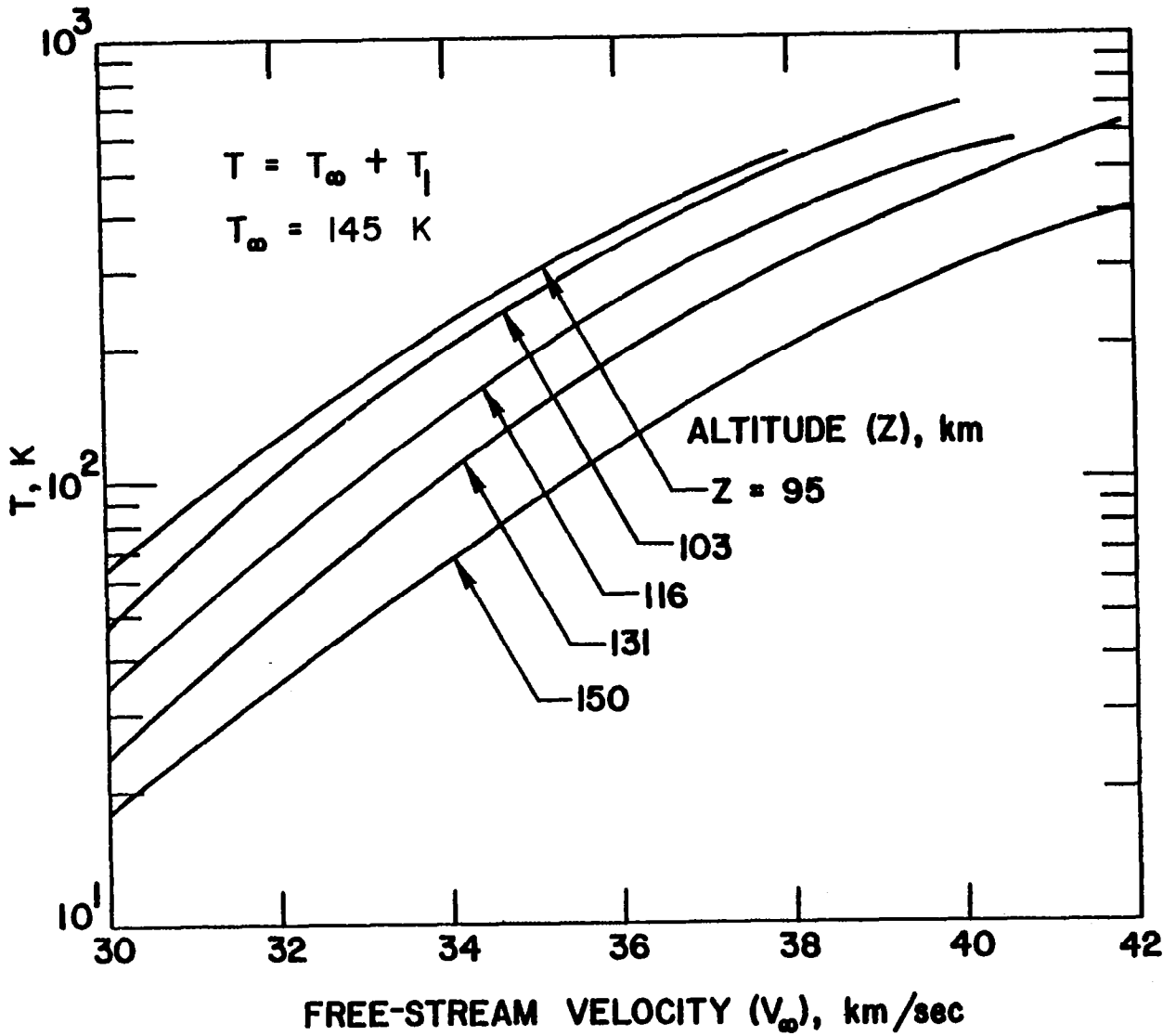

Fig. 22 Temperature perturbation (just ahead of the shock) as a function of free-stream velocity for constant altitudes.

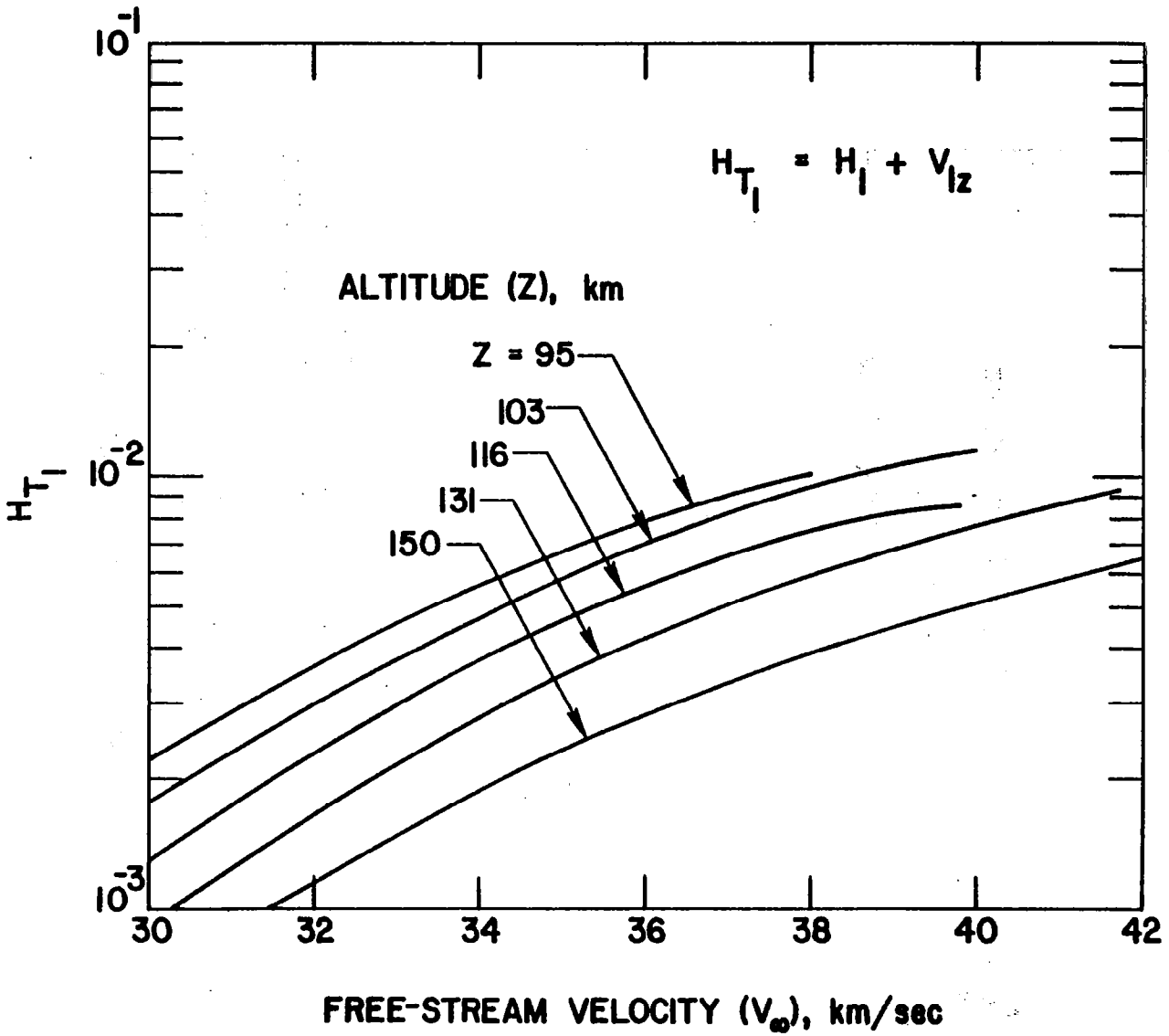

Fig. 23 Specific total enthalpy perturbation (just ahead of the shock) as a function of free-stream velocity for constant altitudes.

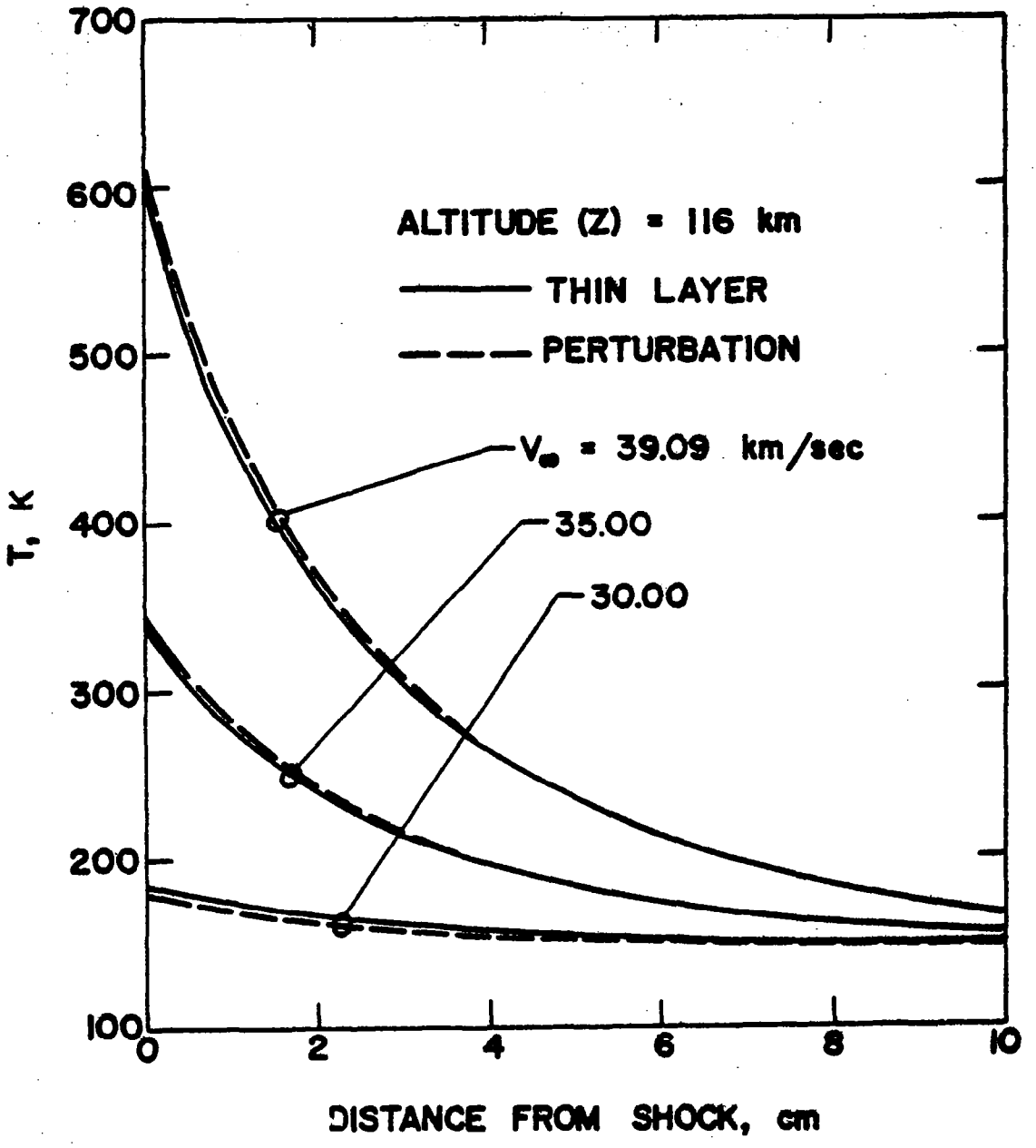

Fig. 24 Comparison of results for temperature variation in the precursor zone.

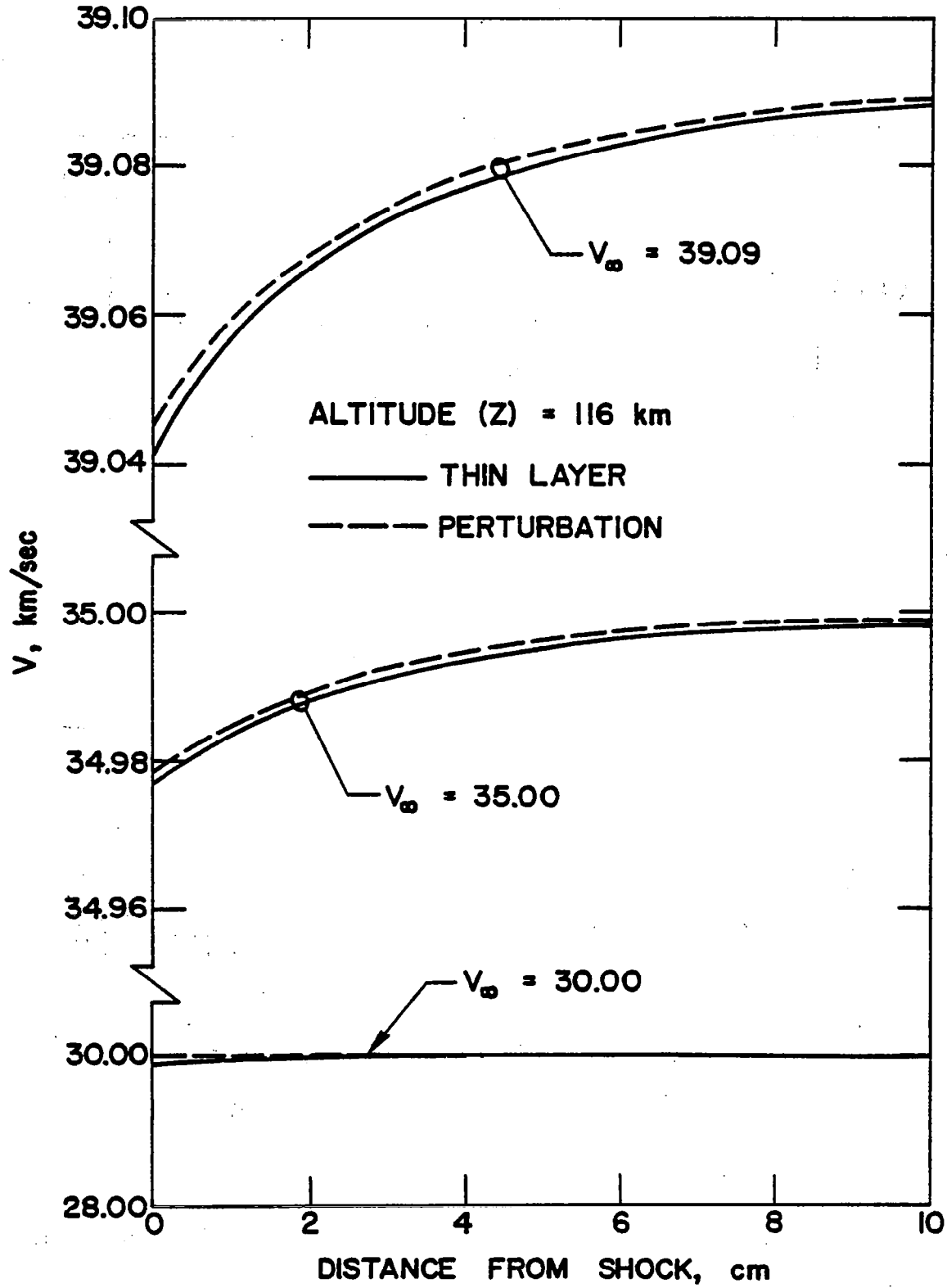

Fig. 25 Comparison of results for velocity variation in the precursor zone.

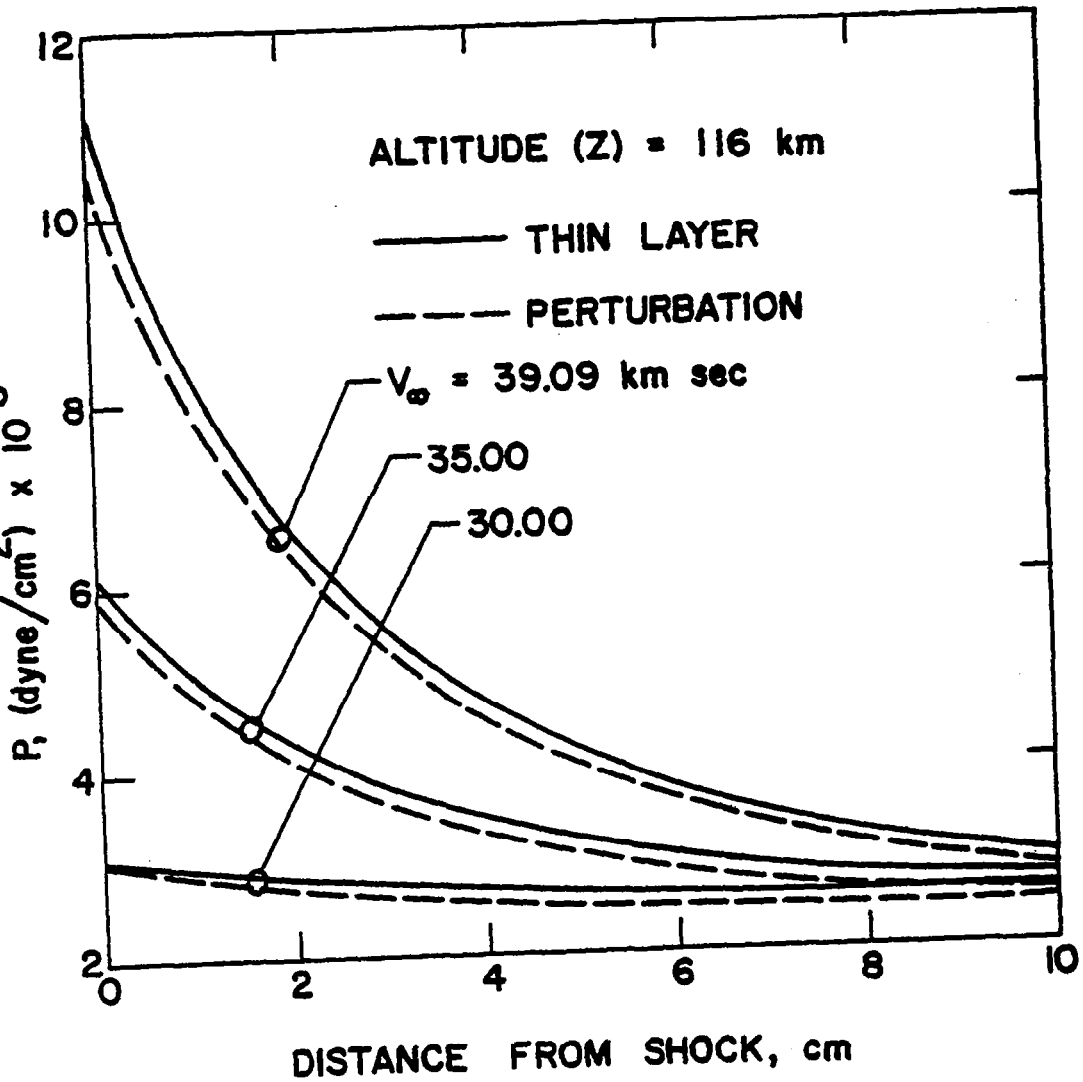

Fig. 26 Comparison of results for pressure variation in the precursor zone.

velocity, pressure and temperature variations for different values of n at s = 0. Specific results for an altitude of Z = 116 km are compared in Figs. 24-26 with corresponding results of the small perturbation theory. For the range of parameters considered, the results obtained by the two procedures are seen to be in excellent agreement. It is obvious from these results that either approach could be utilized in the investigation of the precursor region flow field. It was noted in Sec. 7.1 that for the Jupiter's entry conditions, the general governing equations of the small perturbation theory reduced to the case of simple plane source. As such, use of this method to Jupiter's entry case is restricted to one-dimensional analyses. The advantage of thin layer approximation procedure is that it is physically more convincing and it can be extended easily to three-dimensional and axisymmetric cases.

8.2 Effects of Shock and Body Slip Conditions

By invoking the boyd and shock slip conditions, results for variation in the shock layer flow properties were calculated for higher altitude entry conditions. Some important results of this investigation are presented in this section. Results are presented first for the velocity and temperature jumps at the body surface. Following this, results are presented for the properties immediately behind the shock. Next, the effects of radiation on convective heating at higher altitudes are discussed. Finally, to assess the influence of slip conditions, results are presented for the convective and radiative heating. It should be emphasized here that the term slip conditions (or slip boundary conditions), as used in this study, implies both the body and the shock slip conditions.

The variation in the surface slip velocity is illustrated in Fig. 27 as a function of the entry altitudes. Since u-velocity is almost zero at the stagnation streamline, the results presented in Fig. 27 have been obtained for location (or station) 3 of Fig. 6. Figure 27 clearly illustrates that the condition of no slip is not satisfied at higher altitudes. Since $\bar{u}$ is normalized by the shock value (i.e., $\bar{u} = u/u_s$), the magnitude of velocity slip can be expressed as a percent of u_s. It is evident from Fig. 27 that about 8 percent velocity slip occurs at Z - 261 and only 0.1 percent at Z = 143 km.

The temperature jump at the body surface is shown in Fig. 28 for different entry altitudes. The results presented in this figure are for the case with no radiation and, in obtaining these results, the body surface temperature was taken to be 4,000 K. A temperature jump of about 18 percent (i.e., ∇T = 680 K) is noted at the stagnation point for entry conditions at Z =261 km. At lower altitudes, however, the temperature jump is seen to be relatively small. For example, at Z = 116 km, the temperature jump is only 3 K.

Figures 29-31 show the temperature jump, velocity slip, density and total enthalpy changes just behind the shock. It is evident from Fig. 29 that when the altitude is lower than 225 km, the shock slip conditions are not important. However, a significant temperature difference is noted at Z = 261 km. The results presented in Fig. 30 illustrate that both the u and v velocity components are influenced by the slip conditions. Since both the temperature and velocity components decrease just behind the shock, the slip conditions result in an increase in density and a decrease in total enthalpy. This is clearly evident from the result of Fig. 31.

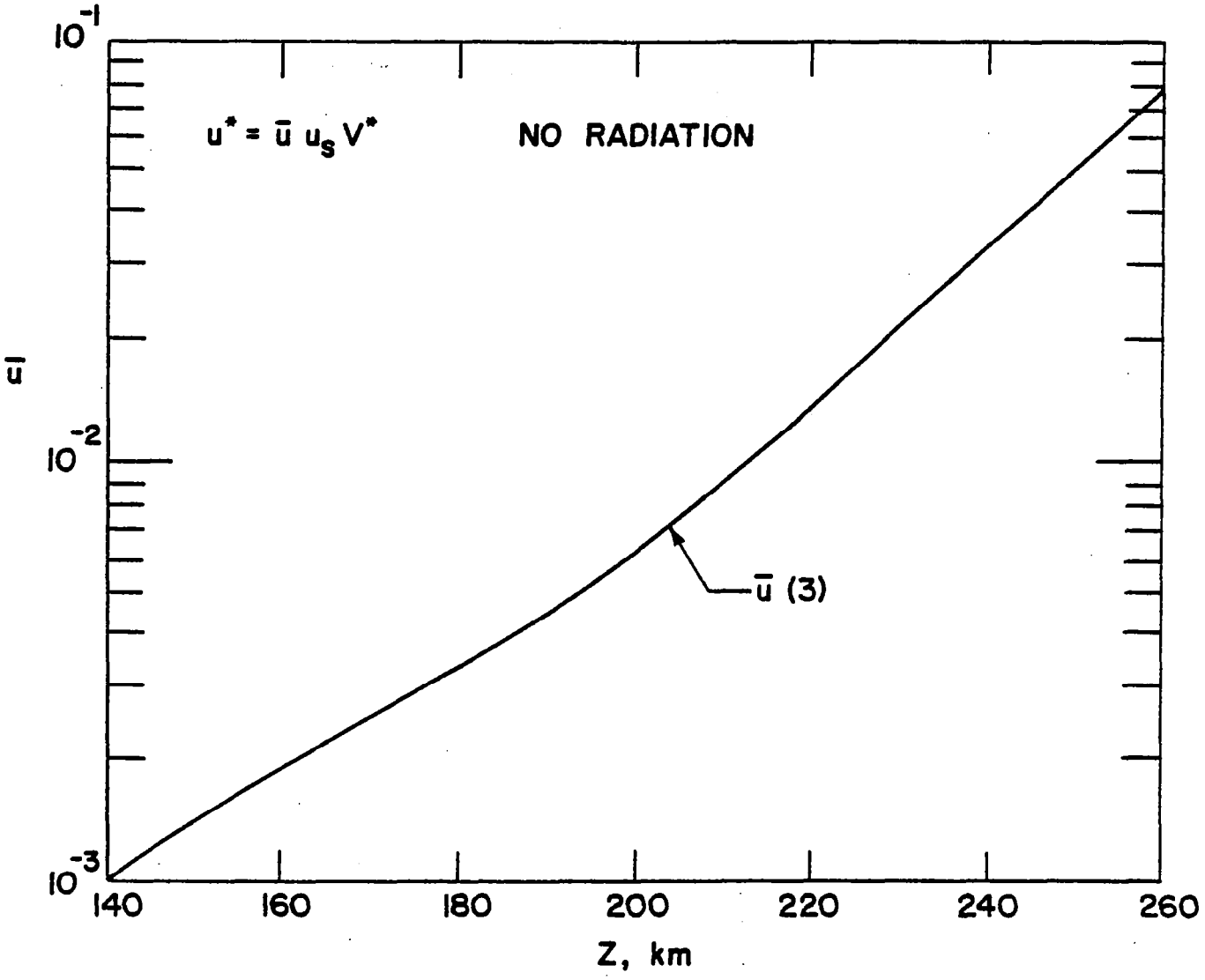

Fig. 27 Velocity slip along the body surface for different entry altitudes.

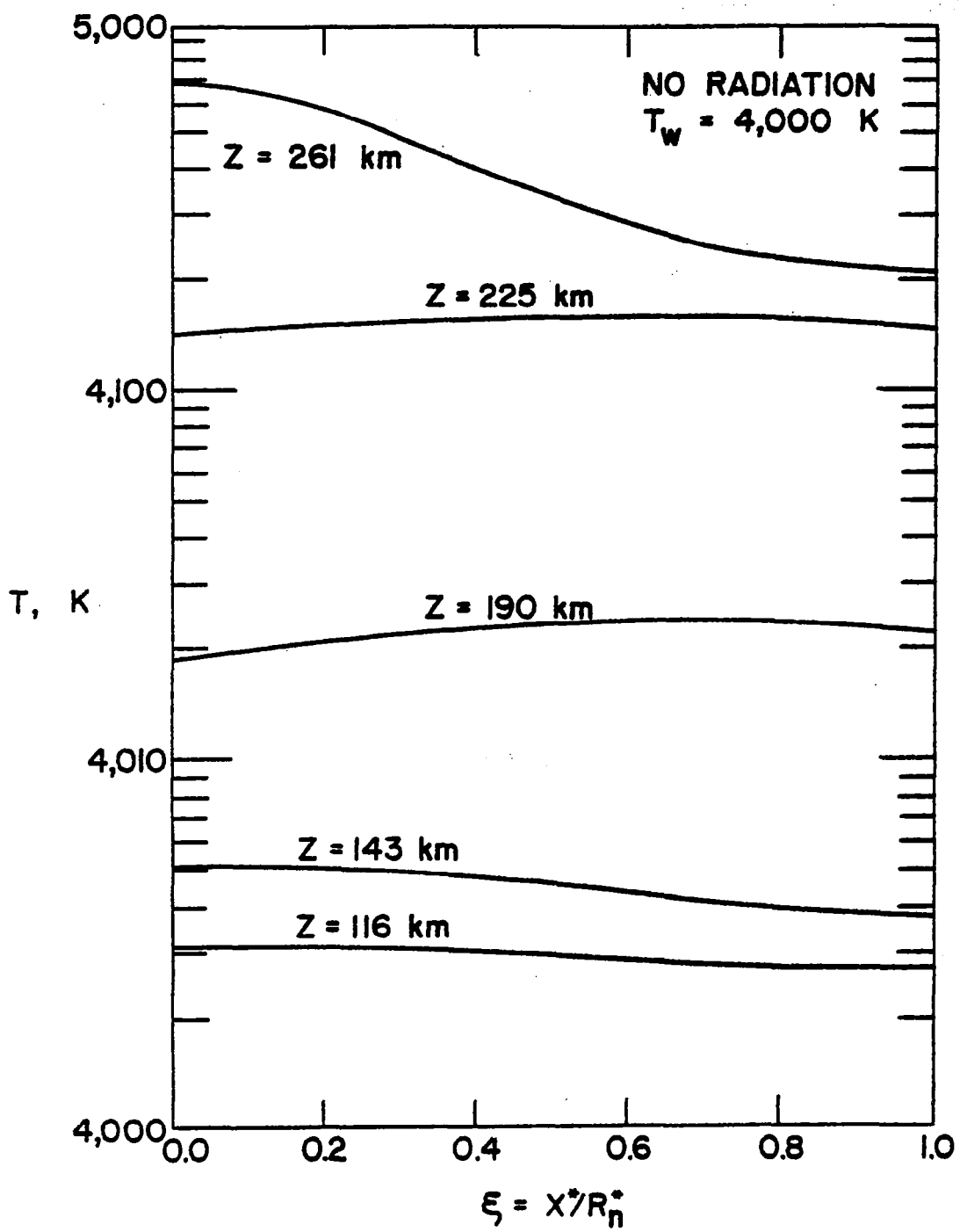

Fig. 28 Temperature jump along the body surface for different entry altitudes.

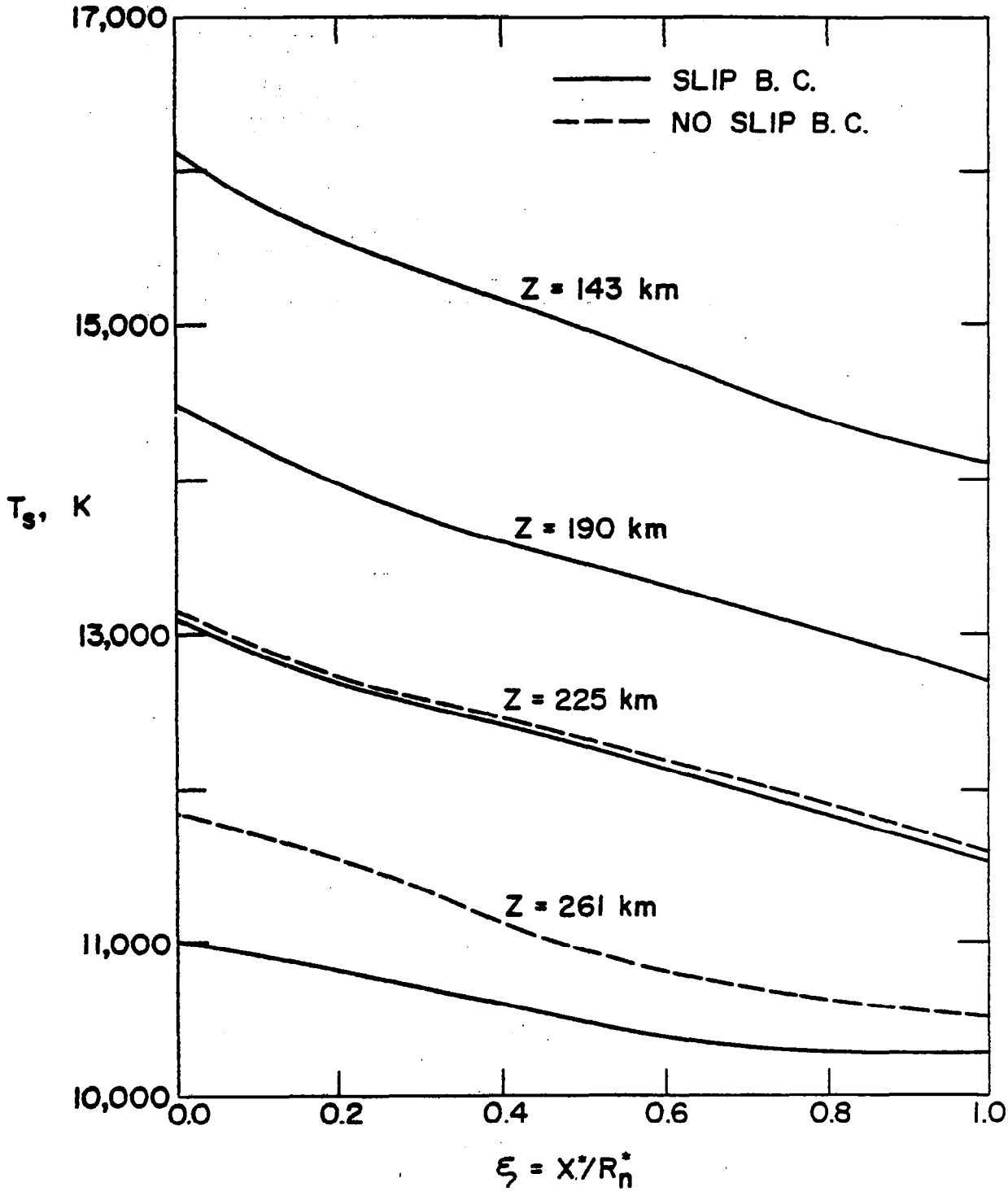

Fig. 29 Temperature variation (just behind the shock wave) as a function of ξ-coordinate.

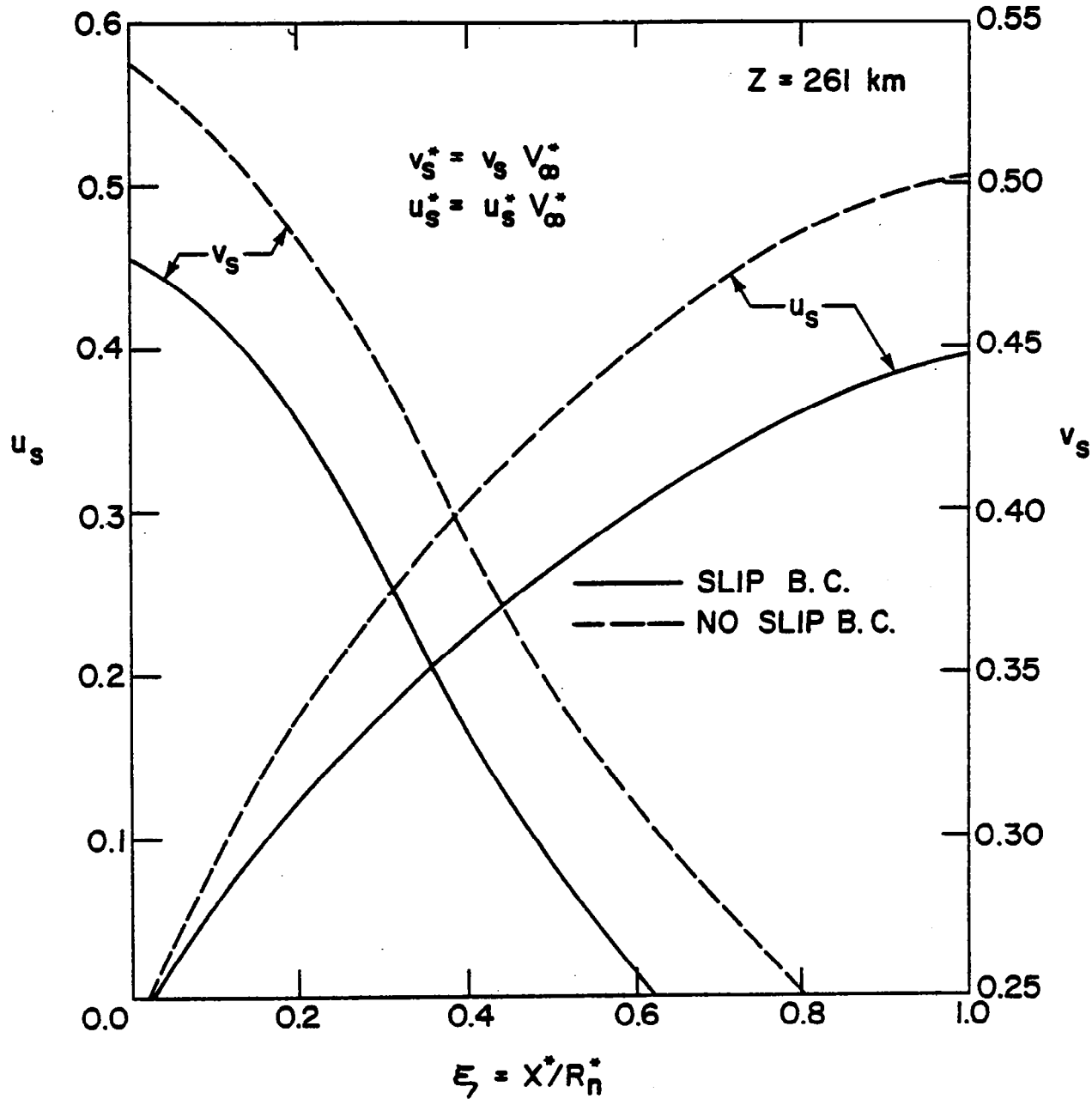

Fig. 30 Velocity variation (just behind the shock wave) as a function of ξ-coordinate.

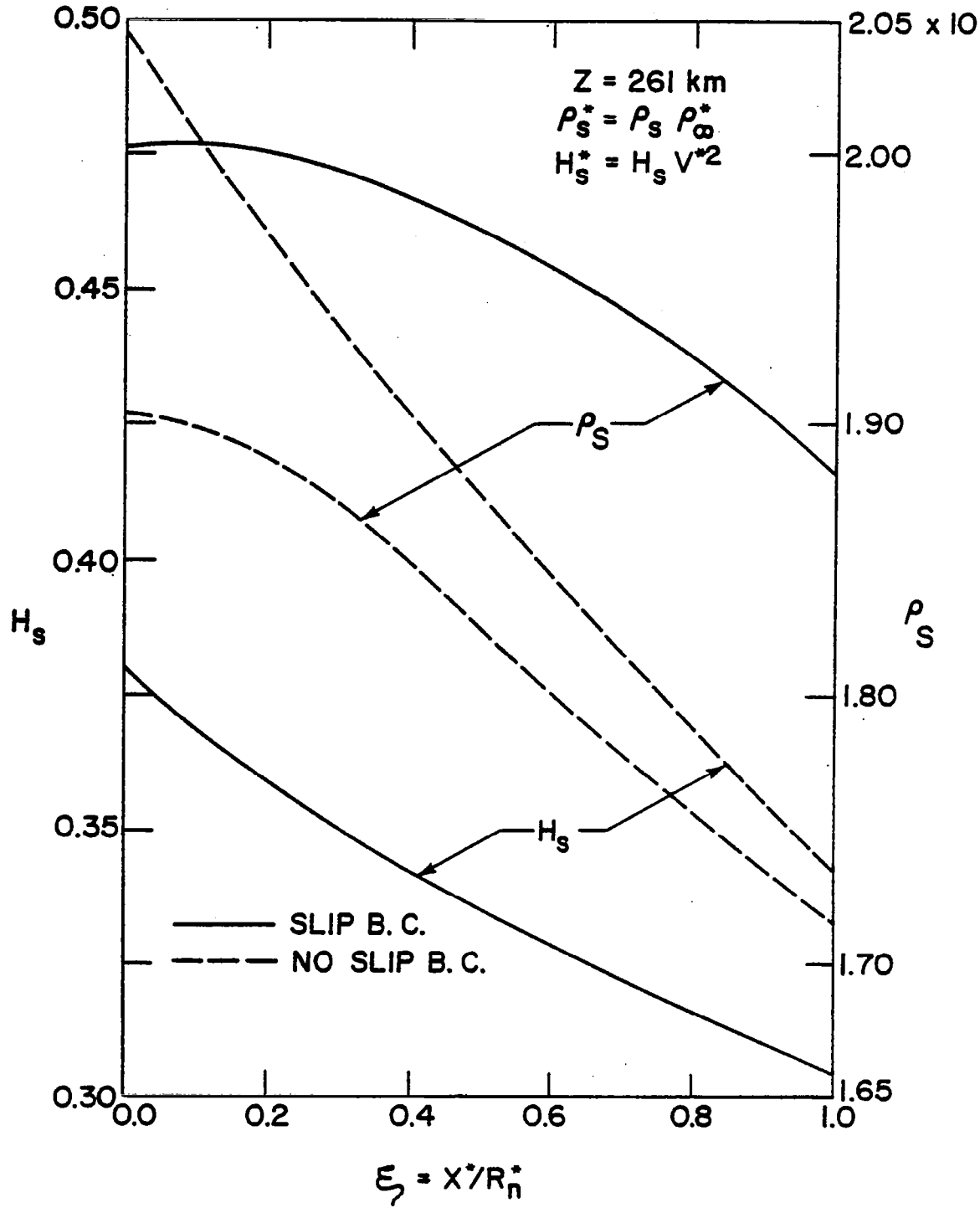

Fig. 31 Total enthalpy and density variation (just behind the shock wave) as a function of ξ-coordinate.

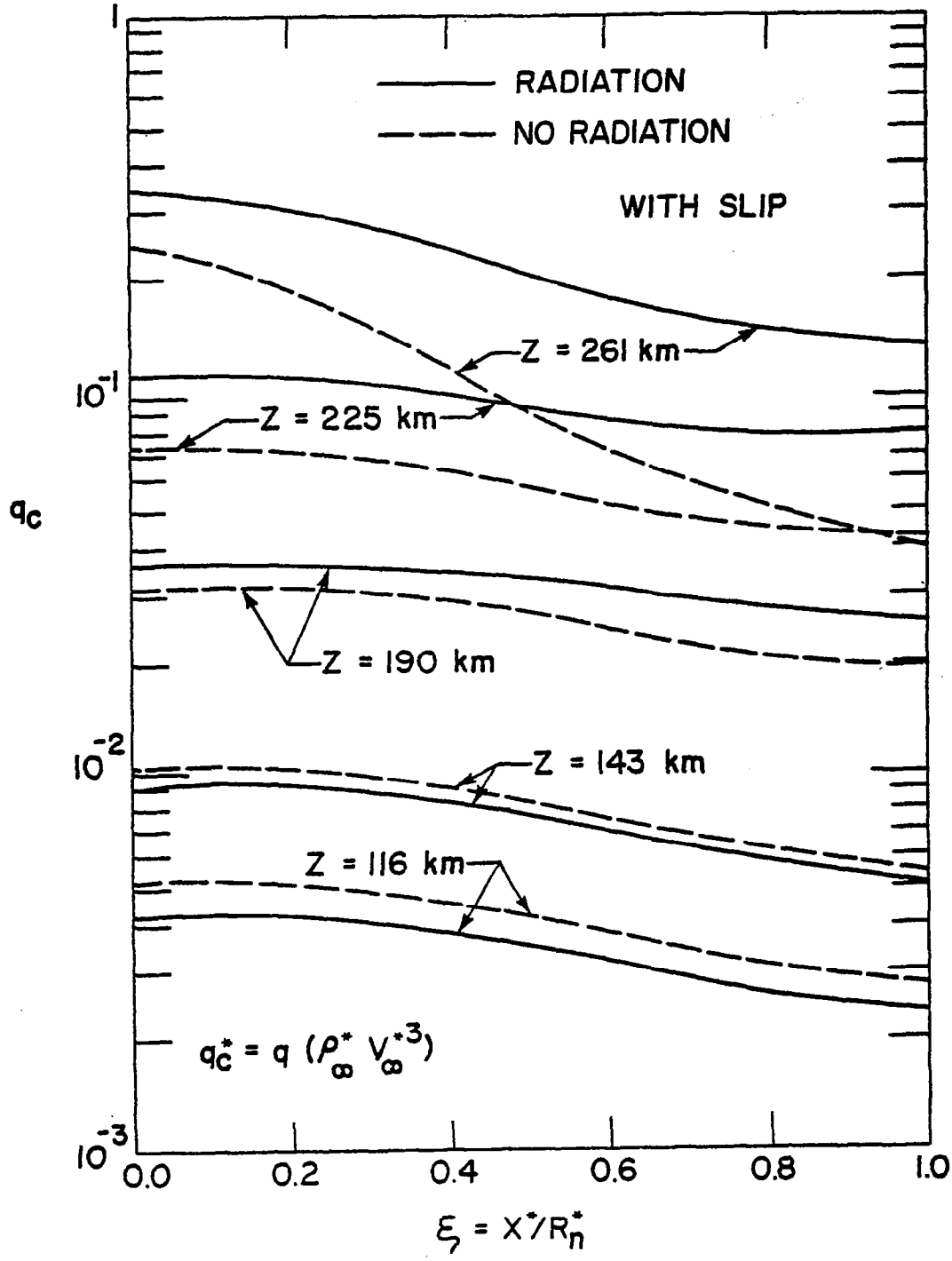

Fig. 32 Effects of the radiative heat flux to the convective heat flux along the body surface.

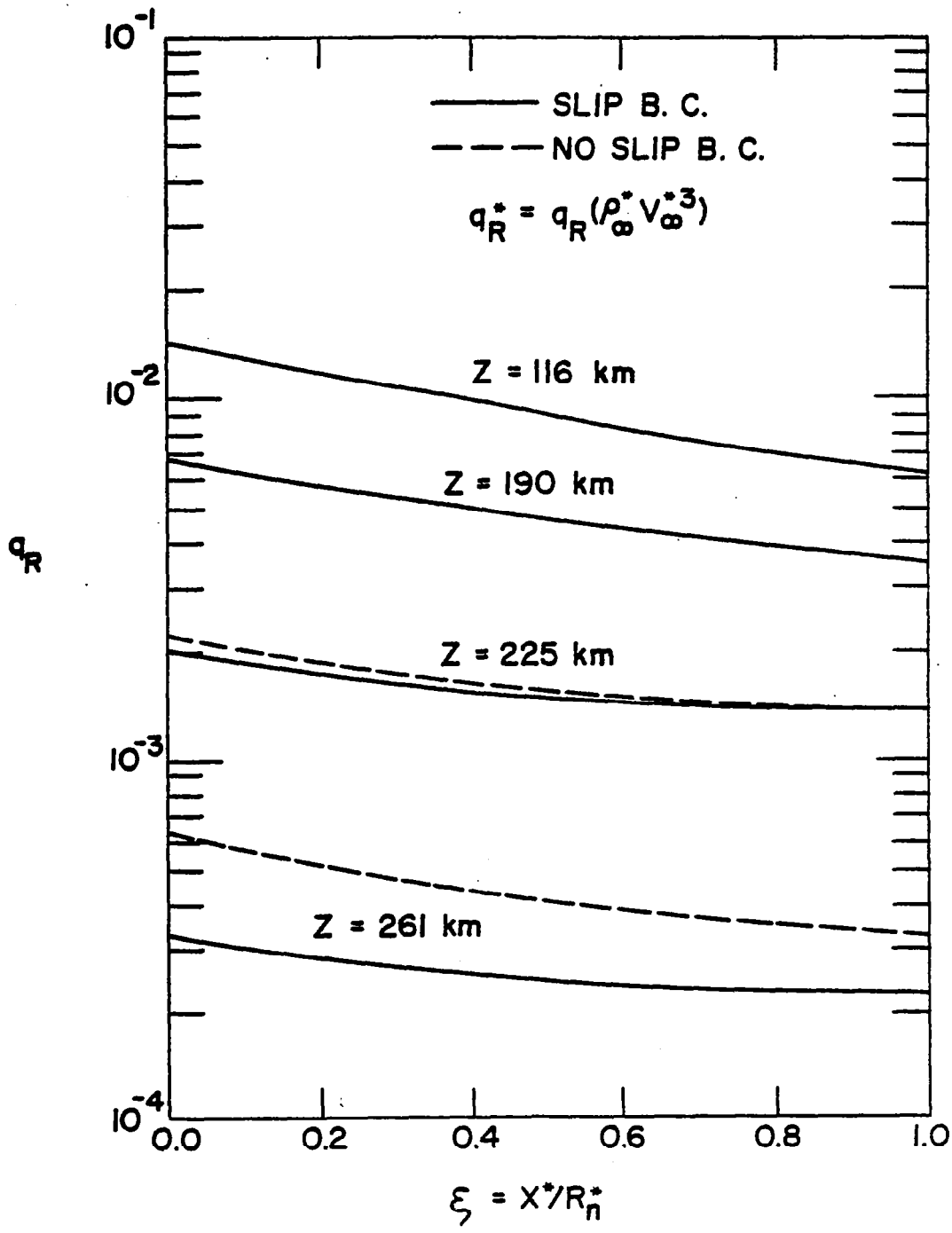

Fig. 33 Comparison of slip and no-slip results for radiative heat flux variation along the body surface.

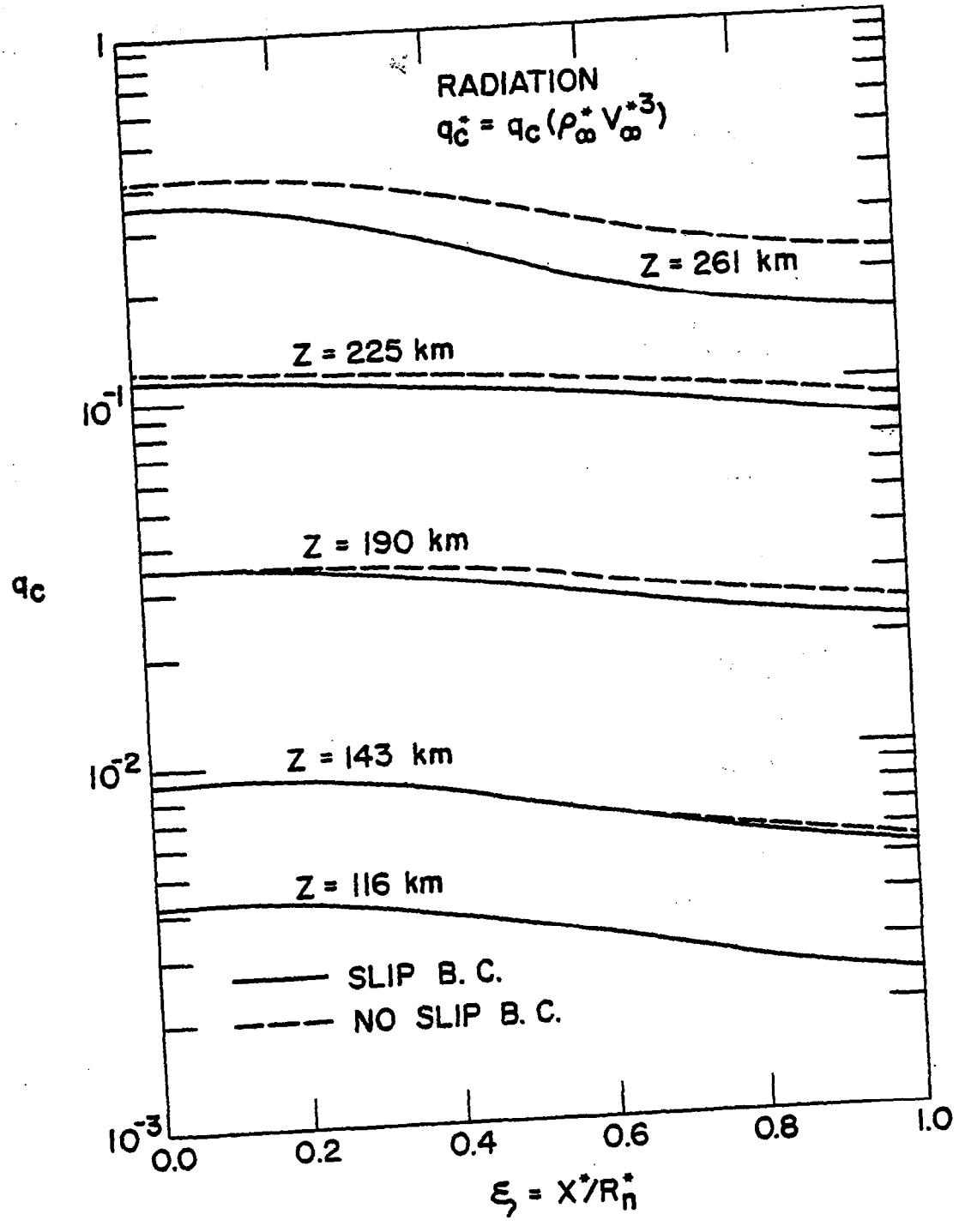

Fig. 34 Comparison of slip and no-slip results for convective heat flux variation along the body surface (with radiation).

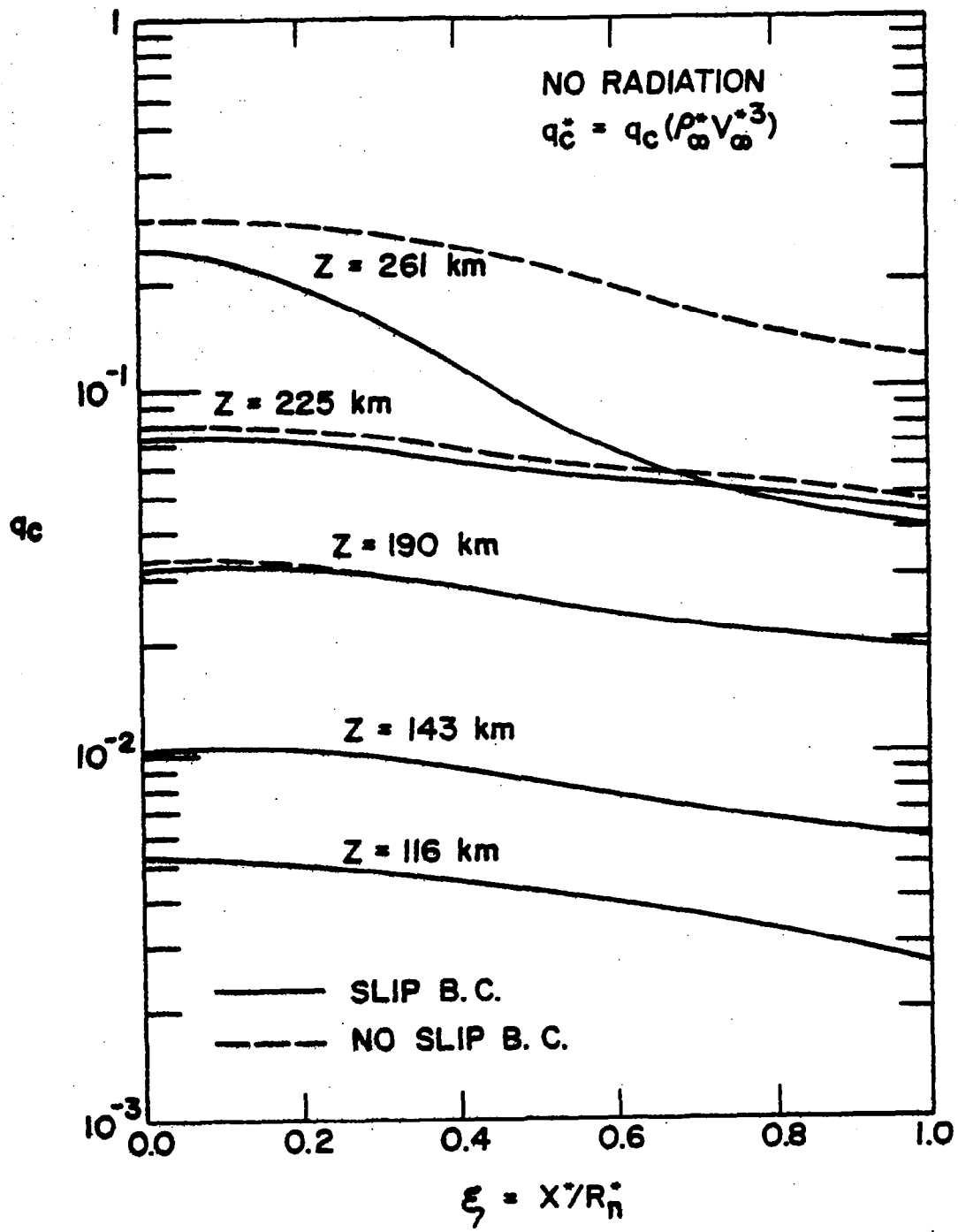

Fig. 35 Comparison of slip and no-slip results for convective heat flux variation along the body surface (with no radiation).

Figure 32 shows how the convective heat flux is effected by radiation. The results indicate that at low altitudes, the convective heat flux decreases with increasing altitude and at high altitudes it increases with the altitude. This is because at different ranges of altitude, the temperature distribution is rearranged by the radiation effects. It is noted that a maximum of 50 percent change in convective heat transfer occurs at Z = 261 km and a 25 percent change at Z = 225 km.

Figure 33 shows how the radiative heat flux is affected by slip boundary conditions. It is seen that the effect is very small at altitudes lower than 225 km. It is found that there is approximately 50 percent reduction in radiative heat flux due to the shock temperature jump at 261 km.

The effects of slip boundary conditions on convective heat flux towards the body (along the body surface) are illustrated in Figs. 34 and 35, for the cases with and without the radiation interaction. The results indicate that the slip conditions start to effect the convective heat flux at Z = 225 km (ε = 0.09064) by approximately 8 percent (at stagnation point) and this increases to 27 percent at Z = 261 km (ε = 0.2129). The effect is seen to increase with the distance away from the stagnation point, and inclusion of radiation is seen to suppress this influence. When the altitude is less than 225 km, the effect of slip boundary conditions is relatively small and it can be neglected.

8.3 Influence of Precursor Heating on Viscous Equilibrium Flow

By considering the conditions of chemical equilibrium in the shock layer, governing equations of both the precursor and shock layer regions

were solved for physically realistic Jovian entry conditions. Results of complete parametric study are presented in this section. First, the results are presented for quantities just behind the shock wave, and then a few results of flow variables within the shock layer are presented. Next, results are presented for the entire shock-precursor region. Finally, a few results are presented to demonstrate the influence of precursor heating on the magnitude of different heat fluxes in the shock layer.

The radiative flux from the shock layer towards the precursor region is found to be highest at the stagnation line shock location. Results of the radiative flux from the shock front are shown in Fig. 36 for different altitudes of entry. As would be expected, precursor heating results in a higher radiative flux at the shock front. It is seen that the radiative flux reaches a maximum value for an altitude of about 116 km, and the largest precursor effect (PE) of about 8 percent is found to be for this altitude. This is a direct consequence of the free stream and entry conditions at this altitude. For other entry conditions (altitudes), precursor effects are seen to be relatively lower.

Figure 37 shows the shock standoff variation with distance along the body surface for different entry altitudes. The shock standoff distance, in general, is seen to decrease with increasing altitudes. This is because higher entry velocities are associated with higher altitudes. The precursor heating results in a slight increase in the shock standoff distance (a maximum of about 2 percent for Z = 116 km) because the density of the shock layer is slightly reduced.

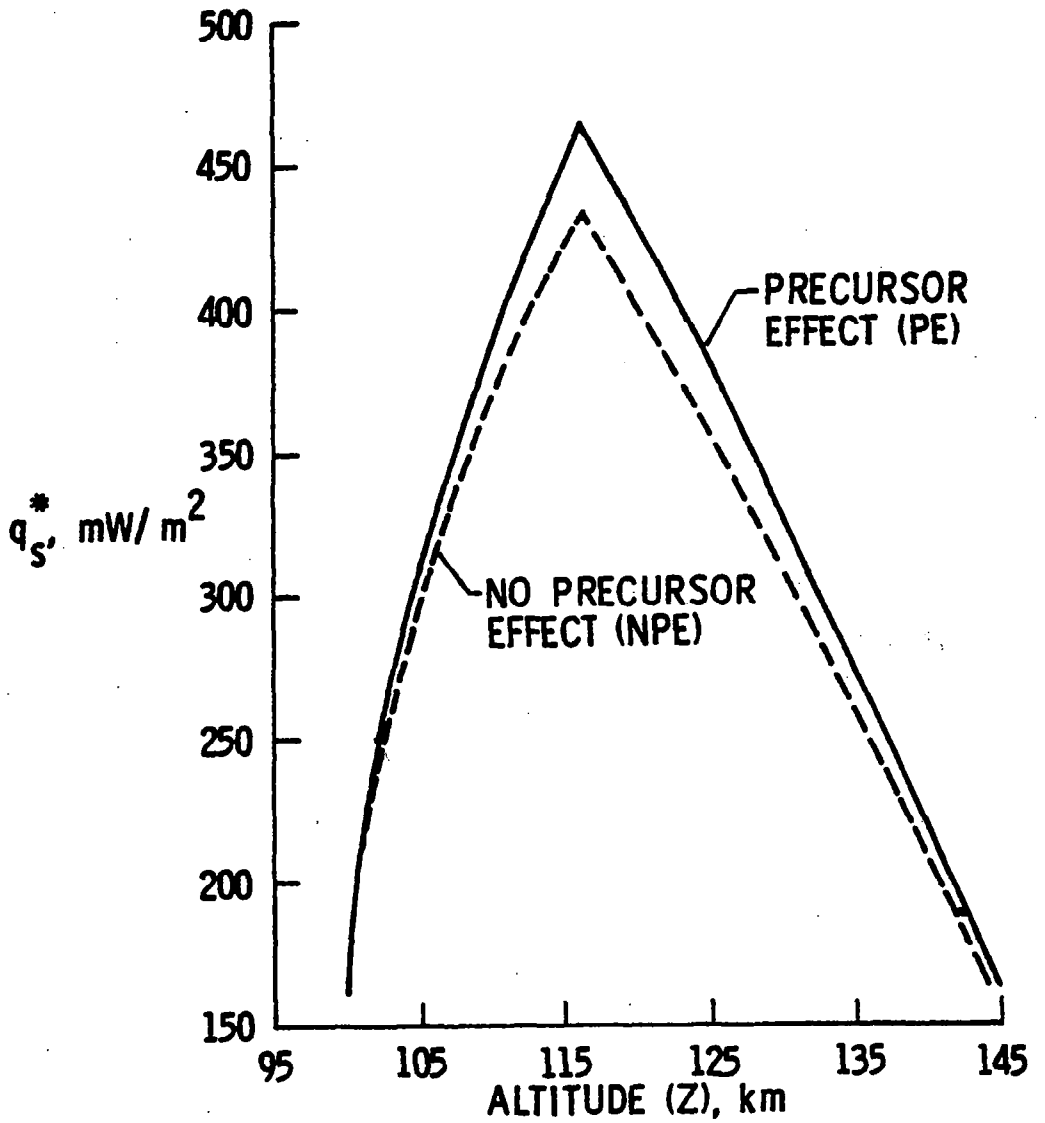

Fig. 36 Radiation flux towards the precursor region at the stagnation line shock location.

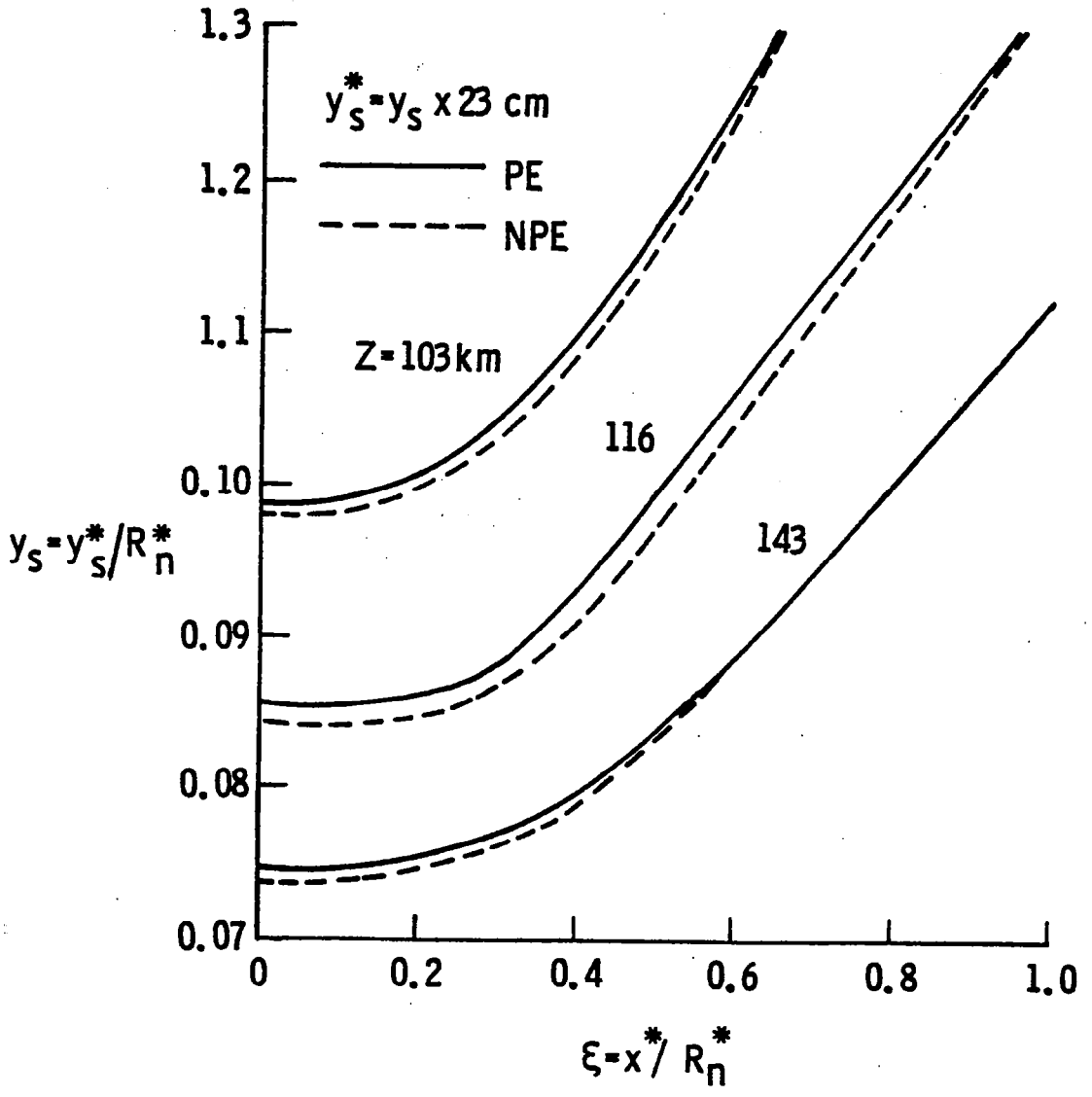

Fig. 37 Shock standoff distance variation with distance along body surface.

The conditions just behind the shock are illustrated in Figs. 38-41 as a function of distance along the body for different entry altitudes. For z = 116 km, Fig. 38 shows that precursor heating increases the enthalpy by a maximum of about 2 percent at the stagnation line. The change in shock temperature is shown in Fig. 39 for different altitudes. As would be expected, precursor heating results in a relatively higher temperature. The effect of precursor heating on the pressure just behind the shock was found to be small and, therefore, it could not be shown in a figure conveniently. Since the pressure essentially remains unchanged, precursor heating results in a decrease in the density (see Fig. 40) mainly because of an increase in the temperature. It was found that precursor heating had no significant influence on the u-component of velocity, but the v-component is slightly increased (see Fig. 41) as a result of decrease in the shock density.

Variations in pressure, density, velocity, and chemical species across the shock layer are shown in Figs. 42-44 for an altitude of Z = 116 km. Results presented in these figures are normalized by their shock values and they show that precursor effects are felt throughout the shock layer. Results presented in Figs. 42 and 43 for two body locations (ξ = 0 and 1) indicate the relative change in pressure, density, and velocities as compared to their shock values. For ξ = 0, Fig. 44 shows that precursor heating slightly decreases the concentration (mole fraction) of atomic hydrogen and increases the concentration of ions and electrons throughout the shock layer.

Variations of temperature, pressure, density, and velocity along the stagnation streamline in the entire shock layer-precursor zone are illustrated in Figs. 45-48 for different altitudes. Since higher entry

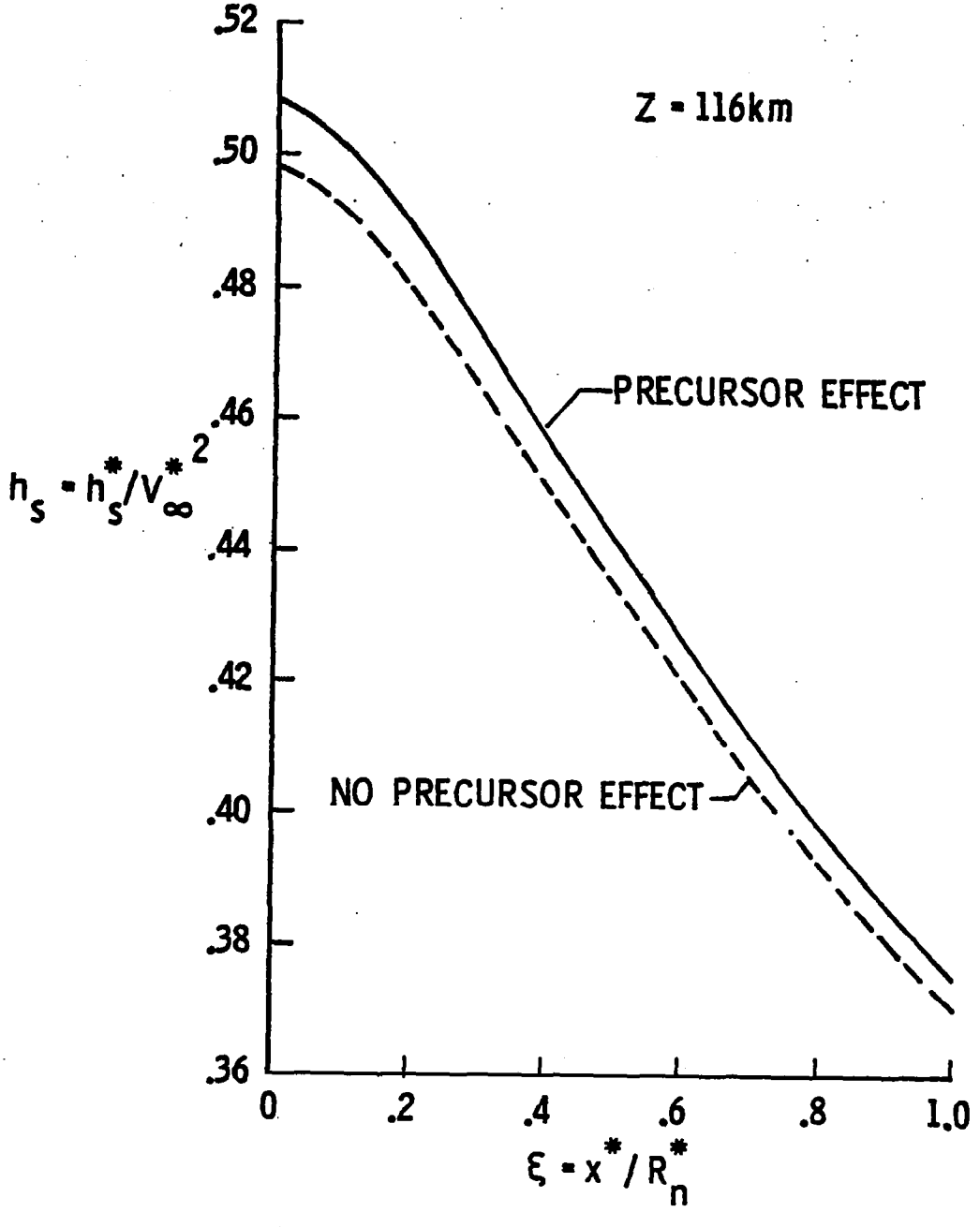

Fig. 38 Enthalpy variation just behind the shock with distance along the body surface.

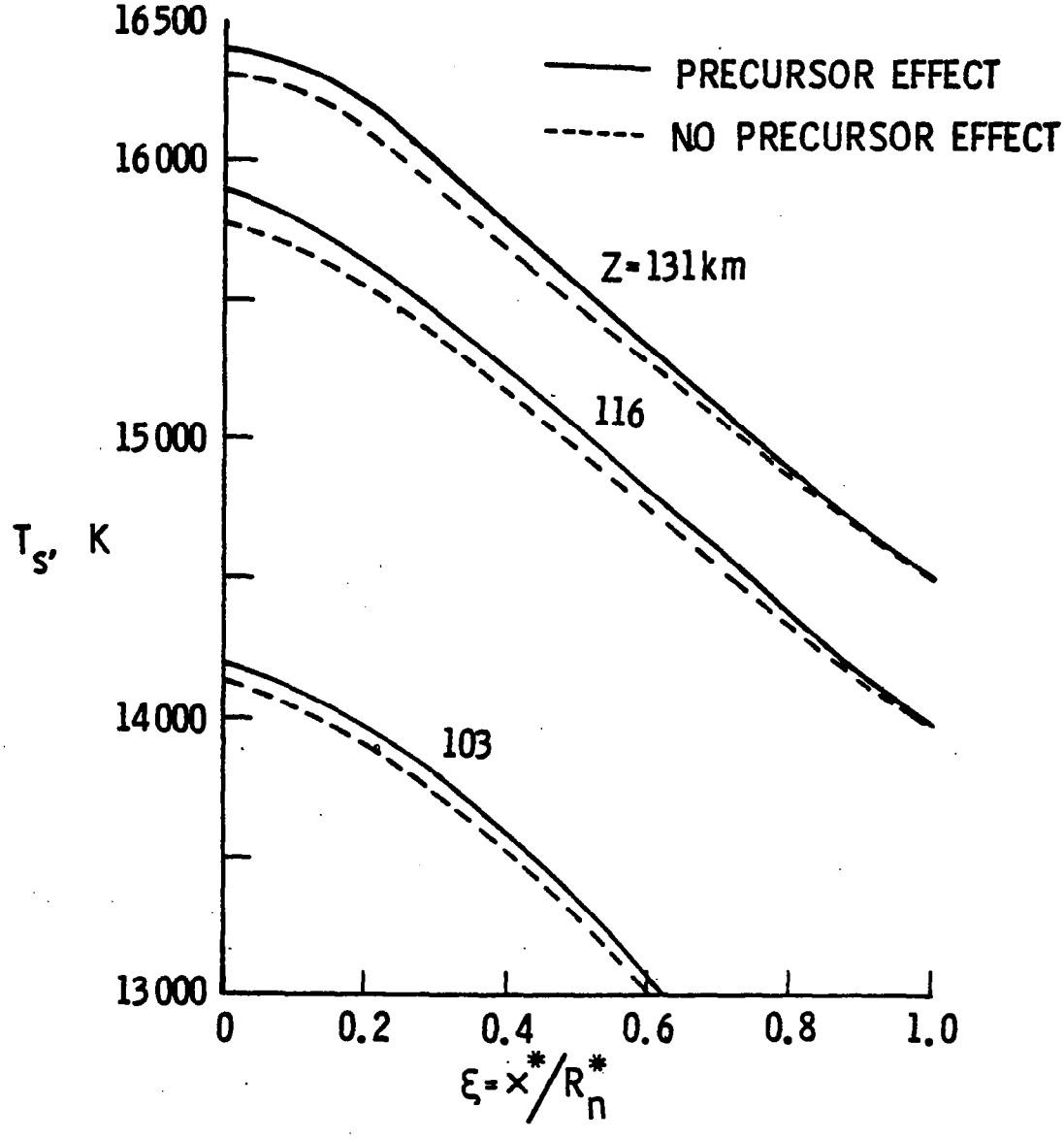

Fig. 39 Temperature variation just behind the shock with distance along the body surface.

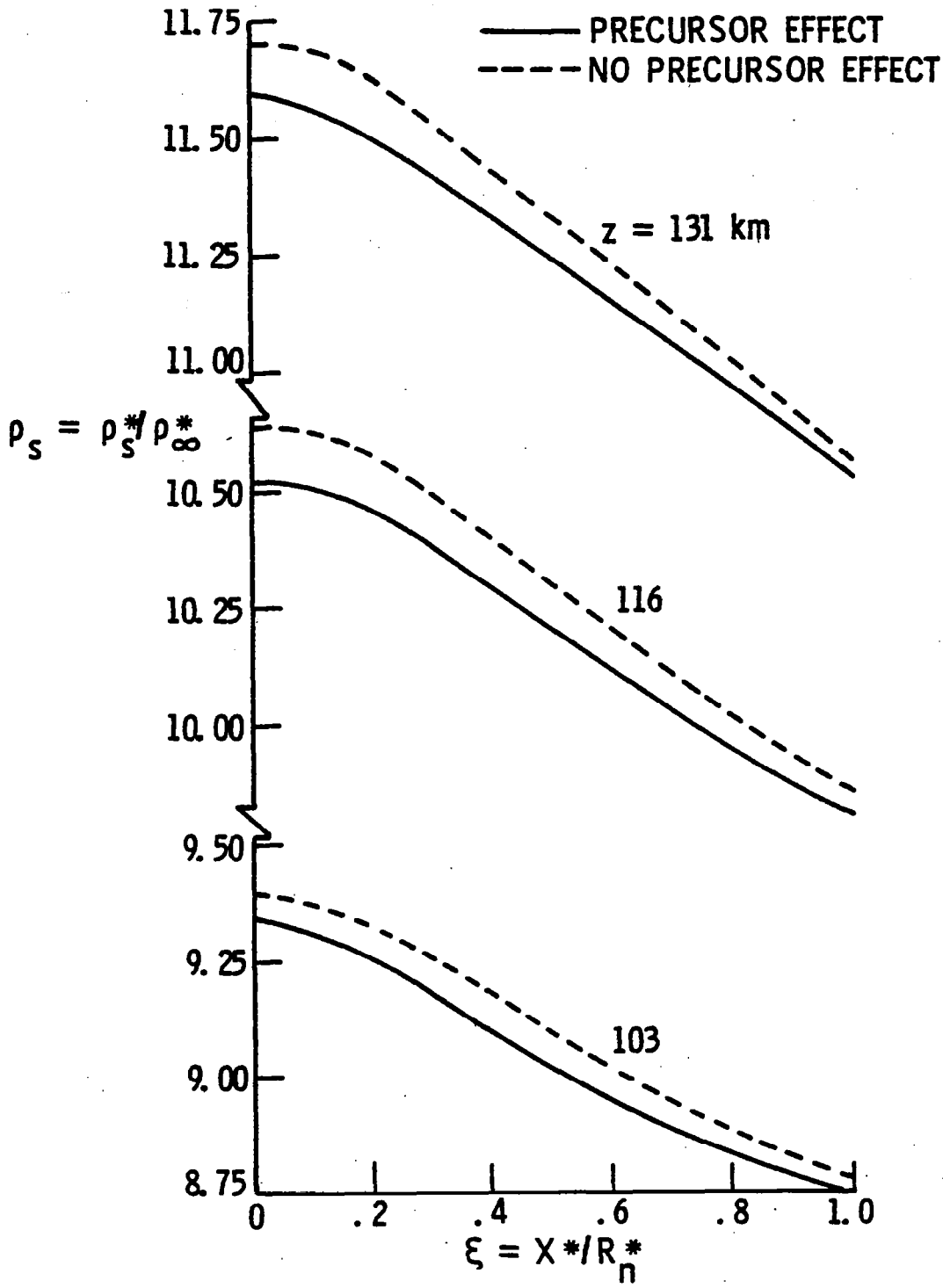

Fig. 40 Density variation just behind the shock with distance along the body surface.

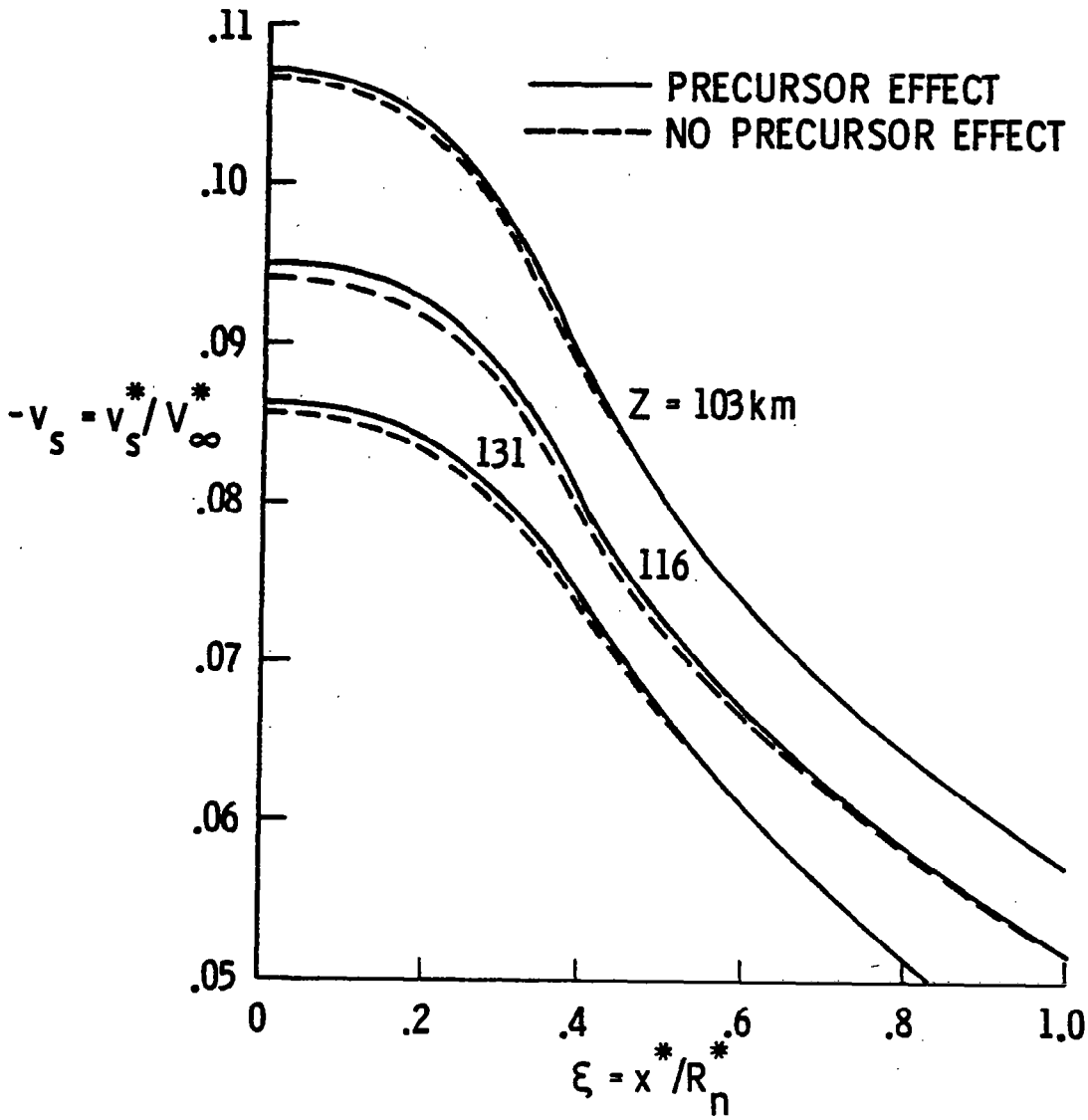

Fig. 41 Variation of v-velocity component just behind the shock with distance along the body surface.

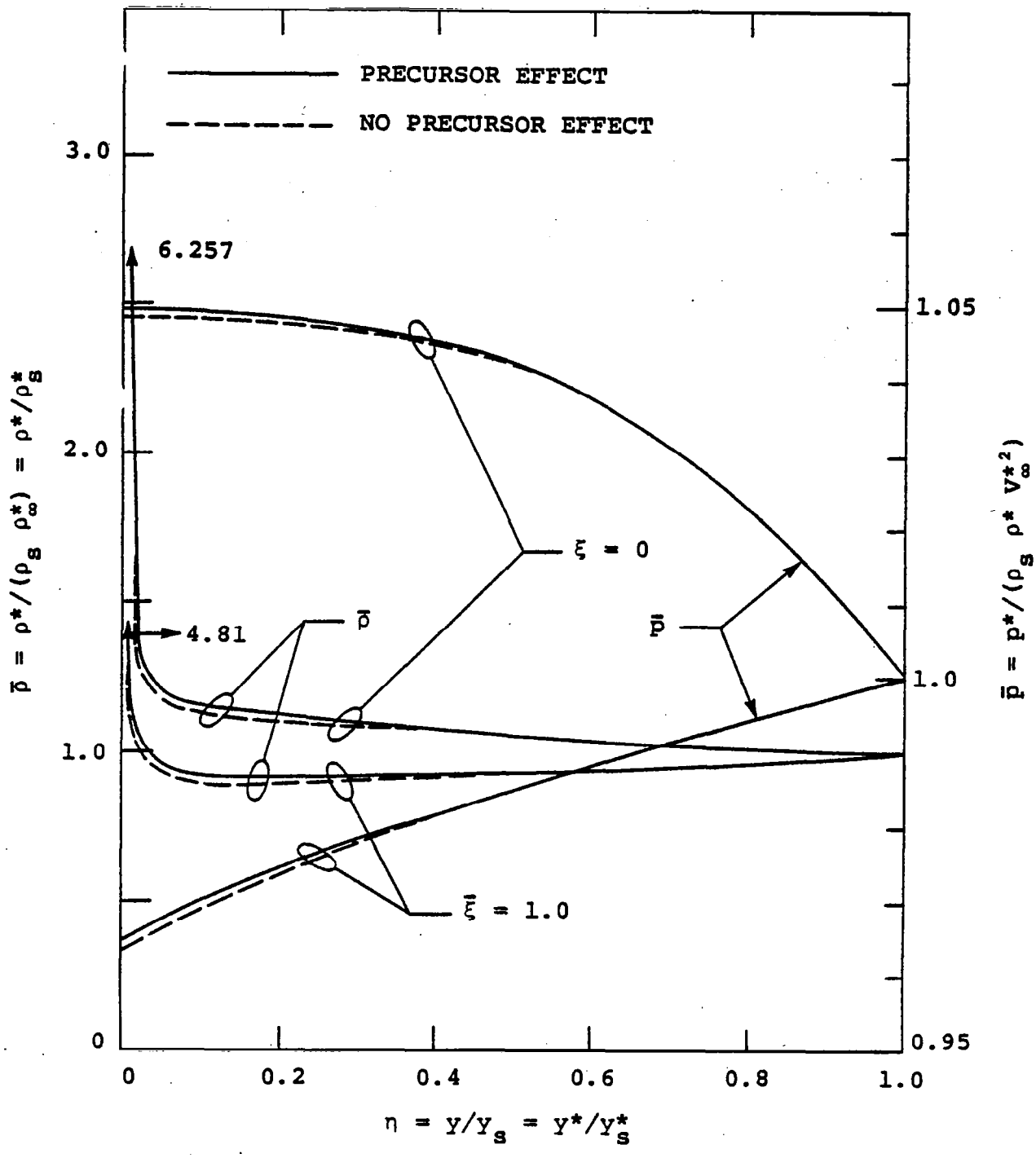

Fig. 42 Variation of pressure and density in the shock layer for two body locations (ξ = 0 and 1).

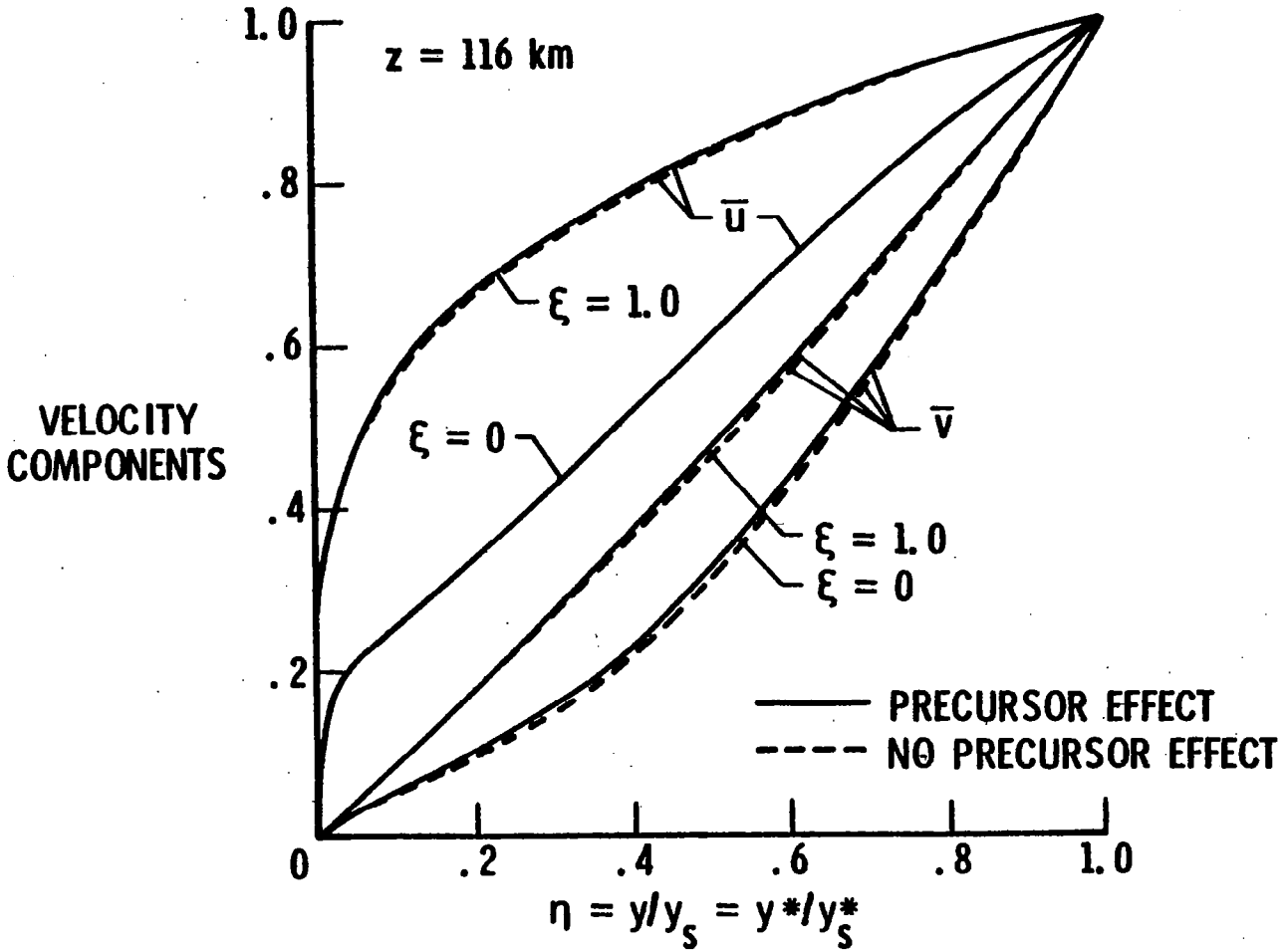

Fig. 43 Variations of velocity components in the shock layer for two body locations (ξ = 0 and 1).

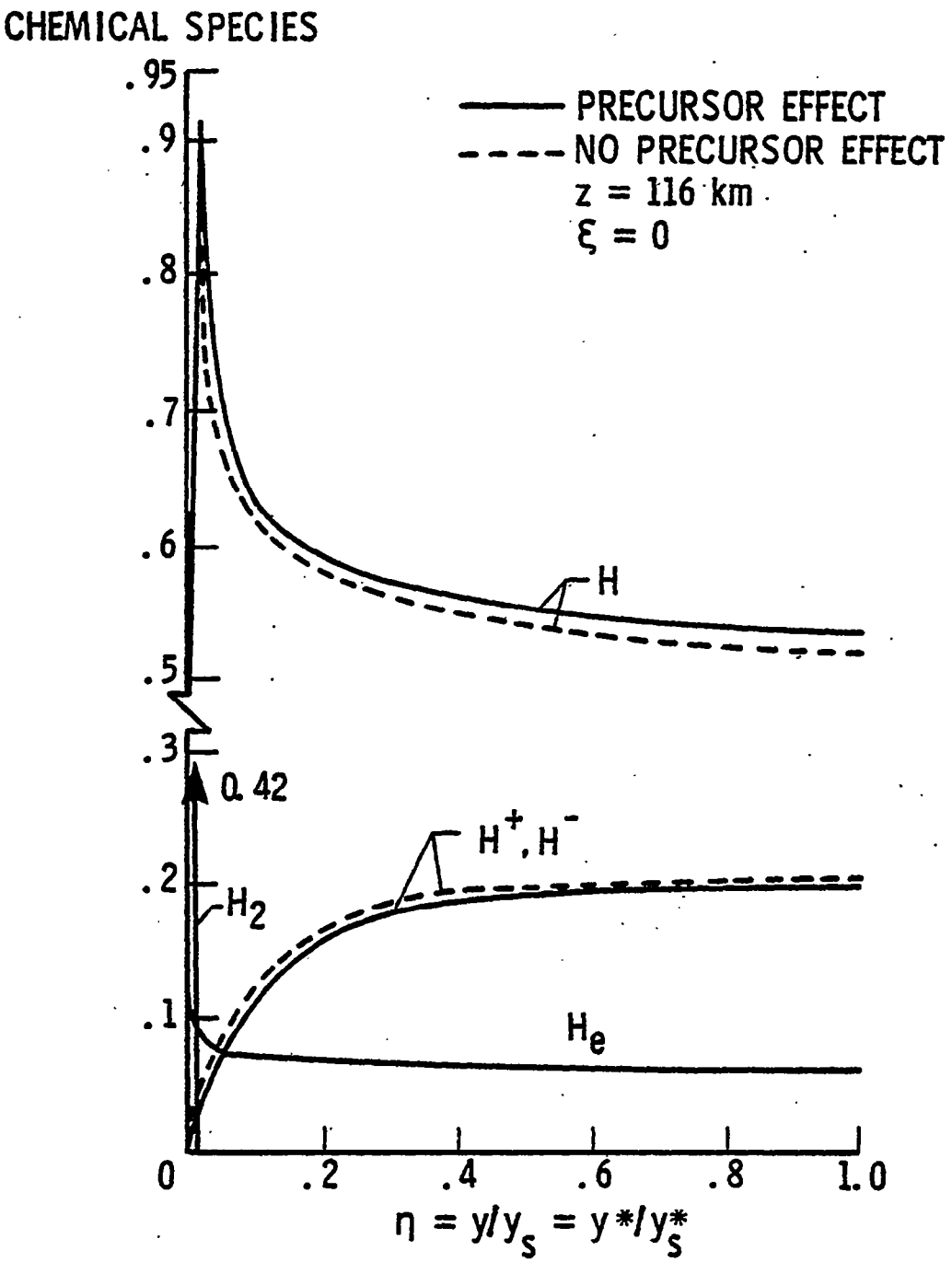

Fig. 44 Species concentration in the shock layer for $\xi = 0$.

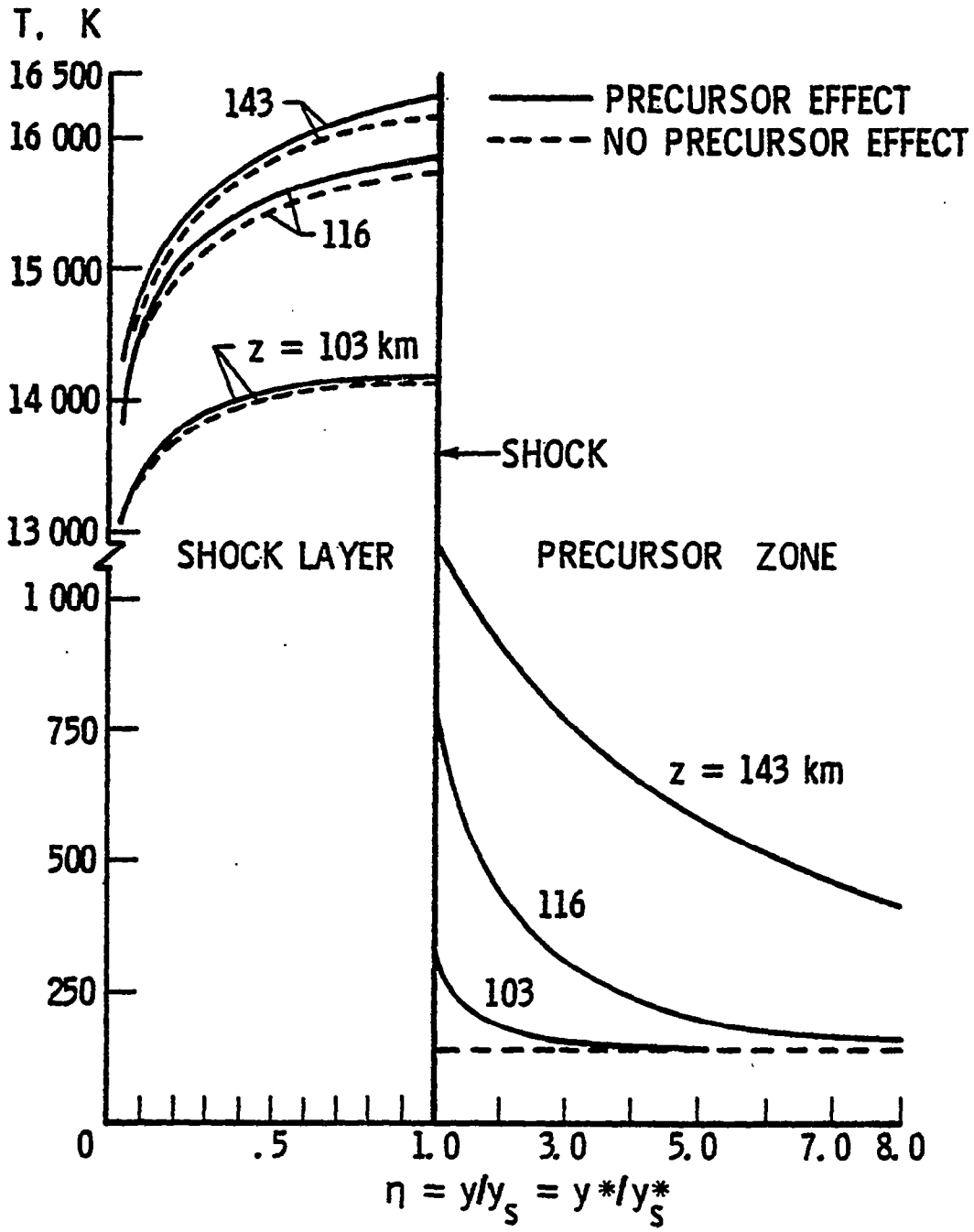

Fig. 45 Temperature variation in the shock/precursor region along the stangation streamline.

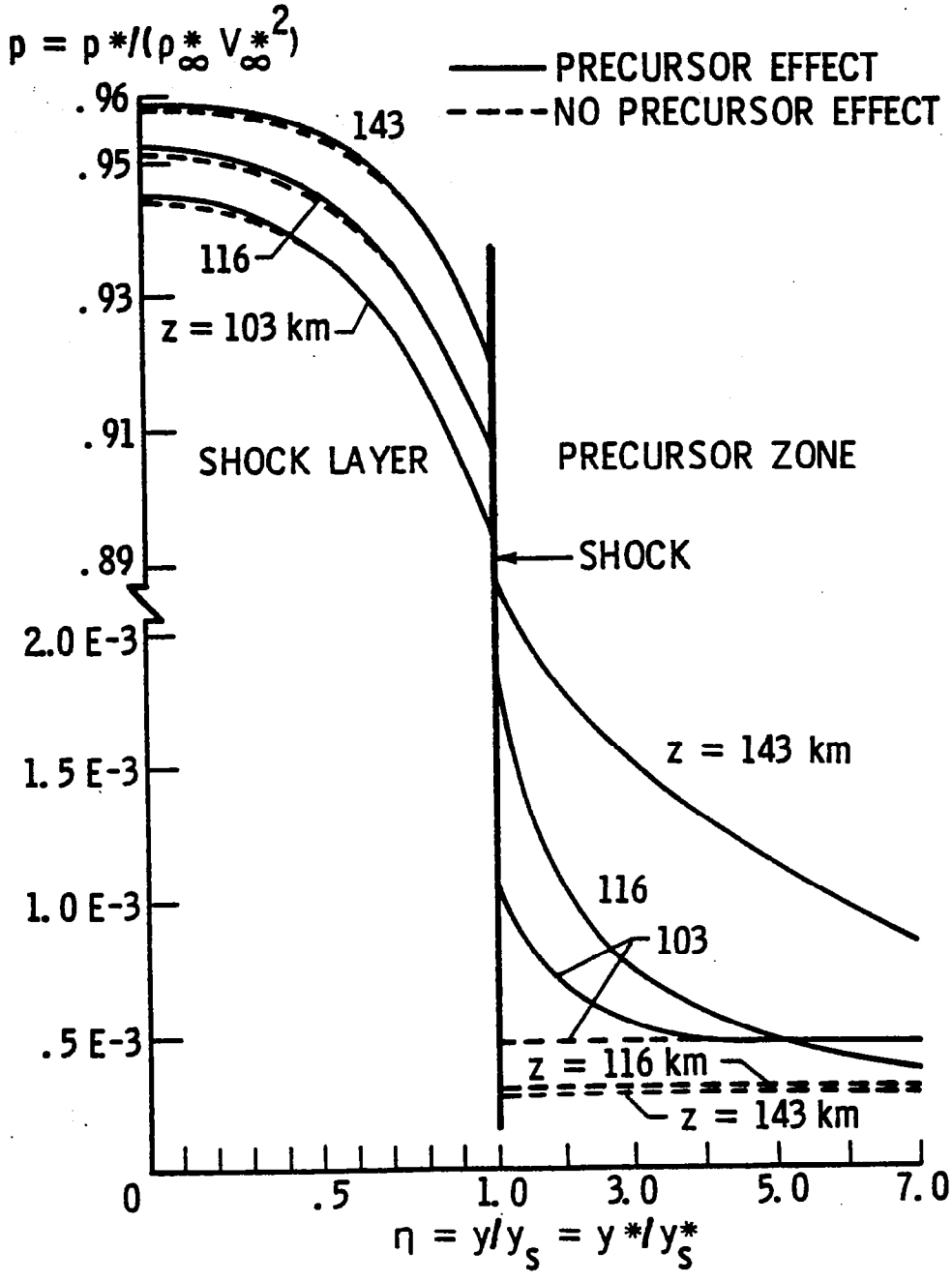

Fig. 46 Pressure variation in the shock/precursor region along the stagnation streamline.

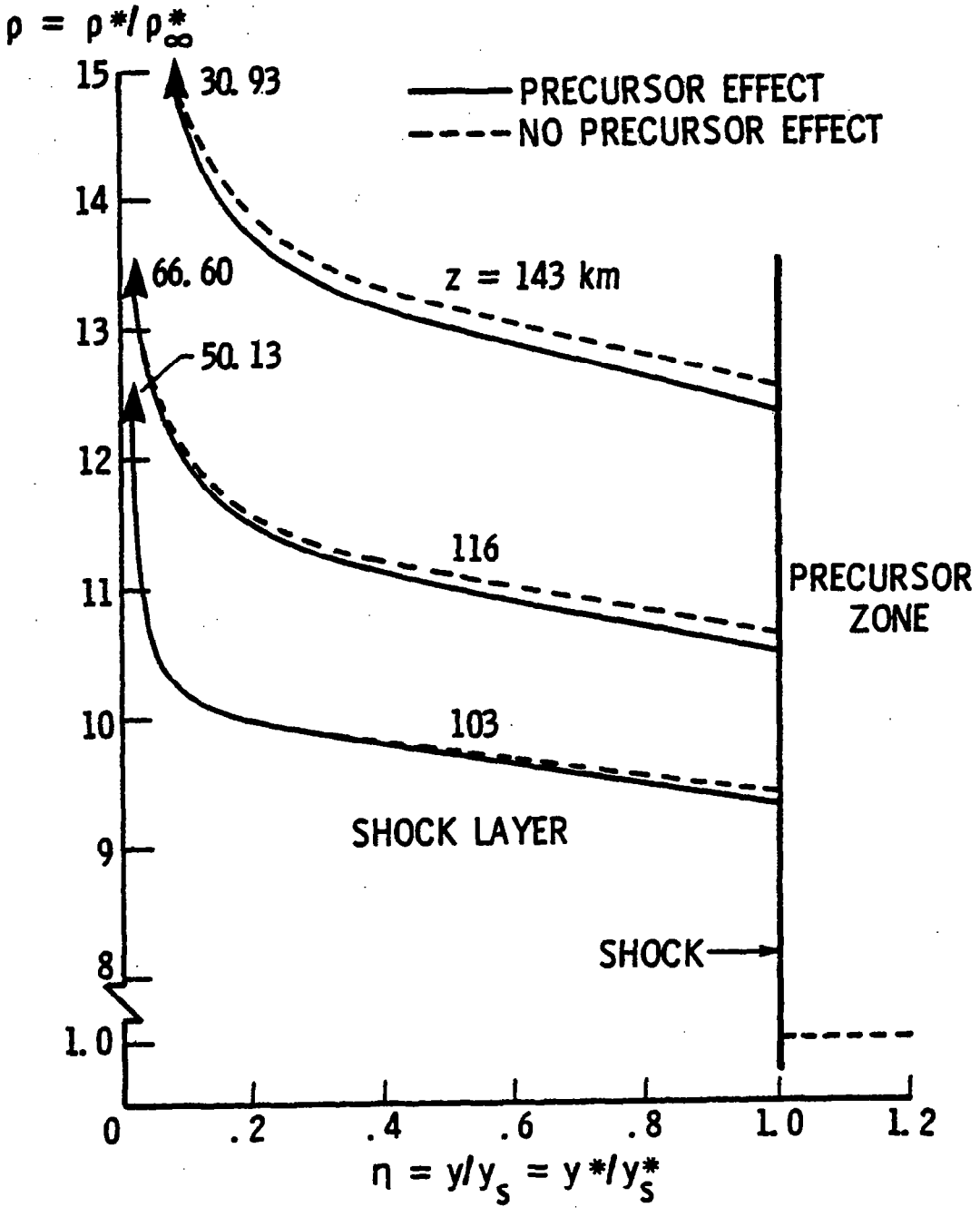

Fig. 47 Density variation in the shock/precursor region along the stagnation streamline.

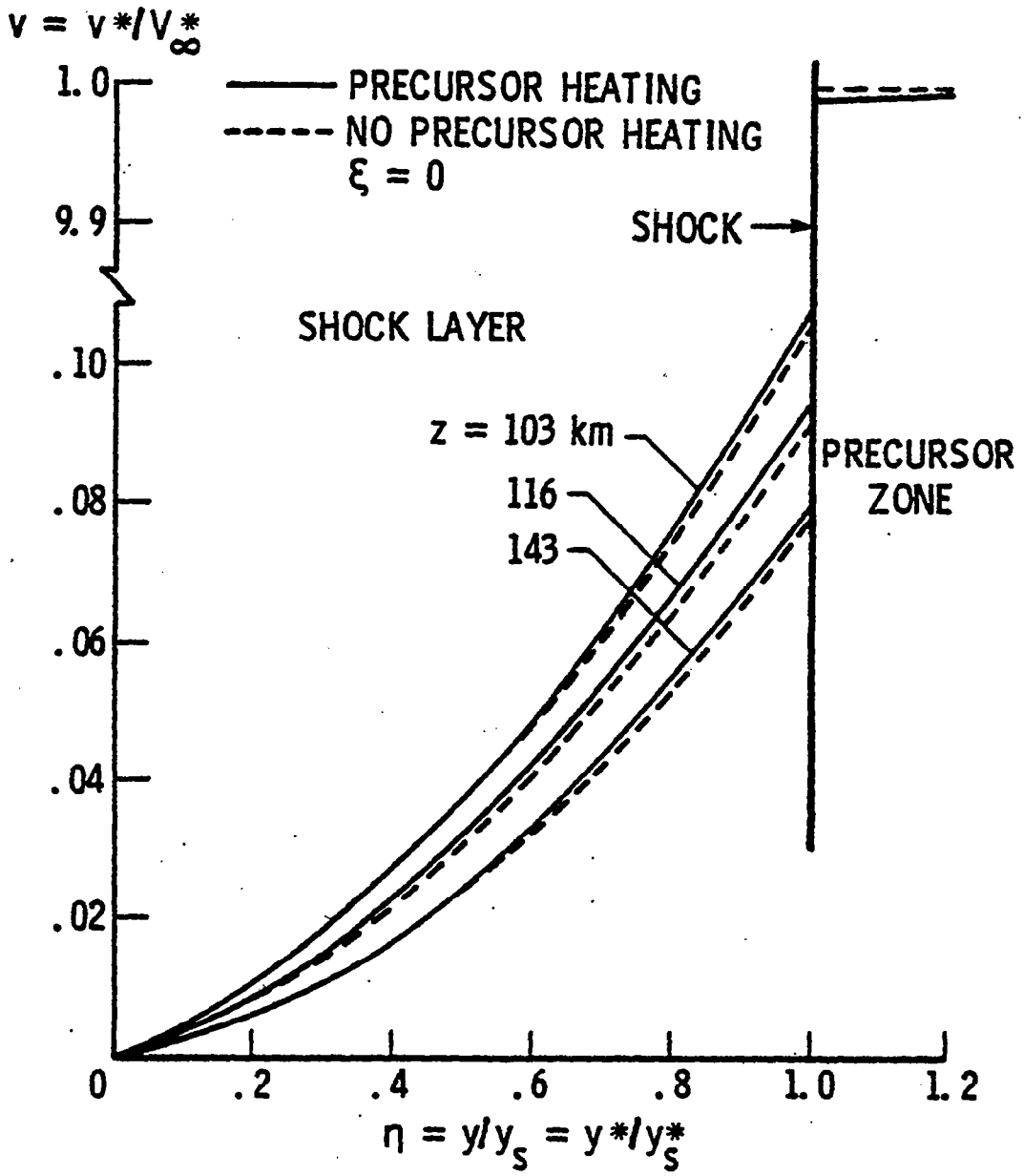

Fig. 48 Variation of v-velocity component in the shock/ precursor region along the stagnation streamline.

velocities are associated with higher altitudes, precursor effects, in general, are found to be larger for higher altitudes. The results for the precursor region show a dramatic increase in the pressure and temperature but only a slight change in the density and velocity. The changes are largest near the shock front because a major portion of radiation from the shock layer gets absorbed in the immediate vicinity of the shock front. Figures 45 and 46 show that, in spite of a large increase in the temperature and pressure in the precursor region, precursor heating does not change the temperature and pressure distribution in the shock layer dramatically. The change in temperature, however, is significant and (as would be expected) the maximum change occurs just behind the shock. There is a slight change in the pressure near the body but virtually no change closer to the shock. Figure 47 shows that the change in density in the shock layer is higher for higher altitudes and towards the shock. As discussed before, precursor heating results in a slight decrease in the shock layer density. Virtually no change in the u-component of shock layer velocity was found, but, as shown in Fig. 48, the v-component is slightly increased.

The effects of precursor heating on different heat fluxes in the shock layer are illustrated in Figs. 49-51. These results clearly demonstrate that precursor heating has a significant influence on increasing the heat transfer to the entry body. This increase essentially is a direct consequence of higher shock layer temperatures resulting from the upstream absorption of radiation. Figure 49 shows the variation of radiative and convective heat flux with distance along the body surface for Z = 116 km. It is noted that the precursor heating results in a

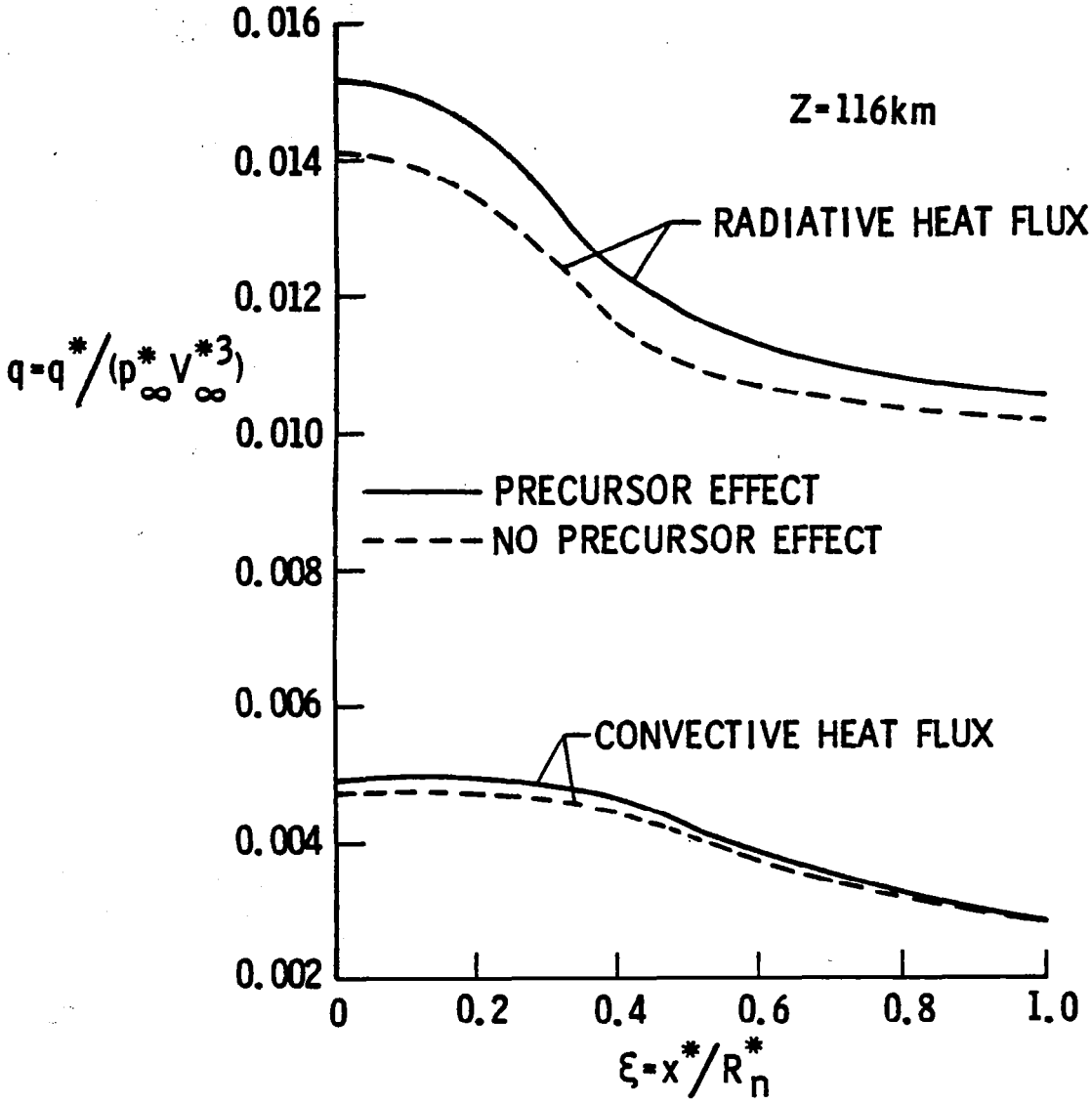

Fig. 49 Variation of radiative and convective heat flux with distance along the body surface for Z = 116 km.

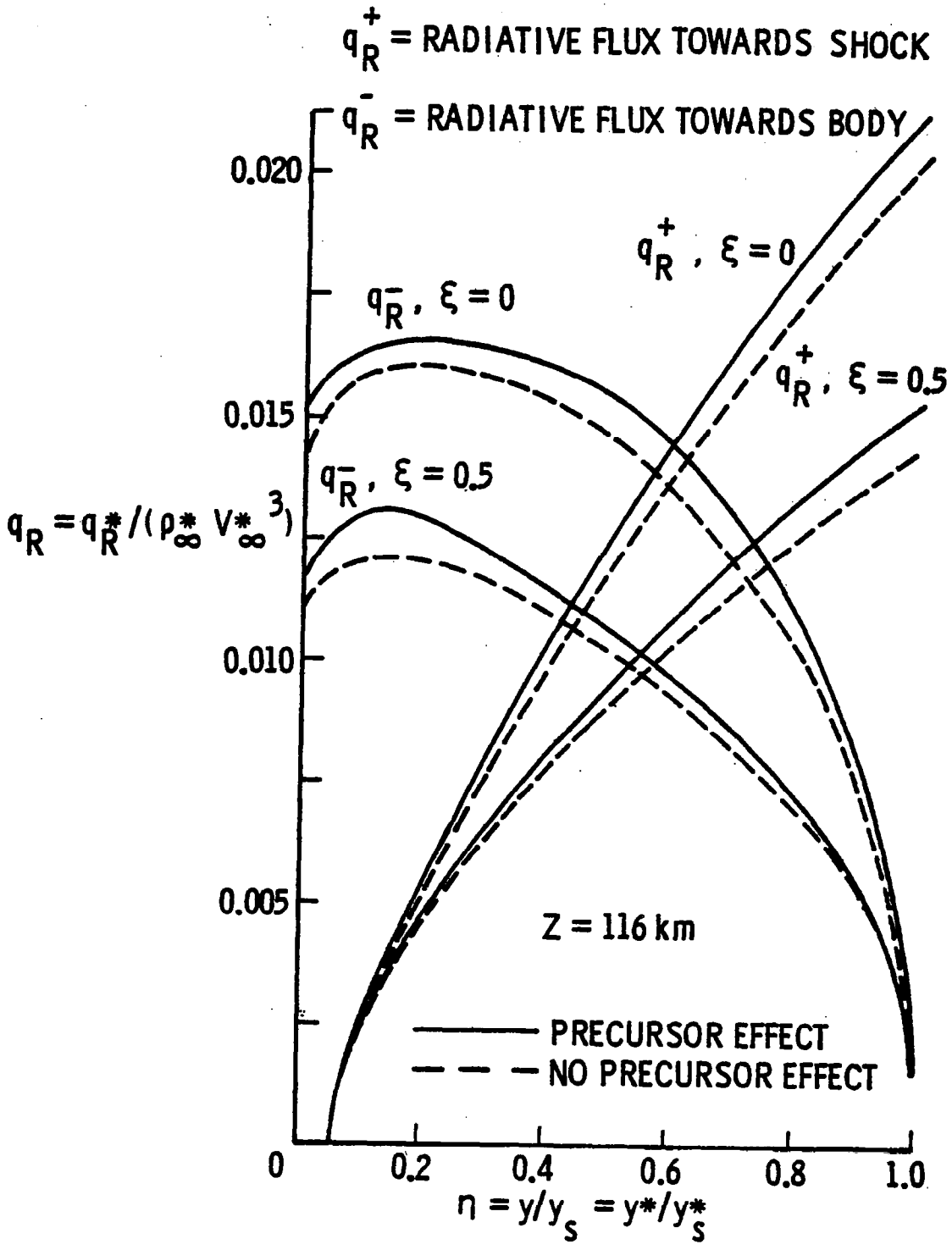

Fig. 50 Variation of radiative heat flux in the shock-layer for two body locations (ξ = 0 and 0.5), Z = 116 km.

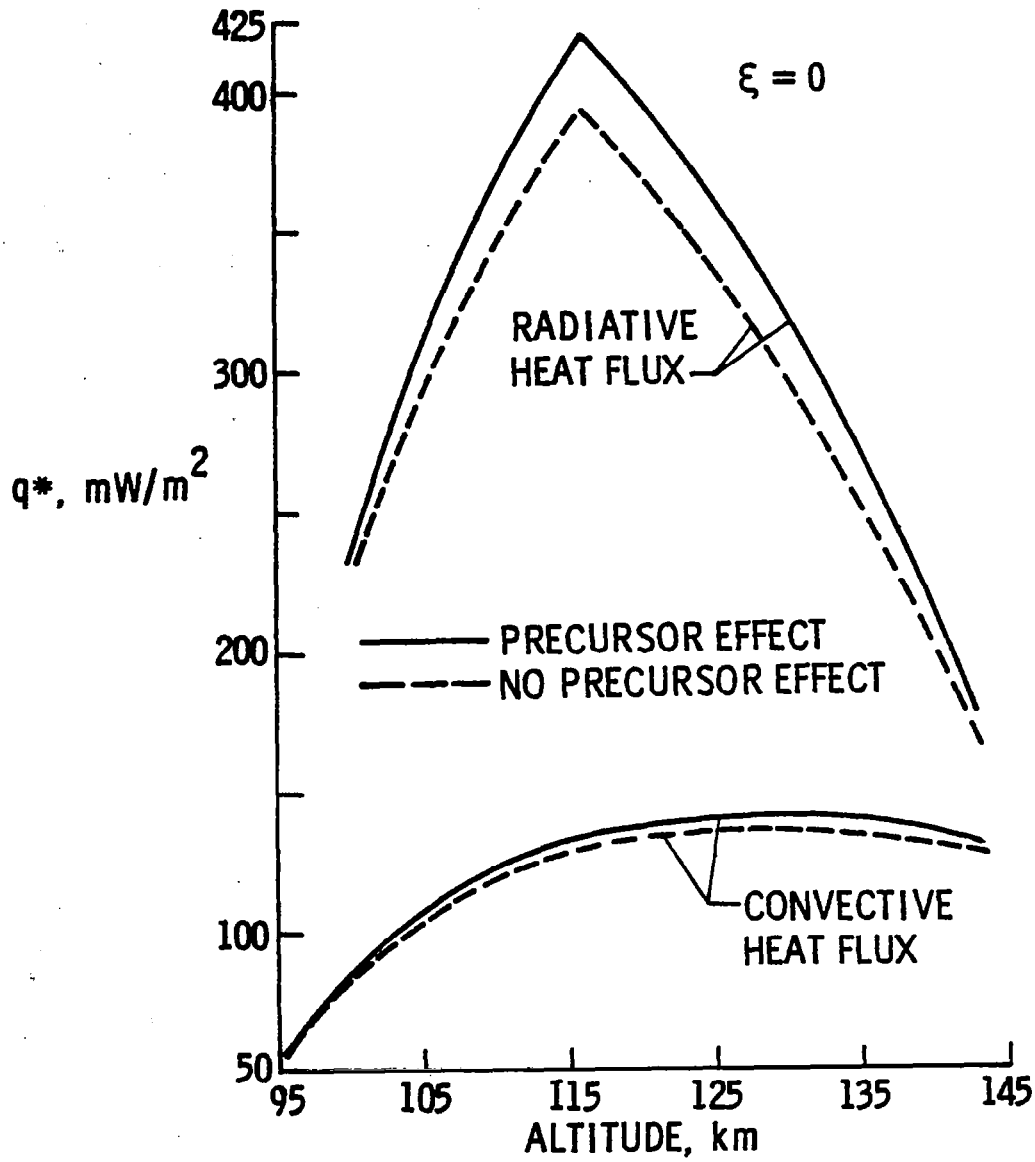

Fig. 51 Radiative and convective heat flux to the body (at $\xi = 0$, $\eta = 0$) for different entry altitudes.

7.5 percent increase in the radiative flux and about 3 percent increase in the convective flux to the body at the stagnation point. The increase in heat transfer at other body locations are relatively lower. A similar conclusion can be drawn from the results presented in Fig. 50 for the radiative flux towards the shock and the body for two body locations (ξ = 0 and 1) at Z = 116 km. Results of radiative and convective heat flux at the body (for ξ = 0) are illustrated in Fig. 51 for different altitudes of entry. The radiative flux results are seen to follow the trend exhibited in Fig. 36 for radiation at the shock front. The convective heat flux, however, is seen to increase slowly with the altitude up to Z = 131 km and thereafter decrease with increasing altitudes. The precursor effect is found to increase the radiative heating by a maximum of about 7.5 percent at Z = 116 km and the convective heating by 4.5 percent at Z = 131 km.

8.4 Influence of Precursor Heating on Viscous Nonequilibrium Flow

The influence of precursor heating on the flow phenomena around a Jovian entry body was investigated under the conditions of chemical nonequilibrium in the shock layer. As mentioned before, the entry body considered for this study is a 45° hyperboloid blunt body. The body enters the Jupitor's atmosphere at zero angle of attack. The two nominal atmospheres considered for Jovian entry consist of 85 and 89 percent hydrogen (by mole fraction) respectively. Also, to investigate the influence of change in the body nose radius on the thickness of the nonequilibrium layer, three different nose radii (12, 23, and 45 cm) were considered. To illustrate the important features of the nonequilibrium analysis, most

results were obtained for entry conditions which closely correspond to the peak heating conditions (i.e., for conditions at Z = 116 km). However, a few illustrative results have also been obtained for other entry conditions. Equilibrium and nonequilibrium results are presented first for variation of different properties in the shock layer. Results are then presented to illustrate the influence of precursor heating. Finally, results are presented for variation of different heat fluxes in the shock layer under the influence of both the nonequilibrium conditions and the precursor heating.

Two assumptions can be made about the molecular hydrogen entering the shock layer immediately behind the shock. One criteria is to assume that chemical reactions are "completely frozen" and initial composition of hydrogen just behind the shock corresponds to the free stream value. The second criteria is to consider that all hydrogen molecules have been dissociated immediately behind the shock. This is referred to as the "half-frozen" condition. Nonequilibrium results obtained for these two cases (for entry conditions at Z = 116 km and for 85 percent hydrogen nominal atmosphere) are illustrated in Figs. 52 to 54 as a function of the normal coordinate at the stagnation point. Figure 52 shows the mole concentration of different species across the shock layer. It is evident from this figure that molecular hydrogen is completely dissociated within about 4 percent of the total shock standoff distance from the shock wave. This is referred to as the dissociation zone (or the dissociated region). The variation in nondimensional v-velocity component and density is illustrated in Fig. 53. Since molecular weights change rapidly in the dissociated region, there is an increase in

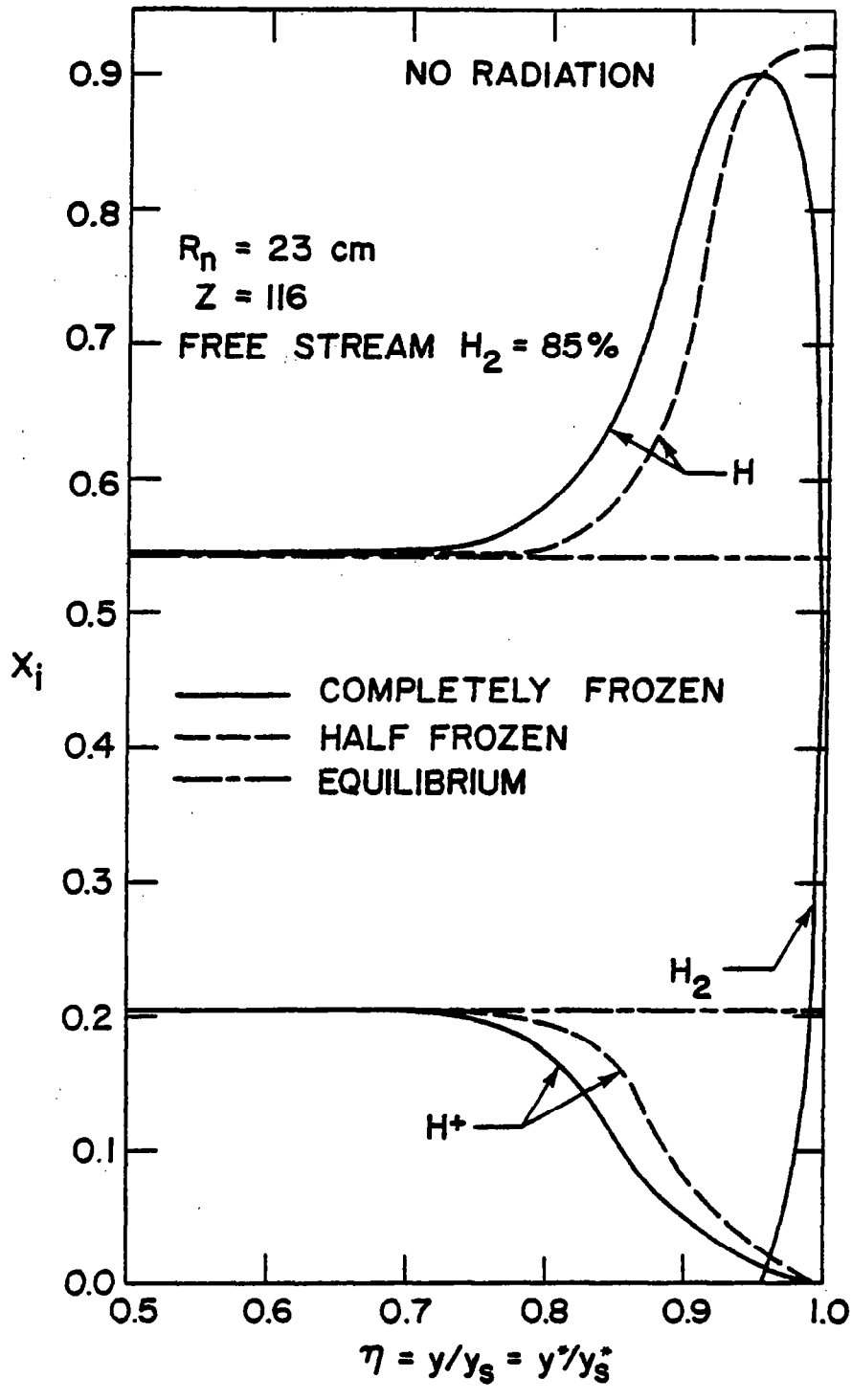

Fig. 52 Species concentration variation in nonequilibrium shock layer region for $\xi = 0$.

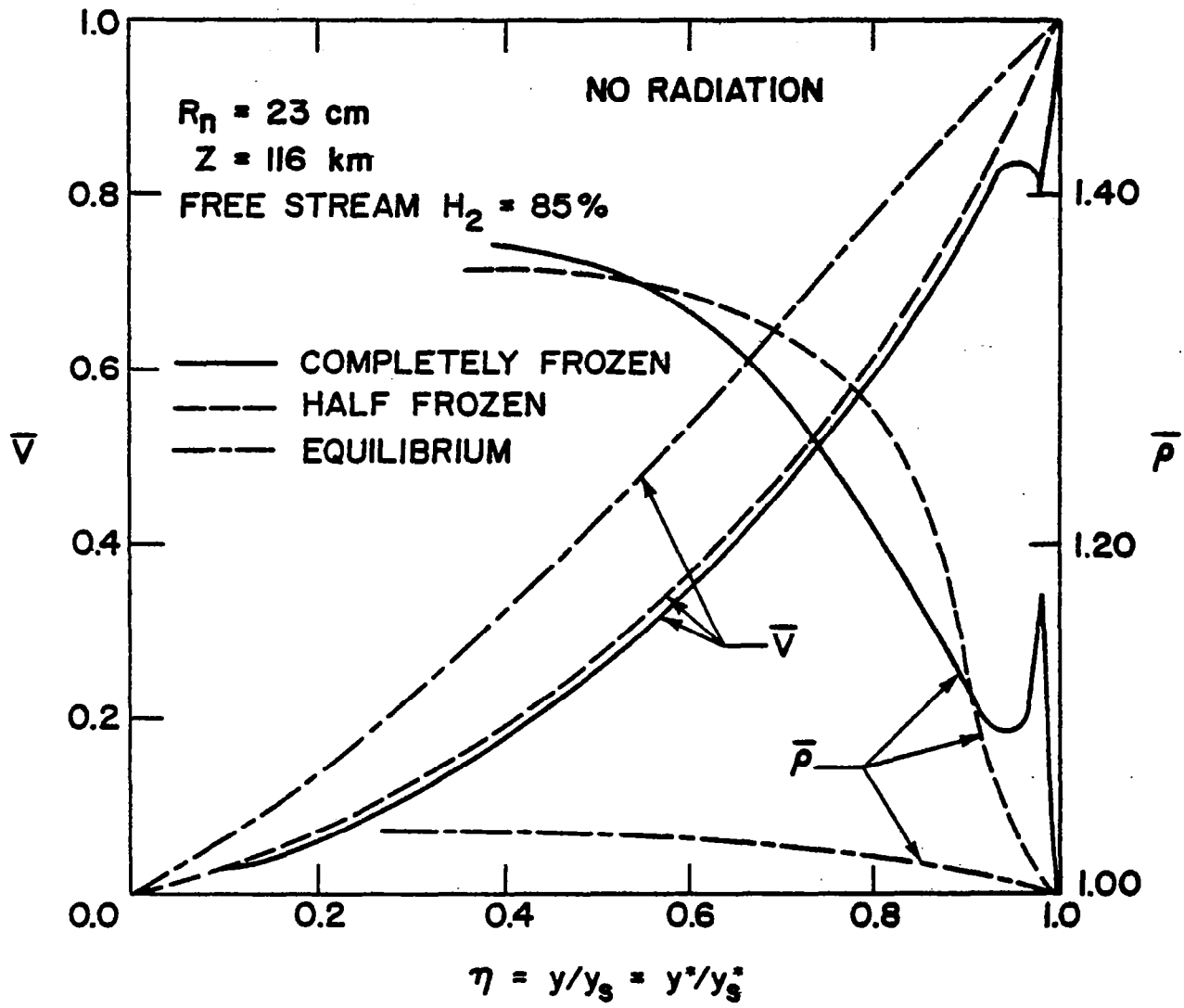

Fig. 53 Equilibrium and nonequilibrium $\bar{v}$-velocity component and density variation in the shock layer for $\xi = 0$.

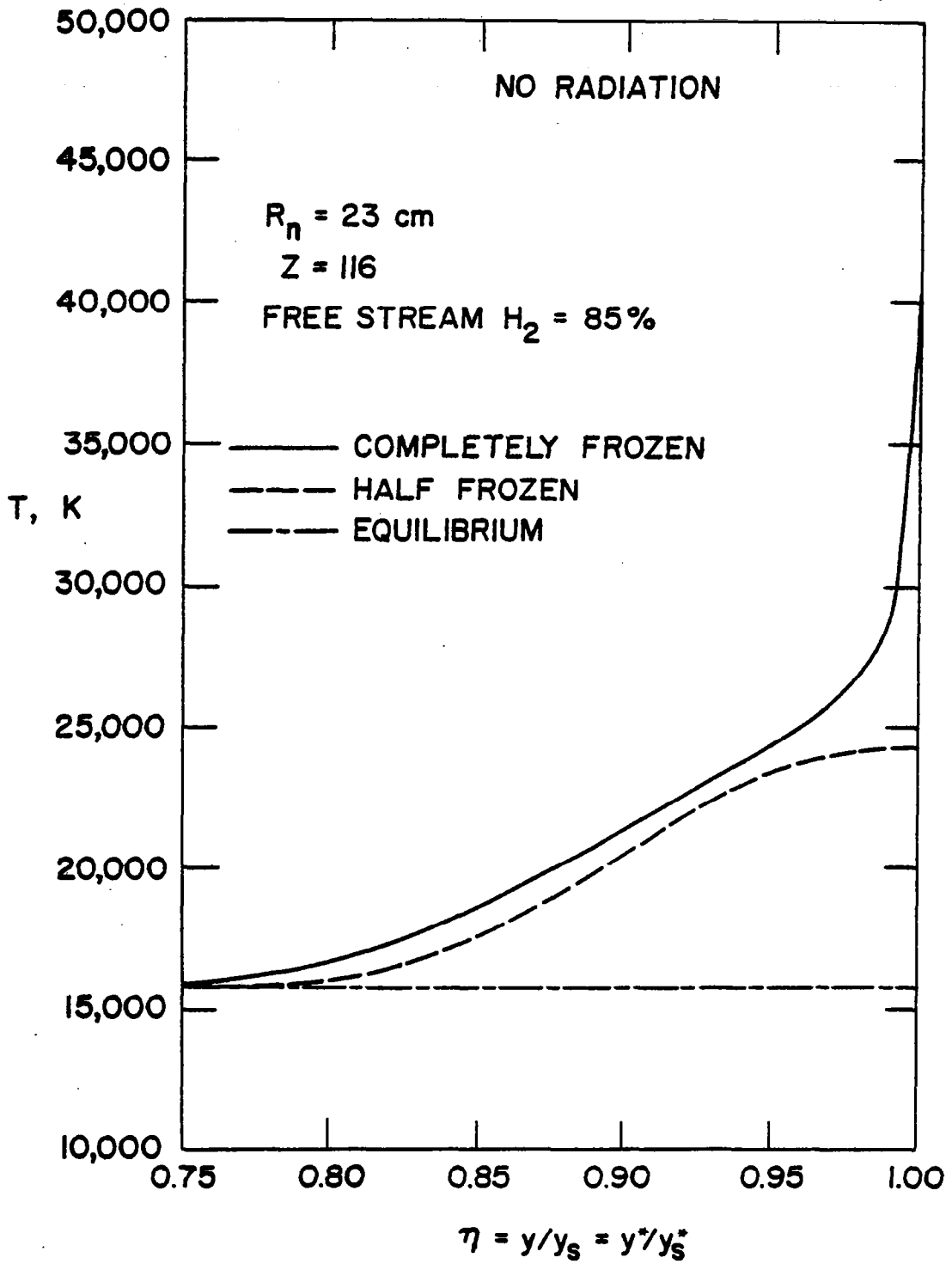

Fig. 54 Temperature variation in nonequilibrium shock-layer region for $\xi = 0$.

velocity and a decrease in density near the outer edge of the dissociation zone. The temperature distribution is shown in Fig. 54. It is noted that the temperature just behind the shock wave reaches a value of approximately 45,000 K in the completely frozen condition. After a short interval, however, all hydrogen molecules are dissociated and temperature drops to about 25,000 K. Next, ionization occurs and, as a result of this, temperature continues to decrease until it reaches the equilibrium value. From the results presented in Figs. 52-54, it is concluded that the half-frozen and completely frozen assumptions are quite close except in the dissociated region near the shock wave, and that the half-frozen flow computation is a reasonably good assumption for conditions of chemical nonequilibrium at altitudes near the peak heating region. Thus, all other results presented in this section have been obtained by considering only the half-frozen condition behind the shock.

As discussed in the previous section, the shock standoff distance (for a given body nose radius) varies with the altitude of entry and entry velocity. It should be pointed out here that, in general, the shock standoff distance increases with increasing the body nose radius. For entry conditions at Z = 116 km, equilibrium and nonequilibrium results for the shock standoff distance are illustrated in Fig. 55 as a function of the coordinate along the body surface. It is noted that the shock standoff distances for equilibrium and with radiation are considerably lower than for nonequilibrium and with no radiation. This, however, would be expected because shock-layer densities are greater for radiation and equilibrium conditions than for no radiation and nonequilibrium conditions.

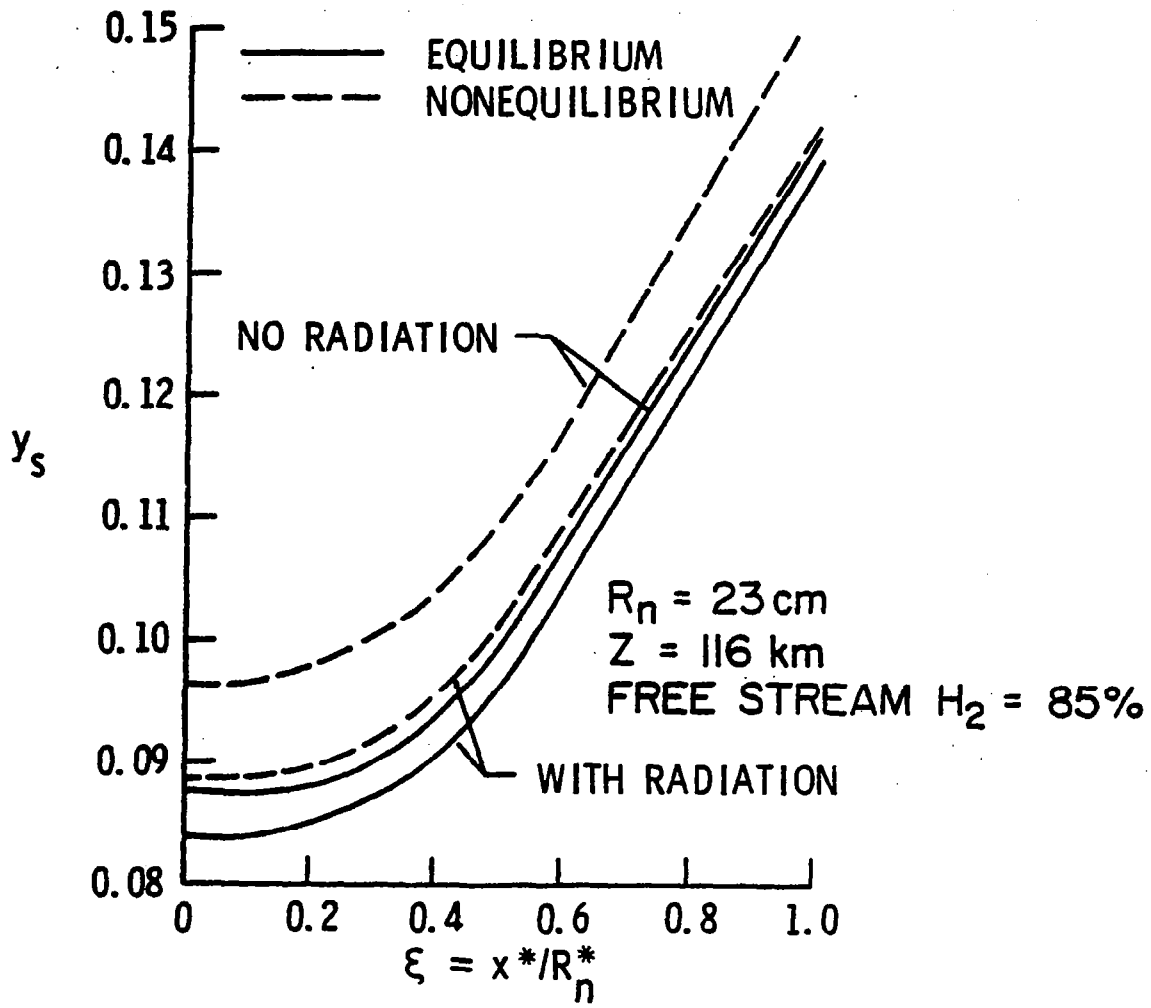

Fig. 55 Shock standoff variation with distance along the body surface.

Variations in chemical species across the shock layer are shown in Figs. 56-59 for different conditions. For entry conditions at Z = 116 km, results presented in Figs. 56 and 57 show that the nonequilibrium layer is about 25 percent of the total shock-layer thickness for no radiation case and about 50 percent for the case with radiation. This is because inclusion of radiation results in a different temperature distribution in the shock layer. This point will be discussed further while presenting results for the temperature variation. Near the wall, the mass fractions of atomic hydrogen and electrons are higher for nonequilibrium conditions with radiation. This is because cold gases near the wall absorb relatively more radiative heat flux in nonequilibrium case. For no radiation case, a comparison of results presented in Figs. 56 and 58 reveal that the nonequilibrium layer increases from 25 percent at Z = 116 km to about 40 percent at Z = 143 km. This is because density is lower at higher altitudes and, therefore, it will take a relatively longer time to reach equilibrium condition. For Z = 116 km entry conditions, Fig. 59 shows the species concentrations for three different body nose radii (12, 23, and 45 cm). These results indicate that the thickness (or range) of the nonequilibrium layer decreases with increasing nose radius. In particular, it is seen that the thickness is about 40 percent for R_n = 12 cm but it is only 10 percent for R_n = 43 cm. This is because the shock standoff distance is proportional to the body nose radius and the relaxation time for chemical reactions is about the same for all cases.

Temperature distributions across the shock layer are illustrated in Figs. 60-62 for different conditions. For the case with no radiation, the heavy particle and electron temperature variations across the shock

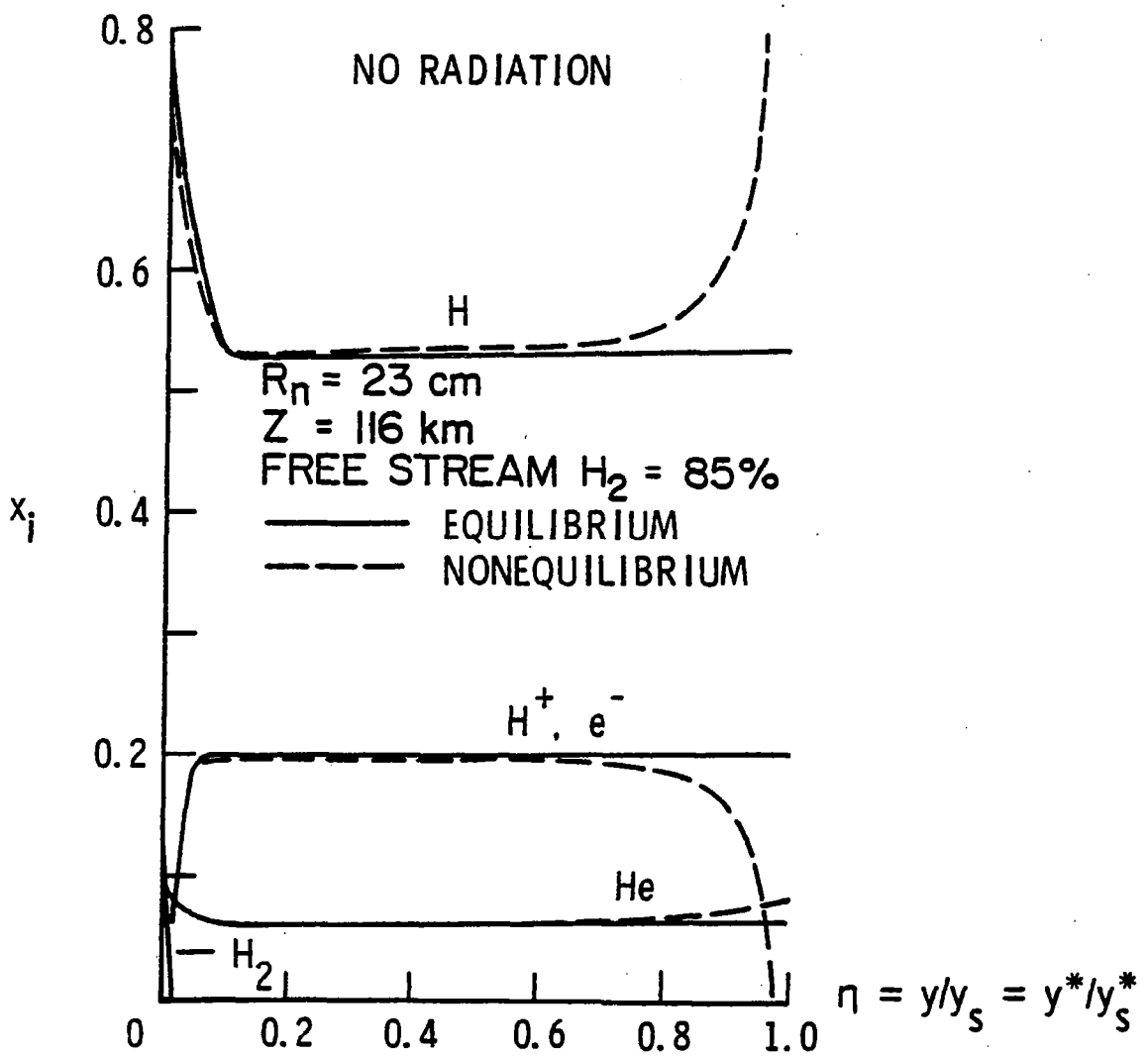

Fig. 56 Species concentration in the shock layer for $\xi = 0$ (with no radiation).

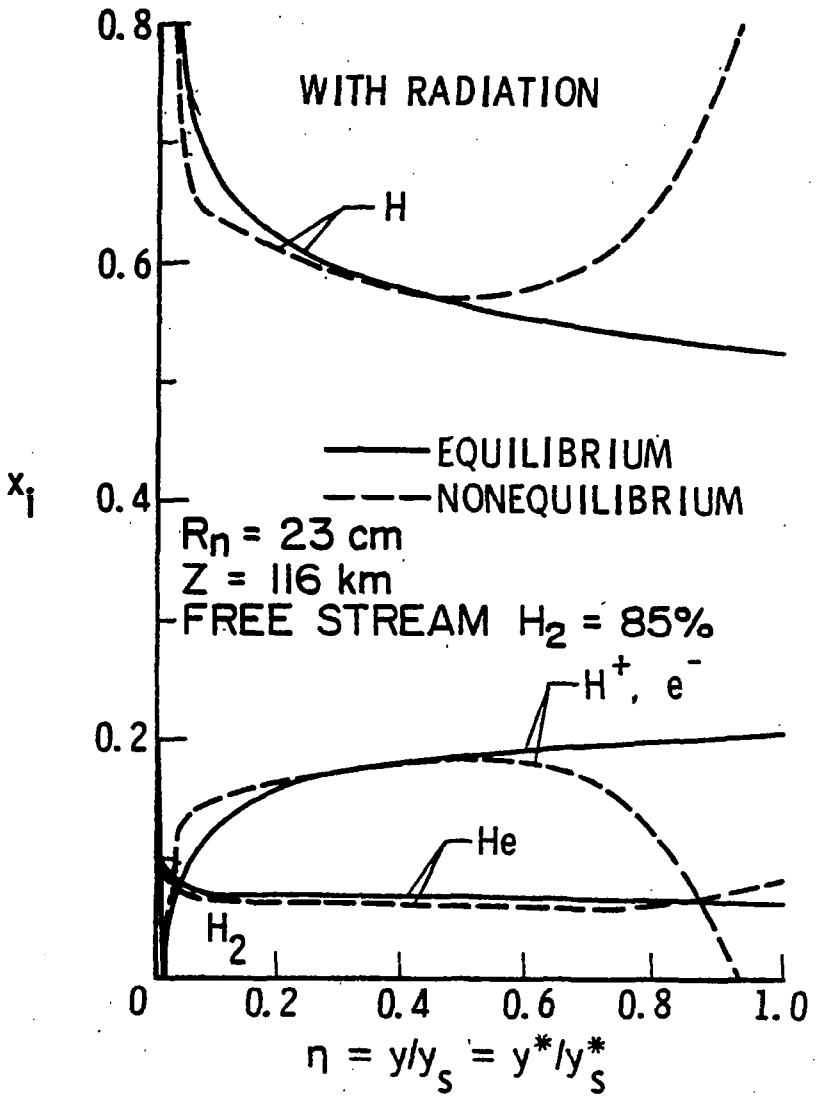

Fig. 57 Species concentration in the shock layer for $\xi = 0$ (with radiation).

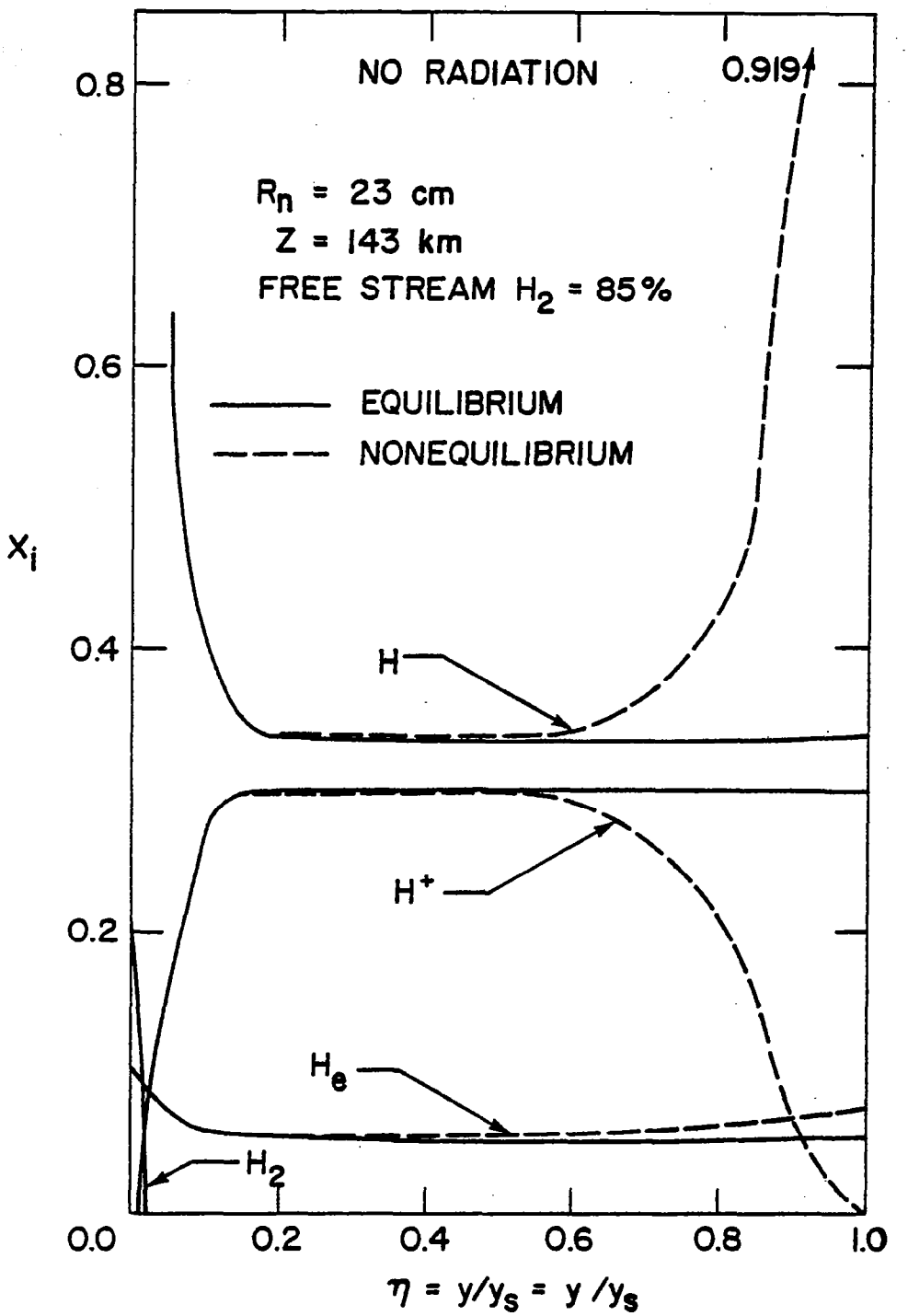

Fig. 58 Species concentration in shock layer for $\xi = 0$ at Z = 143 km (with no radiation).

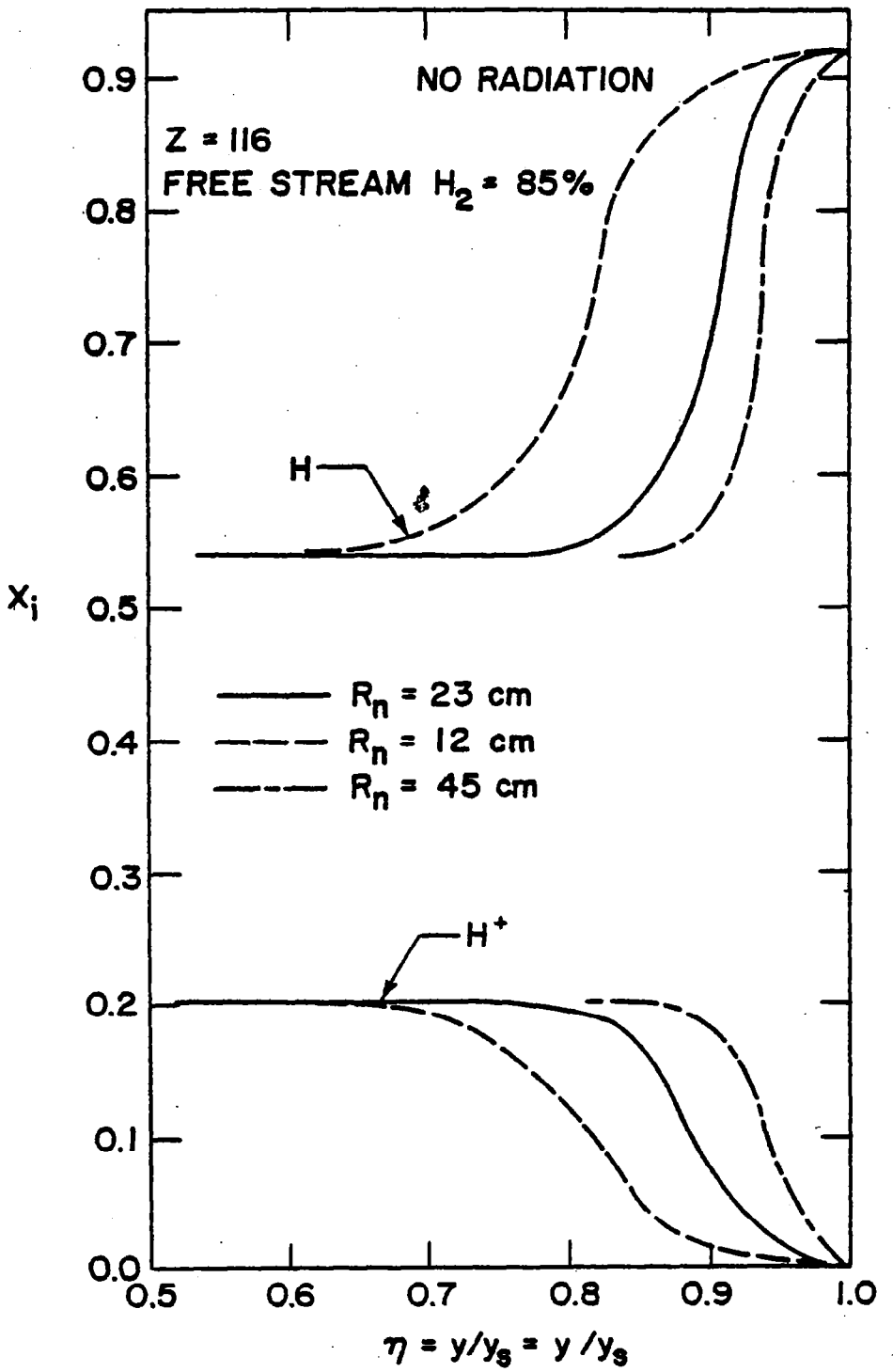

Fig. 59 Species concentration for different body radius in the shock layer for $\xi = 0$ at Z = 116 km (with no radiation).

tion) in Fig. 60 for different entry conditions. The results show that in the absence of radiation, the nonequilibrium temperature is higher than the equilibrium temperature throughout the shock layer for each entry condition. It is also noted that the electron temperature, which is lower than the heavy particle temperature during early stages of ionization, asymptotically approaches the heavy particle temperature during the later stages of ionization. As discussed in the previous section, the temperature distribution in the shock layer is relatively higher for higher altitudes because of higher entry velocities. For entry conditions at Z = 116 km, the electron temperature distributions (without and with radiation) are shown in Figs. 61 and 62 for three different body nose radii. As noted earlier, the thickness of the nonequilibrium layer decreases with increasing nose radius. Also, for a given nose radius, inclusion of radiation increases the thickness of the nonequilibrium layer. This is because the loss of radiation from the shock layer results in an entirely different temperature distribution (see Fig. 62) and leaves relatively less energy for dissociation and ionization of the gas.

For entry conditions at Z = 116 km, Fig. 63 shows the mass fraction of atomic hydrogen and hydrogen ion along the stagnation streamline in the precursor region. While equilibrium results indicate that only 5 percent hydrogen is dissociated and 0.018 percent is ionized, the nonequilibrium results show that 15 percent hydrogen is dissociated and 0.8 percent ionized. It should be pointed out that the composition of the precursor gas will be different for different entry conditions. It should be emphasized here again that in investigating the precursor region flow

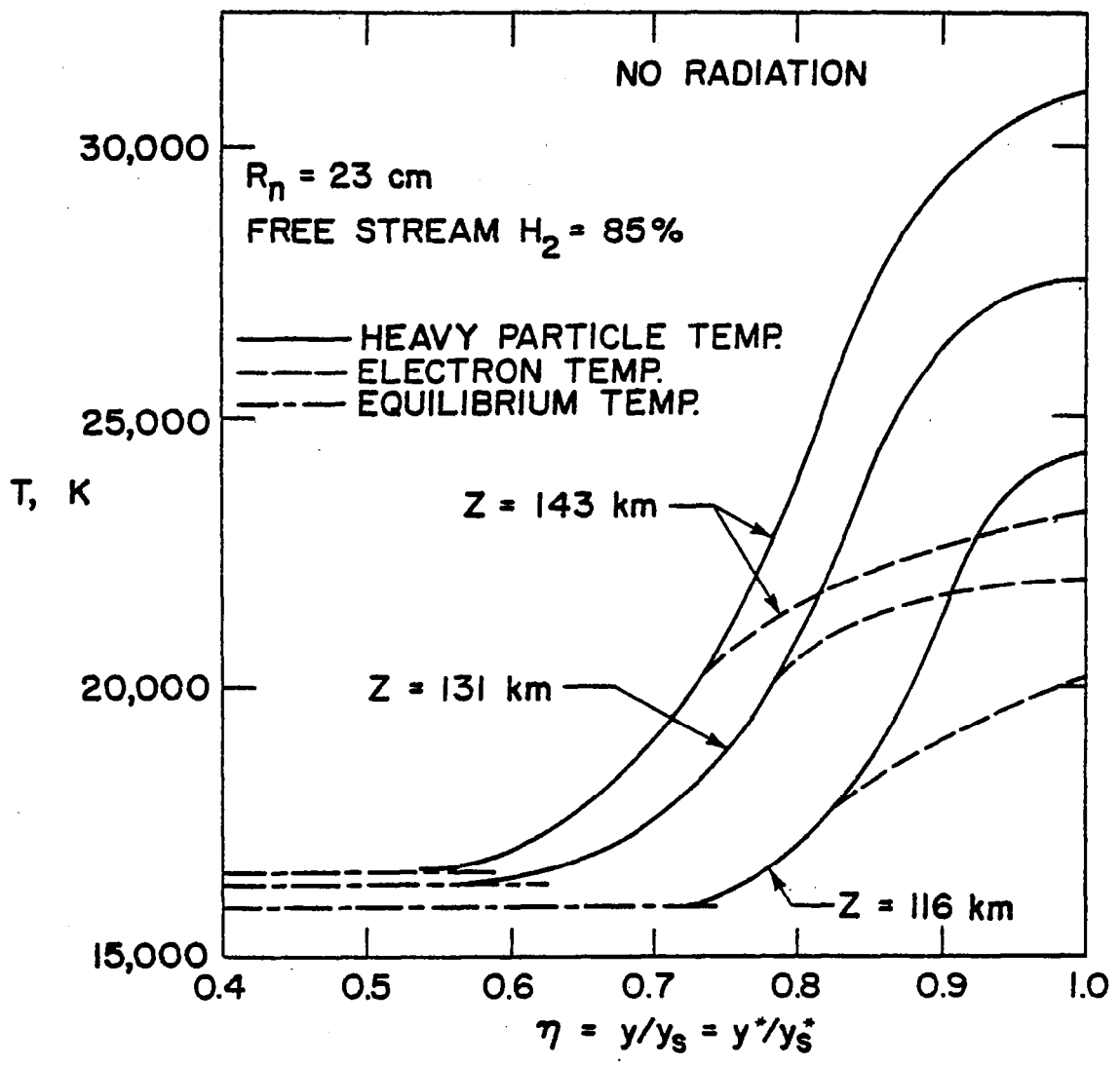

Fig. 60 Heavy particle and electron temperature variation in the shock-layer nonequilibrium region.

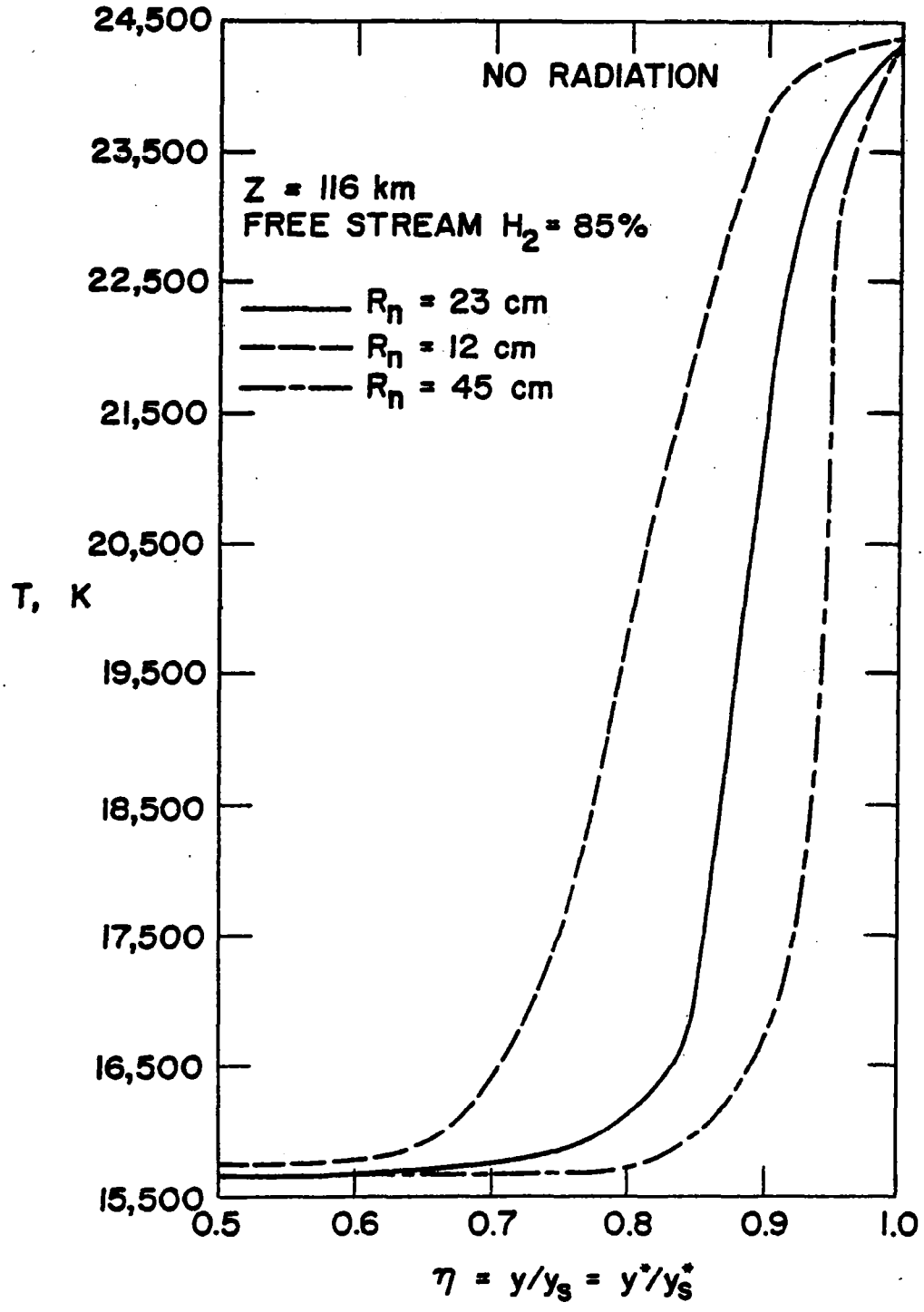

Fig. 61 Temperature variation for different body nose radius in the nonequilibrium region at $\xi = 0$ (with no radiation).

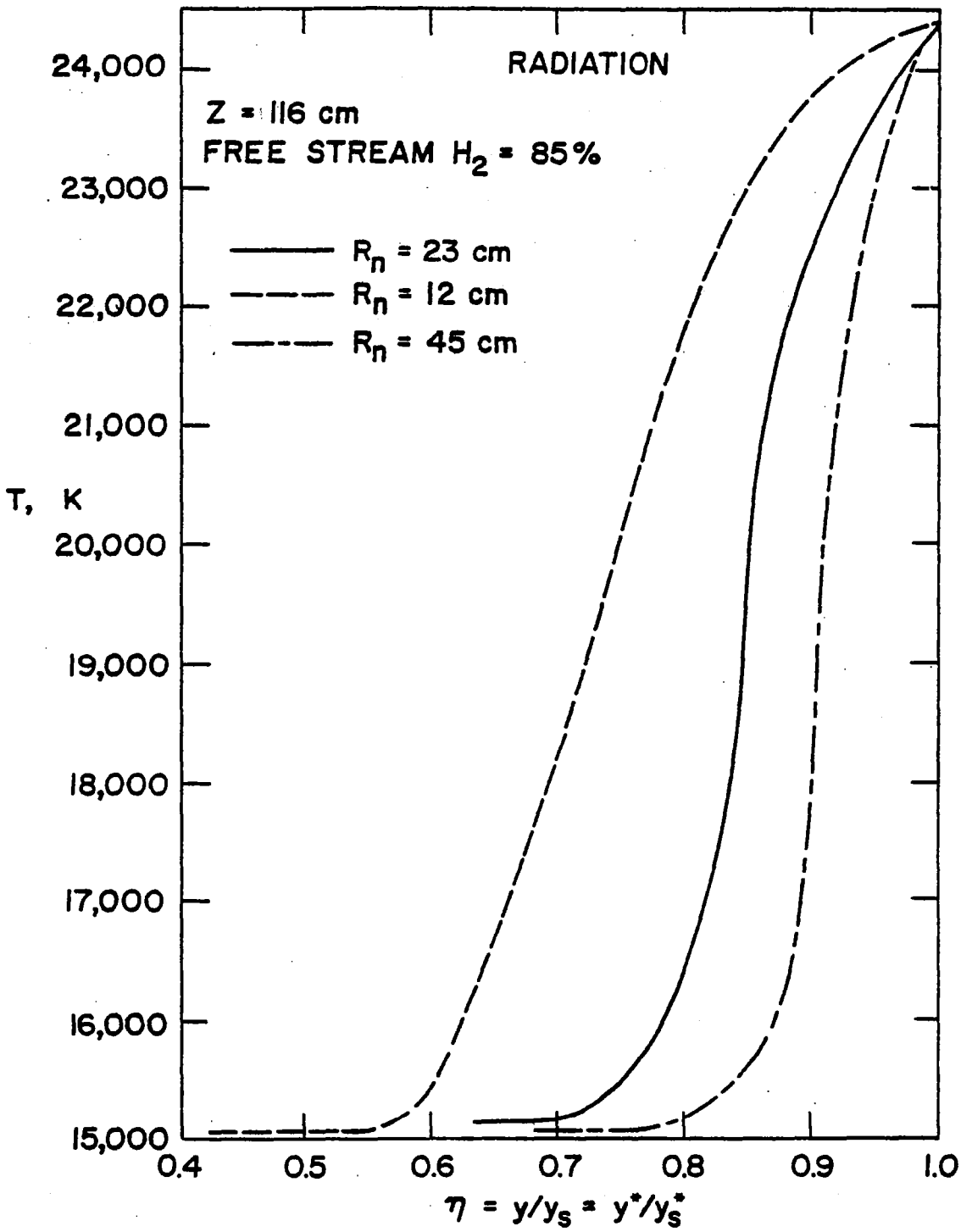

Fig. 62 Temperature variation for different body nose radius in the nonequilibrium region at $\xi = 0$ (with radiation).

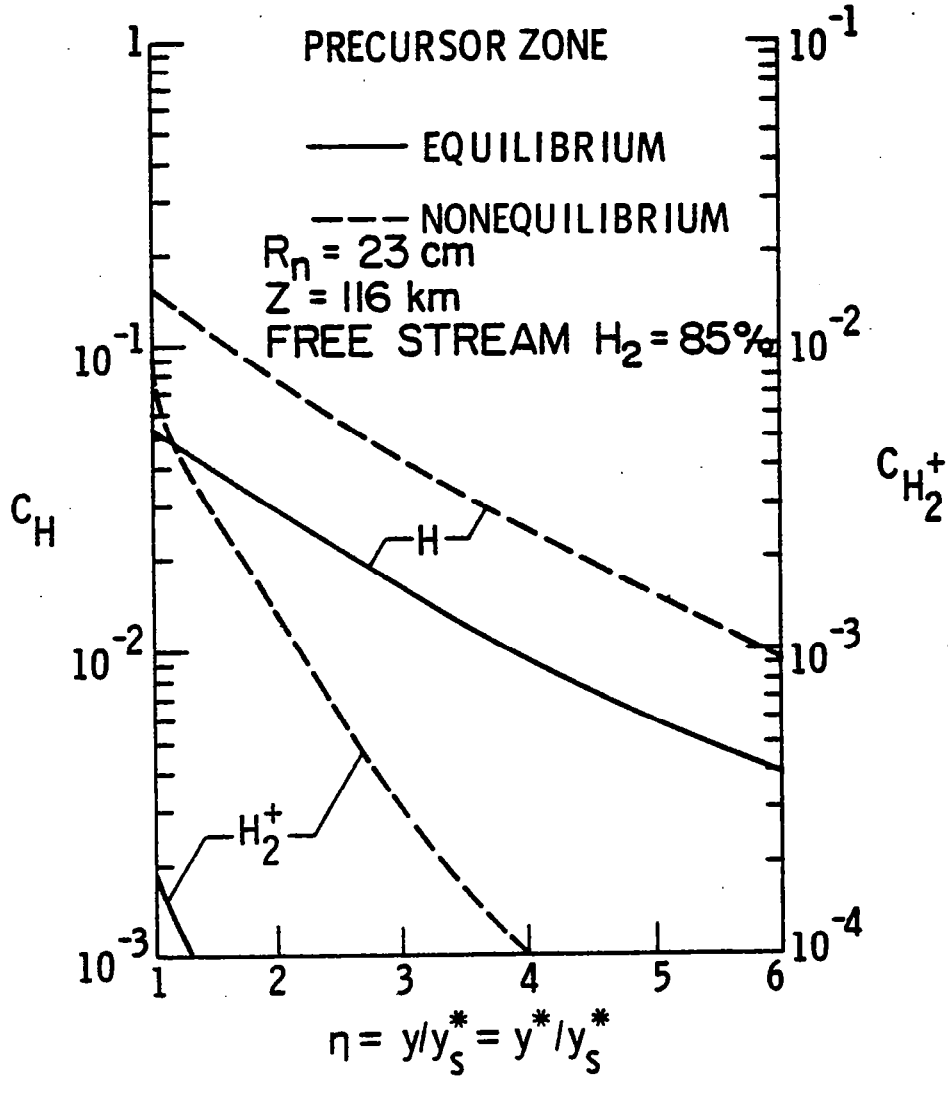

Fig. 63 Species concentration in the precursor region for $\xi = 0$.

properties and their influence on the shock layer flow phenomena, the entire precursor-shock layer solutions are obtained by iterative procedures.

For the case with radiation and for entry conditions at Z = 116 km, the heavy particle and electron temperature variations across the shock layer are illustrated in Fig. 64 along with the equilibrium temperature distribution. In comparision with results of Fig, 60, it is seen that in the present case, the nonequilibrium temperature is lower than the equilibrium temperature in certain portions of the shock. This is a direct consequence of the radiation cooling (i.e., radiation loss to the free stream) of the shock layer. Also, in this case, the nonequilibrium temperature is slightly higher than the equilibrium temperature in the vicinity of the wall. This is because cold gases near the wall absorb radiation from the high temperature region of the shock layer. As would be expected, precursor heating results in a slightly higher shock-layer temperature distribution.

Variations of temperature, pressure, and density along the stagnation streamline in the entire shock layer-precursor zone are illustrated in Figs. 65-68 for different conditions. These results show that precursor effects are higher for the nonequilibrium conditions. This, however, would be expected since in this case, the radiative heat flux towards the precursor region is considerably higher. The shock-layer nonequilibrium condition significantly influences the temperature and pressure variations in the precursor zone, but its effects on density changes are quite small. As noted earlier, in the shock layer, nonequilibrium results approach the corresponding equilibrium values at

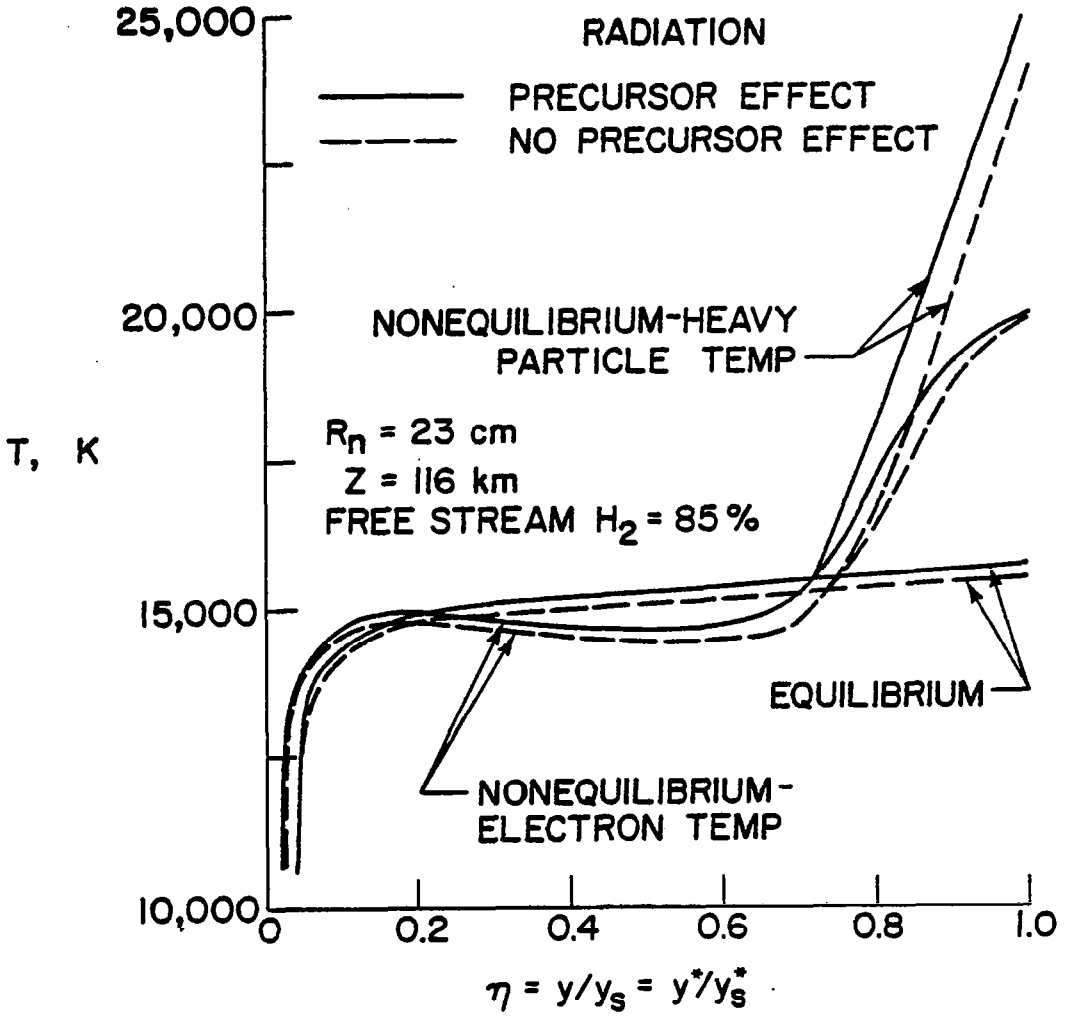

Fig. 64 Equilibrium and nonequilibrium temperature variation in the shock layer (with radiation).

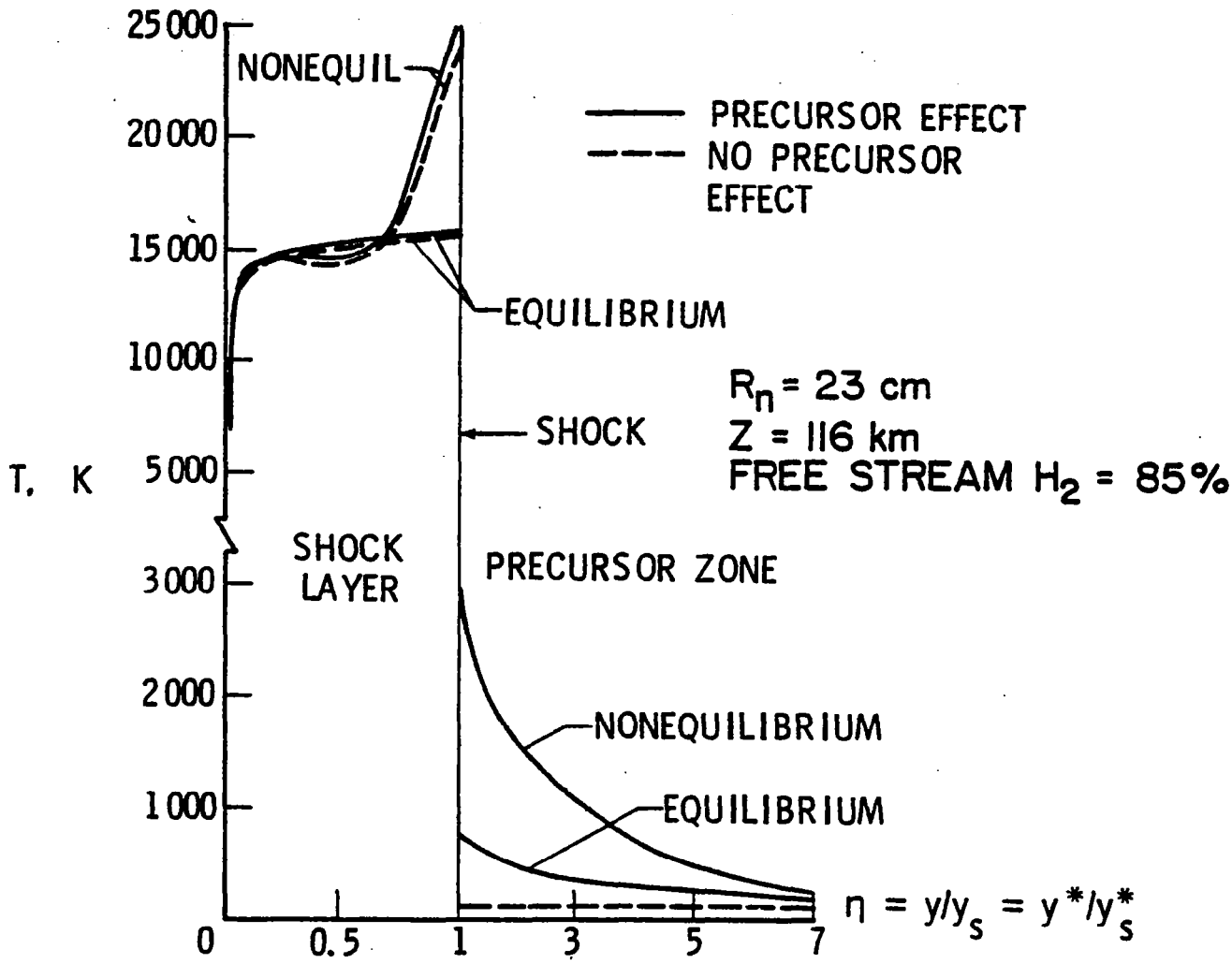

Fig. 65 Temperature variation in the shock/precursor region along the stagnation streamline, Z = 116 km.

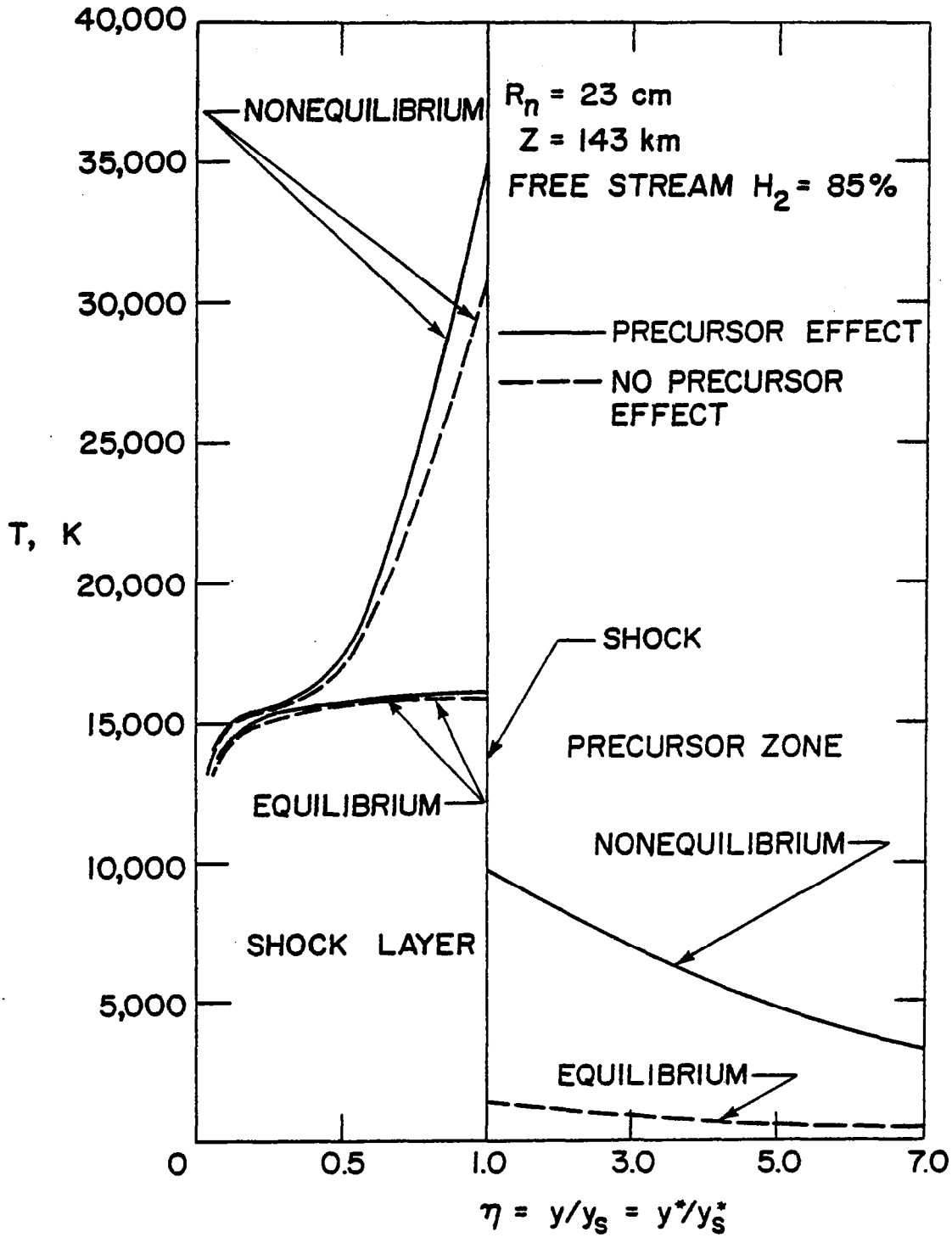

Fig. 66 Temperature variation in the shock/precursor region along the stagnation streamline, Z = 143 km.

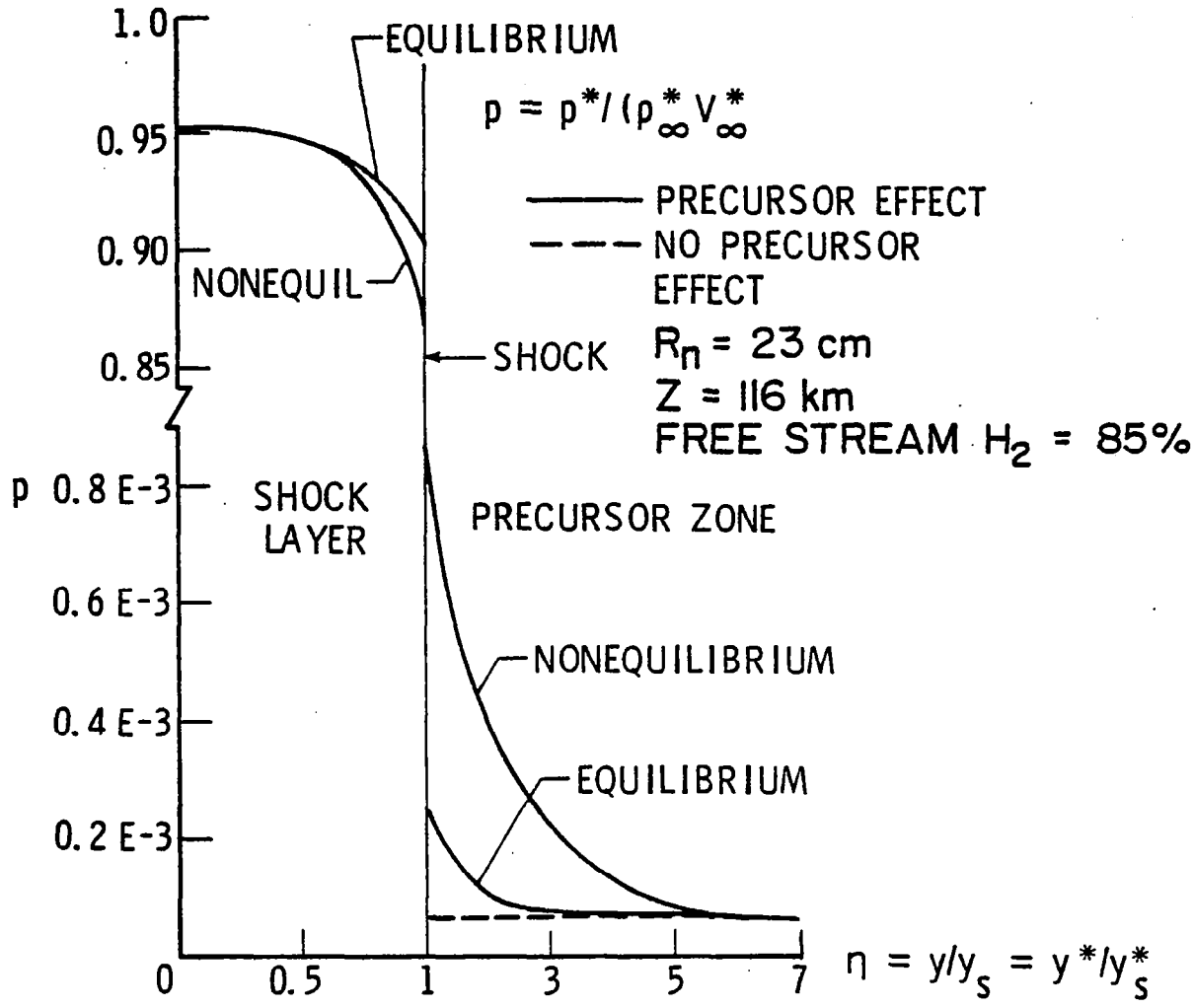

Fig. 67 Pressure variation in the shock/precursor region along the stagnation streamline.

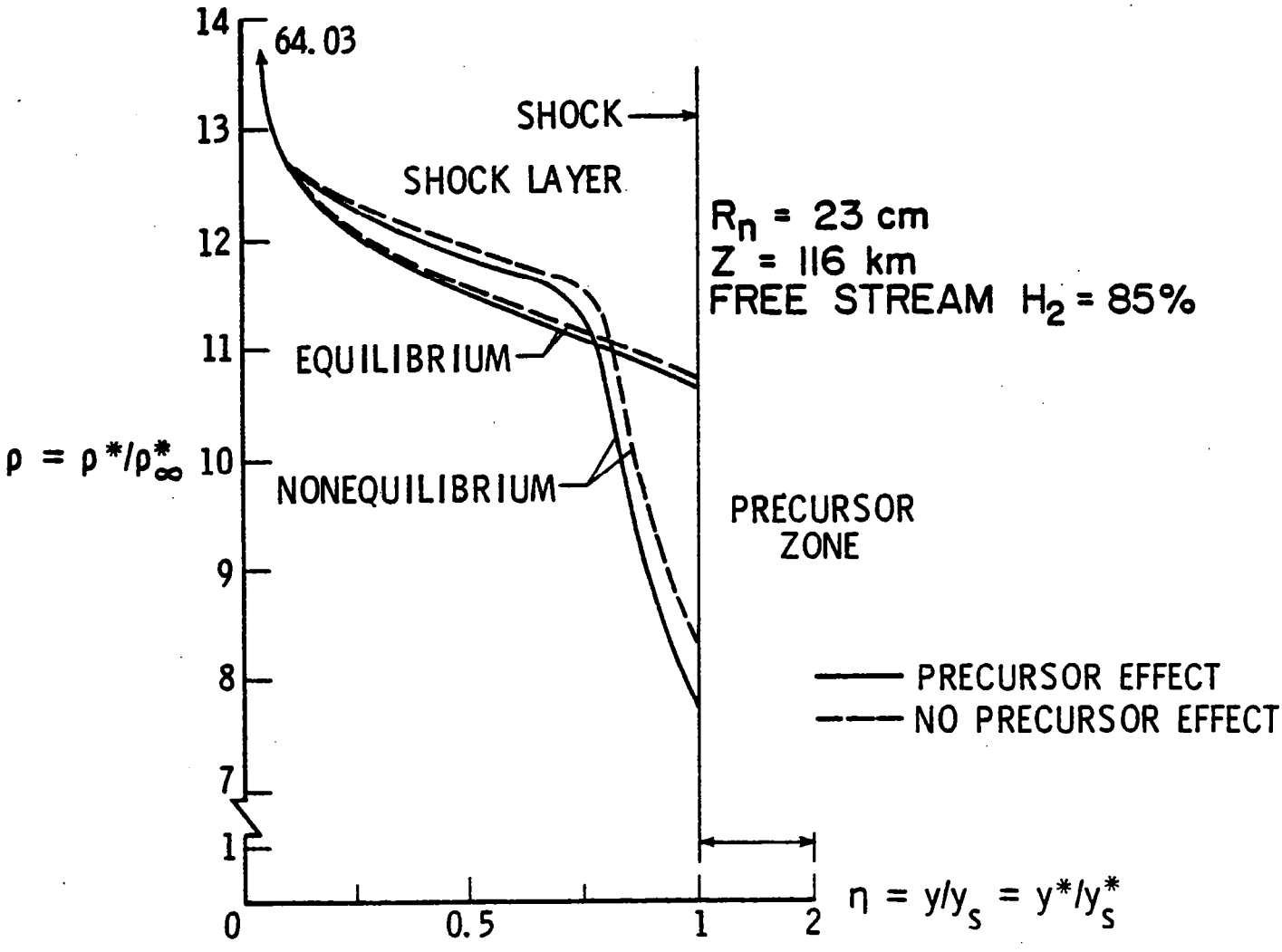

Fig. 68 Density variation in the shock/precursor region along the stagnation streamline.

about 25 percent of the shock layer thickness from the shock wave. For the equilibrium case, the influence of precursor heating on shock-layer temperature, pressure, and density variations is discussed in the previous section.

For a comparision of the shock-layer flow phenomena for the two nominal compositions of the Jovian atmosphere, illustrative results were obtained for entry conditions at Z = 116 km. Results for the temperature variation immediately behind the shock and for the radiative heat flux across the shock layer are illustrated in Figs. 69-71. It is evident from Fig. 69 that the shock temperature is lower by about 2 percent for case of 89 percent hydrogen atmosphere. This is because, in this case, relatively more energy is required to dissociate the molecular hydrogen. Since the shock temperature is lower in this case, the radiatve heat fluxes (q^+ as well as q^-) are lower for both equilibrium and nonequilibrium conditions (see Figs. 70 and 71).

To investigate the extent of heating on an entry body, the variations in radiative heat flux in the shock layer were calculated for different conditions. As discussed earlier, the chemical nonequilibrium effects are more important with small body nose radius and for higher altitude entry conditions. Results for radiative flux towards the shock and body are shown in Fig. 72 for R_n^* = 12 cm and Z = 116 km. The results indicate that, in the nonequilibrium case, the radiative heat flux is increased to about 70 percent toward the body and almost 2.5 times toward the shock (i.e., toward the precursor region). Results for radiative heating of the body for R_n^* = 23 cm and Z = 143 km are shown in Fig. 73. The results show that the heat flux is about three times higher

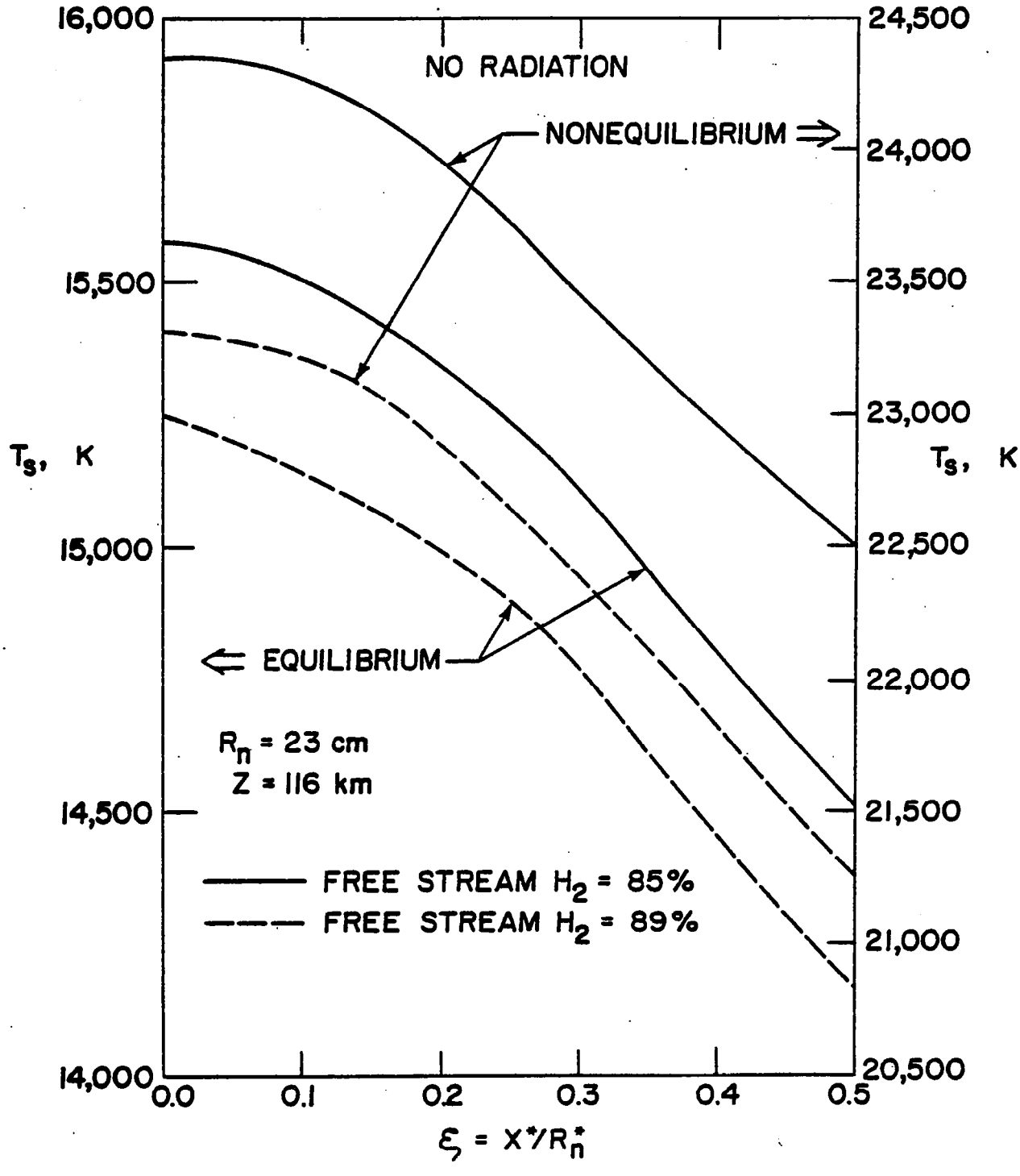

Fig. 69 Equilibrium and nonequilibrium shock temperature variation for different free-stream gas compositions.

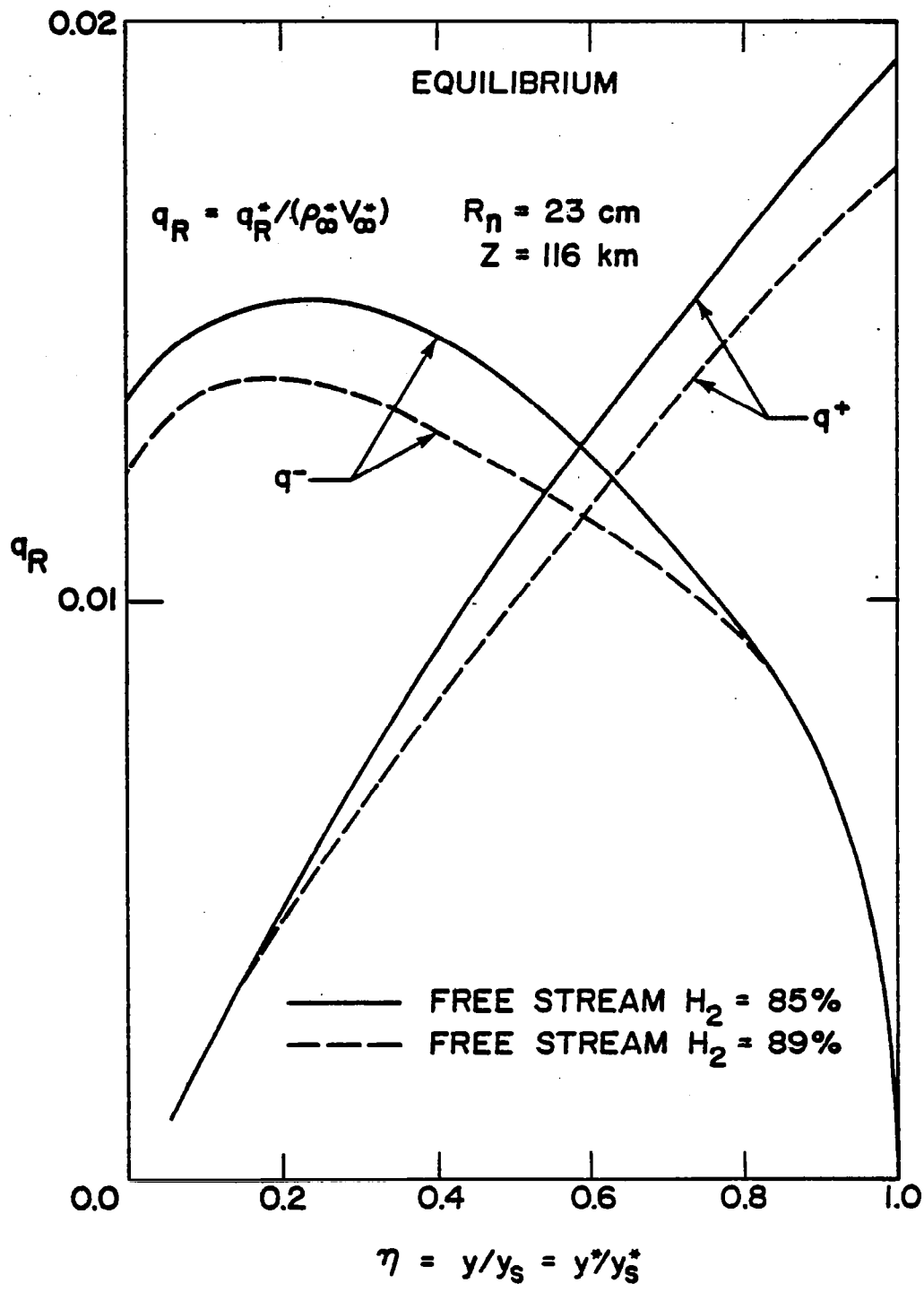

Fig. 70 Equilibrium radiative heat flux variation in the shock layer for different free-stream gas compositions.

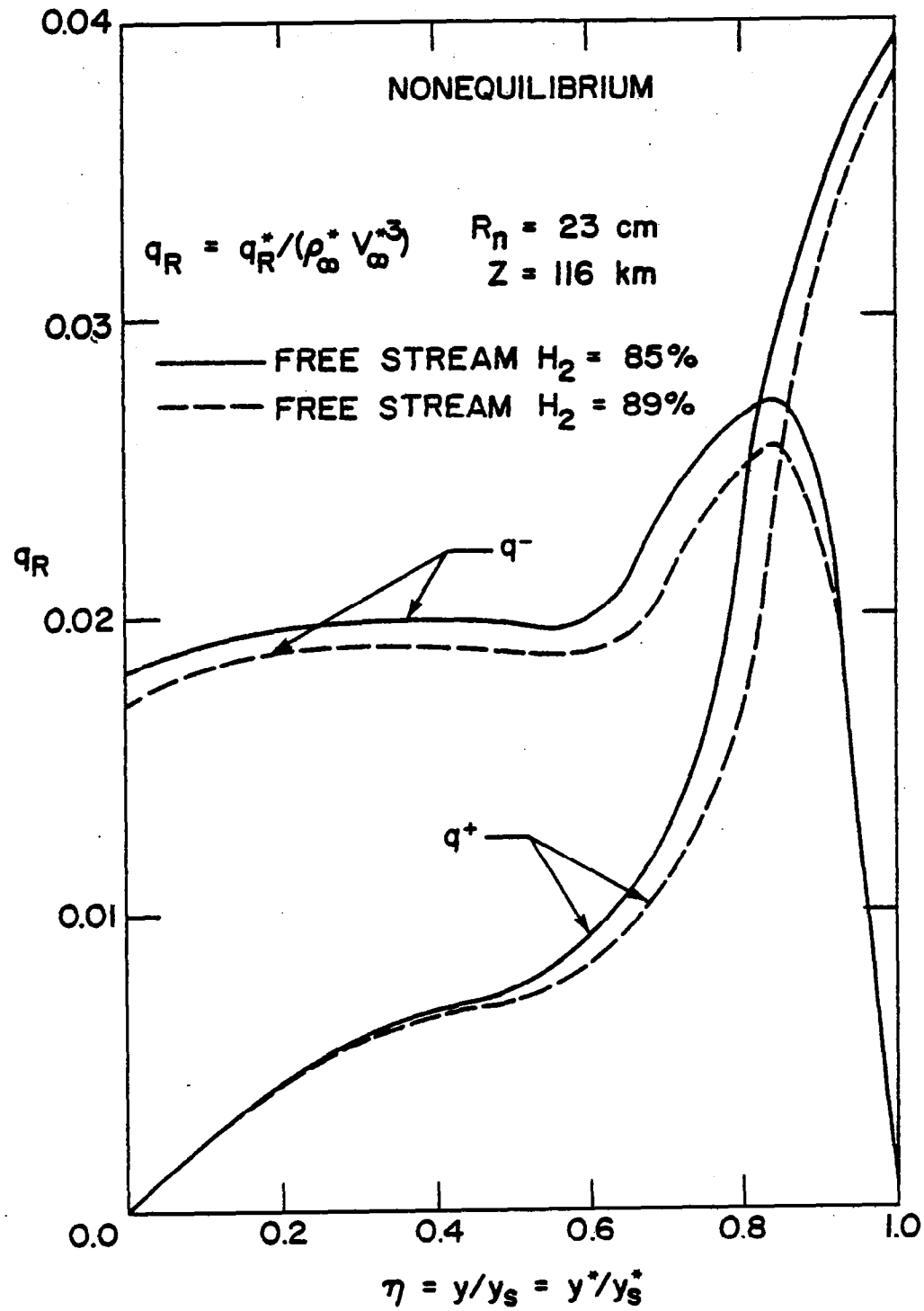

Fig. 71 Nonequilibrium radiative heat flux variation in the shock layer for different free-stream gas compositions.

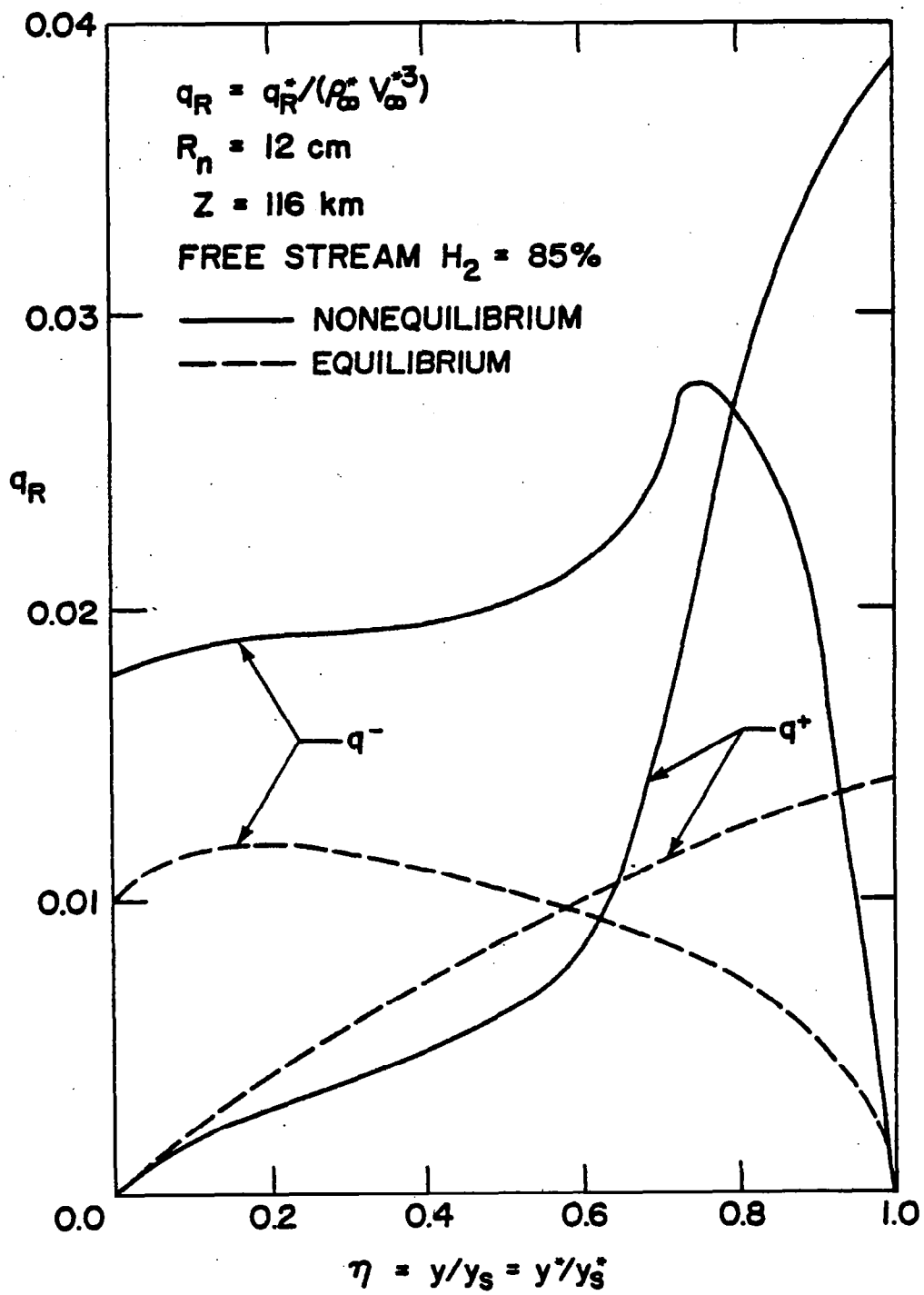

Fig. 72 Equilibrium and nonequilibrium radiative heat-flux variation in the shock layer for R_n = 12 cm.

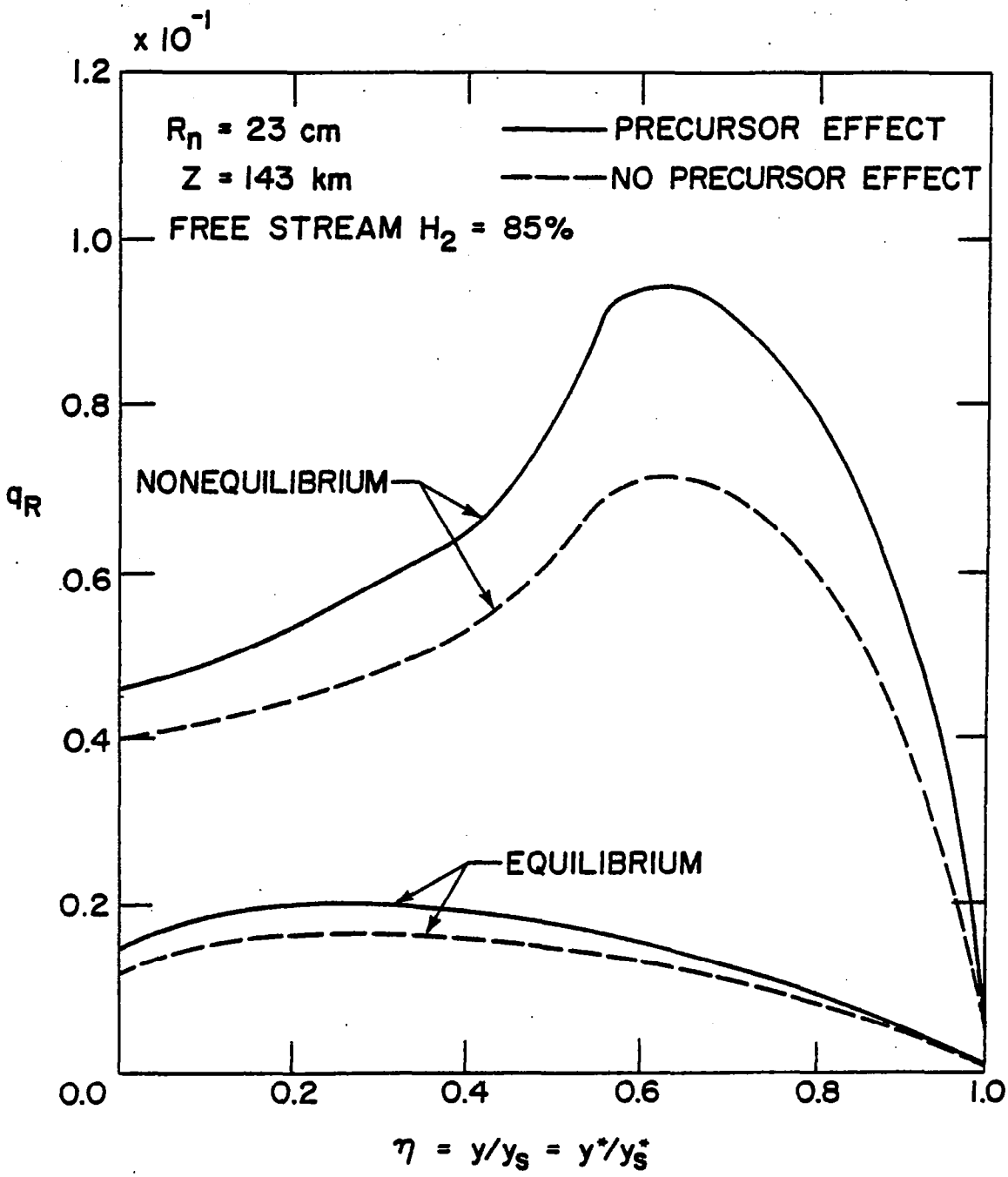

Fig. 73 Equilibrium and nonequilibrium radiative heat-flux variation in the shock layer, Z = 143 km.

for the nonequilibrium conditions. This is a direct consequence of the higher temperature in the nonequilibrium layer near the shock.

To investigate the influence of precursor heating on viscous nonequilibrium shock-layer flow phenomena, specific results were obtained for the peak heating entry conditions and for an entry body with a nose radius of $R_n^* = 23$ cm. These are presented here as final results of the present study.

The radiative heat flux from the shock layer towards the shock front and the precursor region is shown in Fig. 74 for both equilibrium and nonequilibrium conditions. The results clearly indicate that heat flux toward the precursor region is considerably higher for nonequilibrium conditions. This is again a direct consequence of higher nonequilibrium temperature in the shock layer. As discussed before, precursor heating results in a higher radiative flux at the shock front. The results of Fig. 74 indicate that precursor heating results in a 15 percent increase in radiative flux in the nonequilibrium case while only 8.5 percent increase is noticed for the equilibrium condition.

The results of equilibrium and nonequilibrium radiative flux towards the body (along the stagnation line) are illustrated in Fig. 75. Although it is realistic to calculate the radiative flux based on the electron temperature, results (for the case with no precursor effects) have been obtained also by using the heavy particle temperature only for comparative purposes. The nonequilibrium results are seen to be significantly higher than the equilibrium results. This is primarly due to the high temperature region near the shock where nonequilibrium temperature overshoots occur.

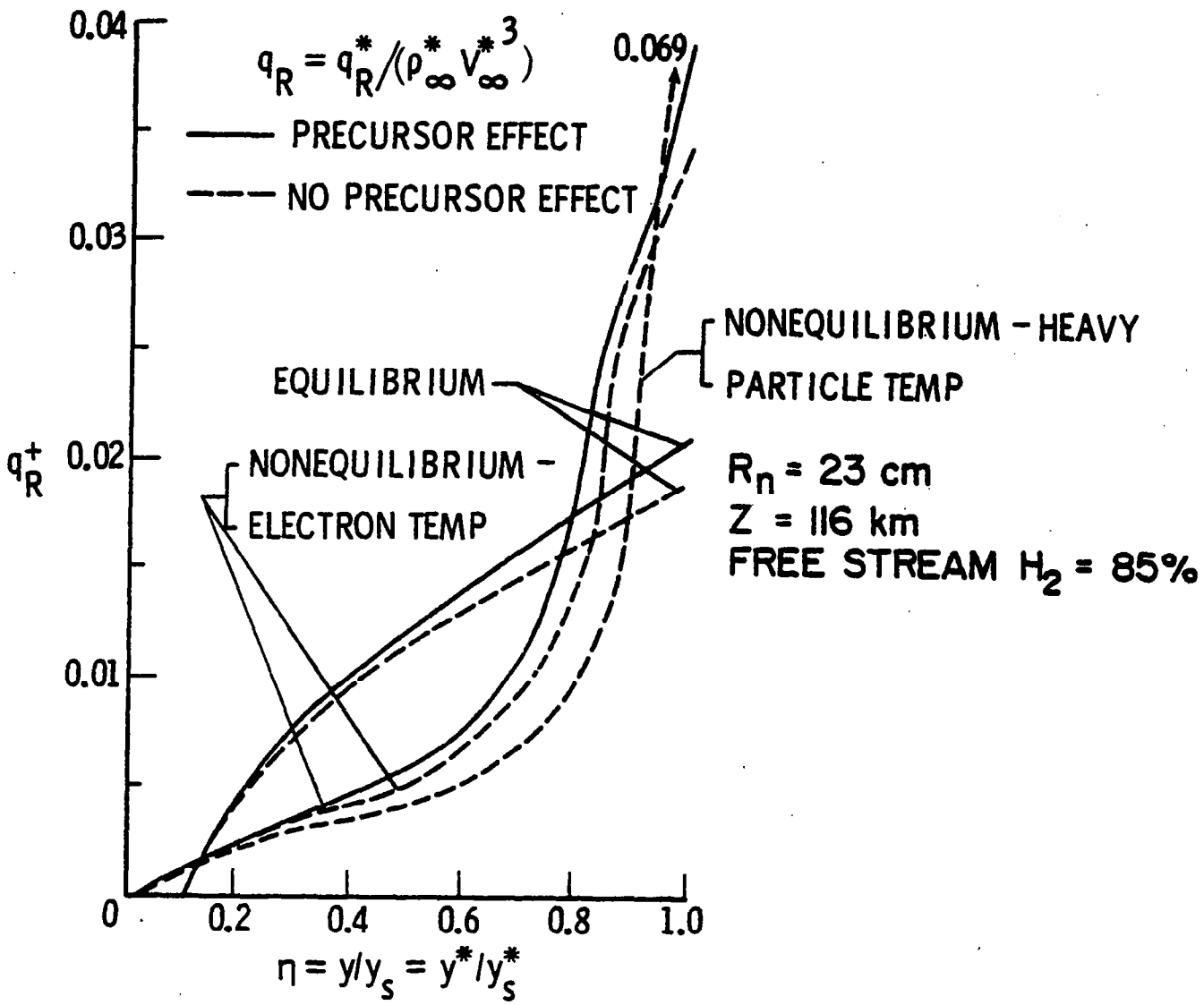

Fig. 74 Equilibrium and nonequilibrium radiative heat flux towards the shock for $\xi = 0$.

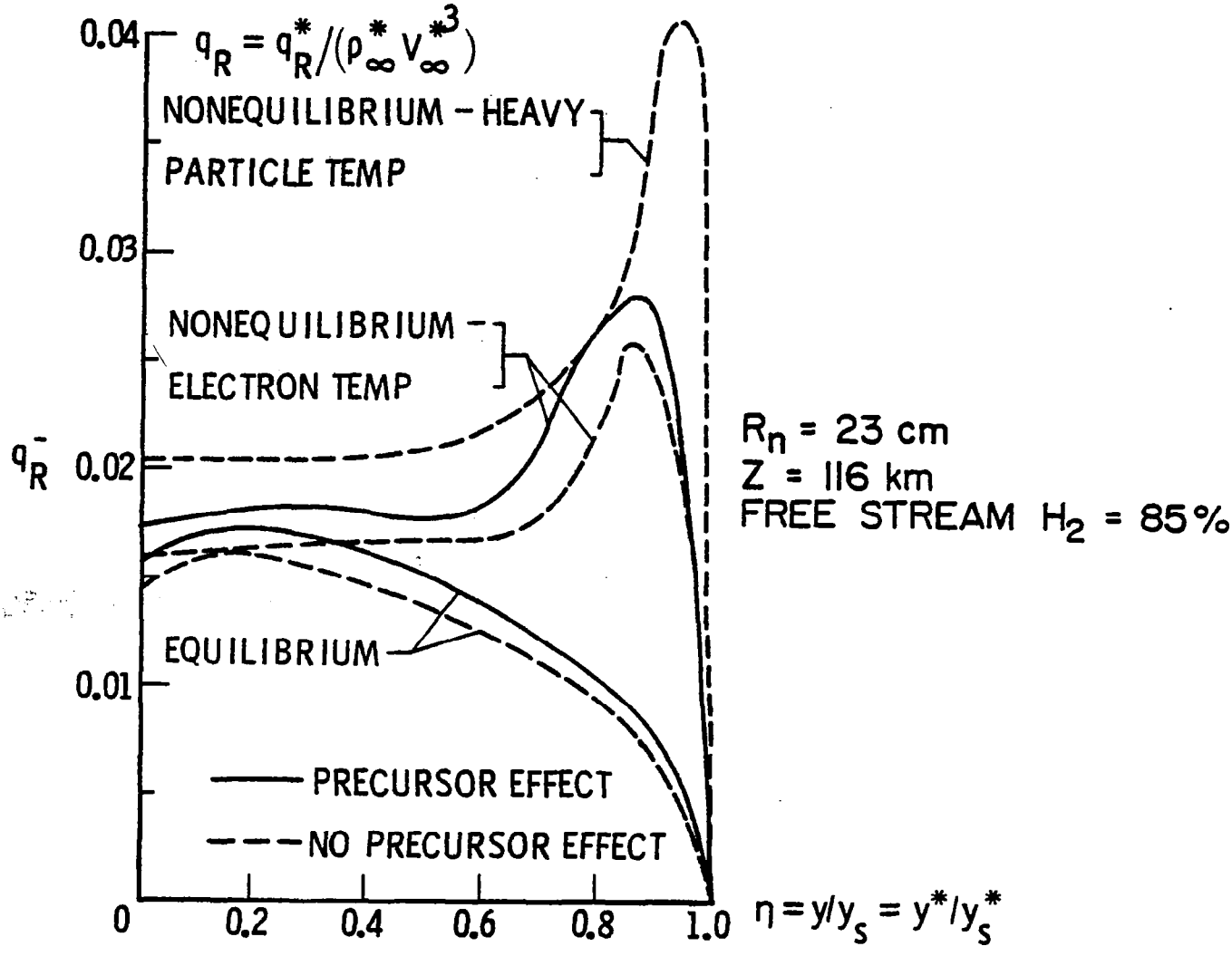

Fig. 75 Equilibrium and nonequilibrium radiative heat flux towards the body for $\xi = 0$.

Figure 76 shows the variation of radiative and convective flux with distance along the body surface. The radiative as well as convective heat transfer to the body surface is seen to be enhanced by the nonequilibrium conditions. As discussed above, the increase in radiative heating is a direct consequence of higher electronic temperature. For the case with no radiation, the convective heat flux toward the body was found to be the same for equilibrium and nonequilibrium conditions. For the case with radiation, however, Fig. 76 shows that the convective heat flux for the nonequilibrium case is about 20 percent higher than the corresponding equilibrium value at the stagnation point. This is because the cold gas near the wall absorbs higher radiative flux from the shock layer under the nonequilibrium conditions. As discussed before, the influence of precursor heating is enhanced due to nonequilibrium conditions. Figure 76 shows that precursor heating results in a 10.5 percent increase in the radiative flux at the stagnation point in the nonequilibrium case while only about 7 percent increase is noted for the equilibrium case.

For the entry conditions considered in this study, therefore, it is logical to conclude that nonequilibrium heating of the body is significantly higher than equilibrium heating. Results similar to this were also obtained by Grose and Nealy [76] for Venusian entry conditions. For certain Jovian entry conditions, results presented in [8,59] indicate that nonequilibrium heating is considerably less than the equilibrium heating. This obviously is in contradiction to the present findings. It should be pointed out that for the entry conditions considered in this study, the temperature just behind the shock is very high and all hydrogen molecules are completed dissociated. Under these conditions,

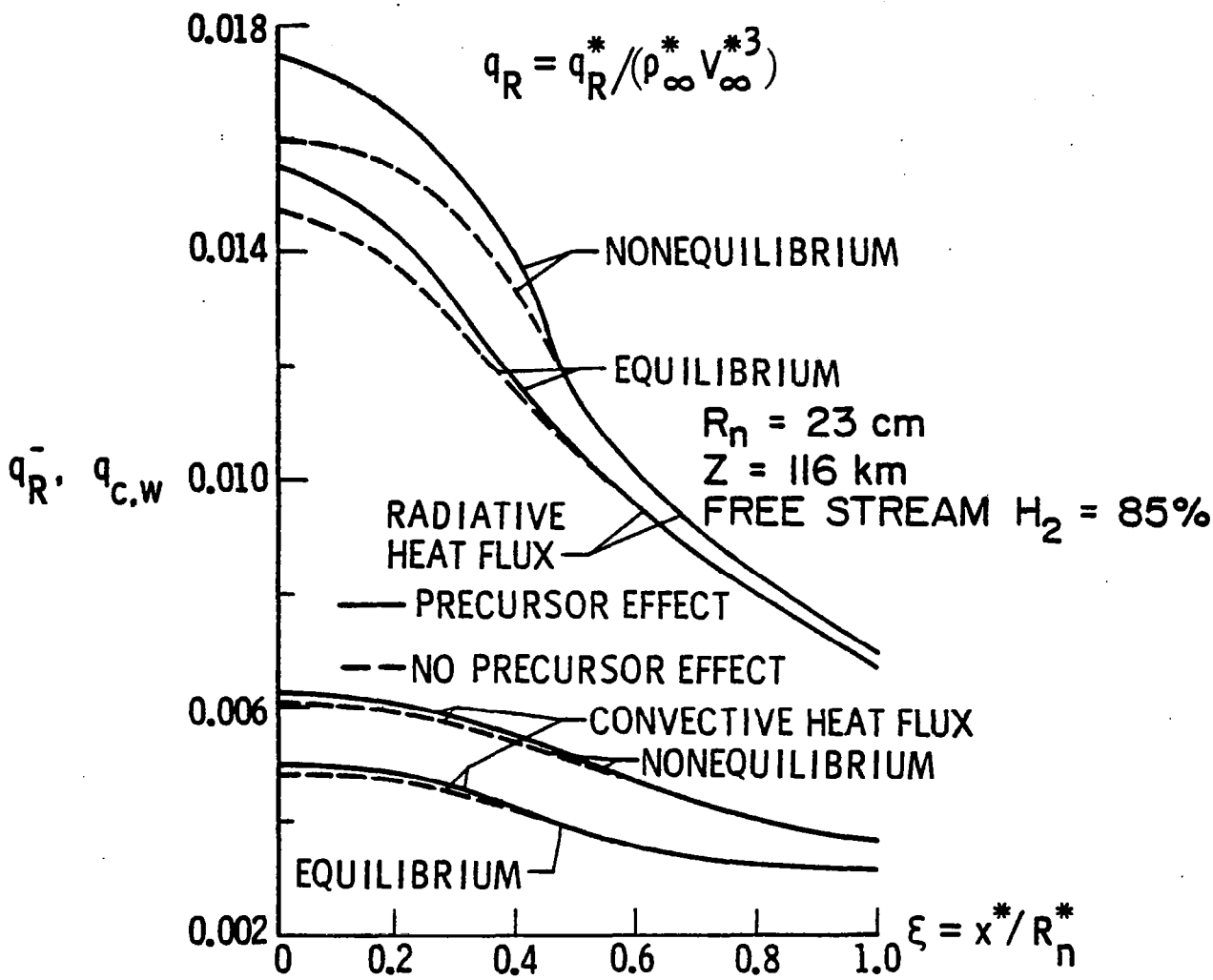

Fig. 76 Variation of radiative and convective heat flux with distance along the body surface.

H_β line emissions are higher than for the equilibrium conditions. This is because, in addition to high temperature, the number density of atomic hydrogen is considerably higher than the equilibrium value. Thus, findings of the present study appear to be completely justified.

CONCLUDING REMARKS

The main objective of this study was to investigate the influence of precursor heating on the entire shock layer flow phenomena around a Jovian entry body under physically realistic conditions. For this purpose, the flow in front of the entry body was divided into three regions, the shock layer, the precursor zone, and the free stream. The problem was formulated by considering the chemical equilibrium as well as non-equilibrium composition of the shock layer gas.

In the precursor region, flow phenomena was investigated by employing the small perturbation theory of classical aerodynamics and the thin layer approximations of hypersonic flow. For Jovian entry conditions, one-dimensional results obtained by the two methods were found to be in good agreement for the range of parameters considered. The results, in general, indicate that for certain combinations of entry speeds and altitudes of entry, the precursor effects cannot be ignored while analyzing flows around Jovian entry bodies. The usefulness of the thin-layer approximation in analyzing the precursor region flow is demonstrated. The main advantage of this method is that it is physically more convincing and its use can be extended easily to axisymmetric and three-dimensional cases.

In the shock layer, results of flow variables were obtained along the body and the bow shock and across the shock layer for different entry conditions. The results show that the slip boundary conditions (both at the shock wave and the body) should be used when the entry altitudes are higher than 225 km. Specific results for the chemical equilibrium condition indicate that, in most cases, precursor heating

has a maximum influence on flow variables (except the pressure) at the stagnation line shock location. It was found that while pressure essentially remains unchanged in the shock layer, the precursor heating results in an increase in the enthalpy, temperature, and v-component of velocity, and a decrease in the shock layer density. For the entry conditions considered in this study, results clearly demonstrate that precursor heating has a significant influence on increasing the heat transfer to the entry body. Chemical nonequilibrium results reveal that there exists a nonequilibrium layer of considerable thickness in the shock layer region and inclusion of the radiative heat flux term in the energy equation increases the thickness of this layer. Under nonequilibrium conditions, temperature (heavy particle as well as electronic) overshoots occur near the shock wave. As a result of this, the radiative as well as convective heat transfer to the body surface is increased significantly. The influence of precursor heating is enhanced due to nonequilibrium conditions; a 9.5 percent increase in the stagnation point radiative heating has been observed at an altitude of 116 km.

For further studies, it is suggested that the precursor region flow phenomena be investigated without making the thin layer approximation. Since precursor region is relatively thin for most entry conditions, this improvement probably will not change the findings of the present study. However, it would be advisable to consider turbulent flow in the shock layer, especially for analyzing the flow away from the stagnation region. Also, a more general model for radiative transport (instead of the tangent slab approximation) should be used, and conditions of different angles of attack for the entry body should be considered.

REFERENCES

1. Smith, G. L., "Radiation-Induced Precursor Flow Field Ahead of a Reentering Body," Ph.D. dissertation, Virginia Polytechnic Institute, March 1968.

2. Smith, G. L., "Radiation Induced Precursor Flow Field Ahead of a Reentering Body," AIAA Paper No. 68-667, June 1968.

3. Liu, J. T. C., "Synoptic: Influence of Upstream Absorption on the Stagnation Region Shock Layer Radiation," AIAA Journal, Vol. 8, No. 10, Oct. 1970, pp. 1730-1737.

4. Liu, J. T. C., "Influence of Upstream Absorption on the Stagnation Region Shock Layer Radiation," AIAA Journal, Vol. 8, No. 10, Oct. 1970, pp. 1730-1737.

5. Murty, S. S. R., "Effect of Line Radiation on Precursor Ionization," J. Quantitative Spectroscopy & Radiative Transfer, Vol. 8, No. 1, Jan. 1968, pp. 1605-1617.

6. Nelson, H. F. and Goulard, R., "Structure of Shock Waves with Nonequilibrium Radiation and Ionization," The Physics of Fluids, Vol. 12, No. 8, Aug. 1969, pp. 1605-1617.

7. Perri, A. N. and Clarke, J. H., "Radiative Ionization Patterns in Cold Precursor of Axisymmetric Detached Shock," AIAA Journal, Vol. 8, No. 9, Sept. 1970, pp. 1574-1581.

8. Leibowitz, L. P. and Kuo, T. J., "Ionizational Nonequilibrium Heating During Outer Planetary Entries," AIAA Journal, Vol. 14, No. 9, Sept. 1976 , pp. 1324-1329.

9. Livingston, F. R. and Poon, T. Y., "Relaxation Distance and Equilibrium Electron Density Measurement in Hydrogen-Helium Plasmas," AIAA Journal, Vol. 14, No. 9, Sept. 1976, pp. 1335-1337.

10. Garrett, L. B., "An Implicit Finite Difference Solution to the Viscous Radiating Shock Layer with Strong Blowing," NASA TMX-67584, 1971.

11. Anderson, J. D., Jr., "An Engineering Survey of Radiating Shock Layer," AIAA Journal, Vol. 7, No. 9, Sept. 1969, pp. 1665-1675.

12. Sutton, K., "Characteristic of Coupled Nongray Gas Flows with Ablation Product Effects About Blunt Bodies During Planetary Entries," Ph.D. Dissertation, North Carolina State University, 1973.

13. Kumar, A.; Tiwari, S. N.; and Graves, R. A.: Effects of Small Angle of Attack on Radiating Viscous Shock Layer Solutions for Jovian Entry. AIAA Paper, No. 78-909, May 1978. Also, Technical Report NSG-1464, May 1978, School of Engineering, Old Dominion University, Norfolk, Virginia.

14. Davis, R. T.: Numerical Solution of the Hypersonic Viscous Shock-Layer Equations. AIAA Journal, Vol. 8, No. 5, May 1970, pp. 843-851.

15. Moss, J. N.: Reacting Viscous-Shock-Layer Solutions with Multicomponent Diffusion and Mass Injection. NASA TR R-411, June 1974.

16. Moss, James N.: Stagnation and Downstream Viscous-Shock-Layer Solutions with Radiation and Coupled Ablation Injection. AIAA Paper 74-73, AIAA 12th Aerospace Sciences Meeting, Washington, D.C., Jan. 1974.

17. Moss, J. N.: Radiative Viscous-Shock-Layer Solutions with Coupled Ablation Injection. AIAA Journal, Vol. 14, No. 9, Sept. 1976, pp. 1311-1316.

18. Lasher, L. E.; and Wilson, K. H.: Effect of Shock Precursor Absorption on Superorbital Entry Heating. AIAA Journal, Vol. 6, No. 12, Dec. 1968, pp. 2419-2420.

19. Lasher, L. E.; and Wilson, K. H.: Effect of Shock Precursor Heating on Radiative Flux to Blunt Bodies. NASA CR-1265, Feb. 1969.

20. Hudson, R. D.: Critical Review of Ultraviolet Photoabsorption Cross Section for Molecules of Astrophysical and Aeronomic Interest. Review of Geophysics and Space Physics, Vol. 9, No. 2, May 1971, pp. 305-406.

21. Lee, L. C.; Carson, R. W.; and Judge, D. L.; The Absorption Cross Sections of H_2 and D_2 from 180 to 780 A, Journal of Quantitative Spectroscopy & Radiative Transfer, Vol. 16, No. 10, Oct. 1976, pp. 873-877.

22. Nicolet, W. E.: User's Manual for the Generalized Radiation Transfer Code (RAD/EQUIL), Aerotherm Report No. UM-69-9, Aerotherm Corp., Mountain View, California, 1969. Also: User's Manual for RAD/EQUIL/1973. A General Purpose Radiation Transport Program, NASA CR-132470, 1973.

23. Wilson, K. H.: RATRAP - A Radiation Transport Code. Report No. 6-77-67-12, Lockheed Missiles & Space Co., Sunnyvale California, March 14, 1967.

24. Thomas, M.; The Spectral Linear Absorption Coefficient of Gases - Computer Program SPECS (H 189). Douglas Report DAC-59135, McDonnell-Douglas Astronautics Co., Western Division, Santa Monica, California, 1967.

25. Falanga, R. A.; and Olstad, W. B.: An Approximate Inviscid Radiation Flow-Field Analysis for Sphere-Cone Venusian Entry Vehicles, AIAA Paper No. 74-758, July 1974.

26. Zoby, E. V.; Sutton, K.; Olstad, W. B.; and Moss, J. N.; A Approximate Inviscid Radiation Flow Field Analysis of Outer Planet Entry Probes. AIAA Paper No. 78-189, Jan. 1978.

27. Tiwari, S. N.; and Subramanian, S. V.; Significance of Radiation Models in Investigating the Flow Phenomena Around a Jovian Entry Body. Technical Report NAS1-14193-26, Jan. 1978, School of Engineering, Old Dominion University, Norfolk, Virginia. Also, AIAA Paper No. 78-188, Jan. 1978.

28. Vincenti, W. G.; and Kruger, C. H.: Introduction to Physical Gas Dynamics, John Wiley and Sons, 1965.

29. Sparrow, E. M.; and Cess, R. D.: Radiation Heat Transfer, Brooks/Cole Publishing Co., Belmont, California, 1966.

30. Penner, S. S.; and Olfe, D. B.: Radiation and Reentry, Academic Press, 1968.

31. Hayes, W. D.; and Probstein, R. F.; Hypersonic Flow Theory, Academic Press, New York, 1959.

32. Cheng, H. K.: The Blunt-Body Problem in Hypersonic Flow at Low Reynolds Number. Inst. Aerospace Science Paper, No. 63-92, 1963.

33. Shidlovsky, V. P.: Introduction to Rarefied Gases, New York, American Elsevier Publishing Company, Inc., 1967.

34. Probstein, R. F.; and Pan, Y. S.: Shock Structure and Leading Edge Problem. Rarefied Gas Dynamics, Vol. 2 (Laurmann, J. A. Ed.), New York, Academic Press, 1963.

35. Pan, Y. S.; and Probstein, R. F.: Rarefied-Flow Transition at a Leading Edge. Proceedings of International Symposium on Fundamental Phenomena in Hypersonic Flow, Cornell Univ. Press, 1966, pp. 259-306.

36. Rott, N.; and Lenard, M.: The Effect of Slip, Particularly for Highly Cooled Walls. Journal Aerospace Science, Vol. 29, 1969, pp. 591-595.

37. Anon: The Planet Jupiter. NASA SP-8069, Dec. 1971.

38. Moss, J. N.; Anderson, E. C.; and Bolz, C. W.: Aerothermal Environment for Jovian Entry Probes. AIAA Paper No. 76-469, June 1976.

39. Sutton, K.; Jones, J. J.; and Powell, R. W.: Effects of Atmospheric Structure on Radiative Heating for Jupiter Entry Probe. AIAA Paper, No. 78-185, Jan. 1978.

40. Shapiro, A. H.: The Dynamics and Thermodynamics of Compressible Fluid Flow, Vol. I, The Ronald Press, New York, 1953.

41. Liepmann, H. W.; and Roshko, A.: Element of Gasdynamics, John Wiley and Sons, 1957.

42. Tiwari, S. N.; and Szema, K. Y.: Radiation Induced Precursor Flow Field Ahead of a Jovian Entry Body. NASA CR-145221, 1977.

43. Tiwari, S. N.; and Szema, K. Y.: Radiation-Induced Precursor Flow Field Ahead of a Jovian Entry Body. AIAA Paper No. 77-768, June 1977.

44. Blottner, F. G.: Finite Difference Methods of Solution of the Boundary-Layer Equation. AIAA Journal, Vol. 8, No. 2, Feb. 1970, pp. 193-205.

45. Tiwari, S. N.; and Szema, K. Y.: Influence of Precursor Heating on Viscous Flow Around a Jovian Entry Body. NASA CR-3174, 1979.

46. Tiwari, S. N.; and Szema, K. Y.: Influence of Precursor Heating on Viscous Flow Around a Jovian Entry Body. AIAA Paper No. 78-190, Jan. 1978.

47. Zoby, E. V.; Gnoffo, P. A.; and Graves; R. A.: Correlations for Determining Thermodynamic Properites of Hydrogen-Helium Gas Mixtures at Temperatures from 7,000 to 35,000 K. NASA TN D-8262, Aug. 1976.

48. Street, R. E.: Problem of Slip Flow in Aerodynamics. NASA RM S-7A30, 1957.

49. Street, R. E.: A Study of Boundary Conduction in Slip-Flow Aerodynamics. Rarefied Gas Dynamics (Devienne, F. M. Ed.), London Pergamon Press, 1960, pp. 276-292.

50. Davis, R. T.; and Flüge-Lotz, I.: Second Order Boundary-Layer Effect in Hypersonic Flow Past Axisymmetric Blunt Bodies. Journal of Fluid Mechanics, Vol. 20, May 1964, pp. 593-623.

51. Scott, C. D.; Reacting Shock Layer with Slip and Catalytic Boundary Condition. AIAA Journal, Vol. 13, Oct. 1975, pp. 1271-1278.

52. Chow, R. R.; and Ting, L. J.: Aerospace Science. Vol. 28, 1961, pp. 428-430.

53. VanDyke, M. D.: Perturbation Method in Fluid Mechanics. New York Academic Press, 1964.

54. Probstein, R. F.; and Kemp, H. N., Jr.; Viscous Aerodynamic Characteristic in Hypersonic Rarefied Gas Flow, Aero/Space Science, Vol. 27, 1960, pp. 174-193.

55. Ditchburn, R. W.: Absorption of Ultra-Violet Radiation by the Atmospheric Gases. Proceedings of the Royal Society, Series A, Mathematical and Physical Sciences, No. 1205, Vol. 236, Aug. 1956, pp. 216-226.

56. Babu, S. G.: Approximate Thermochemical Tables of Some C-H and C-H-O Species. NASA CR-2187, March 1973.

57. McBridge, B. J.; Heimel, S.; Ehlers, J. G.; and Gordon, S.: Thermodynamic Properties to 6000 K for 210 Substances Involving the First 18 Element. NASA Report SP-3001, 1963.

58. Bird, R. B.; Stewart, W. E.; and Lightfoot; E. N.: Transport Phenomena. John Wiley and Sons, 1960.

59. Hall, N. A.: Thermodynamics of Fluid Flow. Prentice Hall, Inc., 1957.

60. Esch, D. D.; Pike, R. W.; Engle, C. D.; Farmer, R. C.; and Balhoff, J. F.: Stagnation Region Heating of a Phenolic Nylon Ablator During Return from Planetary Mission. NASA CR-112026, Sept. 1971.

61. Leibowitz, L. P.: Measurement of the Structure of an Ionizing Shock Wave in a Hydrogen-Helium Mixture. The Physics of Fluids, Vol. 16, No. 1, Jan. 1973, pp. 59-68.

62. Tiwari, S. N.; and Szema, K. Y.: Effects of Precursor Heating on Chemical and Radiative Nonequilibrium Viscous Flow Around a Jovian Entry Body. AIAA Paper No. 78-907, May 1978.

63. Tiwari, S. N.; and Szema, K. Y.: Effects of Precursor Heating on Chemical and Radiative Nonequilibrium Viscous Flow Around a Jovian Entry Body. NASA CR-158132, 1978.

64. Blottner, F. G.: Viscous Shock Layer at the Stagnation Point with Nonequilibrium Air Chemistry. AIAA Journal, Vol. 7, No. 12, Dec. 1969, pp. 2281-2288.

65. Appleton, J. P.; and Bray, K. N. C.: The Conservation Equations for a Nonequilibrium Plasma. Journal of Fluid Mechanics, Vol. 20, Part 4, Dec. 1964, pp. 659-672.

66. Kennet, H.; and Strack, S. L.: Stagnation Point Radiative Heat Transfer. ARS J., Vol. 31, No. 3, 1961, pp. 370-372.

67. Hoshizaki, H.; and Lasher, L. E.: Convective and Radiative Heat Transfer to an Ablating Body. AIAA Journal, Vol. 6, No. 8, 1968, pp. 1441-1449.

68. Chien, Kuei-Yuan: Application of the S_n Methods to Spherically Symmetric Radiative-Transfer Problems. AIAA Paper No. 71-466, 1971.

69. Wilson, K. H.: Evaluation of One-Dimensional Approximations for Radiative Transport in Blunt Body Shock Layers. NASA CR-1990, 1972.

70. Page, W. A.: Aerodynamic Heating for Probe Vehicles Entering the Outer Planets. AAS Paper No. AAS-71-144, 1971.

71. Lee, P.; and Weissler, G. L.: Absolute Absorption of the H_2 Continuum. Astrophysical J., Vol. 115, 1952, pp. 570-571.

72. Cook, G. R.; and Metzer, P. H.: Photoionization and Absorption Cross Section of H_2 and D_2 in the Vacuum Ultraviolet Region. J. Opt. Soc. America, Vol. 54, No. 8, Aug. 1964, pp. 968-972.

73. Samson, J. A. R.; and Cairns, R. B.: Total Absorption Cross Section of H_2, N_2, and O_2 in the Region 550-200 A. J. Opt. Soc. America, Vol. 55, No. 8, Aug. 1965, p. 1035.

74. McCarty, R. D.: Hydrogen Technology Survey: Thermophysical Properties. NASA Report SP-3089, 1975.

75. Gerald, C. F.: Applied Numerical Analysis, Addison Wesley, 1970.

76. Grose, W. L.; and Nealy, J. E.: Estimates of Nonequilibrium Radiation for Venus Entry. AIAA Journal, Vol. 13, No. 4, April 1975, pp. 421-424.

*U.S. GOVERNMENT PRINTING OFFICE: 1979 - 635-004/32

1. Report No.	2. Government Accession No.	3. Recipient's Catalog No.
NASA CR- 3186		

4. Title and Subtitle	5. Report Date
Effects of Precursor Heating on Radiative and Chemically Reacting Viscous Flow Around a Jovian Entry Body	October 1979
	6. Performing Organization Code
7. Author(s)	8. Performing Organization Report No.
S. N. Tiwari and K. Y. Szema	
9. Performing Organization Name and Address	10. Work Unit No.
Old Dominion University Research Foundation P. O. Box 6369 Norfolk, Virginia 23508	11. Contract or Grant No. NSG-1492
12. Sponsoring Agency Name and Address	13. Type of Report and Period Covered Contractor Report Feb. 1, 1978-Mar. 31, 1979
National Aeronautics and Space Administration Washington, DC 20546	14. Sponsoring Agency Code

15. Supplementary Notes

Langley Technical Monitor: Randolph A. Graves, Jr.
Final Report

16. Abstract

The influence of changes in the precursor region flow properties on the entire shock-layer flow phenomena around a Jovian entry body is investigated under physically realistic conditions. In the precursor region, the flow is considered to be inviscid and the variations in flow properties are determined by employing the small perturbation technique as well as the thin-layer approximation. The flow in the shock layer is assumed to be steady, axisymmetric, and viscous. The analysis is carried out by considering both the chemical equilibrium and nonequilibrium composition of the shock-layer gas. The effects of transitional range behavior are included in the analysis of high altitude entry conditions.

Realistic thermo-physical and radiation models are used, and results are obtained by employing the implicit finite difference technique in the shock layer and an iterative procedure for the entire shock layer-precursor zone. Results obtained for a 45^{o} hyperboloid blunt body entering Jupiter's atmosphere at zero angle of attack indicate that preheating of the gas significantly increases the static pressure and temperature ahead of the shock for entry velocities exceeding 36 km/sec. The nonequilibrium radiative heating rate to the body is found to be significantly higher than the corresponding equilibrium heating. The precursor heating, in general, increases the radiative and convective heating to the body, and this increase is slightly higher for the nonequilibrium conditions.

17. Key Words (Suggested by Author(s))	18. Distribution Statement
Shock-Layer Precursor Heating, Nonequilibrium Radiative Heating, Heating of Entry Bodies	Unclassified - Unlimited Subject Category 34

19. Security Classif. (of this report)	20. Security Classif. (of this page)	21. No. of Pages	22. Price*
Unclassified	Unclassified	180	$9.00

* For sale by the National Technical Information Service, Springfield, Virginia 22161